Universidade de Aveiro Departamento de Engenharia Mecânica
2017

Fábio António Oliveira Fernandes

Análise Biomecânica de impactos com capacetes: novos materiais e geometrias

Biomechanical analysis of helmeted head impacts: novel materials and geometries

Universidade de Aveiro Departamento de Engenharia Mecânica
2017

Fábio António Oliveira Fernandes

Análise Biomecânica de impactos com capacetes: novos materiais e geometrias

Biomechanical analysis of helmeted head impacts: novel materials and geometries

Tese apresentada à Universidade de Aveiro para cumprimento dos requisitos necessários à obtenção do grau de Doutor em Engenharia Mecânica, realizada sob a orientação científica do Doutor Ricardo José Alves de Sousa, Professor Auxiliar do Departamento de Engenharia Mecânica da Universidade de Aveiro e do Doutor Rémy Willinger, Professor da Universidade de Estrasburgo.

Thesis presented to the University of Aveiro as a requirement to obtain the Doctoral Degree in Mechanical Engineering, and carried out under the scientific supervision of Doctor Ricardo José Alves de Sousa, Assistant Professor at Department of Mechanical Engineering, University of Aveiro and Doctor Rémy Willinger, Professor at Strasbourg University.

Apoio financeiro da FCT e do FSE no âmbito do III Quadro Comunitário de Apoio.

o júri

presidente

Prof. Doutor Aníbal Manuel de Oliveira Duarte
Professor Catedrático do Departamento De Eletrónica, Telecomunicações e Informática da Universidade de Aveiro

Prof. Doutora Teresa Maria Salgado de Magalhães
Professora Associada Convidada da Faculdade de Medicina da Universidade do Porto

Prof. Doutor Renato Manuel Natal Jorge
Professor Associado com Agregação da Faculdade de Engenharia da Universidade do Porto

Prof. Doutor Robertt Angelo Fontes Valente
Professor Associado do Departamento de Engenharia Mecânica da Universidade de Aveiro

Prof. Doutor Ricardo José Alves de Sousa
Professor Auxiliar do Departamento de Engenharia Mecânica da Universidade de Aveiro

Prof. Doutora Ofélia Maria Serralha dos Anjos
Professora Adjunta da Escola Superior Agrária do Instituto Politécnico de Castelo Branco

agradecimentos

Ao completar mais uma fase do meu percurso académico, é com o maior orgulho que aqui presto os meus sinceros agradecimentos às pessoas que me ajudaram na realização deste trabalho, a qual não estaria terminada sem o seu apoio.

Em primeiro lugar, os meus sinceros agradecimentos ao meu orientador Professor Ricardo Sousa pelo apoio prestado ao longo deste percurso. A sua motivação, visão e orientação muito contribuíram para o meu crescimento científico e também pessoal. O meu sincero obrigado pela amizade e orientação ao longo deste últimos anos.

To Professor Mariusz Ptak from the Wroclaw University of Technology for all the productive scientific discussions, sharing of expertise and also his friendship.

À Fundação Portuguesa para a Ciência e a Tecnologia (FCT) pelo seu apoio financeiro com a bolsa SFRH/BD/91292/2012.

À Corksribas, Sofalca e Petibol pelas amostras de material cedidas.

A todos os colegas do GRIDS, com um especial obrigado aos ex-colegas de gabinete e também amigos pelo excelente ambiente de trabalho proporcionado, pelas discussões com e sem teor científico e sobretudo pela boa disposição.

Aos meus pais por terem sido dois pilares ao longo da minha vida.

À Cátia, pela sua importância na minha vida, pelo seu apoio, carinho e sobretudo pela paciência e amor.

A todos aqueles que de alguma forma fizeram parte deste percurso, um obrigado.

palavras-chave

absorção de energia, caracterização de material, cérebro, cortiça, impacto, lesões cerebrais, materiais celulares, materiais naturais, modelo de cabeça humana, proteção individual, segurança passiva, simulação numérica, traumatismo craniano

resumo

A cortiça é um material celular natural capaz de suster quantidades consideráveis de energia. Estas características tornam este material ideal para determinadas aplicações como a proteção de impactos. Considerando equipamentos de segurança passiva pessoal, os materiais sintéticos são hoje em dia os mais utilizados, em particular o poliestireno expandido. Este também é capaz de absorver razoáveis quantidades de energia via deformação permanentemente. Por outro lado, a cortiça além de ser um material natural, é capaz de recuperar grande parte da sua forma após deformada, uma característica desejada em aplicações com multi-impacto. Neste trabalho é efetuada uma avaliação da aplicabilidade da cortiça em equipamentos de segurança pessoal, especificamente capacetes. Vários tipos de cortiça aglomerada foram caracterizados experimentalmente. Impactos foram simulados numericamente para avaliar a validade dos modelos constitutivos e as propriedades utilizadas para simular o comportamento da cortiça. Capacetes foram selecionados como caso de estudo, dado as energias de impacto e repetibilidade de impactos a que estes podem ser sujeitos. Para avaliar os capacetes de um ponto de vista biomecânico, um modelo de cabeça humana em elementos finitos foi desenvolvido. Este foi validado de acordo com testes em cadáveres existentes na literatura. Dois modelos de capacete foram modelados. Um modelo de um capacete rodoviário feito de materiais sintéticos, o qual se encontra disponível no mercado e aprovado pelas principais normas de segurança de capacetes, que serve de referência. Este foi validado de acordo com os impactos da norma. Após validado, este foi avaliado com o modelo de cabeça humana em elementos finitos e uma análise ao risco de existência de lesões foi efetuado. Com este mesmo capacete, foi concluído que para incorporar cortiça aglomerada, a espessura teria de ser reduzida. Então um novo modelo de capacete foi desenvolvido, sendo este uma espécie de modelo genérico com espessuras constantes. Um estudo paramétrico foi realizado, variando a espessura do capacete e submetendo o mesmo a duplos impactos. Os resultados destes impactos e da análise com o modelo de cabeça indicaram uma espessura ótima de 40 mm de cortiça aglomerada, com a qual o capacete tem uma melhor resposta a vários impactos do que se feito de poliestireno expandido.

keywords

brain, cellular materials, cork, energy absorption, head trauma, human head model, impact, material characterisation, natural materials, numerical simulation, passive safety, protective devices, traumatic brain injury

abstract

Cork is a natural cellular material capable of withstanding considerable amounts of energy. These features make it an ideal material for some applications, such as impact protection. Regarding personal safety gear, synthetic materials, particularly expanded polystyrene, are typically used. These are also able to absorb reasonable amounts of energy by deforming permanently. On the other hand, in addition to cork being a natural material, it recovers almost entirely after deformation, which is a desired characteristic in multi-impact applications. In this work, the applicability of agglomerated cork in personal safety gear, specifically helmets, is analysed. Different types of agglomerated cork were experimentally characterized. These experiments were simulated in order to assess the validity of the constitutive models used to replicate cork's mechanical behaviour. In order to assess the helmets from a biomechanical point of view, a finite element human head model was developed. This head model was validated by simulating the experiments performed on cadavers available in the literature. Two helmet models were developed. One of a motorcycle helmet made of synthetic materials, which is available on the market and certified by the main motorcycle helmets safety standards, being used as reference. This helmet model was validated against the impacts performed by the European standard. After validated, this helmet model was analysed with the human head model, by assessing its head injury risk. With this helmet, it was concluded that a thinner helmet made of agglomerated cork might perform better. Thus, a new helmet model with a generic geometry and a constant thickness was developed. Several versions of it were created by varying the thickness and subjecting them to double impacts. The results from these impacts and the analyses carried out with the finite element head model indicated an optimal thickness of 40 mm, with which the agglomerated cork helmet performed better than the one made of expanded polystyrene.

Contents

List of Figures

List of Tables

List of Acronyms

ABPT	Applied Brain Pressure Tolerance
ABS	Acrylonitrile-Butadiene-Styrene
AIM	Angular Impact Mitigation
AIS	Abbreviated Injury Scale
ANSR	Autoridade Nacional de Segurança Rodoviária (Portuguese Road Authority)
ASDH	Acute Subdural Haematoma
CAD	Computer-Aided Design
CNS	Central Nervous System
COG	Centre Of Gravity
CPSC	Consumer Product Safety Commission
CPU	Central Processing Unit
CRP	Carbon fibre Reinforced Plastic
CSDM	Cumulative Strain Damage Measure criteria
CSF	Cerebrospinal Fluid
CT	Computer Tomography
DAI	Diffuse Axonal Injury
DBI	Diffuse Brain Injury
DDM	Dilatation Damage Measure
DOT	Department Of Transportation (from USA)
EDH	Epidural Haematoma
EPP	Expanded Polypropylene
EPS	Expanded Polystyrene
FE	Finite Element
FEA	Finite Element Analysis
FEHM	Finite Element Head Models
FEM	Finite Element Method
FIA	Federation Internationale de l'Automobile
FRP	Fibre-Reinforced Plastic
GRP	Glass fibre Reinforced Plastic
FMVSS	Federal Motor Vehicle Safety Standard
GAMBIT	Generalized Acceleration Model for Brain Injury Threshold
GSI	Gadd Severity Index
HIC	Head Injury Criterion
HIP	Head Impact Power
HIPS	Head Impact Protective System
HUMOS	Human Model for Safety
ICH	Intracerebral Haematoma

JHTC	Japan Head Tolerance Curve
KTH	Kungliga Tekniska Högskola (FEHM of Royal Institute of Technology)
MIPS	Multi-direction Impact Protection System
MTBI	Mild Traumatic Brain Injury
MRI	Magnetic Resonance Imaging
NDTs	Neutral-Density Targets
NHTSA	National Highway Traffic Safety Administration
PC	Polycarbonate
PET	Polyethylene Terephthalate
PHPS	Phillips Head Protection System
PLA	Peak Linear Acceleration
PRHIC	Power Rotational Head Injury Criterion
PU	Polyurethane
PVC	Polyvinyl Chloride
PS	Polystyrene
RIC	Rotational Injury Criterion
ROI	Region Of Interest
SDH	Subdural Haematoma
SEM	Scanning Electron Microscopy
SHPBH	Split-Hopkinson Pressure Bars
SIMon	Simulated Injury Monitor
SMF	Snell Memorial Foundation
STL	STereoLithography
SUFEHM	Strasbourg University Finite Element Head Model
TBI	Traumatic Brain Injury
THUMS	Total Human Model for Safety
UCDBTM	University College Dublin Brain Trauma Model
VNP	Vinyl Nitrile Polymer
VSI	Versace Severity Index
WSTC	Wayne State Tolerance Curve
WSUHIM	Wayne State University Head Injury Model
YEAHM	YEt Another Head Model

List of Symbols

GSI	Gadd Severity Index
VSI	Versace Severity Index
HIC	Head Injury Criterion
a	Translational acceleration
α	Rotational acceleration
v	Translational velocity
ω	Rotational velocity
t	Time
T	Time interval
G	GAMBIT
n, m, s	GAMBIT's empirical constants
HIP	Head Injury Power
$I_x x, I_y y, I_z z$	Moments of inertia
ϵ	Strain
$\tilde{U}$	Strain energy function for hyperfoam
U	Augmented strain energy function
N	Polynomial order
λ_i	Principal stretches
J	Elastic volume ratio
μ_i	Shear moduli
α_i, β_i	Curve-fitting material parameters
K	Bulk modulus
ν	Poisson's ratio
$\phi(\eta)$	Function of the damage variable
η	Damage function
σ	Stress
σ_{pl}	Yield stress
σ_{el}	Elastic buckling collapse stress
σ_c	Yield stress in uniaxial compression
r, β, m	Mullins effect material parameters
erf	Error function
$\phi(\eta_m)$	Residual value of the augmented energy function
ρ	Density
E	Young's modulus
D	Diameter
L	Length

p_c	Yield stress in hydrostatic compression
p_t	Yield strength in hydrostatic tension
k_t	Ratio of the initial yield pressures in hydrostatic tension
k	Ratio of the initial yield pressures in hydrostatic compression
W	Strain energy function for hyperelastic materials
I_1, I_2, I_3	Invariants
$\boldsymbol{S}$	Deviatoric stress tensor
$\boldsymbol{F}$	Deformation gradient tensor
$\boldsymbol{B}$	Left Cauchy-Green deformation tensor
$\bar{\lambda}_i$	Deviatoric principal stretches
α_i, D_i	Material parameters
τ_k	Characteristic relaxation times
g_k	Relaxation coefficients
C_{10}, C_{01}	Material parameters
$\bar{I}_1$, $\bar{I}_2$	First and second deviatoric strain invariants
x, y, z	Coordinates

Chapter 1

Introduction

In this first chapter, a brief introduction is made. The scope, motivation and main objectives of this research are presented. In addition, a reading guide with information about each chapter is also provided.

1.1 Motivation

Natural materials have been showing a tremendous potential to replace the synthetic ones in a great variety of engineering and design applications. Nowadays, consumer awareness and go-green tendencies are pushing manufacturers to provide eco-friendly alternatives to current market solutions. Additionally, government policies and the natural chase for profit will drive new business opportunities in the years to come. Currently, goods based on natural materials are mostly designed to mimic the original, classical functions expected from a given product. Nevertheless, more than mimicking or improving existing functionalities of products that resort to synthetic materials, exploring new improvements is important in order to create highly innovative and sustainable engineered goods.

Currently, a great variety of personal safety gear employs energy absorption liners. Examples are sport accessories, protective vests and helmets, among others. The vast majority of these liners are usually made of synthetic cellular materials, such as expanded polystyrene (EPS) and expanded polypropylene (EPP). These are able to absorb reasonable amounts of energy by deforming permanently. Under compressive loading, cellular materials can undergo large strain deformation while maintaining its low stress level almost constant before the material's densification, which allows them to absorb large amounts of energy [Fernandes et al., 2014, Tchepel et al., 2016a].

In a society continuously searching for new environmentally friendly and sustainable resources, a material such as cork would be a great substitute of these synthetic materials. Cork is a natural cellular material capable of absorbing great amounts of energy. In addition, cork recovers almost entirely after deformation, which is a desired characteristic in multi-impact applications [Fernandes et al., 2014, 2015, Jardin et al., 2015]. These features make cork an ideal substitute of synthetic cellular materials [Coelho et al., 2013, Fernandes et al., 2015].

In general, helmets are subjected to considerable multi-impact loads. Helmet liners

are usually made of EPS, which absorbs impact energy by deforming permanently. Thus, helmet liners are an interesting application for cork. Therefore, the main objective of this work is to analyse the applicability of agglomerated cork as energy absorption liner in personal safety gear. More specifically, it is analysed if agglomerated cork is an alternative to EPS helmet liners.

Europe's 2020 strategy assigned research, technology and innovation as leading activities in order to promote a sustainable and smart economic growth. Such activities must be carried out along with a strong consciousness about the environment, using the lowest possible amount of resources.

Helmets are one of the most important types of personal safety gear. They protect our heads and especially our brains. An impact to the head can have serious consequences and could even be fatal. Thus, head protection and safety helmets are a matter of extreme importance.

Since a long time that helmets are used as a protective system, first to protect the head in ancient wars. More recently, it was noticed that head injuries could easily occur without penetration, such as brain injuries due to inertial loading [Fernandes and Alves de Sousa, 2015]. Nowadays, helmets are used in a large number of different applications such as military, in emergency and protective services, in different types of work, in different types of sports and by bicyclists and motorcyclists, among others. Since each of these applications have different technical requirements, helmets evolved according to their specific applications. The main differences are in the shells, the outer part of the helmets. The materials, the geometries and the configurations are different according to the application. Nevertheless, regarding the energy absorption liner, there is no substantial difference between the different types of helmets. The material is almost always the same, EPS [Fernandes and Alves de Sousa, 2013a]. Even the geometries are similar between some types.

The different helmet standards are also very similar. The impact tests have a similar configuration and the impact energies are also similar [Fernandes and Alves de Sousa, 2013a, Pratellesi et al., 2011, Tinard et al., 2012b]. These standards usually take a long period of time to be upgraded or the changes are minimal. There is a general consensus about this subject and a great number of researchers criticized this low evolution rate [Fernandes and Alves de Sousa, 2013a]. One example is the ECE 22.05 standard [ECE R22.05, 2002], which regulates motorcycle helmets available in almost all European countries, including Portugal. This standard has been criticized for assessing helmets with outdated methods and criteria, using "rigid" steel headforms and assessing only the peak translational acceleration and Head Injury Criterion (HIC) as criteria [Fernandes and Alves de Sousa, 2013a, Forero Rueda et al., 2011, Tinard et al., 2012b].

Motorcyclists have only one effective mean of protection, the helmet. In fact, road accidents are the main cause of head injuries and motorcyclists greatly contribute to this [Lin and Kraus, 2008, WHO, 2009, Tinard et al., 2012b]. Thus, helmet standards are responsible for motorcyclists safety by improving the helmet quality and effectiveness. However, some researchers affirm that based on the standards, helmets are designed to reduce headform deceleration and not optimised to reduce head injury [Forero Rueda et al., 2011, Shuaeib et al., 2002a, Tinard et al., 2012b].

Over the decades, experimental studies have been made in human corpses and animals in order to obtain the mechanical properties of head components. The increase of computing power and the advances on computational modelling, led some researchers to try to model the human body, including the head [Tchepel et al., 2016b]. Several finite element head models (FEHM) have been developed during the last decade [Horgan and Gilchrist, 2003b, Kleiven, 2007c, Mao et al., 2013, Takhounts et al., 2008, Sahoo et al.,

2016, Zhang et al., 2001b].

Head modelling provides a strong basis for helmet design over the current headforms used by the standards. Once the FEHM is validated, it can be used to optimise the helmets from a biomechanical point of view [Fernandes and Alves de Sousa, 2013b, Tinard et al., 2012b]. These are more biofidelic than the rigid headforms and optimising a helmet with FEHM saves greats amounts of resources, such as material. A more flexible and cheaper procedure. This biomechanical criteria is based on the proposed head level injury predictors [Fernandes and Alves de Sousa, 2015]. This allows a further accurate, computational-based prediction of brain injuries, relating it to the medical investigations observed in autopsy of real accidents.

The research presented in this thesis intends to assess agglomerated cork as an energy absorbing material in helmets. Different types of agglomerates were tested experimentally. After characterization, these experiments were simulated in order to assess the validity of the constitutive models used. A FEHM was developed in order to assess the helmets using a biomechanical criteria. The desire of developing a FEHM is justified by the expectation that even if a helmet passes the shock absorption tests required by the European standard ECE 22.05, simulations performed with such a model could show that severe injuries may happen. Finite element (FE) helmet models were also developed. One of an existing certified helmet with an EPS liner and currently available on the market in order to be a reference in this study. A second one with a generic geometry, in order to evaluate the applicability of agglomerated cork as energy absorption liner in helmets and to optimise it by performing a parametric study with the developed FEHM, based on biomechanical criteria. An extensive description of the steps and objectives of this work are presented in the next section.

1.2 Objectives

The main goal of this research is to analyse the applicability of agglomerated cork as energy absorption liner in personal safety gear, more specifically in helmets. In the scope of this work, several stages had to be covered:

- Perform a detailed and thorough bibliographic review on several topics, such as cork and its application as an energy absorber, helmets technology and standards, and head biomechanics with insights on injury criteria and FE modelling;
- Quasi-static and dynamic characterisation of the mechanical behaviour of several types of agglomerated cork and EPS;
- Validation of the constitutive models used to simulate the mechanical behaviour of agglomerated cork and EPS;
- Development of an accurate FEHM and validation of this model against two different types of tests. This biomechanical head model will allow a further accurate computational-based prediction of brain injuries;
- Development and validation of a FE helmet model of a certified and commercially available helmet with an EPS liner;
- Biomechanical assessment of the certified and commercially available helmet with EPS liner using FEHM injury criteria;

- Development of a new generic helmet with agglomerated cork liners and its optimisation with regards to biomechanical criteria.

Although the reference for comparison is a motorcycle helmet, the potential applications are all helmets in general. Regarding multi-impact scenarios with substantial impact energies, military helmets and helmets for contact sports such as ice hockey are also interesting options. In addition, cork application is not limited to helmets and has the potential to be applied in other types of personal safety gear or even in other applications where its characteristics are desirable.

1.3 Reading guide

This thesis is divided in 7 chapters. In order to supply the reader with a practical reading guide, a small description of all chapters and their contents is provided.

Chapter 1 - Introduction
Chapter 1 presents a brief introduction along with the motivation for this thesis. A summary of the main objectives of this work is also presented. In addition, a reading guide is provided, giving a brief summary of each chapter.

Chapter 2 - State-of-the-art
This chapter presents the state-of-the-art relative to the topics covered in this thesis. Explains concepts related to cellular materials, specifying the origin and structure of cork and EPS. The mechanical behaviour and properties of both materials are also addressed. In addition, a literature review is made of research works where these materials were employed as energy absorbers, with emphasis on studies where impact tests were performed. A review on constitutive modelling of these materials is also performed.

It also refers to the development of helmets and different types existing today as well as the materials typically used. New helmet configurations are also reviewed, as well as the current state of the main helmet standards, where a comparison is made and drawbacks are highlighted.

It is made a brief review of head injury mechanisms and head injury criteria, as well as the associated thresholds proposed by several studies in the literature. In addition, the topic of finite element head modelling is also covered, presenting the models that represent the state-of-the-art and the experimental studies used to validate such models.

Chapter 3 - Material characterisation and modelling
This chapter describes the procedures and methods used to characterize the mechanical behaviour of cellular materials involved in this work. The experimental characterisation of both static and dynamic behaviour of different types of agglomerated cork and EPS is presented. In addition, numerical simulations are performed in order to verify the validity of the constitutive models and mechanical properties used model the mechanical behaviour of these cellular materials.

Chapter 4 - Finite element head modelling
In this chapter, the methods used to model a new FEHM are described in detail. This includes the geometric modelling, since the medical images to the finite element mesh. The constitutive models and mechanical properties used to model head contents are also presented. The experimental tests on cadavers selected from the literature are also described,

as well as the numerical simulations performed to validate the head model against these experiments.

Chapter 5 - Finite element modelling and evaluation of a helmet available in the market
In this chapter, the modelling and assessment of a commercially available motorcycle helmet is described. This was validated by simulating the impacts required by the standard to certify the helmet. Then, the safety level of this helmet was assessed by using the FEHM developed in chapter 4. Additionally, a preliminary analysis is performed by establishing a direct comparison between liners made of EPS and cork agglomerates.

Chapter 6 - Biomechanical evaluation of a helmet composed of agglomerated cork
This chapter presents the development of a new helmet model based on the findings of the previous chapters. Several versions of it are created, by varying the liner thickness in order to find the best solution with the FEHM developed in chapter 4. A final comparison between the best agglomerated cork helmet solution and the same helmet with EPS liner is performed in order to verify if agglomerated cork liners are an alternative to the ones made of EPS.

Chapter 7 - Conclusions and future work
This chapter presents the general conclusions and discusses the results obtained in this work. In addition, some suggestions and ideas to implement in future works are listed.

Chapter 2

State-of-the-art

This chapter presents the state-of-the-art relative to the topics covered in this thesis. Explains concepts related to cellular materials, specifically cork and EPS, regarding their origin, manufacture, structure, types, mechanical behaviour and properties, and applications. In addition, it introduces concepts of helmet design and testing as well as new configurations. It also includes a literature review on head injury biomechanics, covering injury mechanisms, criteria and their thresholds, and FE modelling.

2.1 Cellular materials

Over the last decades, cellular materials have been used in many applications. For instance, they have been intensively used in applications where a good energy absorption capacity is a desired feature. Damping, insulation and specific stiffness, among others, are also some of the desired properties. Thus, many of these materials have been used in personal safety gear (e.g. in helmets) and goods protection (e.g. in packaging) [Fernandes and Alves de Sousa, 2013a,b, Ozturk and Anlas, 2011, Paulino and Teixeira-Dias, 2012]. Normally, in these applications, the components are rarely subjected to a single impact.

Cellular materials have this designation when constituted by empty cellular elements with a solid fraction under 30% of the total volume [Pereira, 2007]. Among cellular materials, there are open-cell and closed-cell materials. Both of these can either be from natural or synthetic origin. There are many natural cellular materials available in nature, such as cork, wood and even bone. Fig. 2.1 shows the cellular structure of a honeycomb.

Under compression, cellular materials exhibit an approximately linear elastic behaviour for very small strains, which depend on the material. For greater strains, cellular materials undergo large strain deformation while maintaining an almost constant low stress level. This stress plateau corresponds to progressive cell collapse by elastic buckling, plastic yielding or brittle crushing, depending on the nature of the material [Gibson, 2005]. This plateau ends with the collapse of cell walls, known as densification. In terms of failure and damage, cellular materials can absorb energy through bending, buckling and fracture of the cells walls [Sousa-Martins et al., 2013]. This general behaviour makes cellular materials excellent energy absorbers, which can sustain considerable strains for small stress values.

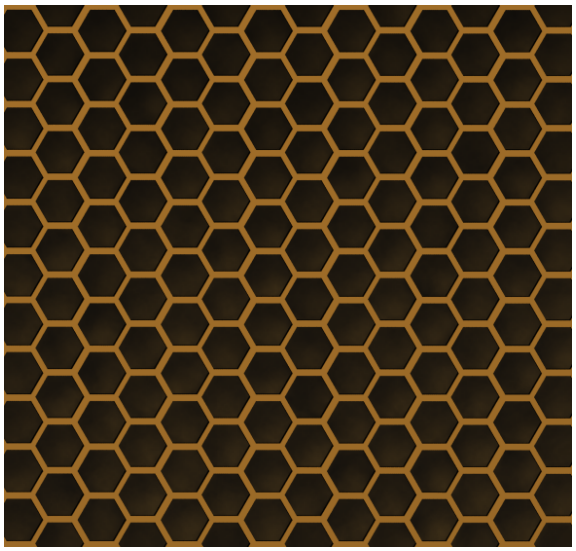

Figure 2.1: Cellular structure of a honeycomb.

Typical compressive stress-strain curves of different celular materials are shown in Figs. 2.6 and 2.16.

Expanded polystyrene (EPS), expanded polypropylene (EPP) or even metal foams are examples of widely used cellular materials. The choice of which one is the best material for each application depends on the application itself. For instance, for extremely high energy impacts, metal foams may perform better. Moreover, the mechanical properties can vary significantly depending on the density, loading strain rate and in some cases on the type of binder used to unify the material's granules. These characteristics attracted many researchers who tried to characterise those materials under quasi-static and dynamic loading [Di Landro et al., 2002, Fernandes and Alves de Sousa, 2013b, Fernandes et al., 2015, Gameiro et al., 2007a, Jardin et al., 2015, Mills, 2007, Mills et al., 2009b, Ouellet et al., 2006, Zheng et al., 2013, Zhu and Mills, 1999].

The great majority of these materials deform by crushing, developing permanent deformation. This means that after an impact where high strains are reached, the energy absorption capacity of these materials is significantly reduced. One cellular material that has the capacity to significantly recover its dimensions after being compressed is cork, a natural cellular material capable of absorbing considerable amounts of energy. For this reason, cork could be a good alternative in applications subject to more than one impact. Natural cellular materials are often mechanically efficient due to its structure. For instance, cork presents a honeycomb-like structure, which gives it an exceptionally high performance index for resisting bending and buckling [Gibson, 2005].

The following subsections address EPS and cork, since both materials are tested in this work. Their origin, manufacturing, applications, structure and mechanical behaviour and properties are reviewed. A wider state-of-the-art review on cork is presented since it is one of the main focus of this research.

2.1.1 Expanded polystyrene

Expanded polystyrene (EPS) is widely used in many applications. For instance, this synthetic foam is extensively used as an impact energy absorber in packaging and in helmets.

In addition, it is also used as thermal and acoustic insulator.

EPS is the most common polymeric foam, mainly due to its convenient cost-benefit ratio. It is cheap and easily injected to manufacture complex shapes. In addition, it is a light material with a low specific weight, where 97% of its volume is air. This set of characteristics explains why it is widely used, even in highly demanding applications such as helmets.

Manufacturing

Bead foams, based on commodity thermoplastics such as EPS, are widely used. Thermal insulation, packaging and energy absorption in personal safety gear are some of the applications. Bead moulding is a relatively economic mass-production process, of complex shaped products, with high dimensional accuracy [Mills, 2007]. Svec and Rosik [2000] reviewed this production process and the foam microstructure. EPS foams are usually manufactured in a two-stage process:

- In the first stage, plastic pellets, containing a low-boiling point hydrocarbon expander (generally pentane) dissolved within, are partially foamed to obtain pre-expanded beads.

- In the second stage, the beads are sintered together and expanded in a mould to produce desired shape with the final density.

First, pentane is introduced to suspension-polymerised polystyrene (PS) beads. When these absorb and contain pentane up to 8% of its weight, the glass transition temperature is reduced from 100℃ to about 60℃ [Mills, 2007]. When PS beads are heated in the first stage of the process, the pentane begins to evaporate at about 50℃. The beads are then cooled and rest for a day within which the air diffuses into the cells and pentane is lost.

Generally, the higher the beads are heated, the lower the density will be. The temperature is important to define the expansion diameter of the beads. Nevertheless, for long heating times, the pentane escapes faster than air diffuses into the cells, and the cells begin to collapse [Mills, 2007].

In the second stage, EPS beads are inserted into a mould with the product's final geometry. Then, steam passes through ports in the mould at a controlled pressure, normally ranging from 1.29 to 1.98 bar. The temperature is generally between 107℃ and 120℃, which is above the glass transition temperature [Mills, 2007].

The partial steam pressure inside the beads is zero before moulding. When the diffusion rate of steam into the beads is higher than the diffusion rate of air or pentane out of the beads, the internal pressure increases, causing expansion and the start of aggregation between the beads. Consequently, flat regions develop between the beads and a welding process starts. Then, the steam is cut off and cooling water is applied to the mould. Finally, when the mould internal pressure falls to zero, the final product is removed.

The final structure consists of expanded beads with dense and stiff walls between each other. The beads size determines the EPS foam density. The beads are made of small closed cells with dimensions of the order of 100 μm . Therefore two sizes of unit cells can be revealed, which are expected to deform interactively [Di Landro et al., 2002]. Fig. 2.2 shows the transition from PS beads to EPS beads and finally to an EPS foam.

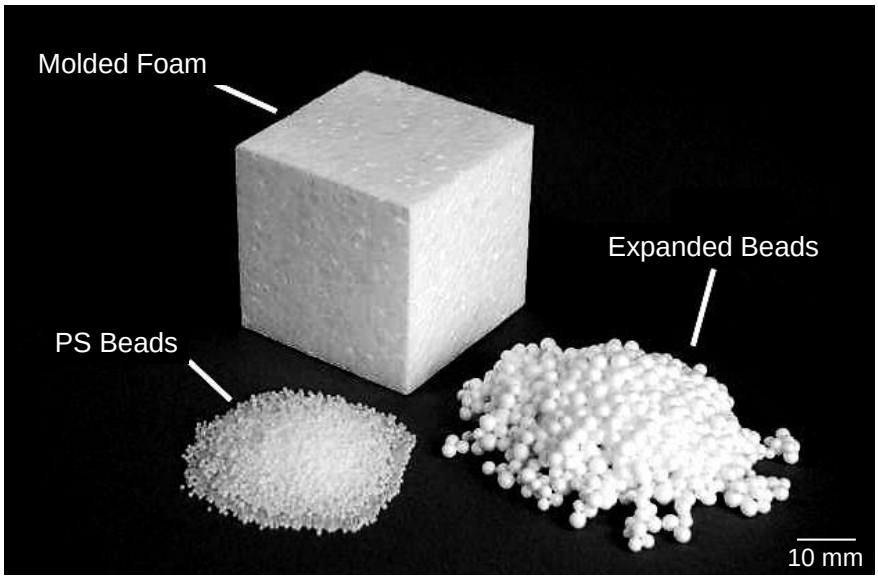

Figure 2.2: Transition from PS pellets to EPS beads and finally to an EPS foam (adapted from Neil Hanekom, epsfoampro.com).

Structure and mechanical behaviour

The expanded beads - in the EPS foam - become approximately polyhedral. Fig. 2.3 shows the macrostructure of an EPS foam, where is possible to observe the beads geometry and to verify that there are empty spaces between them. Thus, the expanded beads are not fully in contact. Generally, when the foam fractures, the crack follows the beads boundaries.

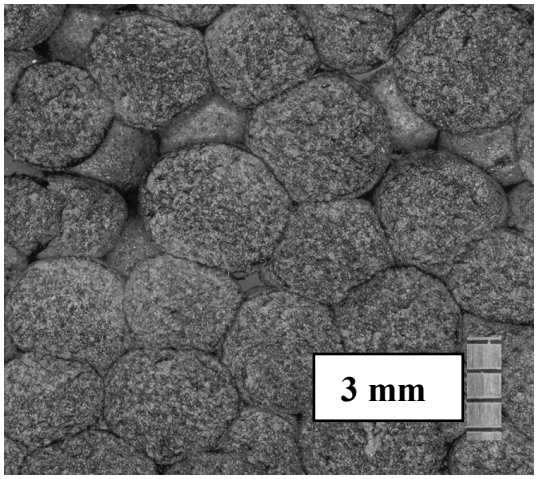

Figure 2.3: Macrostructure of an EPS foam (adapted from Vaiktus et al. [2006]).

Vaiktus et al. [2006] observed that when deformation reaches 3%, spaces between beads diminish lightly. The expanded beads move towards the empty space and the beads structure suffers almost no changes. Vaiktus et al. [2006] added that under compression, the beads move to different directions. It is possible that not only compression stresses but also tensile as well as shear stresses appear between the beads.

Then, until the deformation reaches 60%, the cells get gradually wrinkled. Thus, it can be stated that gradual collapse of microstructure takes place when deformations are below

60% Vaiktus et al. [2006]. At this level of strains, there is no empty space between the beads, leading to pure compression. Thus, for this level of deformation, EPS cells are all wrinkled and densification starts.

The shape of EPS cells is variable. Non-deformed EPS cells are shown in Fig. 2.4, at a macro (left) and micro (right) scales. Cells close to the bead skin tend to resemble bricks, with two of their faces parallel to the bead boundary. On the other hand, cells in the interior of the bead have equiaxed polygonal shapes [Mills, 2007].

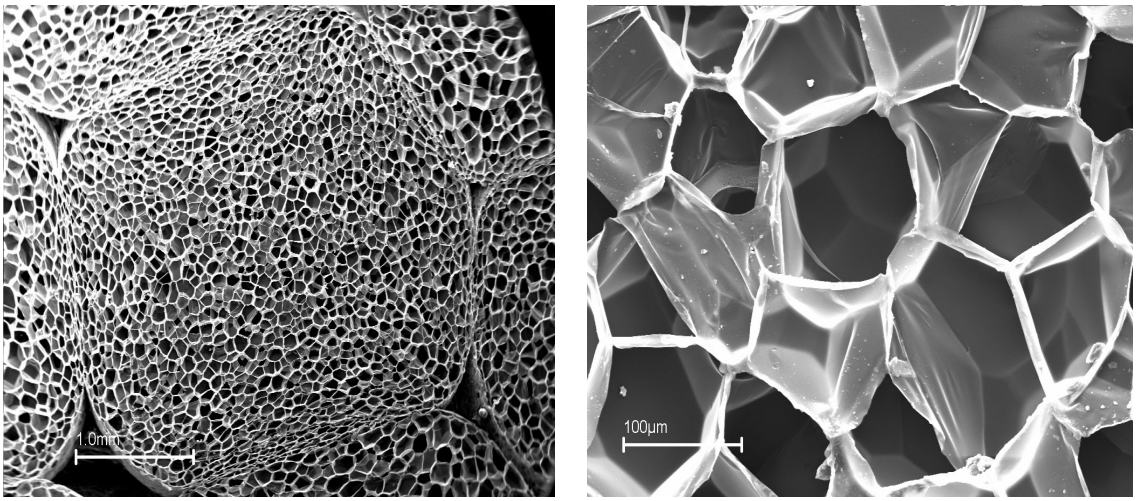

Figure 2.4: EPS macro and microstructure (adapted from Vaiktus et al. [2006]).

EPS is a closed-cell foam used, for instance, in helmets as impact energy absorber. Nevertheless, EPS deforms by crushing, developing permanent deformation. Fig. 2.5 shows the beginning of densification at 60% of deformation, where crushed cells are visible.

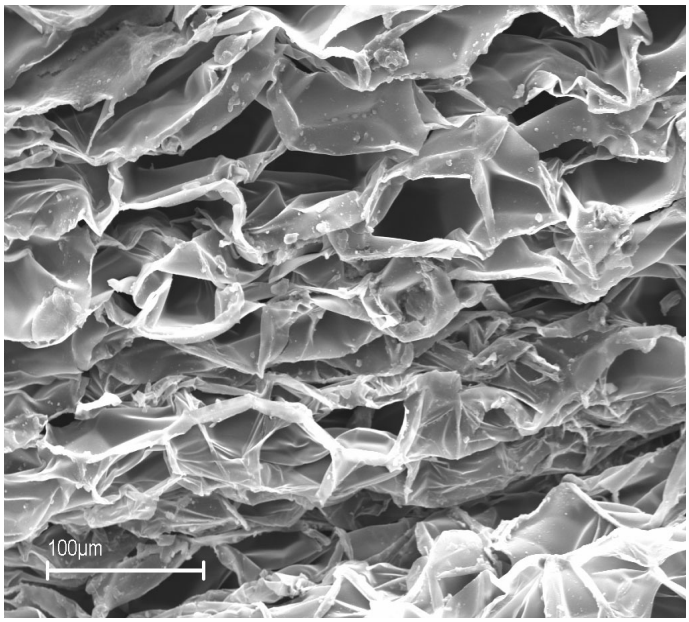

Figure 2.5: Crushed EPS cells at 60 % of deformation (adapted from Vaiktus et al. [2006]).

Generally, three stages characterise the compression stress-strain curve of EPS [Gib-

son, 2005], as illustrated in Fig. 2.6:

- I - For very small strains, there is a linear elastic regime, which corresponds to bending of the cell walls;
- II - At this level of strain, yield stress is reached and deformation is unrecoverable. The compressive stress is almost constant during the compression within this range of strains. In Fig. 2.6 is possible to observe a stress plateau. Progressive cell collapse occurs by plastic yielding until all cells are collapsed [Tan and Qu, 2010];
- III - For such strains, cells are collapsed, loading the cell edges and walls against one another, leading to densification where the stress rises steeply. Thus, the capacity to absorb energy is significantly reduced.

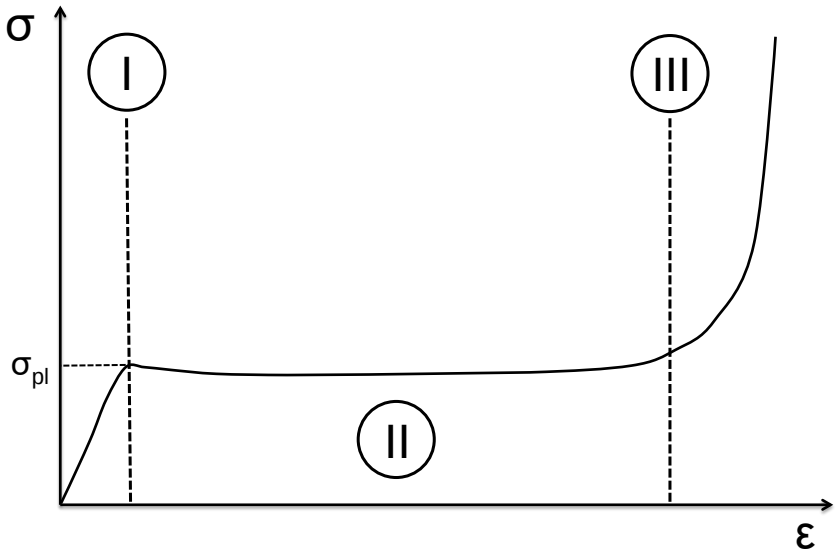

Figure 2.6: Typical uniaxial stress-strain curve of an EPS foam under compression.

2.1.2 Cork

The majority of cellular materials, including EPS, deform by crushing, developing permanent deformation. This means that after an impact, the energy absorption capacity of these materials is significantly reduced. High strains are reached, the material gets stiffer and can no longer be used for energy absorption.

One cellular material that has the capacity to significantly recover its dimensions after being compressed is cork. Cork is a natural cellular material that has the capacity to withstand considerable amounts of energy. Thus, in contrast to other cellular materials such as EPS, cork is characterized by having both a good energy absorption capacity and viscoelastic recover. Therefore, after an impact, the capacity of this material to keep absorbing energy is almost unchanged, deforming mainly elastically. In addition, cork appears as a sustainable alternative, once it is fully recyclable.

In addition to cork's great compressibility and dimensional recovery, this material has good insulation properties, very low permeability to liquids and gases, chemical stability and durability [Pereira, 1988, 2007]. Due to this excellent set of properties, cork is applied in a vast variety of applications, since cork stoppers to thermal and acoustic insulation, footwear and clothes, flooring and vibration control, among many others.

Origin, manufacturing and applications

Cork is the bark of the cork oak, which is scientifically known as *Quercus Suber* L. This type of tree grows mainly in the Iberian Peninsula, being Portugal the largest manufacturer of cork products. *Quercus Suber* L has a typical life span from around 150 to 200 years [Tchepel et al., 2016a].

Cork oaks are ready for their first harvest around the age of 25 years old, when the tree diameter is approximately 20 to 25 cm [Fortes et al., 2004]. Cork from this first harvest is called virgin cork. This presents an irregular structure and surface, with fractures due to high tangential stresses originated by the radial growth. Cork with this quality is not suitable for production of natural cork stoppers. Nevertheless, this raw material is not wasted, being used to manufacture cork agglomerates for flooring, insulation, etc.

From this point onwards, every 9 years, the tree is ready for a new a harvest. This is the period necessary to grow a new layer of cork with the necessary thickness for its primary application, the production of stoppers. The cork from the second harvest is called secondary cork and the ones thereafter amadia. Cork is harvested by cutting the bark and by extracting the planks from the tree. Fig. 2.7 shows the cork harvesting process, which is usually done manually by expertise and skilled professionals between late spring and summer.

Figure 2.7: Extraction of cork planks (courtesy of APCOR).

Cork is produced by a meristematic tissue, the phellogen [Fortes and Rosa, 1992]. The cells in each column are produced by the same phellogen cell and are packed base-to-base. After extracting the bark, the phellogen layer is destroyed. Nevertheless, cork oak has the capacity to regenerate, creating a new layer of cork. This regenerative capacity is

what makes it possible to sustainably explore these trees, approximately 15-16 harvests during their life span.

Although the cork obtained in the second extraction has better quality than virgin cork, presenting a regular structure and smoother surfaces, it is also not suitable for production of stoppers. There are still considerable stresses that originate cracks and other irregularities. Nevertheless, in the next harvests, cork usually presents a regular structure with a uniform thickness and smooth surfaces with just a few low depth cracks. Thus, amadia is the raw material used by the industry to manufacture natural cork stoppers.

Before producing the stoppers or other products, cork planks rest for half a year in order to mature and stabilise. Then, planks are boiled, which makes them softer, flatter and cleaner. Fig. 2.8 shows planks stacked on pallets, ready for further processing. Fig. 2.9 shows a close-up of boiled planks, capturing the lines running in the radial direction. These structures are called lenticular channels and are the gas exchange pores that allow air exchange between the atmosphere and the living tissue of the tree.

Figure 2.8: Boiled planks stacked on pallets.

In the cork industry, nothing is lost, everything is harnessed and transformed. Cork from the first two harvests, as well as the cork that is not used for the production of stoppers, are used to manufacture cork agglomerates. In addition, cork waste from manufacturing products such as stoppers and other cork products are also used. Even cork stoppers and other products can be recycled and used to create new products. Thus, it can be said that cork is fully recyclable, reusable and its manufacturing is sustainable.

Regarding agglomerates, depending on the manufacturing process, two general types are possible to obtain. One is agglomerated cork, created by mixing cork granules with some binder, for instance, thermosetting resins. The other type is black agglomerated cork, also known as expanded agglomerate or expanded cork. This one is just made of cork suberin, without adding binder. Fig. 2.10 shows examples of each type of agglomerate.

Some of the natural cork characteristics may affect its application in new technologies, for instance, its anisotropy. In addition, the cells size dispersion and even the growth period

Figure 2.9: Close-up of boiled planks, capturing the lenticels.

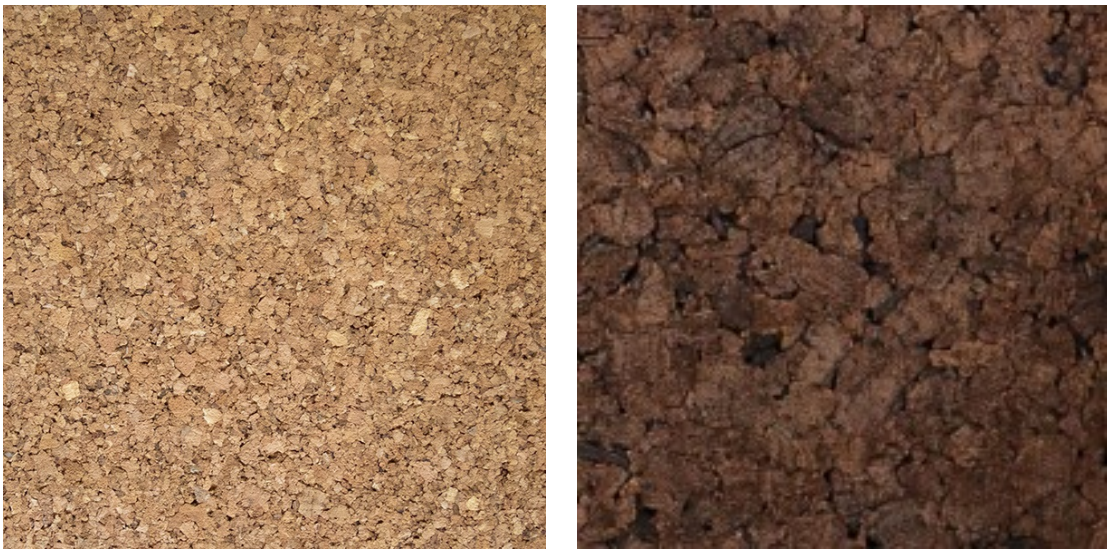

Figure 2.10: Two types of agglomerates: agglomerated cork (left) and expanded cork (right).

affects the cells shape and size. Thus, cork is not completely homogeneous and therefore its mechanical behaviour will depend on the specific particularities of the structure, such as porosity and cracks [Anjos et al., 2011a].

Agglomerated cork, commonly known as white agglomerate, is one alternative in order to have an isotropic material with controlled properties. Agglomerated cork results from moulded agglomeration of cork granules ranging from 0.5 to 20 mm with other materi-

als such as polyurethane (PU), phenolic and melamine thermosetting resins or vegetable-based resins, among many others. The binder represents an important role in the mechanical properties of the final product since it is responsible for bounding cork granules. The choice depends on the final product or application. Thus, agglomerated cork is an isotropic material that can be manufactured in different shapes and sizes, keeping the advantages of using natural cork.

The granules are obtained using different types of mills. The granules dimensions depend on the final product or application. After being milled, the granules are normally cleaned and dried by forced circulation of hot air, giving the granulate the required moisture content. The agglomerate is created by agglutination of granules with a specific size and density using pressure, heat and a binder, depending on the product and application required.

Following automatic or manual dosage, the mixing of the granules with the binder is achieved by mechanical blade or helical mixers. The mixture is then placed in a mould with the desired shape, which is pressed. The mould is then placed in a heating chamber with temperatures between 110 and 150℃. Next, the agglomerate is removed from the mould and cooled.

The density resulting from this process will depend on the final application. For instance, agglomerates for decorative purposes commonly have densities of 200 to 350 kg/m^3 and use fine to medium granule sizes, while for flooring the density is around 450 kg/m^3 to 600 kg/m^3. Generally, some agglomerates have similar densities to natural cork, which has densities ranging between 120 and 300 kg/m^3 [Fortes et al., 2004]. In general, agglomerated cork can be considered an isotropic material.

Expanded agglomerate, also known as black agglomerate, is made by agglutination of virgin cork granules. This cork is mostly obtained from the pruning of oak trees branches, with a high concentration of extractives, which act as a natural adhesive. Expanded cork is industrially manufactured without the use of additives, being 100% natural.

The grinding process is exactly the same used for white agglomerates. After grinding, impurities are removed, specifically wood, with the aid of densimetric separators and sometimes pneumatic separators or rotating drums. The granulate is stored and dried until the ideal moisture level is reached.

The granules are placed in autoclaves and pressures around 40 kPa and temperatures approximately between 300-370℃ (usually steam from water overheated) are used to manufacture expanded cork. With these conditions, the granules expand and exude their natural resin, driving agglomeration without being necessary to add any additive. Basically, by heating the granules, these expand and agglutinate due to the action of its own resins.

The final material colour is given to it by the high temperatures reached with this process, without adding pigments. This is a 100% natural process, without use of any kind of additives. With these two types of agglomerates, complex shapes can be manufactured, which allows cork to be applied in several applications.

Cork properties make it an all-purpose problem solver and suitable for a wide range of applications. For instance, flooring, flotation, insulation and sealing. Cork stoppers are used for sealing wines for more than two millennia. Over the ages, cork has evolved into a versatile material used in several activities. Cork is even used for its aesthetic characteristics, as shown in Fig. 2.11 a cork sculpture.

Today, cork is used in construction, decoration, transportation, clothing, sporting goods, shoes, cladding panels, fishing buoys, among many others. The fact that we live in a society constantly searching for environmental friendly solutions, cork stands out for its properties. These are better reviewed in the next section.

Figure 2.11: Cork sculpture by Vhils at Santa Maria da Feira's City Hall.

Portugal leads export figures with a share around 65% [APCOR, 2016]. It is also the leader in the global area of cork oaks and cork production. Cork oak plantations cover an area of almost 2.5 million hectares and Portugal concentrates 34% of it.

Structure

The first known written reference about cork dates to 77 A.D., made by Pliny the Elder (*Gaius Plinius Secundus*) in his book *Naturalis Historia*. In this, he refers the utility of the bark and the capacity of the tree to regenerate it. Some years later, Plutarch refers the utilisation of cork in boats [Fortes et al., 2004].

Many centuries later, Robert Hooke published *Micrographia*, describing his observations made with the compound microscope [Hooke, 1665]. By looking with it into a piece of cork, Hooke coined the term cell (from latin *cella*, which means small compartment) for describing biological organisms. In this publication, Hooke described cork as a porous material with cells resembling a honeycomb. Fig. 2.12 shows Hooke's illustration of cork's microstructure.

Hooke also noticed the anisotropy of cork. In Fig. 2.12 is possible to observe the differences between the two directions of observation. The right structure shows hexagonal cells, disposed in a uniform manner, resembling a honeycomb. On the other hand, the one at the left shows rows of quadrilateral cells. The orientation of the cells is defined by the way cork grows. Fig. 2.13 shows an illustration of cork cells' orientation in a section of the bark. The axial direction is the tree's growth direction.

Currently, with scanning electron microscopy (SEM), it is possible to precisely observe

cork's microstructure. An example is shown in Fig. 2.14. Cork cells present a prismatic hexagonal geometry along the radial direction and a quadrilateral geometry in the remaining directions, being piled in columns with non-aligned bases.

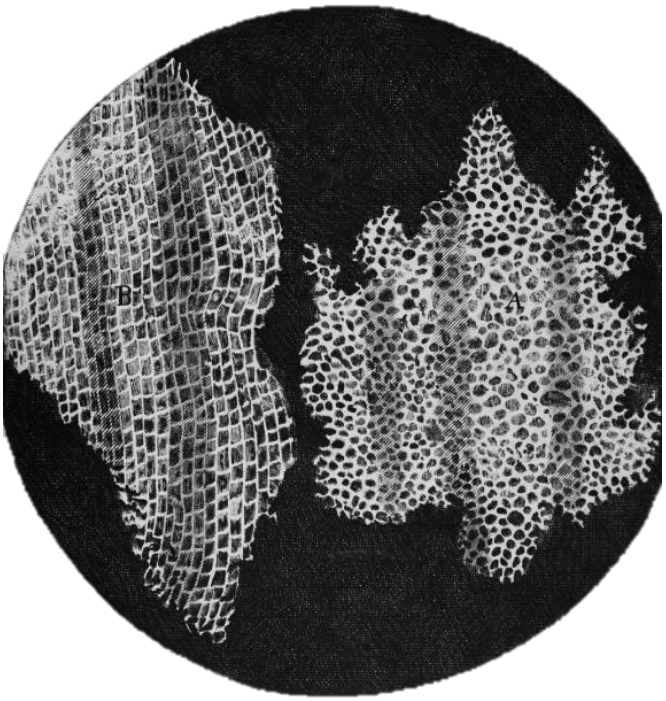

Figure 2.12: Hooke's drawing of cork's microstructure (adapted from [Hooke, 1665]).

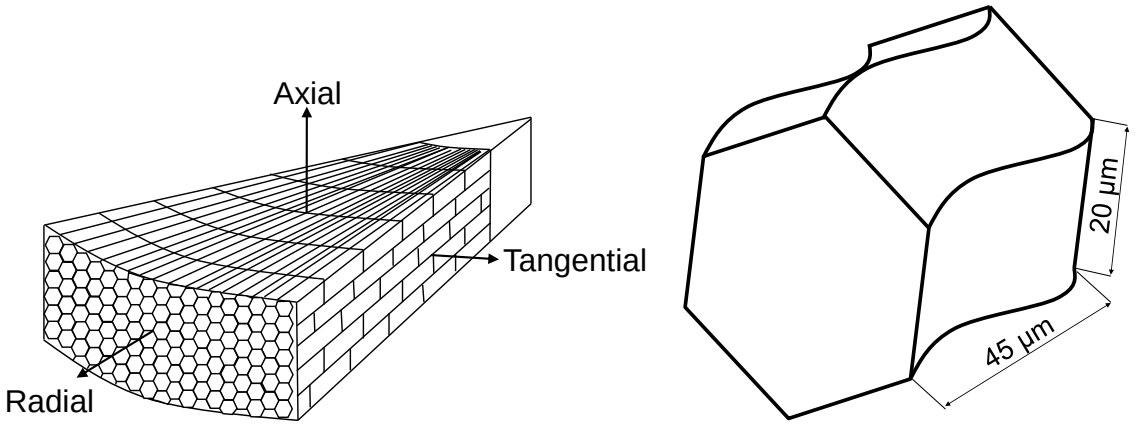

Figure 2.13: Illustration of cork cells' orientation in a section of the bark (left) and a cork cell showing its corrugations (right).

All the cells in the same column are created by the same phellogen cell, one by one. In this same direction, the cell walls present undulations. The buckling of the cell walls is originated by the stress created by the growth of new cork cells. These corrugations give a high flexibility to the cell walls which determines cork's mechanical behaviour [Anjos et al., 2014]. Fig. 2.13 shows an illustration of a corrugated cork cell. On average, there are around 40 million cells per cubic centimetre.

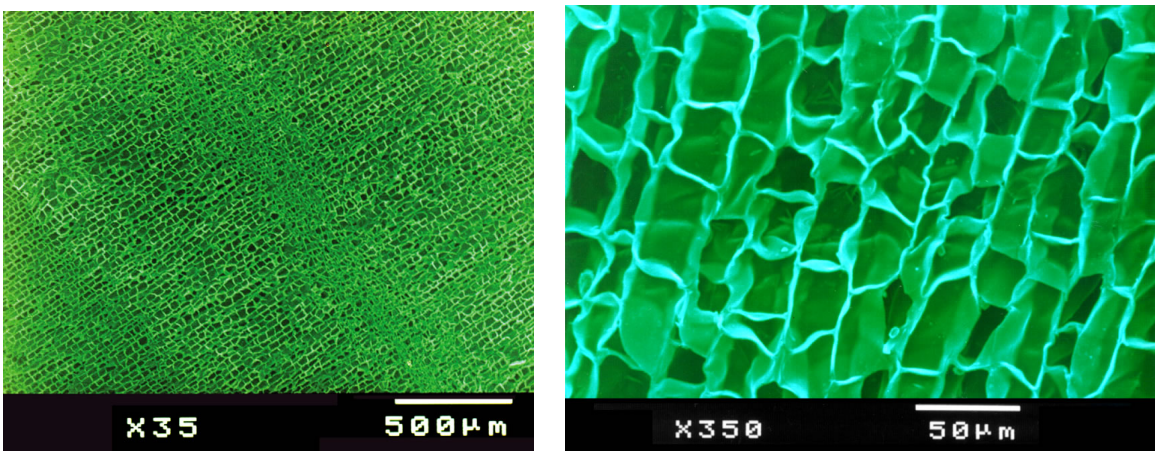

Figure 2.14: SEM micrograph of cork, showing its cellular structure arranged in rows parallel to the radial direction (courtesy of APCOR).

A cork cell usually have a mean length of 45 μm, an average hexagonal base side of 20 μm and a mean wall thickness of 2 μm [Fortes et al., 2004]. Nevertheless, cork cells dimensions and its organisation are very variable. Therefore, it is almost impossible to have two equal pieces of cork.

In addition, the cells growth depends on the season. Cork shows a layered structure, corresponding to the continuous growing of rings. Cells formed during spring (the main growth period) are longer and its walls are thinner and more undulated than those formed during autumn (the end of the growth period), which are smaller and thicker-walled [Pereira et al., 1987]. Shorter and thicker cell walls are more resistant to bending and buckling [Fortes et al., 2004]. Thus, as already referred, there is significant variability in the properties of natural cork.

Cork is a closed-cell material with a solid volume fraction of approximately 15% of its total volume [Sousa-Martins et al., 2013]. The solid volume ratio is smaller than the volume occupied by gas, which explains its lightness. Cork properties greatly depend on its relative density and chemical composition.

Cork cell walls contain predominantly suberin in association with lignin and a lesser content of polysaccharides and even lower of extractives [Pereira, 1988]. Suberin is a lipophilic biopolymer greatly responsible for cork's properties, such as impermeability to water and gases. Suberin is practically infusible and it is insoluble in water, alcohol, ether, chloroform, concentrated sulphuric acid, hydrochloric acid, among others. As previously referred, cork is also composed by lignin, polysaccharides such as cellulose and hemicelluloses, and extractives. Typical compositions are within: 35-45% of suberin, 17-27% of lignin, 13-23% of polysaccharides and 10-20% of extractives (% of weight) [Aroso et al., 2015, Conde et al., 1998, Fortes et al., 2004, Pereira, 1988, Pinto et al., 2009, Silva et al., 2005].

Simply, there are five inter-cellular layers in a cell wall: the outer layers are cellulose, two are formed by suberin and the inner one is made of lignin. Fig. 2.15 shows an illustration of cork cells walls structure and its constituents. The cork cell wall chemical composition plays an important role in its compression properties [Oliveira et al., 2014]. According to Pereira [2013], lignin is responsible for the resistance under compression and suberin is the main contributor to the elasticity and relaxation properties.

The fact of cork being rich in suberin, makes it a highly impermeable and resilient

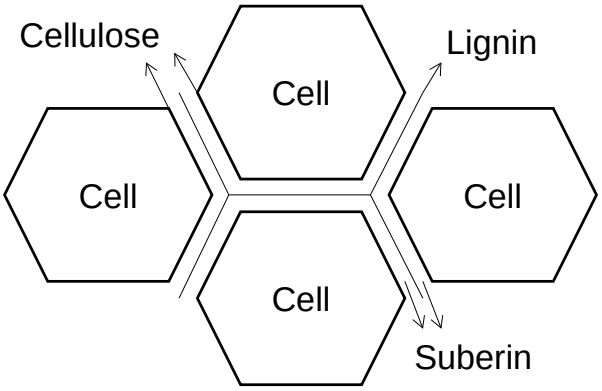

Figure 2.15: Illustration of cork cells walls structure and its constituents.

material, with low thermal conductivity, being a good thermal and acoustic insulator, as well as a good absorber and dissipater of energy. Summarising, cork has:

- low density - due to the very low solid volume ratio and the gas inside its cells, cork is a light material. Natural cork's density typically ranges between 130 and 250 kg/m^3 [Anjos et al., 2014];
- resiliency - as cork is elastic at a cellular level, it is also very resilient;
- durability - cork is resistant to wear, thanks to its honeycomb structure, which makes it less affected by impact or friction than other hard surfaces;
- high elasticity and compressibility - it can be compressed to high strains without losing any flexibility and recovers its initial shape and volume almost completely as soon as unloaded. This flexibility is given by its structure, composition and airtight cells containing a gas mixture similar to air;
- low Poisson's ratio - cork has a Poisson's ratio of approximately zero. It can be compressed on one side and the other two dimensions will not change. This is true for cork agglomerates and for natural cork when loaded axially or tangentially;
- capacity to withstand impacts - cork is a good shock-absorbing material;
- low thermal and sound conductivity - cork is an excellent thermal and acoustic insulator. The 40 million cells per cubic centimetre of cork make it an excellent sound and vibration insulator as well as an excellent thermal insulator;
- very low permeability to liquids and gases - the cellular membranes are impermeable, protecting the cork from moisture. It is impermeable to liquids and practically impermeable to gases, thanks to the suberin present in its composition;
- insulating and fire retardant properties - prevents the quick spreading of fire. The slow combustion of cork makes it a natural fire retardant;
- low conductivity and antistatic - cork is a good insulator of electricity;
- appealing aesthetics and comfort - cork has appealing colour patterns and is comfortable to touch;

As already referred, the cellular structure of cork is responsible for its low density. The majority of cork's mechanical properties is defined by its cellular structure. Suberin is responsible for some of the cork's mechanical properties and other characteristics such as impermeability. This explains the vast number of existing cork applications.

Mechanical behaviour and brief literature review

Over the last decades, several studies have been made on the characterisation of cork [Anjos et al., 2008, 2010, 2011a,b, 2014, Dart and Eugene, 1946, Fernandes et al., 2014, Fortes and Nogueira, 1989, Gameiro et al., 2007a, Gibson et al., 1981, Jardin et al., 2015, Sousa-Martins et al., 2013, Moreira et al., 2010, Rosa and Fortes, 1988a,b, 1991, Vaz and Fortes, 1998]. The aim of some of these studies was not just cork's characterisation but also the study of its applicability in new solutions as well as its improvement in the existing ones. In this section, the mechanical behaviour of cork is reviewed with focus on compression.

One of the first references about cork's characterisation was performed by Dart and Eugene [1946], by studying the mechanical behaviour and stress relaxation of cork at quasi-static rates and various degrees of compression. They found that the stress-time curves for various compressions could be obtained from each other by multiplication. This was justified by the essentially identical S-shaped load-compression curve of cork. Dart and Eugene [1946] justified this shape with the cellular structure of cork.

At very low strains, Dart and Eugene [1946] observed a region in which Hooke's law holds, which means this is a linear elastic region. At slightly higher stresses, there is a general breakdown of the structure and hence a region where compression changes rapidly, with small stress changes, observing a stress plateau. Then, the cells collapsed and the material itself was compressed, resulting in a steep rising of the stress. However, and contrary to other cellular materials such as EPS, the unique thing about cork is that after a deformation it recovers its original dimensions to a remarkable degree, as observed by Dart and Eugene [1946].

The mechanical behaviour of cork under compression is the typical one of elastomeric foams in compression. Generally, three regimes characterise the compression stress-strain curve of cork [Gibson, 2005], as illustrated in Fig. 2.16:

- I - For very small strains, there is a linear elastic regime, which corresponds to cell edge bending. In Fig. 2.16, σ_{el} represents the elastic buckling collapse stress;
- II - Within this range of strains, the compressive stress is almost constant during the compression. In Fig. 2.16, it is possible to observe a stress plateau. This stress plateau corresponds to progressive cell collapse by elastic buckling;
- III - For such strains, cells are collapsed throughout the material and subsequent loading of the cell edges and faces against one another leads to high stresses.

This mechanical behaviour is the same for all types of cork. In compression, the properties of cork were found to vary with density, cellular dimensions and porosity [Anjos et al., 2008, 2014, Gibson and Ashby, 1997, Pereira et al., 1992]. Detailed information about cork, for instance, its growth, harvest structure, chemical composition, quality, mechanical behaviour and properties can be found in Fortes et al. [2004], Gibson and Ashby [1997], Gibson [2005] and Pereira [2007].

Many years later, Gibson et al. [1981] analysed the deformation characteristics of cork cell walls and its structure by performing tensile and compression tests. Gibson et al. [1981]

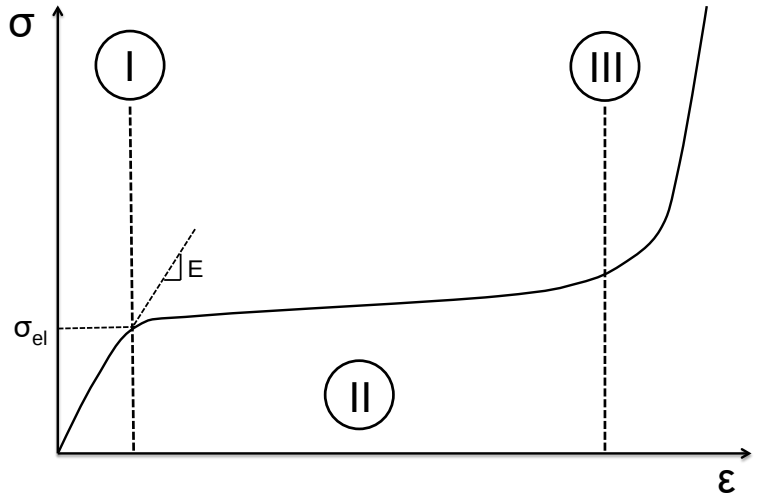

Figure 2.16: Typical uniaxial stress-strain curve of cork in compression.

justified the excellence of cork for stopping bottles, for thermal and sound insulation and as shock-absorbing material for flooring and packaging with the shape, size and structure of its cells. Gibson et al. [1981] added that under compressive load, cork cells walls bend or buckle, giving large recoverable deflections and a large energy absorption capacity. According to Gibson et al. [1981], cork's structure and its mechanical properties can be explained in terms of cell-wall deformation. Later, Gibson et al. [1982a,b] presented in detail their theory about cellular materials walls deformation when subjected to different types of loading.

Rosa and Fortes [1988a] studied the effect of strain rate on the compression behaviour of cork, taking into account the cork's anisotropy. Compression curves at three different quasi-static rates were obtained for each direction (radial, axial and tangential). Rosa and Fortes [1988a] concluded that the recovery rate decreases appreciably with time and increases with the degree of deformation previously imposed. The same authors, in other publication [Rosa and Fortes, 1988b], performed compression loading-relaxation-unloading cycles on cork. A softening was observed, particularly between the first two compressions, being explained in terms of an increased undulation of the cell walls. In subsequent compressions, few differences were observed.

Fortes and Nogueira [1989] studied the Poisson's effect in natural cork and determined the Poisson's ratio by compressing it experimentally with strains up to 30% in each of the principal directions. Fortes and Nogueira [1989] found values of approximately zero for compression in axial and tangential directions. A Poisson's ration of 0.3 was obtained for compressions in the radial direction. Fortes and Nogueira [1989] explained this effect based on the cellular structure of cork, more specifically the cells geometry and their arrangement.

Regarding the influence of cork growth, Pereira et al. [1992] studied cork samples with different growth rates and observed by SEM a considerable difference in the amount of cells. These samples were compressed and the results showed that the samples with higher growth rates have lower Young's moduli and lower strength. In other study, Fortes and Rosa [1992] concluded that strains due to growth are not recovered when the cork planks are removed, unless the planks are heated, for example, by immersion in boiling water.

As already referred, characterising natural cork is a hard task since there is a significant

amount of variables, for instance, the structural variability. Cells may have different sizes depending on the season and the number of cells is influenced by cork's growth rate, which influences the mechanical behaviour [Pereira et al., 1992]. Costa et al. [2003, 2008] studied some of these variabilities, trying to create some useful background information.

Rosa et al. [2004] performed torsion tests on cork cylinders, obtaining the corresponding shear moduli and studying the effect of the torsion rate on it. In other publication, Rosa and Fortes [1991] performed tensile tests, determining the Young's modulus and the stress and strain at fracture. Two fundamental mechanisms of fracture were identified: crack propagation along the lateral cell walls in non-radial tension and crack propagation by breaking the cell walls in radial tension. In addition, Rosa and Fortes [1991] concluded that the strain necessary to fracture in the radial direction is considerably larger than in the other directions.

Vaz and Fortes [1998] determined the friction coefficient between cork and other materials, such as glass and steel. The sliding tests were performed for various compressive stresses and sliding velocities. The values obtained in this study ranged between 0.4 and 1.2. These high friction coefficients were explained with the contribution of some open cells on the surface.

More recently, Mano [2002] investigated the viscoelastic properties of cork at temperatures ranging from -40℃ to 120℃. A decrease in the intensity of the relaxation and an increase of the storage modulus is observed when cork is previously subjected to temperatures above 60℃. Later, Mano [2007] performed creep tests on cork samples under compression at temperatures ranging between 0 and 50 ℃. It was indicated that a fraction of the strain resulting from creep is preserved permanently, especially if the load is applied along the axial direction.

Anjos et al. [2008] studied the effect of cork quality, porosity and density on its compression properties. The direction of compression was a highly significant factor of variation, with cork showing higher strength for the radial compression. Density influenced compression, since denser cork showed overall larger resistance to compression in the three directions. Thus, the greater the density is, the higher the Young's modulus will be [Anjos et al., 2008]. Regarding the effect of porosity and cork quality on cork's compressive behaviour, no significant difference was observed.

More recently, the density influence on cork's mechanical behaviour under compression, as well as the subsequent recovery of dimensions were studied by Anjos et al. [2014]. Denser corks presented higher stiffness in the three directions, as previously concluded in Anjos et al. [2008]. Regarding the dimensions recovery, an average 50% of the initial deformation was recovered on the first day, and almost totally after 15 days. Anjos et al. [2014] added that the recovery was higher for low density corks and in non-radial directions.

The behaviour of cork under tensile load is lesser documented than under compression, mainly due to its performance under tension, easily fracturing. Anjos et al. [2011a] studied the cork behaviour under tensile stress in the axial direction of samples with different qualities and at three radial positions within the plank (inner, mid and outer positions). Anjos et al. [2011a] found out that these are highly influential factors in cork's tensile properties in the axial direction. The highest strength was found for good quality cork in the inner part of the plank. Previously, the same authors published a similar study in which cork was tested in the tangential direction [Anjos et al., 2010]. The tensile properties were highly dependent of the radial position in the plank.

The same authors published a study in which the behaviour of cork under three point bending stress in the radial direction was evaluated [Anjos et al., 2011b]. The stress-strain curves obtained in bending were similar for the different test specimens and similar to

those observed for tensile tests in cork but the mechanical resistance of cork in bending was higher than in tension and lower than in compression. In addition, Anjos et al. [2011b] concluded that Young's modulus, fracture stress and fracture strain are influenced by cork's density and porosity. From these publications, it is possible to conclude that fracture usually occurs when cork is submitted to tensile or torsion loading [Anjos et al., 2011a, 2010, 2011b].

Recently, Oliveira et al. [2014] investigated the variability of the compression properties of cork, from 10 different sites in Portugal. As in other studies, the radial direction offered higher strength. Density, annual growth ring width and chemical composition influenced compression. Cork samples with relatively higher suberin content required less stress for deformation.

Although the great variability of natural cork properties, Garcia et al. [2015] evaluated the accuracy of mathematical techniques to predict Young's modulus, compressive stress at 30% strain and instantaneous recovery velocity of cork. Acceptable results were only predicted for compressive stress at 30% strain, using neural networks. The heterogeneity of natural cork makes its modelling a difficult task. Iglesias et al. [2015] applied a mathematical tool to predict the tensile properties of cork in the tangential and axial direction, indicating a reasonable prediction for both Young's modulus and fracture stress.

Regarding cork agglomerates, Gil [1994, 1996] observed expanded cork with SEM, prior and after different compressions. Maximum densification was achieved with a pressure of 3 MPa. In other study, Teixeira et al. [1996] studied the mechanical behaviour of agglomerated cork through compression and three-point bending tests. Moreira et al. [2010] performed quasi-static and dynamic tests in order to characterize agglomerated cork for vibration damping applications.

Castro et al. [2010] investigated the applicability of agglomerated cork as an ideal core material for sandwich components of lightweight structures. Results from the experiments revealed that cork agglomerates' performance, essentially depends on the cork granule size, its density and the bonding procedure used for the cohesion of granulates. Thus, as the author concluded, these parameters can be adjusted in function of the final application intended for the sandwich component. These findings are important for specific optimisations using cork agglomerates. Castro et al. [2010] also added that for some specific applications, cork can compete with its synthetic rivals. By comparing the specific compressive strength (σ_c/ρ) against the specific modulus (E/ρ), cork has a better mechanical behaviour than flexible polymer foams and is comparable to some rigid polymer foams.

Sousa-Martins et al. [2013] also investigated the applicability of agglomerated cork as core material for sandwich structures. In this study, the sandwich structures were subjected to blast waves from explosions. According to Sousa-Martins et al. [2013], the results indicate the possibility of energy dissipation by the core, most probably due to crushing of the cellular structure of cork.

Lakreb et al. [2015a,b] investigated the applicability of both expanded and agglomerated cork as core material for eco-friendly sandwiches with face sheets made of wood. Both solutions performed well, specially under compression, presenting a high performance. In a different study, Lagorce-Tachon et al. [2016] analysed the effect of hydration on the mechanical properties of natural and agglomerated cork. For both, the Young's modulus was significantly and similarly affected by hydration. A review on cork agglomerates was performed by Gil [2009].

In general, the mechanical behaviour of cork has been studied mainly at quasi-static rates. This may be justified by the main cork application, which is bottle stoppers. Studies focuses on quasi-static compressions, Poisson's ratio, friction, the influence of humidity and

porosity on cork. Basically, the important variables to control when using cork stoppers.

Nevertheless, cork is a material with a wide group of desirable properties. In the last years, these attracted many researchers that tried to employ cork in new applications, by creating new cork-based materials. For instance, Novoa et al. [1995] investigated the mechanical behaviour of a cork modified polymer mortar in order to use cork in lighter modified polymer concretes. Later, Alcântara et al. [2013] analysed the characteristics, properties and behaviour of a new composite material, called Core-Y, resulting from the combination of cork granules with an epoxy resin to be confined in tubular structures.

Many other studies, where new cork-based materials were created with different purposes, may be found in the literature. For instance, Niknejad and Moradi [2016] introduced a new composite material based on cork inserts as stiffener particles and silicone rubber as the resin, to be used as an energy absorber. There are also other examples where the authors were aiming for eco-friendly solutions for different applications [Fernandes et al., 2015b, Pullar et al., 2015, Vilela et al., 2013]. More information may be found in the reviews on new cork-based materials and applications performed by Gil [2009, 2015].

In fact, we live in a time where new sustainable solutions, including natural and environmental friendly materials are extremely desirable. Thus, cork with its outstanding properties has been used in almost everything. However, few researchers studied cork's mechanical behaviour when subjected to dynamic compressions.

Only in the last decade, the first investigations of cork mechanical behaviour under impact were performed. In order to use it as an energy absorber, Gameiro et al. [2005, 2007a] performed dynamic compressions at different strain rates. Numerical simulations of these impacts were also performed. The cork samples were compressed axially at strain rates from 10^{-3} s^{-1} to 600 s^{-1}. The test rig used was Split-Hopkinson Pressure Bars (SHPBH) and both natural and agglomerated cork were tested. The same authors inserted cork in aluminium tubes in order to increase the structure's energy absorption capacity [Gameiro et al., 2007b].

Some of the researchers that recently studied cork, also tried to employ it in passive safety systems, using it as an impact energy absorber [Paulino and Teixeira-Dias, 2011, Alves de Sousa et al., 2012, Coelho et al., 2013]. In one of these numerical studies, Paulino and Teixeira-Dias [2011] used agglomerated cork as padding material in vehicle's doors in order to absorb the impact energy. This application was justified by the great capacity of cork to absorb energy and due to its elastic recover without loss of properties. The numerical simulation results showed that there is a significant improvement in terms of both absorbed energy and peak acceleration.

With a similar purpose, Alves de Sousa et al. [2012] studied the viability of applying agglomerated cork liners in a motorcycle helmet. However, it was a preliminary numerical analysis where the material model was not validated for dynamic regimes, being validated only for quasi-static rates, using the quasi-static experiments from Gameiro et al. [2007a]. In addition, the results were worse than a common EPS liner, concerning the helmets standard criteria. Nevertheless, the results were promising, which launched the basis for a more thorough work on the application of cork as a new material for advanced applications on energy absorption systems. In other words, the basis for this thesis.

Another numerical study that explored the capacity of cork to act as an impact energy absorber within passive safety systems and crashworthiness applications was performed by Coelho et al. [2013]. This work focused on testing of hybrid paddings consisting agglomerated cork and EPS, through simulations of multi-impacts. Nevertheless, the material laws were only validated for quasi-static compression tests and no experimental data was used to validate the multi-impact simulations.

In a more recent study and related to the development of this thesis, Fernandes et al. [2014], using data from the experiments performed by Gameiro et al. [2005, 2007a], simulated the dynamic compressive behaviour of agglomerated cork (using finite element analysis(FEA)), including the material's initial relaxation during the unloading. It should be pointed out the difficulty to obtain experimental data from dynamic compressions, specially concerning the material's relaxation at such strain rates. Fernandes et al. [2014] validated the constitutive models for compression and the part of the relaxation reported by Gameiro et al. [2007a]. None of the previous numerical studies modelled cork's relaxation when unloaded. Until this point, only hyperelastic models were used, without simulating any type of damage.

In addition, Fernandes et al. [2014] performed guided drop tests, by dropping a mass from a 3 meters height. These experiments were simulated with success, using the same constitutive models used to replicate the experiments of Gameiro et al. [2005]. In order to obtain the proper mechanical properties for the constitutive model, Fernandes et al. [2014] also performed quasi-static uniaxial compression tests. In compressions up to 50% strain, the immediately recovery was 90%. Fernandes et al. [2014] also noticed that agglomerated cork's relaxation was faster for higher compressive strain rates.

Rosa and Fortes [1988a] reported a similar behaviour for compressions up to 80%. The recovery rate decreased appreciably with time and increased with the degree of deformation imposed. Fernandes et al. [2014] also reported a prompt recovery of more than 95% after submitting agglomerated cork to dynamic compressive loadings. According to Anjos et al. [2008], when cell buckling occurs during cork compression, the initial dimension recovery is associated with the unfolding of the buckled cell walls which occurs quickly. This shows the high elastic behaviour of cork and its agglomerated versions.

In other work related to the development this thesis, Jardin et al. [2015] investigated the mechanical behaviour of several types of agglomerated cork and expanded cork, under quasi-static and dynamic loading. The quasi-static compression tests gave an interesting insight into the stress-strain curve of agglomerates and Poisson's ratio variation during deformation, which are useful data for numerical simulations. Jardin et al. [2015] determined low Poisson's ratio with mean values of 0.02 and 0.08 for agglomerated and expanded cork respectively. In addition, the results from the double impacts demonstrate a clear influence of agglomerated density and granule size on the resulting mechanical properties, and point out a tremendous potential for this sustainable material to be tailored to fit diverse crashworthiness applications.

The most promising agglomerates from Jardin et al. [2015] were used in Fernandes et al. [2015], another work related to this thesis. In this study, Fernandes et al. [2015] compared the mechanical performance of agglomerated cork and expanded cork against synthetic materials typically used as impact energy absorbers, more specifically EPP and EPS. Thus, Fernandes et al. [2015] performed the same quasi-static and double impacts on EPS and EPP, as Jardin et al. [2015] on cork. In addition, the double impacts performed by Jardin et al. [2015] and Fernandes et al. [2015] were simulated with success, using the same constitutive models used in Fernandes et al. [2014]. Results showed that agglomerated cork is an excellent alternative to the synthetic materials. In addition to the fact of being a natural and sustainable material, agglomerated cork has the capacity to withstand considerable impact energies. Also, its capacity to keep some of its mechanical properties and dimensions after loading, makes this material highly desirable for multiple-impact applications.

Recently, Sanchez-Saez, et al. [2015b] studied the multi-impact behaviour of agglomerated cork by performing consecutive impacts (three impacts per sample) in a drop weight

tower. The impact energies were lower than the impacts performed by Fernandes et al. [2014], Gameiro et al. [2007a], Jardin et al. [2015] and Fernandes et al. [2015]. Nevertheless, the results showed the great capability of agglomerated cork to continue absorbing energy after three consecutive impacts.

In other study, with even lower impact energies, Galindo-Rosales et al. [2015] engraved a network of microchannels in agglomerated cork samples and filled these with a non-Newtonian fluid. The author tried to combine the mechanical properties of agglomerated cork with the enhanced shear thickening response of the non-Newtonian fluid.

2.2 Helmets

Since ancient times, helmets have been used as a primary form of protection. Helmets were introduced as combat armour, protecting the head in combats. Following the evolution of societies, materials and manufacturing techniques became more advanced. Therefore, helmets have evolved over the ages, still being used in modern warfare.

Helmets did not just evolve, they have diversified, being used in all sort of applications. Independently of the application, all types of helmets are designed to protect the head against impacts. Nevertheless, different types of helmets present different designs due to the requirements of each application.

The concept of a hard shell dates back to ancient Greek time. It was realized that a hard shell was needed, not only to prevent the penetration of sharp objects, but also to distribute the applied force and thereby reduce the localization of the impact load, improving the force distribution. Over the centuries, helmets with metal shells were used in wars all over the world. For instance, the helmets worn by soldiers in World War II.

At some point, in the early 20^{th} century, new structures started to be used under the shells. This new feature increased the helmets capacity to absorb and distribute impact energy more effectively [Newman, 2005]. This new device was the solution to the need of introducing a good impact energy absorber in order to reduce the inertial loading on the head and thus, reduce the probability of injuries due to induced accelerations.

At this stage, helmets were still very similar to each other, with some exceptions regarding the military helmets. Nevertheless, hard shells for racing drivers and for other sports were already made of materials other than metals, such as linen impregnated with varnish resins. In 1939, the first helmet with a moulded plastic shell was introduced by Riddell for American football practise [Newman, 2005].

There was almost no difference between helmets until the middle of the 20^{th} century, when it was recognized the specific risks of each application. For instance, motorcyclists deal with one-time life threatening blow that can occur easily in a road accident [Newman, 2005]. On the other hand, in contact sports such as ice hockey and American football, players deal with repetitive impact loading throughout an entire game.

At this point, Holbourn [1943, 1945] performed important studies from which he understood that non-penetrating head injuries are caused by short-duration accelerations acting on the head and on its contents. These injuries are a common and dangerous form of head injuries resulting from road accidents and sports activity, being often caused by blunt impacts.

One decade later, Turner and Havey [1953] introduced the padding of modern helmets, which consisted in a resilient closed-cell rubber foam placed under the shell in order to dissipate impact energy effectively. However, this design was relatively heavy. In the same year, Roth and Lombard [1953] presented the modern helmet as it is known today. Fig.

2.17 shows an illustration of this helmet. The shell was manufactured by four layers of fibre glass and several materials were used as liner, such as EPS and PU foam. Currently, EPS is the most used material as helmet liner, mainly due to its properties (cheap, relatively easy to manufacture and a good energy absorbing material).

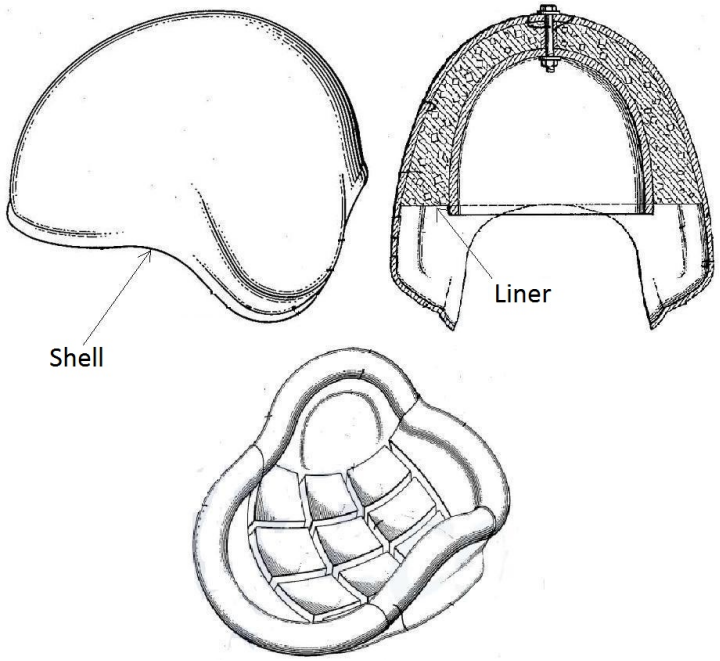

Figure 2.17: Roth's and Lombard's crash helmet (adapted from Roth and Lombard [1953]).

With the awareness of the head injury risk associated with some sports, works and road accidents and the improvement of safety conditions in developed countries, new types of helmets were created. These are usually constituted by similar liners, made of the same materials. The main differences between helmet types are in the helmets geometry and shell material.

In addition, for each of these new applications, organisations were created with governmental authorization to regulate a specific helmets market. Currently, each type of helmet has its own safety standard. Nevertheless, the vast majority of helmet safety standards are similar to each other, especially in what concerns the certification tests.

This means that helmets evolution was influenced by the criteria of these standards. For instance, Snively [1957], founder of the Snell Memorial Foundation (SMF) that is responsible for Snell standards, had a profound impact on modern helmet design and performance by showing that the only helmet that didn't allow a life threatening skull fracture was a helmet made by Roth and Lombard [1953]. The main difference between this and the other helmets was its EPS liner.

Currently, modern helmets are capable of distributing the impact load over a large area of the head, reducing the total force that reaches the user's head. Nevertheless, some substantial improvements are still possible [COST327, 2001]. Some researchers have criticized specific helmet standards for being outdated and thus, not improving helmets quality [Newman, 2005].

Statistics show that the adoption of laws or rules that compel the use of helmets resulted in a considerable number of lives saved. In 2008, 42% of fatally-injured motorcyclists (822 deaths) in the USA were not wearing helmets and it is estimated that the majority would

have survived if they had worn helmets [NHTSA, 2011]. It is also estimated that motorcycle helmets are 37% effective in preventing fatal injuries [NHTSA, 2008]. Nevertheless, the number of fatalities and head injuries resulting from helmeted impacts is still a concern. As shown in Fig. 2.18, head injuries occurred in 66.7% of the cases of COST database [COST327, 2001] and the majority of these injuries were severe.

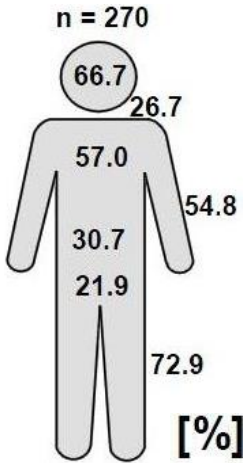

Figure 2.18: Injured body regions of helmeted motorcyclists (adapted from COST327 [2001]).

Head injuries resulting from helmeted impacts also occur in a great variety of sports. Some examples are motorsports, cycling, skiing and other winter sports, horse riding, mountaineering, skateboarding and many other extreme sports, and most of the contact sports such as ice hockey and American football. Sports are a major cause of traumatic brain injury (TBI) [Levy et al., 2012]. Worldwide, it is estimated that approximately 1.6-3.8 million sport-related TBI occur each year [Collins et al., 2003, Langlois et al., 2006, Schulz et al., 2004].

For instance, in a total of 7210 patients with equestrian-related injuries, head injuries accounted for 44% of injuries, including one death, one vegetative state and other patients requiring rehabilitation [Hughes et al., 1995]. In other study, Ball et al. [2007] reported a 7% mortality rate of a total 151 injured patients on horse riding and all fatalities were a result of the 48% head injuries. As in equestrian activity, there are other sports where helmets are used for protection but there is still a high risk of head injury, mainly due to the high impact energies in these sports. Some examples of these are skiing, snowboarding, cycling and automobile and motorcycle racing.

Studies identify the head as one of the most frequently injured body regions among skiers and snowboarders [Macnab and Cadman, 1996, Yamakawa et al., 2001] and concussion as the most frequent outcome [Levy et al., 2002]. In addition, in a total of 350 skiers and snowboarders, Levy et al. [2002] reported that 14% suffered severe brain injuries, with an overall mortality rate of 4%. Severe injuries are also common in motorsports, probably due to the very high speeds that can be reached [Siegel et al., 2001]. In motorcycle racing, 10-30% of all injuries are head injuries and 25% of these are severe and even mortal [Varley et al., 1993].

Head trauma was reported in 29% of all injuries in professional auto racing, with open head injuries comprising only 5% [Trammell and Olivary, 1991] and closed head injuries, such as diffuse axonal injury (DAI), being common [Gennarelli, 1987]. Probably due to the helmet usage, closed head injuries are very common in motorsports [Lister et al., 1998].

Although cycling is not a motorsport, head injuries are common and account for most of the fatal accidents [Mellion, 1991]. A study based on 13684 cyclist casualties estimated that about two-thirds of the severe injuries (122 cases) were head injuries [Amoros et al., 2011]. According to Monea et al. [2014], the most frequent head injuries resulting from bicycle accidents include skull fracture, acute subdural haematoma (ASDH), cerebral contusions and DAI.

In addition, exposure to repetitive head impacts is common in several contact sports and it has been suggested as a possible cause of chronic brain injury [Chamard et al., 2012, Koerte et al., 2012a,b, Mori et al., 2006]. In one football season, Delaney et al. [2000] suggested a 45% concussion incidence rate, with a 70% incidence of multiple concussions. Concussion is also reported as the most common ice hockey-related injury [Honey, 1998, Tegner and Lorentzon, 1996]. Severe brain injuries such as epidural haematoma and subdural haematoma (SDH) are rare, but also reported [Honey, 1998].

The following sections will give a detailed overview on the developments carried out so far on the content of safety helmet technology. First, it is presented some insights regarding helmet design and how it protects its user under impact. The influence of the helmet main components is discussed, regarding mainly their geometry and materials. In addition, the different types of helmets existing nowadays and the standards associated to each type are reviewed, focusing on their influence on design, manufacture and testing, and a summarized comparison between them is also performed. New helmet solutions and new design concepts are also approached.

Finally, it is performed a literature review on studies where the finite element method (FEM) was used to investigate helmets. More information about helmets can be found in Fernandes and Alves de Sousa [2013a]. This state-of-the-art review article is related with the development of this thesis.

2.2.1 Components, design and materials

A typical modern helmet is composed by a hard outer shell, an impact energy absorbing liner, a comfort padding and a retention system (Fig. 2.19). In some cases, for instance in motorcycle helmets, there is also a visor. This is usually made of a transparent material such as polycarbonate (PC) in order to shield the face from dust, debris and even from bad weather conditions, providing a clear vision. Besides protecting the head, helmets have to be comfortable, by insulating and shielding.

Helmets are the most common and best protective headgear to prevent head injuries caused by direct cranial impact [Chang et al., 2003]. Essentially, the purpose of protective helmets is to prevent head injury by decreasing the amount of impact energy that reaches the head, reducing the severity or risk of injury [Deck et al., 2003a, Liu et al., 2003]. Helmets protect the head by absorbing the impact, cushioning the head. In order to have a perception of how a helmet behaves during an impact, it is necessary to understand all the mechanisms involved.

Regarding the impact performance, helmets can be divided into two main parts. There is a hard outer shell that distributes the impact force on a wider area of the liner, reducing the localization of the impact load and increasing the energy absorption. Therefore, reducing the total force that reaches the head and the likelihood of injuries such as skull fractures [Shuaeib et al., 2002b]. In summary, the outer shell is responsible for:

- spreading the impact load over a larger area, therefore reducing the concentrated load and increasing the amount of energy absorbed by having a larger area of the

liner effectively absorbing energy;

- preventing penetration by a pointed or sharp object that might otherwise puncture the cranium;
- providing a structure to the inner liner so it does not disintegrate upon abrasive contact with the pavement or other surfaces. The foams used as liner materials have low resistance to penetration and abrasion as showed by Richter et al. [2001]. Thus, one of the shell's primary roles is to provide integrity against multiple impacts;
- absorbing the initial shock. However, just a small amount of energy is absorbed. From the literature, there are several values determined, such as 30% of the total impact energy [Mills, 1995], 10-30% of the total energy [Gilchrist and Mills, 1994a,b, Mills and Gilchrist, 1991], 12-15% in a study performed by Ghajari et al. [2009b] and a higher value of 34% was determined Di Landro et al. [2002]. The discrepancies among these values may be explained by the different shell materials and geometries, and the different impact conditions.

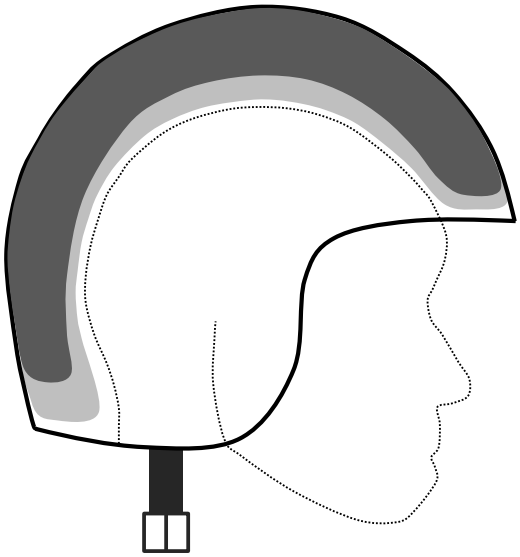

Figure 2.19: An illustration of a helmet and its main components: shell, impact energy absorbing liner (dark gray), comfort padding (light gray) and chinstrap.

The other main component is the energy absorbing liner. The purpose of this inner liner is to absorb the great amount of impact force that was partially absorbed and dispersed by the outer shell. The liner absorbs the impact energy by deforming and thereby reducing the head deceleration and thus, the load transmitted to the head. Therefore, a helmet liner is generally made of an excellent impact energy absorbing material in order to reduce the inertial loading on the head, reducing the likeliness of injuries due to induced accelerations, such as brain injuries.

Closed head injuries are examples of this type of brain injury, being the commonest form of injuries from helmeted impacts. These injuries occur due to relative motion of the brain inside skull, without skull fracture. This behaviour is explained by the brain consistency and by the cerebrospinal fluid (CSF) that surrounds it, which enables the brain to move relatively to the skull. In this sense, when an impact occurs and the helmet's energy

absorption capacity is not enough, the skull stops suddenly but the brain keeps moving due to inertia. From these collisions and relative motions, severe brain injuries may occur due to brain tissue shearing, which may cause internal bleeding. This bleeding and consequent inflammation causes brain swelling, which leads to high intracranial pressures. These and other head injuries and their mechanisms are addressed in the section 2.3.

In addition to the energy absorbing liner, there is another type of padding inside the helmets. Comfort padding is usually used to fit the helmet comfortably. This consists in a sufficiently firm foam covered by a fabric layer that contacts and surrounds the head. This comfort foam is generally made of soft and flexible foams with low density, such as open-cell PU or polyvinyl chloride (PVC) [Brands, 1996, Chang et al., 2003, Gilchrist and Mills, 1993, Mills, 2007, van den Bosch, 2006].

In summary, this foam keeps the comfort and the adequate helmet fitting [Gilchrist et al., 1988, Gilchrist and Mills, 1993, van den Bosch, 1998]. As a result of its low stiffness, the comfort foam deforms completely without absorbing any relevant amount of energy, and therefore, has no influence in impact protection [Beusenberg and Happee, 1993, Cernicchi et al., 2008]. Manufacturers generally produce foams with different thicknesses for each helmet size, improving the helmet wearing stability [Chang et al., 2001].

Helmets usually have some kind of ventilation system involving holes in shell and channels in the liner. The ventilation system ensures that fresh air is conducted into the helmet and humidity and exhaled air are vented out, decreasing temperature inside the helmet. A study performed by Pinnoji and Mahajan [2006] indicates that the ventilation channels grooved in liner are not detrimental to the dynamic performance of helmets.

Helmets also have a retention system known as chinstrap, which keeps the helmet attached to the head. All types of helmets have a retention system and the chinstrap is usually made of polyethylene terephthalate (PET) or nylon. The retention system generally consists of a strap bolted to each side of the outer shell. Nevertheless, there are records of a considerable number of roll off helmets even with the chinstrap intact and closed [Richter et al., 2001], leaving the head unprotected from any following impact. A complete description of the manufacturing process of each helmet component can be found in Shuaeib et al. [2002c].

Design

The performance of a helmet during an impact is mostly affected by its design [Aare, 2003]. Post et al. [2012b] performed impact tests on American football helmets, concluding that it is possible to significant influence the strains incurred by the brain by changing some design characteristics of a helmet.

The liner material properties and its thickness are important variables in order to decelerate the head at a mild rate as it compresses the liner. Thicker foams remain in the plateau regime of the stress-strain curve for longer compression lengths [Kim et al., 1997]. However, a helmet cannot be excessively thick due to practical and aesthetic constraints [Shuaeib et al., 2002b]. A typical liner, depending on the helmet type, is usually between 25 and 60 mm and is also limited by comfort and shape constraints [Yettram et al., 1994]. In addition, the use of a thick liner increases both the volume and mass of the helmet, with obvious disadvantages with respect to loading of the cervical spine [Huang, 1999, Huston and Sears, 1981] and inertial loading of the brain.

Shuaeib et al. [2007] indicated foam density and foam thickness as the most contributing factors in preventing head injury. Therefore, it is important to find the perfect balance between the density and the thickness of the inner liner. For instance, if the liner is too soft

or thin, the head may crush it completely upon impact, stopping the head suddenly and resulting in high accelerations induced to the brain. On the contrary, if a liner is excessively dense, the head will be decelerated more abruptly than necessary. Thus, the ideal liner is stiff enough to decelerate the impact in a smooth and uniform manner, until its limit is reached. However, the ideal stiffness depends greatly on the impact speed [Chang et al., 2000, 2003, Gilchrist and Mills, 1994a, Mills and Gilchrist, 1991, Yettram et al., 1994].

In the studies performed by Deck et al. [2003a] and by Deck and Willinger [2006], they concluded that the elastic limit of the energy absorbing foam has a greater influence on acceleration response but its Young's modulus has the most important influence on head response. The liner density is also an important property because the yielding stress at which the foam crushes is directly related to it [Gibson and Ashby, 1997].

In practice, manufacturers design the helmets based on the impact energies specified by the standards in their energy absorption tests. For instance, the ECE 22.05 standard, which is a motorcycle helmet standard, specifies an impact velocity of 7.5 m/s for their tests. Richter et al. [2001] reported that the range of the most common head impact speeds in real crashes is 5.83-8.33 m/s. Mills [2007] agree that most crashes occur at a range of low impact velocities, adding that helmets cannot prevent all injuries, as some crashes are too severe for any wearable helmet.

Bourdet et al. [2012] reported that current motorcycle helmets are very effective for moderate speed impacts, but its protection reaches its limits at higher energies, where helmet deformation reaches its limits. This is supported by the analysis conducted in the COST 327 project [COST327, 2001], which shows that serious injuries occur at impact speeds above 13.89 m/s, almost the double of those considered on the most demanding standard tests. Bourdet et al. [2012] and Mellor and StClair [2005] postulated that if helmets could be made to absorb more energy, the number of injuries and its severity can be reduced.

Furthermore, van den Bosch [2006] showed that the optimal liner density may depend on multi-density solutions, using different densities for different regions. Gilchrist and Mills [1994a] demonstrated that shell geometry has influence on the shell stiffness, as helmet shells are stiffer when loaded at the crown, since that site has a double-convex curvature and is distant from any free edges. Hence, soft liners should be located in the crown region with the objective of compensating high shell stiffness and attempting to make helmet impact response site-independent [Mills et al., 2009a]. Besides geometry, the exterior finish of the shell is also important, influencing the friction against the impact surface, which has a tremendous effect on the rotational acceleration [Halldin et al., 2001, Mellor and StClair, 2005, Phillips, 2004].

As previously referred, helmets design is influenced by standards requirements [Chang et al., 1999b, Gilchrist and Mills, 1987, Hopes and Chinn, 1989, Kostopoulos et al., 2002, Yettram et al., 1994]. Some of these studies showed the influence of a few standards requirements, such as the penetration test of Snell M2015 [Snell M2015, 2015] and BSI 6658 [BSI, 1985], concluding that these tests force helmets to be designed with stiffer shells, leading to higher acceleration values. In fact, this could result in a helmet with a thick shell that typically weights about 6-8 times more compared to the liner [Shuaeib et al., 2002b]. This aspect was also criticized by Hume et al. [1995], since the frequency of accidents involving sharp objects is extremely small, and this test causes the outer shell of the helmet to be excessively thick, resulting in a heavier helmet. Otte et al. [1997] and Mills [2007] concluded exactly the same. Nevertheless, some standards do not require this type of test, such as ECE 22.05 [ECE R22.05, 2002]. Helmet shells are typically 3-5 mm thick, considering the currently used materials [Mills, 2007].

Helmet improvement is also achieved by defining an adequate material [Bourdet et al., 2012]. The force generated when a helmeted head impacts, depends on the material compressive characteristics, its strength and on the loaded area size [Zellmer, 1993]. Nevertheless, what a helmet designer normally changes to affect helmet response is foam thickness, foam material and shell material [DeMarco et al., 2010].

Materials

Generally, the shell is made from thermoplastic materials such as polycarbonate (PC) or acrylonitrile-butadiene-styrene (ABS), or from composite materials such as carbon fibre, Kevlar® or fibre-reinforced plastics (FRP) such as glass fibre reinforced plastic (GRP) and carbon fibre reinforced plastic (CRP). The shells made of thermoplastics materials are isotropic while the FRP shells show an anisotropic behaviour in the plane of the shell [Mills and Gilchrist, 1992]. The most common FRP is GRP, commonly known as fibreglass.

GPR is a relatively cheap material with a fairly good mechanical performance [Tinard et al., 2012a]. Nevertheless, thermoplastic shells are even cheaper when compared with the composite ones. Carbon fibre and Kevlar® are normally used for the most advanced helmets [Cernicchi et al., 2008]. Helmet shells made of advanced composite materials are progressively substituting the thermoplastics ones. However, composite materials are generally more expensive and their application is still evaluated in a cost-benefit basis.

During an impact, the shell may also absorb some energy during impact [Liu et al., 2003, Pinnoji and Mahajan, 2010]. This fact makes composite materials desirable, since composite shells may absorb energy through damage mechanisms such as matrix cracking and delamination [Maimi et al., 2011]. The main advantage of using composite outer shells lies in their capability of absorbing more energy through damage in comparison with thermoplastic shells. Thermoplastics shells may absorb energy by plastic deformation, usually involving fractures. However, it is a relative small amount compared to composite shells, mainly due to its main forms of damage, matrix cracking and delamination.

Such behaviour cannot be achieved at low energy impacts, showing a dependence of composite shells on the impact energy, which is greater than the thermoplastic ones [Mills and Gilchrist, 1991]. Gilchrist and Mills [1994a] showed that to occur delamination a great amount of impact energy is necessary. Nevertheless, at higher energy impacts, composite shells provide substantial protection by improving the impact energy absorption capacity of the helmet system [Kostopoulos et al., 2002]. Therefore, at high energy impacts, composite shells are more effective. Kostopoulos et al. [2002] studied different composite shells and the one made of Kevlar® performed better, exhibiting a much higher absorbed energy and increasing the energy absorbed by the liner. In another study, Mellor and Dixon [1997] carried out experiments on helmets with GRP shells in order to investigate the influence of the impact surface shape, concluding that for kerbstone anvils and edgy surfaces, the GRP shells effectively spread the load, and better than on flat surfaces.

On the other hand, at low energy impacts, a thermoplastic may be more effective, having better protective characteristics with softer shells, as demonstrated by Markopoulos et al. [1999]. This finding is also present in other studies [Chang et al., 2000, 2003, Gilchrist and Mills, 1994a, Mills and Gilchrist, 1991, Yettram et al., 1994]. Stiffer FRP shells are often used in combination with a low-density EPS foam, whereas the softer PC and ABS shells are usually combined with high-density EPS foam [van den Bosch, 2006].

Nevertheless, the shell stiffness has an important influence in the overall dynamic performance of the helmet. The stiffness of FRP shells is higher than the stiffness of a thermoplastic shell made of Polycarbonate (PC), as demonstrated by Beusenberg and Happee

[1993]. By comparing both experimentally, the stiff FRP shell showed only minor deformation, maximising the liner loaded area and thus, the impact energy was predominantly absorbed by liner deformation. Gilchrist and Mills [1994a] studied the deformation mechanisms of ABS and GRP and concluded the same as Beusenberg and Happee [1993], that composite shells deform less than the thermoplastic ones. Moreover, fibre-based materials had a much lower fracturing rate, whereas plastic shells fractured more often and the rebound of a helmet with a thermoplastic shell is much higher than a fibreglass helmet, which makes the thermoplastic one less effective and thus less safe [Aare, 2003].

Currently, the most common material used as liner in safety helmets is EPS. This synthetic cellular material has excellent shock absorption properties and a convenient cost-benefit ratio [Di Landro et al., 2002]. This is the main reason why EPS is widely used by the majority of the manufactures, with rare exceptions. Densities applied in helmets vary from approximately 30 to 90 kg/m^3 [Brands, 1996, van den Bosch, 2006]. EPS absorbs the impact energy through its capacity to develop permanent deformation by crushing (foam collapsing). High-density EPS is able to absorb larger amounts of energy than low-density EPS, but transfer larger forces to the head [Di Landro et al., 2002]. Nevertheless, to obtain the same energy absorption, lower thickness of high-density foam is sufficient [Di Landro et al., 2002].

Although this type of foam has an excellent first impact performance in case of a subsequent impact in the same area, the protection level offered by EPS would be minimal since the material deforms permanently without elastic recovery [Gilchrist and Mills, 1994b, Shuaeib et al., 2002b,c, 2007]. Thus, its energy absorption capability is significantly decreased after a first impact, particularly in high energy impacts. Although EPS is widely used by the majority of helmet manufactures, this material is not perfect, and new materials and solutions have been proposed. These are reviewed in section 2.2.4.

Statistical results pointed out that helmets are effective in reducing fatalities and severe injuries [Shuaeib et al., 2002a]. However, the brain injuries that result from induced accelerations are still a problem, mostly the rotational acceleration that remains underestimated, specially by main helmet standards [Johnson, 2000, Richter et al., 2001, Willinger and Baumgartner, 2003a,b]. Nowadays, some researchers criticise this aspect in standards and also some of their outdated requirements. These are reviewed in section 2.2.3. In helmet optimisation studies, Deck et al. [2003a] and Deck and Willinger [2006] affirmed that nowadays helmets are designed to just reduce the linear headform deceleration. Thus, there are still needs of improvements respecting helmet design.

2.2.2 Types of helmets

Nowadays, helmets are used in several applications. There are different helmets for different activities. Independently of the application, helmets are constituted by similar liners, which are usually made of the same material. The main differences between helmet types are in its geometry and shell material. Currently, there are several types available in the market, even within the helmets for the same application. This is the case of motorcycle helmets, which can be classified into four types:

- Full face helmet;
- Modular Helmet;
- Open face or jet helmet;
- Half Helmet.

Full Face

Full face motorcycle helmets are by far the most common type of helmet [MAIDS, 2004, Richter et al., 2001]. A full face helmet covers the entire head, protecting also the face. The fact that full face helmets cover the entire head means that they are among the safest types of helmets, providing extra strength around the entire skull. Fig. 2.20 shows the main types of motorcycle helmets, including full face helmets.

Figure 2.20: Main types of motorcycle helmets (adapted from Silva [2016]).

However, the fact that full face helmets involve the entire head may have some disadvantages such as heat. Also, they are one of the heaviest types helmets, mainly due to the shell, which covers a larger area. This aspect can be detrimental in a crash due to inertial loading on the neck and brain [Huang, 1999, Huston and Sears, 1981]. Nevertheless, the COST 327 final report [COST327, 2001] and Richter et al. [2001] showed that approximately 16% of helmet impacts are at the chin area. Otte [1991] also concluded that impacts on the face and jaw areas are common in motorcycle crashes.

In addition, Chang et al. [1999a, 2000], Mills [1996] concluded that full face helmets offer an essential protection and that its energy absorbing capacity could be improved by placing a liner in the chin area. Currently, some helmets already have a rigid foam in this area Mills [2007]. According to Mills et al. [2009a], for frontal impacts, this foam came into play. Thus, wearing a helmet with less coverage eliminates that protection. According to the COST 327 final report [COST327, 2001] and Aare [2003], full face helmets offer better protection than the others.

Modular helmet

A modular helmet is a combination between full face and open face helmets. When fully assembled and closed, it resembles a full face helmet by covering the face. This part may be pivoted upwards to allow access to the face, as in an open face helmet, which is a great

advantage in terms of comfort and practicability, as shown in Fig. 2.20. However, this same mechanism makes this type of helmets the heaviest type.

Although modular helmets do look the same as full face helmets, they might offer less protection at the chin area. Nevertheless, there aren't scientific studies that assess the protective capacity of modular helmets for face impacts. The actual state of the standards contributes somehow to this. The DOT standard does not require chin guard testing. The ECE 22.05 allows the certification of modular helmets with or without face impact test, since it is only indicated if the helmet protects the chin area. Nevertheless, Snell tests this region, and modular helmets are not an exception. Snell certified a modular helmet for the first time only in 2009, the Zeus ZS-3000.

Open face helmet

Open face helmets, also known as jet helmets, cover almost the entire head, except for part of the face, leaving for instance the chin area unprotected, as shown in Fig. 2.20. Thus, a jet helmet provides the same protection as a full face helmet, except when the impact is to the face [COST327, 2001]. Hitosugi et al. [2004] observed that users of open face helmets are significantly more likely to sustain severe head injuries, specially brain contusions, than users of full face helmets.

This helmet style is the most common among all helmet types. Fig. 2.21 shows some of the different types of open face helmets according to the application. Open face helmets are used in almost all applications, since sports such as American football and ice hockey to equestrian and winter sports. Even military helmets use this style, although with some differences such as the used materials. One application with a different style is cycling, albeit bicycle helmets are also open face helmets, they have have a different geometry. In addition, there are other types of helmets with different geometries. For instance, the safety helmets used in constructions, which resemble hard hats and also the already referred full face helmet used by motorcyclists and racing drivers.

Half helmet

Half helmets have an even reduced coverage than jet helmets, without a lowered rear. The half helmet barely provides the minimum coverage generally allowed by some standards, by covering only the top half of the cranium. This issue is also highlighted by Shuaeib et al. [2002a], where the half-shell helmet is considered the most vulnerable to impacts at lateral and back head regions.

In addition, this type of helmet is known for easily coming off during impacts, which led to its prohibition in some countries [DeMarco et al., 2010]. A recent study evaluated the effectiveness of different styles of helmets, including half-coverage, open-face and full-face [Yu et al., 2011]. The riders involved in crashes wearing half helmets were twice more likely to have head injuries than riders wearing full face helmets or even open face helmets. Thus, it can be said that less coverage is equal to less protection provided by a helmet.

2.2.3 Helmet safety standards

Helmet standards have been established in many countries to evaluate the protective performance of helmets. Some standards are regulated by governments, like in Europe and North America, but in other countries they are issued by private organizations. These standards prescribe a number of tests to ensure that a helmet satisfies the safety requirements.

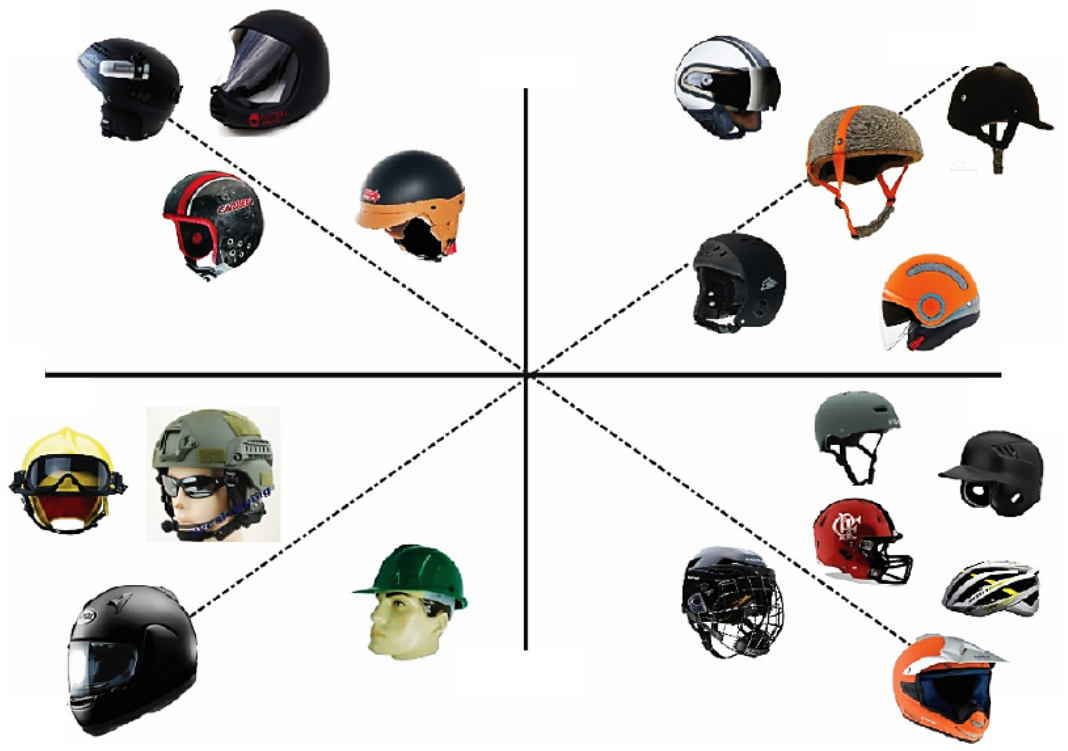

Figure 2.21: Different types of open face helmets (adapted from Silva [2016]).

All standards have different requirements, but the majority of them are similar to each other, specially in what concerns the evaluation of helmets impact performance.

Currently, each type of helmet has its own safety standards. Standards also evaluate other parameters such as comfort, ventilation, weight and fitting, among many others. Nowadays, all helmets are designed, manufactured and tested to meet the standards requirements. Therefore, the performance tests required by any standard eventually influence helmet design. Currently, it is well known that helmets substantially reduce head injury, being safer to wear a helmet rather than none. Nonetheless, today's helmets are primarily designed to reduce headform linear deceleration, instead of being optimised to prevent head injury [Aare et al., 2003, Deck et al., 2003a, Forero Rueda et al., 2011, Kleiven, 2007a, Tinard et al., 2012b]. The following subsections address the requirements of the main safety standards.

Motorcycle helmet standards

In order to evaluate the performance of motorcycle helmets, standards have been established in many countries. Motorcycle helmet standards are usually regulated by governmental institutions and in rare cases by private ones, such as SMF. In Europe, motorcycle helmets are regulated by ECE 22.05 [ECE R22.05, 2002]. This is the most widespread helmet standard, required in over 50 countries worldwide [Pratellesi et al., 2011]. Also in Europe, specifically in the United Kingdom, there are to options: a motorcycle helmet has to meet the requirements of ECE 22.05 or the BSI 6658 [BSI, 1985]. According to Newman [2005], this standard represents the state-of-the-art in performance specifications, partly due to its criteria.

In the USA, motorcycle helmets have to meet the requirements of DOT FMVSS 2188

standard. In addition, some manufactures may try to certify their helmets accordingly to a private standard, the Snell M2015 [Snell M2015, 2015]. These four are the main motorcycle helmet standards. The helmets approved by these standards are not just motorcyclists, these are valid for other activities, for instance, snowmobiling, motocrossing, karting, among many others.

Overall, standards are different from each other but similar in their primary goal which is assessing the helmet performance. These standards prescribe a number of tests to ensure that the helmets satisfy the safety requirements. Almost all the standards follow the same concepts in evaluating the effectiveness of the helmets during an impact, which are:

- the helmet has to be able to absorb enough impact energy;
- it has to remain on the head during the impact;
- it must resist to penetration.

The last updates from Snell M2015 and DOT FMVSS 2188 standards were attempts to approach the ECE 22.05 requirements. Similarities between standards are well accepted and useful for manufacturers that have the possibility to sell the same helmet in countries regulated by different standards, without deep design changes. However, differences are still considerable, which makes it possible to have a helmet approved by one standard and rejected by another. For instance, double impact is required by Snell M2015 and DOT FMVSS 2188, while ECE 22.05 only requires a single impact. In the specific case of motorcycle helmets, it can be argued that double impacts at the same area are not frequent, but the requirement is an acceptable procedure for providing a safety margin [Thom et al., 1998]. A short summary of the tests performed by each standard is presented in table 2.1. Since the focus of this work is the helmets impact performance, only the impact tests are thoroughly reviewed, specially the ones required by the European standard.

Table 2.1: Overview of motorcycle helmet standard tests.

Test \ Standard	ECE 22.05	Snell M2015	DOT FMVSS 218	BSI 6658
Impact	X	X	X	X
Penetration		X	X	
Retention	X	X	X	X
Roll off	X	X		X
Rigidity	X			
Friction	X			X

Prior to all the tests, helmets must be conditioned, by being exposed to ambient temperature, low temperature and high temperature conditioning. Other types of conditioning such as ultraviolet irradiation moisture conditioning are also performed. Penetration tests have been criticized by Hume et al. [1995] since the frequency of motorcycle accidents involving pointed objects is extremely small and this test causes the outer shell of the helmet to be excessively thick leading to heavier helmets. Otte et al. [1997] conducted a statistical study and his findings supported the conclusions of Hume et al. [1995].

A comparison between standards, regarding the impact tests, is performed by summarising the impact conditions and failure criteria in table 2.3. In these tests, a flat anvil is typically used, due to the fact of flat surfaces being the most impacted in real crashes, which is usually the road [Gilchrist and Mills, 1994b, Shuaeib et al., 2002a, Vallee et al.,

1984]. More anvils are used for test purposes, such as the kerbstone anvil (ECE 22.05), the hemispherical anvil (BSI 6658, DOT FMVSS 218 and Snell M2015) and the edge anvil (Snell M2015).

The shock absorption test is designed to ensure that helmets retain structural integrity and attenuate impact energy during a variety of crash scenarios. In all standards, tests are performed in a specially designed test rig. The helmets are dropped by gravity in a guided free fall accelerating the helmet-headform system until a required speed. By varying the drop height, the energy level of the test can be easily adjusted and precisely repeated.

During the impact test, the acceleration is measured and recorded thanks to a built-in triaxial accelerometer positioned at the centre of gravity (COG) of the rigid headform. The headforms mass and size specified by the standards are nearly the same. For instance, the dimensions of ECE 22.05 and Snell M2015 headforms are based on the ISO-DIS-6220 standard [International Standards Organisation, 1983], with their mass increasing with their size. Fig. 2.22 shows the ECE 22.05 headform schematics and table 2.2 presents the mass values for each size. This headform differs from the others by having a short neck. In addition, DOT FMVSS-218 standard employs partial headforms instead of a headform resembling the entire head. In addition, Gimbel and Hoshizaki [2008] concluded that headform's mass plays a significant role in the helmet performance.

Table 2.2: General characteristics of ECE R22.05 test headforms

Symbols	Size [cm]	Mass [kg]
A	50	3.1 ± 0.10
E	54	4.1 ± 0.12
J	57	4.7 ± 0.14
M	60	5.6 ± 0.16
O	62	6.1 ± 0.18

The helmeted headform fall is guided by either a steel track or a pair of steel cables. That guiding system adds friction to slow the fall slightly, so the test technician corrects by raising the initial drop height accordingly. The other standards such as DOT FMVSS 218 and Snell M2015 use a vertically-guided headform that cannot rotate during impact while the unrestrained headform method in ECE 22.05 allows rotation in any direction as the headform responds to the test impact. However, this rotational motion and acceleration is not monitored or recorded and important data is therefore lost. Standards define specific areas of the helmet as impact locations, for instance, ECE 22.05 defines these impact points as represented in Fig. 2.23:

- B, in the frontal area, situated in the vertical longitudinal plane of symmetry of the helmet and at an angle of 20° with the AA' plane,
- X, in either the left or right lateral area, situated in the central transverse vertical plane and 12.7 mm below the AA' plane,
- R, in the rear area, situated in the vertical longitudinal plane of symmetry of the helmet and at an angle of 20° with the AA' plane,
- P, in the area with a radius of 50 mm and a centre at the intersection of the central vertical axis and the outer surface of the helmet shell,

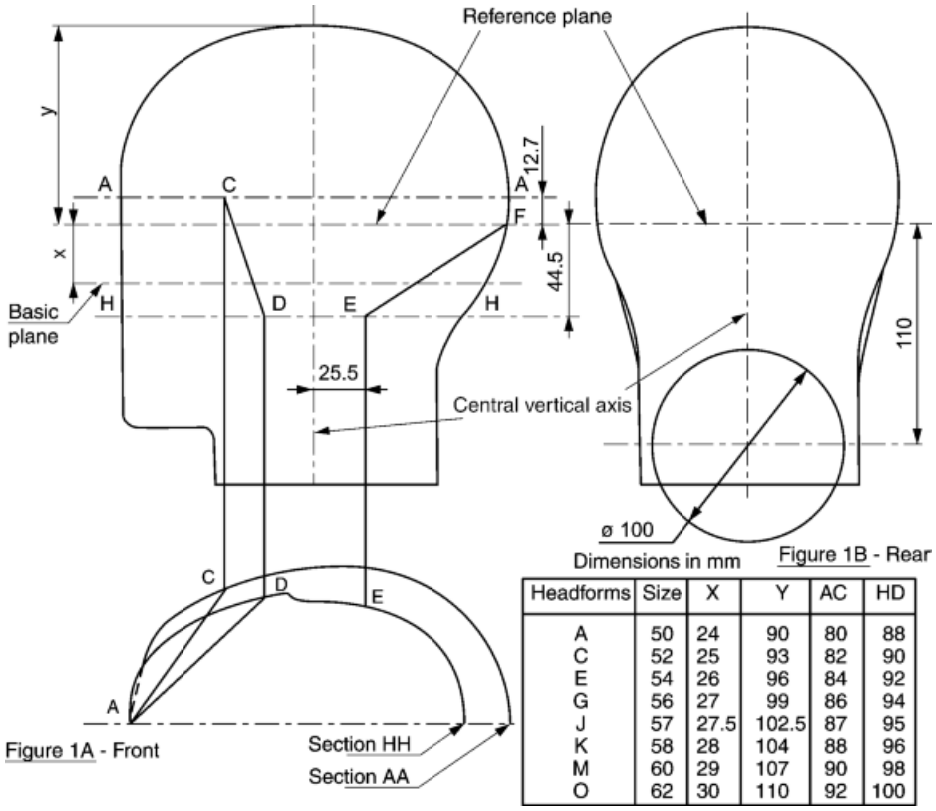

Headforms	Size	X	Y	AC	HD
A	50	24	90	80	88
C	52	25	93	82	90
E	54	26	96	84	92
G	56	27	99	86	94
J	57	27.5	102.5	87	95
K	58	28	104	88	96
M	60	29	107	90	98
O	62	30	110	92	100

Figure 2.22: Geometry and dimensions of ECE 22.05 headform [ECE R22.05, 2002].

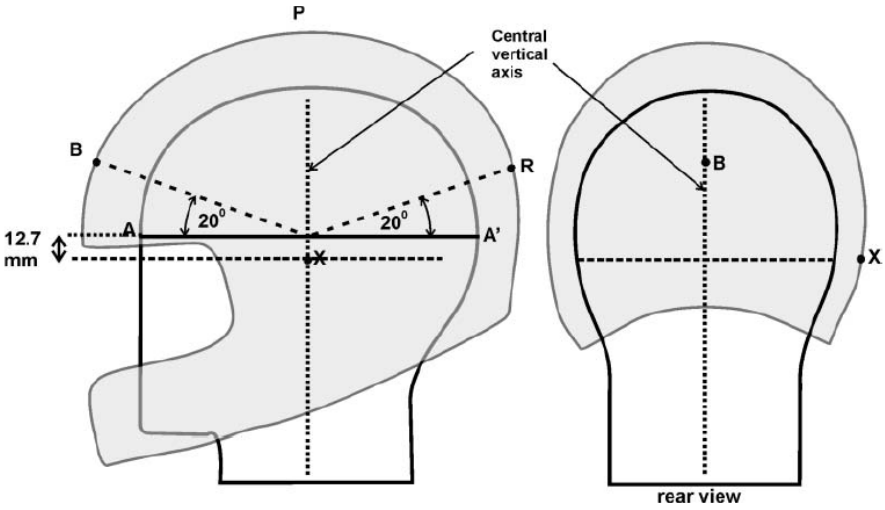

Figure 2.23: ECE 22.05 impact points (adapted from Chinn and Hynd [2009]).

Impacts at points B, X and R should be within 10 mm radius of the defined point. After each impact the helmet shall be repositioned correctly on the headform prior to the next impact, without interfering with the adjustment of the retention system. The shock absorption tests of ECE 22.05 are performed at a velocity of 7.5 m/s, using flat and kerbstone steel anvils as impact surfaces.

The impact speeds defined by standards range up to 7.75 m/s, although much higher

velocities are achieved while riding a motorcycle. Nevertheless, the normal impact speed is usually not the same as the riding speed. When a motorcyclist falls, the impact is usually oblique, which means that the falling speed is decomposed into two components, perpendicular and tangential to the road surface. Nevertheless, this range of impact speeds used in the impact tests of the standards are the most frequent in road accidents [Richter et al., 2001]. However, these are still low velocity impacts. In addition, it is also worth referring that the tangential component is not assessed by any standard.

Recently, SMF created a new standard for competitive automotive sports, Snell SA2015. This one is similar to Snell M2015, but with more and higher impacts [Snell SA2015, 2015]. This is now the standard used by *Federation Internationale de l'Automobile* (FIA) to determine which helmets the professional pilots can use. For a medium size headform, a minimum of three impacts are required, being performed in this order: 8.5, 6.31 and 6 m/s. In order to be used by a professional pilot, the acceleration shall not exceed 300 g. Nevertheless, it is worth noting that the impact sites defined by Snell SA2015 may not occur at exactly the same site, since Snell standards define a significant area where the impact may occur. Fig. 2.24 shows the referred area. The same is verified for Snell M2015 [Snell M2015, 2015]. Thus, there is the possibility of the three impacts occurring on different helmet points.

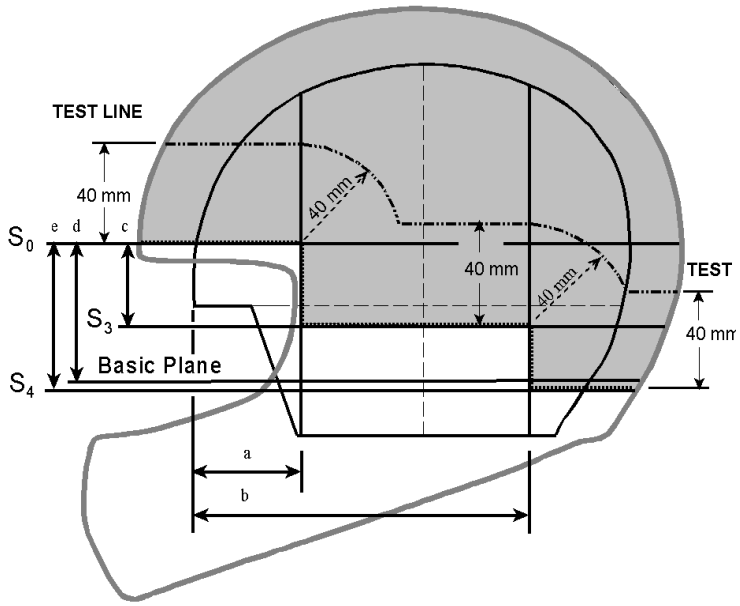

Figure 2.24: Area defined for testing (adapted from Snell SA2015 [2015]).

Standards use the maximum value of acceleration measured during the impact as failure criterion. The thresholds for each standard are presented in table 2.3. In this work, this criterion is defined as peak linear acceleration (PLA). Thus, PLA is the maximum acceleration value measured at the headform's COG by a triaxial accelerometer array.

However, PLA ignores the duration of the impact. DOT FMVSS 218 standard only defines maximum time intervals for different levels of acceleration, while Snell M2015 and BSI 6658 ignore impact duration in their evaluation. Nevertheless, ECE 22.05 standard takes into account the impact duration through the head injury criterion (HIC):

$$HIC = \left(\left[\frac{1}{t_2 - t_1} \int_{t1}^{t2} a(t)dt \right]^{2.5} (t_2 - t_1) \right)_{max} \quad (2.1)$$

where $a(t)$ is the resultant head acceleration in [g], the interval $t_2 - t_1$ is the bound of all possible time intervals defining the total impact duration, less than or equal to 36 ms and t_1 and t_2 are any two points of the acceleration pulse in time, in seconds.

Table 2.3: Comparison of impact conditions and failure criteria of motorcycle helmet standards.

Standard	**Snell M2015**	**DOT FMVSS 218**	**BSI 6658**	**ECE 22.05**
Impact Conditions				
Velocity:	(medium size)		(flat or hemi anvil)	
1st impact	7.75 m/s	6.0 m/s	6.5 m/s or 6.0 m/s	7.5 m/s
2nd impact	6.78 m/s	5.2 m/s	4.6 m/s or 4.3 m/s	-
Failure Criteria				
Peak	275 g	400 g	300 g	275 g
150 g	-	4 msec	-	-
200 g	-	2 msec	-	-
HIC	-	-	-	2400

HIC takes into account acceleration and impact duration. This consists in an improvement in terms of criteria [Newman, 1980]. Nevertheless, many researchers have been criticising HIC for several reasons, such as for not taking into consideration the rotational acceleration, impact direction and head size and for having nonsensical units [Bellora et al., 2001, Kleiven, 2003, 2005, Feist et al., 2009, Fenner Jr et al., 2005, Kim et al., 1997, Kleiven and von Holst, 2002, Newman, 1980, 1975]. Nevertheless and agreeing with HIC drawbacks made by other researchers, Hopes and Chinn [1989] and Deck et al. [2003a] indicate that HIC may still be a useful tool for comparing energy absorbing safety devices in linear impacts.

The acceleration-based head injury criteria used by the standards to access the helmets performance in the impact absorption tests are detailed and further explained in the section 2.3.4. In these sections, the pros and cons of both PLA and HIC are presented, as well as the respective head injury thresholds. A more detailed comparison between motorcycle helmet standards can be found in Thom [2006], Jowitt et al. [2014] and Becker et al. [2015], albeit the reviewed version of Snell is now outdated.

Thus, HIC and PLA remain as the only normative parameters used for helmet homologation. This means that no standard assess the rotational motion that a motorcyclist is subjected, neither the local tissue thresholds. In the case of ECE 22.05, the peak linear acceleration is limited to 275 g and the HIC value should be inferior to 2400 in order to be approved. However, the rotational acceleration occurs in all motorcyclists accidents [Johnson, 2000] and has a tremendous effect in brain injuries. Some researchers affirm that the current trend is to design helmets to pass the standards with no consideration for biomechanical findings [Shuaeib et al., 2002a, Tinard et al., 2012b]. So, optimisation based on biomechanical criteria is different than the optimisation with HIC criterion, which

is correlated with acceleration of a rigid headform's COG.

Pratellesi et al. [2011] tested uncertainties that are related to the homologation procedure in ECE 22.05 and found that HIC values change by up to 30% due to testing uncertainties that are in total agreement with ECE 22.05. This fact may cast the credibility of a standard into doubt as a deviation of 30% is certainly not within the tolerable range of a safety gear.

Helmet standards for other activities

In Europe the helmets for pedal cyclists and for users of skateboards and roller skates are regulated by EN 1078:2012+A1:2012 standard [CEN, 2012]. This European Standard specifies requirements and test methods for helmets worn by cyclists, skateboarders and roller skaters. Since the majority of the tests are similar to the ones performed by motorcycle standards, specially by ECE 22.05, only the impacts test are reviewed.

According to the last version of EN 1078 standard, helmets shall give protection to the forehead, rear, sides, temples and crown of the head. This standard defines different test areas for determination of shock absorbing capacity. Fig. 2.25 shows the correct fitting and test area, which depends on the anvil. The area above the line RR' is the test area for impacts against the flat anvil. The area above the line RWA" is the test area for impacts onto the kerbstone anvil.

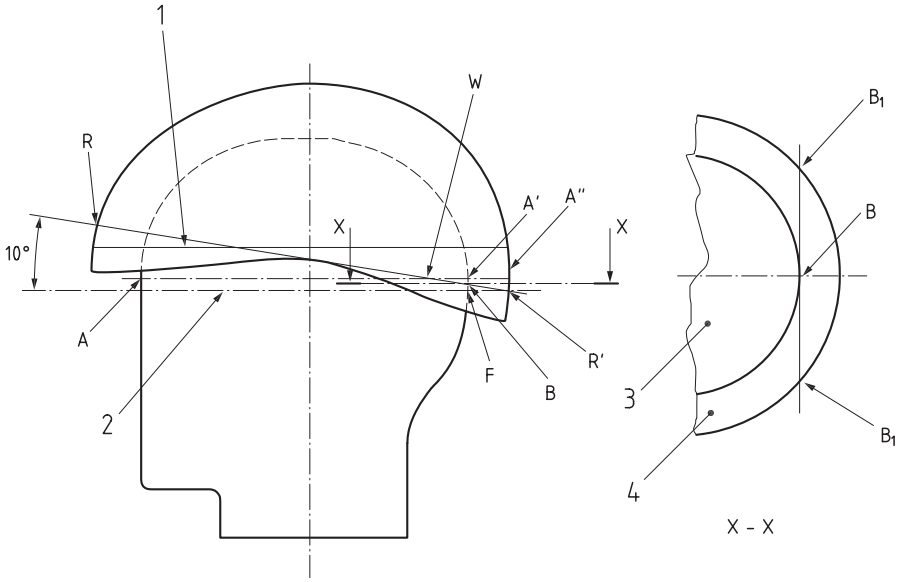

Figure 2.25: Definition of test area (adapted from CEN [2012]).

The headforms used shall comply with EN 960:2006, the same headforms used by ECE 22.05 (Fig. 2.22 and table 2.2). The impact velocities are 5.42 m/s and 4.57 m/s for impacts onto the flat and kerbstone anvil, respectively. These are theoretically equivalent to 1.5 m and 1.1 m drop heights, respectively [CEN, 2012]. Helmets are approved if the peak acceleration does not exceed 250 g. Fig. 2.26 shows the test apparatus for EN 1078:2012+A1:2012, which is the same of ECE 22.05. A EN 1078:2012+A1:2012 test apparatus shall comprise:

- an anvil rigidly fixed to a base;

- a free fall guidance system;
- a mobile system supporting the helmeted headform;
- a metal headform fitted with a triaxial accelerometer;
- an accelerometer output recording and conditioning system;
- a system by which the point of impact can be brought into correspondence with the centre of the anvil.

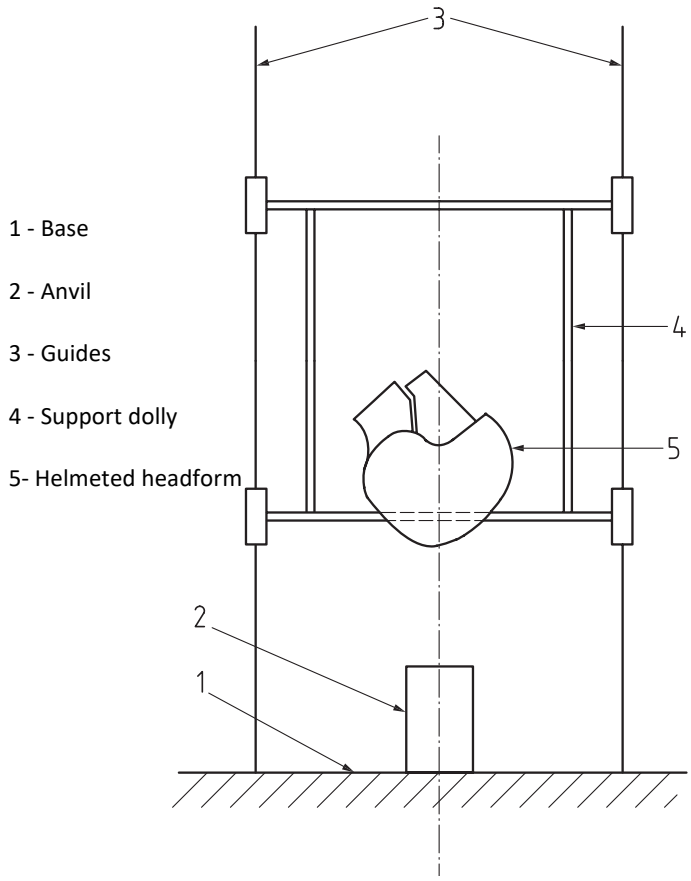

Figure 2.26: Illustration of the test apparatus used for determination of shock absorbing capacity (adapted from CEN [2012]).

In the USA, the mandatory standard that regulates these same helmets is the Consumer Product Safety Commission (CPSC) standard. This standard defines that a helmet shall be dropped onto the flat anvil with an impact velocity of 6.2 m/s. This is equivalent to a minimum drop height of 2 m, plus a height adjustment to account for friction losses. For the hemispherical and kerbstone anvils the impact velocity is 4.8 m/s, which is equivalent to a minimum drop height of 1.2 m, considering also the adjustments to account for friction losses. The peak acceleration of any impact shall not exceed 300 g. This is also the limit defined by Snell B-95, with similar impact energies but with other stringent requirements. Nevertheless, this one is rarely used.

Regarding winter activities, helmets for skiing and snowboarding are regulated by other standards. However, these are very similar regarding the impact tests. In Europe, this type

of helmets is subjected to impact energies of approximately 90 J, as required by the EN 1077 standard. The helmeted headform is dropped from a height of 1.5 m and the peak acceleration measured in it, shall not exceed 250 g. The Snell standard for this type of helmets, Snell RS-98, defines exactly the same impact conditions and approval criterion as its cyclist version, Snell B-95.

In Europe, helmets for horseback riding were regulated by EN 1384, which is similar to other European versions such as EN 1078 standard, defining an impact of 5.4 m/s with an approval criterion of 250 g for maximum peak acceleration. However, it was verified that the level of protection required to pass EN 1384 was low, being criticised due to failure to protect a great number practitioners [Commission to the European Parliament, 2014]. Consequently, this standard was withdrawn and there is no European standard for this activity. Professionals, not just in Europe, are using the recently updated Snell E2016. This standard specifies for a medium size headform, impact velocities of 6.06, 5.42 and 5.07 m/s for an impact onto a flat, hemispherical and horseshoe, respectively. For approval, the peak acceleration measured in the headform's COG shall not exceed 275 g.

In general, the standards for non-motorised activities use low-velocity impacts. However, these standards are typically designed to protect against a single severe impact, such as a bicyclist's fall onto the pavement, even if there is the risk of occurring multi-impacts. Generally, the foam material in the helmet will crush to absorb the impact energy during a fall or collision and can't protect its user from an additional impact.

Nevertheless, there are standards that force the design of helmets to withstand multiple-impacts. Some helmets for contact sports are designed to protect against multiple moderate impacts, typically occurring in sports such as American football and ice hockey, where the user continues to wear the helmet after impacts. Nevertheless, these are usually low energy impacts.

The standards that regulate American football and ice hockey helmets, NOCSAE ND002 and NOCSAE ND030 respectively, define that at least two impacts of 5.46 and 3.46 m/s, have to be performed at the same area. In order to be approved the peak severity index of any impact shall not exceed 1200. Gadd [1966] introduced the concept of a severity index to compare the severity of various head impacts and is given by this empirical expression:

$$GSI = \int a(t)^{2.5} dt \tag{2.2}$$

where a is the instantaneous head acceleration in g and t is the time duration of the acceleration pulse in seconds. However, Gadd [1966] set a value for this failure criterion of 1000, as a concussion threshold for frontal impacts. Later, Gadd [1971] suggested a threshold of 1500 for head non-contact loads. This criterion is thoroughly addressed in section 2.3.4. There are also other standards used in North America regulating American football and ice hockey helmets, ASTM F717 and F1045 respectively, using only one lower-energy impact of 75 J (approximately 5.47 m/s) and the maximum acceleration shall not exceed 275 g or 300 g depending on the impact site. Currently, these specific helmets designed for multi-impacts with low energies are usually made of foam materials other than EPS, for instance EPP. These recent solutions are reviewed in the next section.

2.2.4 Novel geometries and materials

Current helmet safety standards are based on experiments conducted over decades ago, before the current knowledge of head trauma, especially the mechanisms of closed head injuries, including rotational injuries. In order to improve helmets quality in terms of safety,

comfort and aesthetics, new materials have been proposed and used by a few manufacturers and researchers. In addition, new concepts have been proposed in order to enhance the energy absorption properties, improving the current safety levels of helmets. These new solutions and their benefits and problems are reviewed in this section.

Pinnoji et al. [2008a] tested helmets with shells made of aluminium foams. These have high strength and an excellent energy absorption capacity. The results with this new concept showed a lower acceleration on the head and a weight reduction of 30% relatively to helmet with a shell made of ABS. Nevertheless, due to the plastic deformation of the aluminium foam, it might not behave well to a second impact, since the outer geometry is lost. More recently, this concept was optimised [Pinnoji et al., 2010], improving the impact performance, albeit the subsequent impacts remained a problem.

Caserta et al. [2011] replaced part of the helmet's liner by aluminium honeycombs, using these as reinforcement material, as shown in Fig. 2.27. The results indicate that this new configuration provides better protection to the head from impacts against specific surfaces than the original EPS liner. Best results were obtained for impacts against the kerbstone anvil. However, the results obtained for impacts onto a flat surface revealed some limitations, performing even worse than the original EPS helmet at some impact points. In addition, the thickness necessary to accommodate the honeycomb layers is extremely limited. Thus, in a real accident scenario, an excessively thin layer of EPS foam could be easily penetrated, reaching the head.

More recently, Hansen et al. [2013] proposed a novel Angular Impact Mitigation (AIM) system for bicycle helmets, employing an elastically suspended aluminium honeycomb liner. The impact performance under normal and oblique impacts of this new bicycle helmet was compared to a standard EPS one. The results demonstrated that this new helmet could effectively improve impact mitigation, performing better than the EPS helmet for both normal and oblique impacts. However, penetration of the comfort liner or the scalp of the dummy was not addressed.

Recently, Blanco et al. [2014] proposed an innovative ski helmet liner that consists of an ABS lamina with deformable cones, as shown in Fig. 2.28. Energy is absorbed via a combination of folding and collapsing of the cones. The main advantage that such liner may introduce over common EPS pads is that it allows a better optimisation of energy absorption for different impact sites [Blanco et al., 2014]. In this basis, the helmet was optimised and the results showed reductions in both maximum acceleration and HIC for almost all impacts required by the standard.

Other new concept is the conehead™ shock absorbing liner, developed to absorb impact force more effectively. This concept proposed by Morgan [2007] consists in a helmet foam liner made of two density layers, as shown in figure 2.29. The outer layer, which is the black part, is made of high density foam and has truncated cones facing inwards. The inner layer, the grey one, which is close to the head, is made of softer low density foam and has cones facing outwards. With this dual-density liner, the impact performance is improver for both low and high energy impacts.

The collapsing of the cones causes the energy to spread sideways within the thickness of the foam liner instead of towards the head [Morgan, 2007]. In addition, the head will experience a gradual deceleration due to the crushing of the cones, minimizing the energy induced to the head. Hence, there is a reduction in the forces translated across the thickness of the liner. This concept is among the most promising ones, being already used in a few commercial helmets.

POC also developed a dual-density liner, similar to the conehead™ but with a different geometry. Partly similar to conehead™, with a stiffer outer liner and a softer inner liner,

this POC helmet becomes well suited to deal with both high and low energy impacts [POC, 2016].

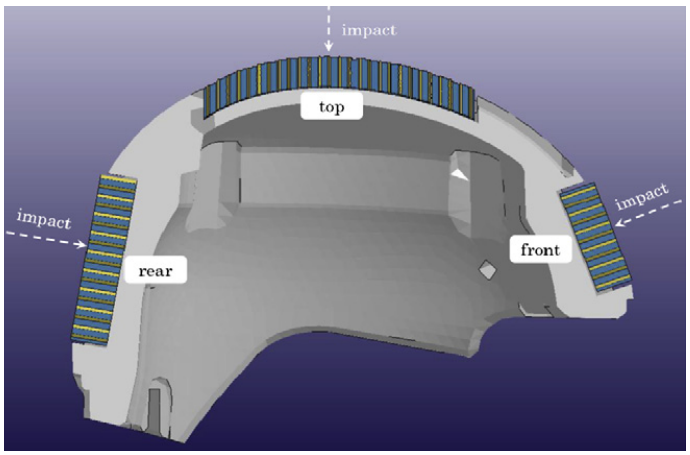

Figure 2.27: Schematic section of the prototype liner proposed by Caserta et al. [2011] (adapted from Caserta et al. [2011]).

Figure 2.28: ABS cone liner proposed by Blanco et al. [2014] (adapted from Blanco et al. [2014]).

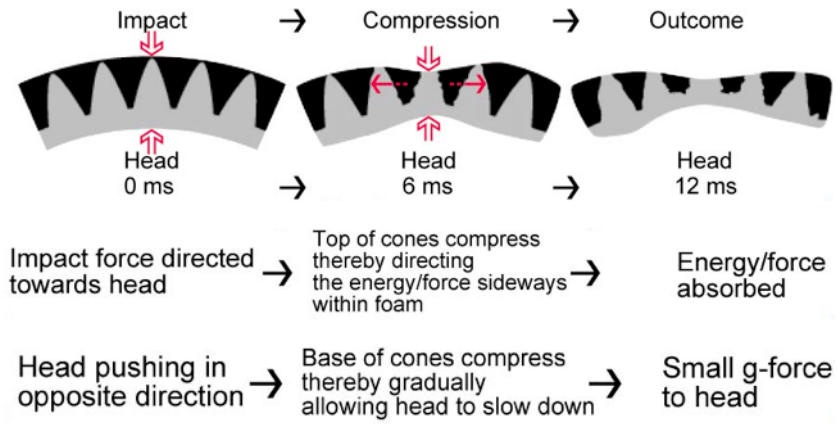

Figure 2.29: Conehead™ - how it works (adapted from Morgan [2007]).

Although EPS foam has an excellent first impact performance, in case of a subsequent

impact in the same area, the protection provided by EPS would be minimal since this material deforms permanently [Gilchrist and Mills, 1994b, Shuaeib et al., 2002b,c, 2007]. Thus, it will have low protective value in the occurrence of a subsequent event [Liu et al., 2003]. In addition, as shown in section 2.2.3, there are already some standards that require multi-impacts. In order to overcome this issue, some materials have been proposed, such as EPP and agglomerated cork.

EPP is somewhat similar to EPS, presenting similar peak accelerations and impact durations for the same helmet, as verified by Shuaeib et al. [2007]. In addition, it has the capacity to recover some of its dimensions depending on the impact severity. This material is already employed in helmets used in American football and ice hockey. Manufacturers of these helmets probably change from EPS to EPP, due to the multi-impacts required by the NOCSAE standards, as referred in the previous section .

In addition, POC is also employing EPP in different types of helmets, in order to offer multi-impact protection [POC, 2016]. Other multi-impact concepts were developed by POC through examination of the helmets used by alpine racers in the last World Cup. POC found out that the majority of the helmets were worn out in the front due to repeated impacts from the gates. According to the developers, these are actually more severe than expected, which led POC to develop a multi-impact deflector panel in the front of the helmet. This deflector increases the rigidity of the shell structure, minimising the transmitted impact force and increasing the helmets shock absorption capacity.

A closed cell foam based on vinyl nitrile polymer (VNP) was also indicated as a good energy absorber that could be used as helmet liner [Goel, 2011]. In fact, stiff VNP is already used at the top of some American football helmets, together with EPP to provide extra protection against tackles and blocks that usually impact this area. Recently, KALI developed a new concept called nano core, which is an acrylic self-healing foam infused with carbon nanotubes. Accordingly to the manufacturer, this new liner dissipates impact energy more efficiently with a smaller volume [Kali, 2016].

Recent brands are creating a great number of new solutions, albeit some standards are not updated for decades. These innovative concepts are welcomed in order to improve the quality of safety helmets. Nevertheless, in a society constantly looking for natural and sustainable solutions, these innovative designs are predominately made of synthetic materials. Thus, as motivation for this thesis, cork will be tested as a helmet liner in order to check its performance against the traditionally used EPS and the recently employed multi-impact version, EPP.

Considering all the attractive properties of cork, for instance, its capacity to withstand multi-impacts and the fact of being a natural material, led Alves de Sousa et al. [2012] to test its agglomerated version as helmet liner. Agglomerated cork makes it possible to manufacture helmet liners in their usual shapes. Nevertheless, in the numerical study performed by Alves de Sousa et al. [2012], the material models used to simulate the mechanical behaviour of both cork and EPS were not validated. Thus, no conclusions were drawn.

Other natural material was proposed as helmet liner, specifically as comfort liner. Taher Halimi et al. [2012] developed a new comfort liner made of wool and Tunisian alfa fibre, which improves sweat absorption and thermal comfort. Although it is not the focus of this work and it was already referred, rotational accelerations are common in accidents, being responsible for severe brain injuries and are not assessed by any existing helmet standard. Nevertheless, as in the previous presented solutions, recent helmet brands have been creating innovative and actually, very effective concepts regarding this matter. Some of these concepts are already in the market with success.

This is the case of the multi-direction impact protection system (MIPS), a technology that mitigates the rotational acceleration on the head [Halldin et al., 2001]. The outer shell and liner slides over the head at the moment of impact. A low-friction layer (for instance Teflon®) makes possible the relative rotation between head and helmet, as shown in Fig. 2.30. According to the developers, the weight is increased by less than 5% relatively to a conventional helmet, keeping the same design and comfort [MIPS, 2012]. In addition, MIPS helmet performed better than a standard helmet, reducing the peak rotational acceleration [Halldin et al., 2001, Aare and Halldin, 2003].

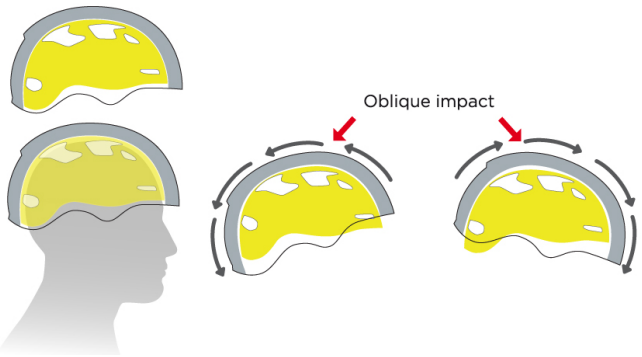

Figure 2.30: Multi-direction Impact Protection System (MIPS) (adapted from MIPS [2012]).

Basically, MIPS mimics the brain's own protection system based on a sliding low friction layer between the head and helmet liner. When the head is subjected to an impact, the brain slides along a membrane on the inner surface of the skull, which reduces the forces transmitted to the brain.

A similar solution to MIPS, but on the opposite side of the helmet, is the Phillips Head Protection System (PHPS). The PHPS enhances traditional helmet design by adding a lubricated polymer membrane over the helmet's shell [Phillips, 2004]. The membrane is designed to slip in a controlled manner over the shell. In this concept, it can be said that it mimics human scalp behaviour. An illustrative example is shown in figure 2.31. An identical concept was proposed by Mellor and StClair [2005].

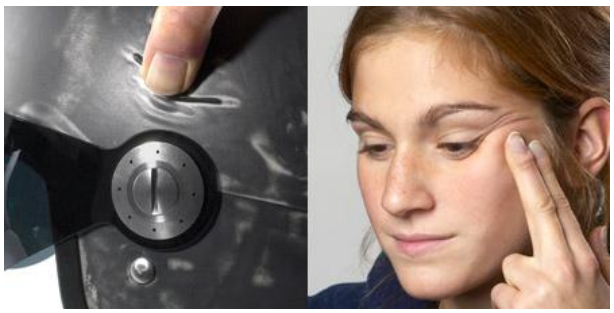

Figure 2.31: Phillips Head Protection System (PHPS) (adapted from Ask Nature [2012]).

According to the creators, this concept decreases significantly the rotational force that reaches the brain. This technology is already available on the market for motorcycle helmets. MIPS is also commercially available and for different types of helmets.

More recently, a new helmet technology has been introduced, the Omni-Directional Suspension (ODS) helmet, which consists of two EPS liners separated by an array of elastomeric rubber dampers [Shaw, 2014]. In low energy impacts, these dampers help

EPS in reducing linear accelerations. Nevertheless, the main advantage of this technology is in reducing rotational acceleration by allowing differential rotational movement between the two EPS liners, which is controlled by the damper array in shear. This solution is also on the market [Shaw, 2014].

2.2.5 Finite element modelling

Initially, motorcycle helmet's design, impact behaviour investigation and optimisation were based on experimental testing. Nevertheless, optimising or testing different helmet models is a hard task with high costs of time and material. However, this is still the way some manufacturers work, mainly based on their know-how.

This methodology was partly surpassed by the development of mathematical models, which have been a useful tool in helmet design and research. The early theoretical attempts to model a helmeted head impact were based on the assumption that the helmeted head system could be approximated by an equivalent set of lumped masses, springs and dashpots [Mills and Gilchrist, 1988, Wilson et al., 1993, Gilchrist and Mills, 1993, 1994b]. These lumped masses systems were then solved using basic dynamic and vibration theories such as modal analysis [Willinger et al., 2000b]. However, the application of these models is very limited, mainly due to its precision and the incapacity of representing most of the essential features, for instance the helmet geometry.

Such fact, allied to the advance of CPU power, led to the development of FE models. These allow a preciser modelling of the helmet components, including their geometry, material properties and contact interactions. The first model was reported by Khalil et al. [1974], using it to study the head biomechanical response to transient impact waves. This is a very simple model, especially regarding its geometry and material models. The next FE helmet models were also very simple, for instance the ones developed by Köstner and Stöcker [1987], van Schalkwijk [1993] and Yettram et al. [1994]. In addition, these were not validated.

A few years later, improved FE helmet models were developed [Brands et al., 1996, Liu et al., 1997, 1998, Liu and Fan, 1998, Scott, 1997, Chang et al., 2000]. However, the geometry of these was still simplified, with either spherical or regular shapes. Nevertheless, Brands et al. [1996] validated the FE helmet model under standard tests in terms of head acceleration.

More recently, realistic and accurate models were developed and validated. These have different components with precise geometries and the material models are no longer purely elastic, including for instance the plastic damage of foams. These models were used for many purposes, for instance to study the applicability of new materials [Alves de Sousa et al., 2012, Caserta et al., 2011, Kostopoulos et al., 2002, Pinnoji et al., 2008a, 2010, Pinnoji and Mahajan, 2010, Tinard et al., 2011], to optimise dummies [van den Bosch, 2006, Willinger et al., 2001], to study real impacts [Aare, 2003, Forero Rueda et al., 2011, Ghajari et al., 2011, Mills et al., 2009a], to determine the effect of impact velocities [Chang et al., 2003], to optimise helmets according to specific criteria [Cui et al., 2009, Deck et al., 2003a, Forero Rueda et al., 2009, Mills and Gilchrist, 1992, Pinnoji and Mahajan, 2006, Pinnoji et al., 2008b, Tinard et al., 2012b], to assess the helmets performance and effectiveness of helmet standards [Aiello et al., 2007, Cernicchi et al., 2008, Ghajari et al., 2009a, Fernandes and Alves de Sousa, 2013b, Fernandes et al., 2013, Klug et al., 2015, Mustafa et al., 2015, Pratellesi et al., 2011, Teng et al., 2013, Tinard et al., 2012a], to study the biomechanics associated with helmeted impacts and to optimise helmets according to biomechanical criteria rather than standards criteria [Deck and Willinger, 2006, Marjoux et

al., 2008, Neale et al., 2004, Shuaeib et al., 2002a, Tinard et al., 2012b, Willinger et al., 2000a, 2002]. In addition, Tinard et al. [2012b] showed that even if a helmet passes the tests of shock absorption required by the standard ECE 22.05, the head injury risk remains high. Therefore, once a numerical helmet model is validated, a great variety of information can be obtained and thus, a helmet model can be optimised according to a specific design criteria much faster and cheaper.

2.3 Human head biomechanics and modelling

Statistical results point out that helmets are effective in reducing the risk of death and injury severity [Shuaeib et al., 2002a]. However, brain injuries that result from induced accelerations are still a problem [Johnson, 2000, Richter et al., 2001, Willinger and Baumgartner, 2003a,b]. These researchers criticise helmet standards for this problem, highlighting their outdated requirements. In helmet optimisation studies, Deck et al. [2003a] and Deck and Willinger [2006] affirmed that nowadays helmets are designed to just reduce the linear headform deceleration.

A helmet designer must have a thorough and comprehensive understanding of head impact biomechanics. The main way by which biomechanics has influenced helmet design is not so much in the understanding of different injury mechanisms, but rather in a better appreciation of biophysical characteristics of the head and the development of kinematic head injury assessment functions [Newman, 2005]. In this section, after a brief introduction to head anatomy and trauma, head injury mechanisms associated with head impact are also summarized. In addition, an overview of the main head injury criteria is presented, including also a literature review concerning FE human head models.

2.3.1 Head anatomy

The human head is a natural complex set of bones and several soft tissues [Pike, 1990]. It can be described as a multi-layered structure covering the brain, where the scalp is the outermost layer followed by skull bone, dura, arachnoid and pia membranes, as well as CSF [Schmitt, 2007]. This multi-layered structure is shown in Fig. 2.32, showing a coronal cross section of a top portion of the human head.

The skull, which is thinner at the sides and at the lower rear of the head [Chinn and Hynd, 2009], protects the brain, working as a stiff braincase. In Fig. 2.32, it is possible to observe that below the skull there are three membranes denoted as meninges, which protect and support the spinal cord and the brain, separating them from the surrounding bones.

The brain is a vital organ made of a fragile soft viscoelastic material, being the main part of the central nervous system (CNS). The space between the skull and the dura mater is called epidural space and it is the region where are the major arteries. Dura mater is a tough fibrous membrane adherent or close to the inner surface of the bone, anchoring the brain. Beneath the dura mater is the thin and fibrous arachnoid. Between the dura mater and the underlying arachnoid is a narrow subdural space filled with a small amount of fluid that acts as a lubricant between the two membranes [Kleiven, 2002].

The third and innermost layer is the very thin pia mater, which is attached to the brain and dips down into the sulci and fissures covering the brain surface and acquiring its shape. The subarachnoid space is a large gap that separates the arachnoid from the pia mater, which is filled with CSF that constantly circulates and surrounds the whole brain, acting

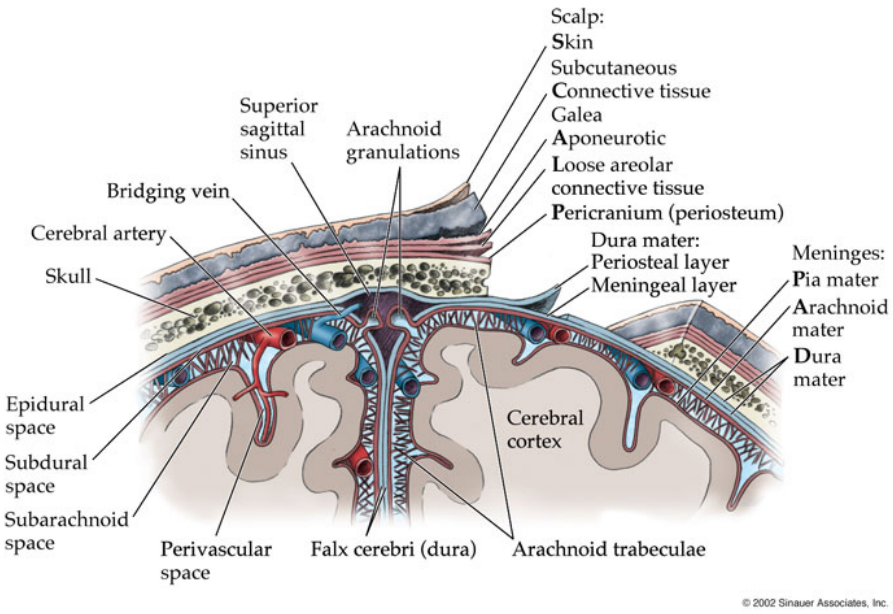

Figure 2.32: Human head anatomy (adapted from Hargreaves [2006]).

as a shock absorber and consequently, protecting the brain. In addition, there are fibrous filaments known as arachnoid trabeculations, which extend from the arachnoid to the pia mater and help holding the brain to prevent it from excessive movement in cases of sudden acceleration or deceleration, acting as a brain natural protection.

In Fig. 2.32, it is also possible to see the folds of the dura mater that form the falx cerebri, which projects into the longitudinal fissure between the right and left cerebral hemispheres. A sagittal dural partition membrane, the falx cerebri, partly separates the left and right hemispheres of the brain. Another dural fold forms the tentorium cerebelli, a membrane that separates the cerebrum from the cerebellum and brainstem. The falx and tentorium cerebelli constrain the brain intracranial motion. The tentorium cerebelli resides on the base of the skull and separates the cerebrum from the cerebellum.

The meninges are crossed by blood vessels, for instance the veins that bridge the subdural space. These bridging veins are associated to frequent and severe injuries [Gennarelli, 1981]. The brain can be divided into three main parts: the cerebellum, the cerebrum and the brainstem, as shown in Fig. 2.33. The cerebrum is the largest and most complex part of the brain. It is composed by two hemispheres connected by the corpus callosum. These hemispheres can also be divided into four lobes: the frontal, the parietal, the temporal and the occipital lobes.

The outermost layer of the cerebrum is called the cortex and consists of grey matter. Beneath the cortex is white matter. The brainstem includes the midbrain, the pons and the medulla oblongata. The cerebellum is located in the posterior part of the head. This is a brief summary of the human head anatomy, where only the main parts concerning this work are addressed.

In conclusion, the referred set of bones and soft tissues that involve the whole brain works together as a natural and complex mechanism that protects the brain. However, this is not enough to prevent injuries in neurotrauma cases, which explains the introduction of restraint systems, such as helmets, seat belts and airbags.

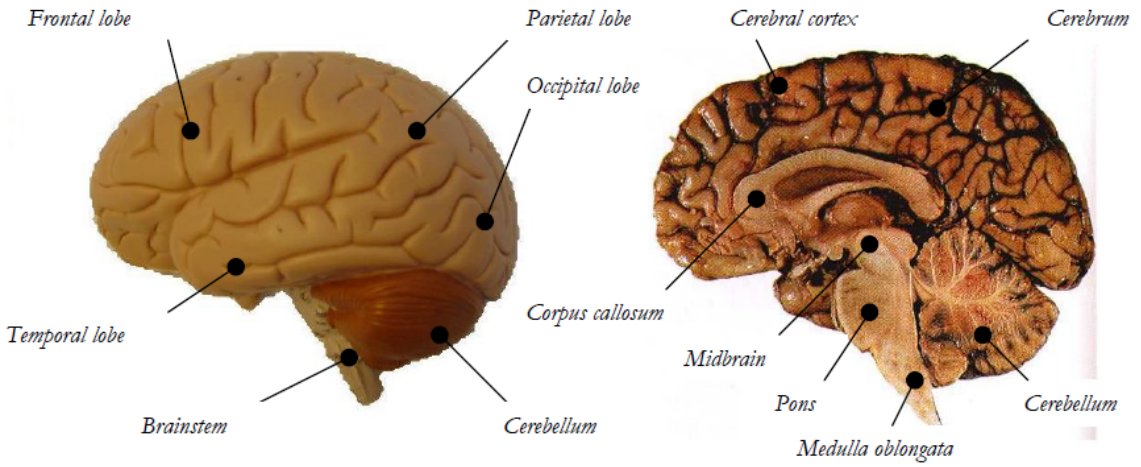

Figure 2.33: Brain (adapted from Aare [2003]).

2.3.2 Head injuries

Head injuries result from excessive loading on the head. When the loading capacity of the head tissues is exceeded, it usually results in severe injuries that may cause disability or even be fatal. The mechanisms of head injuries are still not fully understood, mainly due to the complexity of the brain.

Head injuries can be divided into cranial injuries (for instance, skull fractures) and intracranial injuries (for instance, focal injuries and diffuse brain injuries). The latter is any form of injury to the intracranial contents. Other studies include scalp damage besides skull fractures, focal injuries and diffuse injuries in their head injuries classification [Hume et al., 1995, Hurt et al., 1981, Viano, 1988, Voo et al., 1994]. However, only the latter will be here addressed, since they are more relevant than scalp damage [Shuaeib et al., 2002a].

In helmeted head cases, brain damage is much more frequent than skull fracture, mainly due to the protective effect of the helmet. This can be inferred from statistical studies performed by Hurt et al. [1981] and Otte et al. [1997], where skull fractures account for circa 16% and 13.1% and brain injuries account for 58.4% and 38.2%, respectively.

Skull fractures

A skull fracture is a break in one or more skull bones, usually occurring as a result of blunt force trauma, when the impact force is excessive enough to fracture bone at the impact point or even nearby if the adjacent bones are more fragile than the impacted one.

Skull fractures can be either open or closed. The latter is a bone fracture without substantial injury to the surrounding skin. On the other hand, an open fracture can be more severe than a closed one, because of the severity and the accompanying risk of infections, caused by damage to the surrounding tissues and exposure to pathogens.

Skull fractures can occur with and without brain damage, but is in itself not an important cause of neurological injury [Gennarelli, 1985, Prasad, 1985]. However, when bone fragments penetrate blood vessels or brain tissue, complications may be mild, moderate or severe. Also, even when skull fracture does not occur, bending of the skull may be sufficient to damage underlying blood vessels and brain tissue [Chinn and Hynd, 2009, Newman, 2005].

Skull fractures can also be divided accordingly to fracture location into basilar skull fractures (fractures to the base of the skull) and vault fractures (fractures to the non-base part of the skull). Skull fractures can also be classified accordingly to the type of fracture into linear and depressed fractures. The linear fractures are the most common, and usually the less severe type. These are no more than breaks in the skull bone (through its entire thickness), but no displacement is involved. Nevertheless, dangerous complications may occur [Melvin et al., 1993, Wismans, 1994]. The depressed fractures result usually in portions of bone displaced inward, which may damage the underlying tissues. An illustration of both types is shown in Fig. 2.34.

Thus, despite skull fractures do not necessarily cause neurological disability, bone fragments may penetrate brain tissue or blood vessels when a depressed fracture occurs, probably resulting in brain injury and intracranial haematoma, especially when the depression is deeper than the thickness of the skull [Prasad, 1985]. Depressed skull fractures are frequent mechanisms of brain injury, being often associated with TBI [Motherway et al., 2010].

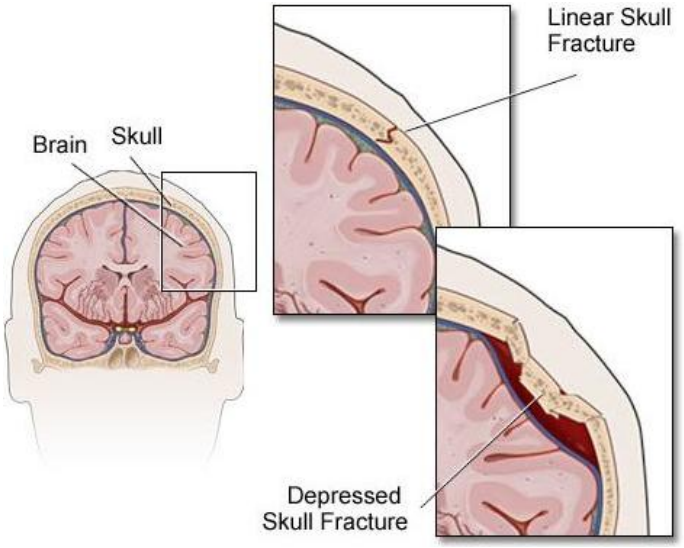

Figure 2.34: Linear and depressed skull fractures (adapted from Krames StayWell [2011]).

It is unlikely that minor skull fracture can cause brain injury, and it could be argued that this is one of the natural mechanisms to absorb energy [Bullock and Graham, 1997]. In helmeted head impacts, brain injuries are usually more frequent and severe. Skull fractures normally occur only in situations of penetration, high deformation or fracture of the shell.

Focal brain injuries

Focal brain injuries are localised injuries that usually occur due to tensile or compressive stresses. This type of injuries is highly correlated with fatalities [Melvin et al., 1993]. According to Aare [2003], approximately two thirds of the deaths associated with head injuries can be attributed to focal brain injuries. These correspond to local damage, consisting of epidural haematomas (EDH), subdural haematomas (SDH), intracerebral haematomas (ICH) and contusions (coup and contrecoup). These are illustrated in Fig. 2.35.

Most focal injuries are due to direct contact with bone fragments from skull fractures and due to relative motion between skull and the brain. An example of injuries dependent on

relative motion between brain and skull are subdural haematomas [Bandak, 1997b, Bullock and Graham, 1997]. Usually, these injuries result from direct impacts, where the greater the force, the more extensive is the focal brain injury, with slight or severe depression skull fracturing [Oehmichen et al., 2006].

Epidural haematoma. An epidural haematoma (EDH) is the result of skull trauma (and consequent skull deformation) or injury to the underlying meninges. EDH is not a direct injury to the brain and greatly depends on skull deformation. However, this may also be injured due to complications associated with the accumulation of blood, originating a significant volume that rises the intracranial pressure [Ho, 2008].

Generally, bleeding above dura mater is a result of this type of injury. This haematoma may cross dura but not cranial sutures [Gean, 1994]. Although skull fracture is usually associated, EDH may also occur in the absence of it. Glowacki [1991] reported that fractures at the posterior fossa are observed in 64% of the EDHs at this region. In addition, Besenski [2006] reported that 95% of the total EDHs result from skull fractures.

Nevertheless, EDH is a infrequent sequel to head trauma, circa 0.2-6% according to Cooper [1982] and 1.2-1.7% according to Oehmichen et al. [2006]. In addition, EDH are not as lethal as SDH [Aare, 2003]. If the haematoma is found below the dura mater, it is called SDH. An injury even rarer is double epidural haematoma (DEDH) with an overall incidence of 2-10% of all epidural haematomas [Görgülü et al., 2000]. However, DEDH mortality rate remains high [Baugh et al., 2013], exceeding 30% [Huda et al., 2004].

Subdural haematoma. A subdural haematoma (SDH) is often caused by a rupture of an artery or bridging vein due to excessive loading, usually excessive rotation, which is the most common mechanism of SDH [Besenski, 2006, Ho, 2008, Kleiven, 2002]. Nearly one third of the acute SDH cases are directly related to bridging vein rupture [Asiminei et al., 2011]. Examples of SDH are lacerations of cortical veins and arteries, large contusions bleeding into the subdural space, and tearing of dural sinuses.

This type of injury arises from tangential force against the skull, and is directly related to rotational effects on the brain [Gennarelli, 1983]. So, it can be considered a direct effect from inertial and non-contact forces. A SDH is caused by short duration and high strain rate loading [Sahuquillo-Barris et al., 1988]. Nevertheless, following a head impact the brain lags relatively to the skull, which leads to a longitudinal strain in the veins that can further lead to vein rupture, as shown in Fig. 2.39.

Acute SDH (ASDH) is usually caused by haemorrhagic contusions that break through the arachnoid mater, by bridging veins rupture, or rarely by laceration of cortical arteries or veins. In an autopsy series, two thirds of the ASDH were associated with contusions [Maxeiner, 1997].

In road accidents, one of the most frequent and fatal type of brain injury is SDH, which is also associated with long-term disability [Gennarelli, 1983]. Gennarelli and Thibault [1982] reported an incidence of acute SDH of 30%, with an associated mortality rate of 60%. More recently, it was reported a mortality rate greater than 30% [Melvin and Lighthall, 2002]. In a study performed by Richter et al. [2001], from a total of 409 head injury cases, it was observed that more than half were brain injuries and from those, a major part was SDH.

Contusion. Contusion is the most frequently found injury following head impact [Aare, 2003, Kleiven, 2002, Schmitt, 2007]. It consists of heterogeneous areas of necrosis, haemorrhage or oedema. Contusions result from local brain tissue motion within the cranium

[Graham et al., 1995] and may also occur at the site of depressed skull fractures [Besenski, 2006]. In general, contact loading may result in a relative motion between the brain surface and the inner surface of the skull, causing contusions on the brain surface.

Generally, there are two distinguished types of contusions: coup and contrecoup. Coup injury occurs at the site of impact while contrecoup occurs at the opposite site of the impact, as shown in Fig. 2.38. Coup and contrecoup contusions are contact injuries [Gennarelli, 1985, Ommaya and Gennarelli, 1974], produced by compressive forces or tensile forces. The latter are usually associated with negative pressures. Nevertheless, contrecoup injuries are considered more significant and more frequent than coup contusions [Melvin and Lighthall, 2002].

For instance, in a frontal impact, the brain moves relatively to the skull, compressing the area near to the impact region (coup) and stretching the opposite region of the brain (contrecoup). Depending on the impact energy, the brain may rebound, compressing the brain in the contrecoup region and stretching it in the coup region.

Intracerebral haematomas. This type of focal injury is distinguished from contusions by a more pronounced localisation of the haematoma [van den Bosch, 1998]. Intracerebral haematomas (ICH) are well defined homogeneous amounts of blood within the brain. They are usually caused by sudden acceleration/deceleration of the head. This type of injury is generally regarded to be of minor importance [Kleiven, 2002].

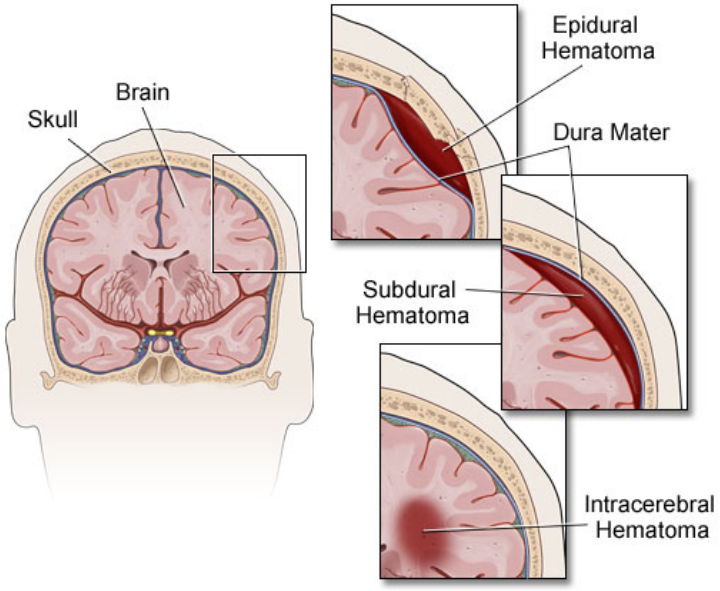

Figure 2.35: Focal brain injuries (adapted from Krames StayWell [2011]).

Diffuse brain injuries

Diffuse brain injuries (DBI) are fundamentally different from focal injuries, being associated with global disruption of brain tissue. This class of injury is usually a consequence of distributed loading conditions that generally induce low energy damage on substantial volumes [Bandak, 1997a]. DBI generally occurs via impact, often without skull fracture, being referred as a closed head injury [Gennarelli and Thibault, 1982, 1985, Goldsmith and

Plunkett, 2004]. DBI accounts for approximately 40% of patients with severe brain injuries, and one third of deaths due to head injury [Whitaker, 1980]. More info about DBI can be found in a detailed study performed by Graham et al. [1995].

Concussion. Concussion is characterized by a slight increase in intracranial pressure [Oehmichen et al., 2006] and by transient loss of consciousness or even post-traumatic amnesia of variable duration in the severe cases. Generally, it is not a severe injury and the recovery time is short [Kleiven et al., 2003, Oehmichen et al., 2006]. For instance, brain tissue disruption does not happen in mild concussions, contrary to other types of DBI. Concussion is a common result from head impacts, even in the helmeted ones [Aare and von Holst, 2003, Richter et al., 2001].

Diffuse axonal injury. Diffuse axonal injury (DAI) is caused by the disruption or elongation of neuronal axons in the brain tissue [Schmitt, 2007]. It is more commonly observed within the deep white matter of the brain [Wright and Ramesh, 2012]. In addition, Adams et al. [1989], Gennarelli et al. [1982b] and Smith and Meaney [2000] identified the corpus callosum and the brainstem as being highly susceptible to this type of injury. Fig. 2.36 illustrates an example of DAI.

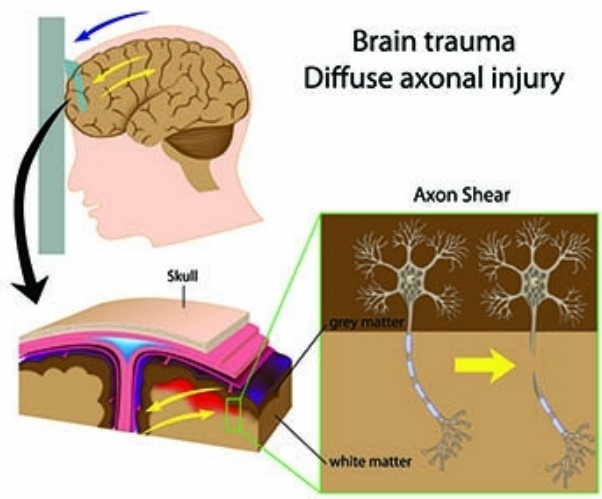

Figure 2.36: Diffuse axonal injury mechanism (adapted from Accident Attorneys [2016]).

DAI arises from the same mechanisms than SDH, i.e. tangential forces applied to the skull. However, DAI is produced by a longer duration and more gradual onset of acceleration than SDH [Aare, 2003, Gennarelli and Thibault, 1982]. According to Oehmichen et al. [2006], DAI is caused by rotational and/or translational acceleration following impact of the head, which exposes the axons to transient tensile strain. It can be produced by impulsive loading of sufficient magnitude, generated by an impact [Gennarelli and Meaney, 1996]. Nevertheless, Povlishock [1993] found that DAI is not associated with direct mechanical tearing of axons in the white matter, but with the discrete focal impairment of axoplasmic transport leading to local axonal swelling and lobulation, which were all found at locations where the axon changed its anatomical path, such as blood vessels. In addition, DAI was identified as the result of brain compression and shear deformation gradients, under high inertial forces [Viano et al., 1997].

DAI is considered the most severe DBI [Gennarelli, 1981] and one of the most frequent types of TBI [Gennarelli et al., 1982a]. Studies indicated that at the end of one month, 55% of the patients are likely to have died, 3% may have vegetative survival and 9% may have severe deficit [Gennarelli, 1981, Gennarelli et al., 1982b, Melvin et al., 1993]. More recently, Bandak [1997a] observed that this type of injury constitutes about more than 50% of all head injuries. Other authors consider DAI as the most common cause of persistent vegetative state and severe disability [Graham et al., 1995, Meythaler et al., 2001, Parizel et al., 1998]. Thus, DAI is a frequent brain injury resulting from head impacts and often results in fatality or in long-term rehabilitation [Gennarelli et al., 1982a, Gennarelli, 1983].

2.3.3 Head injury mechanisms

Head injuries can result from many mechanisms, with immediate mechanical and physiological changes and consequent functional and anatomical damage [Yang, 2011]. Head injury typically results from either a direct impact to the head or from an indirect impact applied to the head-neck system, when the torso is rapidly accelerated or decelerated. For instance, skull fractures, EDH and contusions usually result from direct contact. Contact phenomena typically cause focal brain injuries and these may occur without skull fractures.

Head injury mechanisms can be divided into static and dynamic loading. Any loading with a duration superior to 200 ms is considered a static loading [Schmitt, 2007]. Under such conditions, the head deforms until it reaches a maximum deformation. This type of loading often leads to skull fractures. According to Gurdjian [1950] and Thomas and Hodgson [1973], skull bending is the cause of linear skull fractures.

Rapid contact loading produces pressure waves that propagate across the brain, as show in Fig. 2.37, which may lead to a pressure gradient with positive pressure at the site of impact (coup) and negative pressure on the opposite side of the impact (contrecoup), as demonstrated by Nahum et al. [1977] and shown in Figs. 2.37 and 2.38. Such a mechanism is proposed for the generation of intracranial compression, which causes focal brain injuries [Schmitt, 2007]. In addition, the pressure gradient may originate shear strains within the deep structures of the brain. If the pressure is negative, gases dissolved in fluids such as CSF and blood are released as bubbles (cavitations), with consequent rupture of small vessels [Oehmichen et al., 2006]. This cavitation hypothesis was proposed by Goggio [1941] and generally accepted and confirmed [Bandak, 1997b, Gross, 1958, Gurdjian, 1975, Nahum et al., 1977, Ruan et al., 1993, Sellier and Unterharnscheidt, 1963]. Contact loading may also result in a relative motion between brain and the skull, causing contusions on the surface of the brain and tearing of the bridging veins leading to SDH [Adams, 1980, Chapon et al., 1985, Cooper, 1982, Gennarelli, 1985], as shown in Fig. 2.39.

In non-contact situations, exclusively inertial effects, such as accelerations or decelerations, load the head. Nevertheless, an impact to the head also results in head acceleration, which leads to inertial loading of the intracranial structures, causing injuries such as concussion, SDH, contrecoup contusions, DAI and ICH.

Acceleration can be divided into translational or rotational. Generally, translational acceleration results in focal brain injuries and rotational acceleration causes DBI. Pure translational acceleration creates intracranial pressure gradients, while pure rotational acceleration rotates the skull relatively to the brain, likely tearing bridging veins [Bandak, 1997a], as shown in Fig. 2.39, and can even produce brain tissue shearing through the mechanism shown in Fig. 2.40. Nevertheless, real head impacts combine both translational and rotational acceleration and thus, both types of injuries may occur in any head impact.

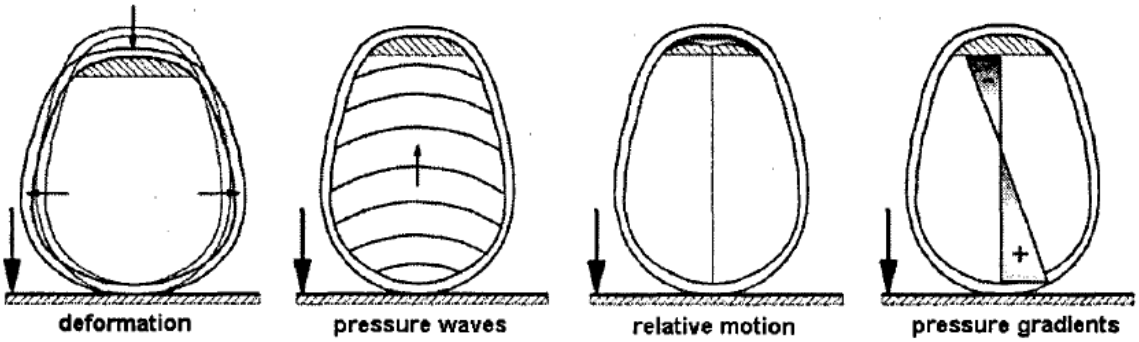

Figure 2.37: Different injury mechanisms related to head impact (adapted from Schmitt [2007]).

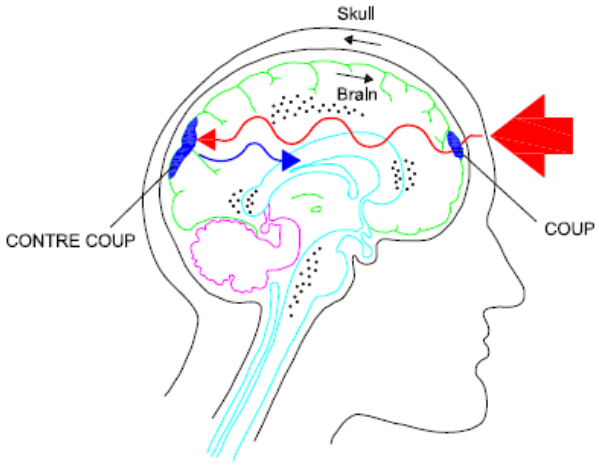

Figure 2.38: Coup-contrecoup injury (adapted from Kleiven [2002]).

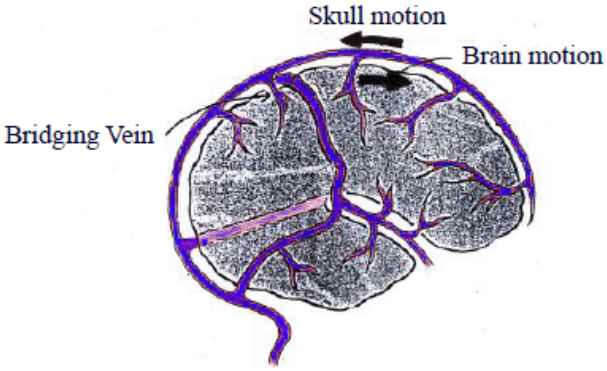

Figure 2.39: Subdural haematoma mechanism (adapted from Kleiven [2002]).

Aare [2003] stated that purely translational or rotational head acceleration is uncommon in reality, as these types of movements are not physiologically possible.

Currently, rotational acceleration is seen by many researchers as one of the principal causes of brain injury, tearing brain tissue and bridging veins. In other words, a significant amount of head injuries can be produced by rotational forces [Bandak and Eppinger, 1994, Gennarelli, 1981, Gennarelli et al., 1987, Glaister, 1997, King et al., 2003, Kleiven, 2005, Ommaya, 1988, Viano and King, 1997]. Fig. 2.41 shows the occurrence of some

severe head injuries by a qualitative relationship between angular acceleration amplitude and pulse duration. The odd curve shape for SDH is believed to be related with the strain rate sensitivity of bridging veins. In order to understand how the knowledge about head injury mechanisms evolve during the last century, a brief literature review is presented.

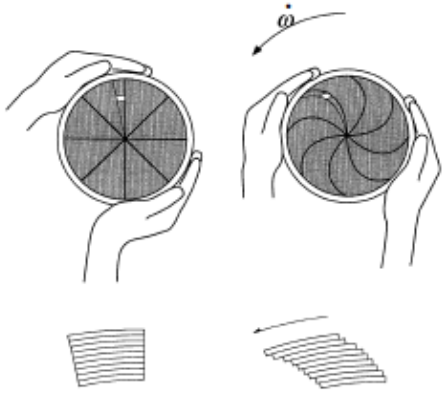

Figure 2.40: Angular acceleration produces shear strains in the contents, as illustrated by the layers sliding across each other (adapted from Anderson and McLean [2005]).

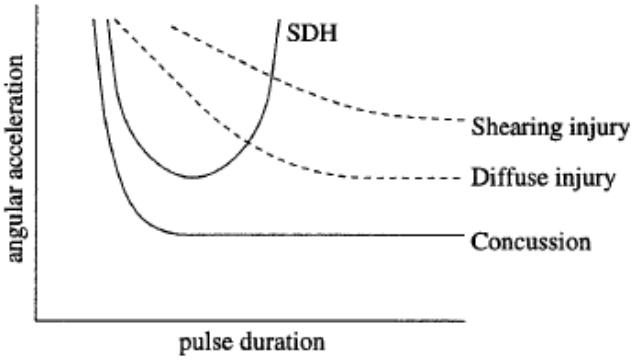

Figure 2.41: Relationship between angular acceleration and pulse duration for some head injuries (adapted from Wismans [1994]).

Thorough literature review

In order to improve the understanding of head injury mechanisms, experimental works were always fundamental [Cairns, 1941, 1946, Gurdjian and Webster, 1945, Holbourn, 1943, 1945]. These studies pointed to brain deformation or strain as the principal cause of injury. Unfortunately, strain measurement is almost impossible during an impact, particularly in vivo [King et al., 2003]. Nevertheless, later, with clinical studies, physical modelling and FEA have helped researchers to hypothesize that resulting strains are the primary cause of neurological deficiencies. A review of some of these studies is here presented.

The type of acceleration that causes severe brain injuries was always a relevant open question. Two theories were adopted. In a pioneering work, Holbourn [1943] was the first to cite angular acceleration, with or without direct impact, as an important mechanism in head injury, mainly in the origin of concussion. It was hypothesized that shear and tensile strains induced by rotational acceleration could cause concussion as well as contrecoup

contusion, tearing of cerebral blood vessels and brain tissue, causing haematoma and DAI. Later, Holbourn [1945] performed experimental tests where it was concluded that shear strains within the brain caused by rotational accelerations can place physical stress on individual neurons.

On the other hand, Gurdjian and his co-workers attributed intracranial damage to skull deformation and subsequent pressure gradients and head acceleration due to direct impacts to the head [Gurdjian and Webster, 1945, Gurdjian et al., 1955, 1961, 1963]. Linear acceleration was considered to be the most important mechanism, while rotational acceleration, negative pressure and cavitation were of minimal or no significance.

Pudenz and Shelden [1946] carried out a study on monkeys, concluding that brain motion lagged at the skull back upon impact, causing a contrecoup injury. This lag was even greater when the CSF was removed, showing the damping effect of it. Later, this was also observed by Gurdjian [1972] using a water-filled physical model, in which high pressure was observed near the impact site (coup) and large negative pressure at the contrecoup site. The same in Viano et al. [1997], that analysed a deformable brain gel model with the purpose of describing brain kinematics and strain for head translation and rotation.

Strich [1956] found diffuse degeneration of white matter in the cerebral hemispheres, as well as in the brainstem and corpus callosum areas in patients who have endured severe head trauma. This observation indicates high shear strains in the white matter adjacent to the cortex.

A few years later, Ommaya et al. [1966] supported the Houlboun's hypothesis and also indicated that rotation alone could not produce the levels of injury resulted from head impact. In addition, Ommaya et al. [1967] proposed a method to extend the results from concussive experiments on lower primate subjects, in order to predict the rotational acceleration required to produce concussions in humans. The results indicate that an acceleration of 40000 rad/s^2 will have a 99% probability of producing concussion in monkeys, which corresponds to a scaled value of 7500 rad/s^2 for humans. Later, Ommaya and Hirsch [1971] suggested that rotation could account for approximately 50% of the potential for brain injury, while the remainder was attributed to translational acceleration.

Rotational effects were also tested by Unterharnscheidt [1969], applying controlled angular accelerations on monkeys, leading to SDH, torn bridging veins and brain damage. Later, Unterharnscheidt [1971] studied the effects of translational and rotational acceleration in closed head injury. Pure translational acceleration created pressure gradients while rotational acceleration produced skull rotation relatively to the brain, with consequent generation of shear stresses.

Gennarelli et al. [1971, 1972] demonstrated that head translation at the horizontal plane produced essentially focal injuries, resulting in contusions and ICH, while diffuse injuries were only observed in the presence of a rotational component. The principal resulting mechanism from purely linear acceleration is pressure gradient, whereas for purely rotational acceleration appears to be shear stresses, once again as result from differential motion between skull and brain. Gennarelli et al. [1972] subjected monkeys to controlled sagittal plane head motions, founding that pure translation and rotation can cause concussion and other brain injuries, where the frequency and severity was greater after rotational motion. Similarly, Ommaya et al. [1973] concluded that both translational and rotational head acceleration caused brain injury, with DBI being caused mainly by rotational motion, agreeing that DBI occurs largely in response to stresses and strains generated by angular loads.

Löwenhielm [1975] stated that the deep brain could be injured oppositely to its sur-

face and that the maximum shear zone became deeper as the duration of the angular acceleration pulse increased. In most of these studies, it was assumed that brain tissue is incompressible and therefore, it is most likely to fail by shear [McElhaney et al., 1976, Stalnaker, 1969]. McElhaney et al. [1976] concluded that the bulk modulus of brain tissue is roughly 10^5 times larger than the shear modulus. Thus, brain tissue deforms mainly by shear, and distortional strain can be used as an indicator of TBI risk.

Voigt et al. [1977] concluded that acceleration and rotational forces may create shearing that results in tearing of axons, myelin sheaths and vessels inserted in the white matter. Hodgson and Thomas [1979] subjected monkey brain models to pure translation and rotation. Pure rotation produced the highest, most diffuse and long lasting shear strain as well as brain displacement, while pure translation produced very low shear strains. Dirnhofer et al. [1979] concluded that rotational acceleration is usually present in accidents such as falls, and clinical observations showed rotation as a mechanism of DAI at the brainstem as well as tearing injuries at the tentorium.

Ono et al. [1980] found that the occurrence of concussion and cerebral contusion is highly correlated with the head translational acceleration from a direct impact. The authors suggested that a rotational component is necessary for the occurrence of brain contusions, but concerning the occurrence of concussion no correlation was found. At the same time, Ward and Chan [1980] developed a 3D FE model of a primate head, subjecting it to angular acceleration pulses reported by Abel et al. [1978]. The maximum shear stresses were 50% lower than the simulations without rotational component.

The importance of impact direction in what concerns SDH was realized by Fruin et al. [1984]. Six out of eight cases with known trauma sites were due to occipital impacts. The anatomical difference between the frontal and occipital regions of the skull, explain the different results obtained in impacts to these areas.

Gennarelli et al. [1971, 1981, 1982b], Gennarelli and Thibault [1982] and Thibault and Gennarelli [1985], with the aim of investigating the influence of rotational acceleration, used live monkeys and physical models. These researchers concluded that angular acceleration contributes more than linear acceleration to generate concussive injuries, DAI and SDH. The authors hypothesized that these injuries were induced by shear strain, generated by angular acceleration.

Gennarelli et al. [1981] placed DAI as the first indicator that white matter involvement is induced by a shear-strain mechanism after non-impact accelerations. The authors also concluded that as the severity of the rotational forces increases, the more probable is the involvement of central brain areas. The same was confirmed by Blumbergs et al. [1995]. Gennarelli et al. [1982b], in experiments with monkeys, shown that the incidence and severity of DAI correlated with the acceleration direction. Rotational acceleration in the coronal plane caused the long lasting coma. In the same plane, Gennarelli [1983] concluded that SDH was mainly produced by short duration and high amplitude rotational accelerations, while DAI was mainly produced by longer and low amplitude rotational accelerations. Gennarelli et al. [1987] also investigated the influence of impact direction on DAI, concluding that lateral loading is more likely to cause DAI on primates than impacts from other directions. The same influence had been previously concluded for concussion on primates [Hodgson et al., 1983].

Low head tolerance to lateral impact in comparison with frontal impact was also observed in human cadaver tests conducted by Tarriere [1985]. He also concluded that DBI results from angular acceleration and focal brain injuries result from linear acceleration, as already concluded in other studies [Gennarelli et al., 1972, 1987, Higgins and Schmall, 1967, Hodgson et al., 1983, Ommaya and Hirsch, 1971, Ono et al., 1980, Stalnaker et al.,

1973, Unterharnscheidt, 1971]. Nevertheless, from later studies on volunteers, Pincemaille et al. [1989] suggests that the human tolerance is largely underestimated using primate experiments and simplistic scaling rules.

Adams [1986] concluded that bridging veins rupture due to high strains are considered to be the main cause of SDH, which had already been suggested [Abel et al., 1978, Gennarelli, 1985, Holbourn, 1943, Löwenhielm, 1974a]. Indeed, brain injuries can be associated to large strains, which exceeded the cerebral tissue tolerance [Thibault et al., 1990].

Margulies et al. [1990] studied the intracranial motion and deformation, by using a brain surrogate in human and primate skull models. In these, head rotational motion caused large strains in the brain tissue, being identified as a possible cause of DAI. According to Margulies and Thibault [1992], the risk of DAI is highly dependent on brain mass, since it commonly results from inertial induced loads. Later, Ivarsson et al. [2002] used the same brain surrogate to study the influence of lateral ventricles and irregular skull base on brain kinematics under sagittal plane rotation acceleration. Ivarsson et al. [2002] concluded that the irregular skull base protects nerves and vessels passing through the cranial floor by reducing brain displacement and that CSF relieves strain in regions inferior and superior to the ventricles.

Over the years, rotational acceleration continued to be reported as cause of DAI to the white matter of animal models, such as porcine and rat models [Dixon et al., 1991, Glaister, 1997, Lighthall et al., 1989, Maxwell et al., 1993, Meaney et al., 1995]. Other researchers have been able to cause DAI in animal brains by application of direct impact to the brain without an associated head angular acceleration [Meaney et al., 1995, Nishimoto and Murakami, 1998, 2000, Supprian et al., 2000]. In fact, this area is still an active area of research. However, it could be concluded that DAI is a critical injury resulting from head trauma, and relating this injury with impact forces or accelerations may provide improvements on restraint systems design.

Contrarily to the studies performed by Gennarelli and his co-workers, McLean [1995] argued that there were no cases of brain injury without head impact, based on his investigation of a series of more than 400 fatally injured road users. According to McLean [1995], it is not possible for the human neck to transmit enough energy to the head in order to produce brain injury without a direct head impact.

Zhou et al. [1995] found higher strains in the bridging veins during the acceleration than during the deceleration phase while applying the acceleration pulse from Abel et al. [1978]. Since the acceleration pulse is directed into the posterior-anterior direction, it was suggested that SDH is more easily produced in an occipital impact than a corresponding frontal one. Later, the same researchers [Zhou et al., 1996b] found that anterior-posterior motion causes higher strains in the bridging veins than a corresponding lateral motion. In addition, Lee et al. [1987] and Huang et al. [1999], using FE models to study SDH mechanisms, found that the contribution of angular acceleration to tearing of bridging veins is greater than the translational acceleration. However, in these first numerical studies, a tied interface was imposed between the skull and the brain leaving out any possibility of precisely and correctly evaluating relative brain motion.

Also in a numerical study, DiMasi et al. [1995] found a higher cumulative volume fraction of the brain experiencing a specific level of maximum principal strain for pure rotation than for pure translation, while a combination of the full kinematics gave the highest values. The authors also showed that pure translational acceleration would induce minimal strain, while a pure rotational acceleration would produce considerably greater strain. A combination of translational and rotational components would induce more strain than pure rotational acceleration. Kinematic head injury predictors are usually based on the assumption that

either linear or rotational acceleration are the main cause of head injury while it has been shown that their combination increases the injury risk [DiMasi et al., 1995].

In a similar study, although using a 2D dummy head model, Ueno and Melvin [1995] found that the use of either translation or rotation alone may underestimate the injury severity. The results also indicated that translational acceleration is related to pressure while rotational acceleration has a dominant effect on shear deformation. However, the nodes at the skull-brain boundary were also rigidly connected, as in the previous studies carried out by other researchers.

Gennarelli and Meaney [1996] indicated that a head impact can generate loadings of sufficient magnitude to produce DAI, and that its severity correlates with the magnitude, duration and rotational velocity as well as the head motion direction. It is also indicated that DAI is the result of shear and/or tensile strains caused by the relative brain tissue motion to structures such as falx and tentorium. According to Meythaler et al. [2001], the crucial factors to the extent of injury are the type of acceleration, its duration and direction.

Bain and Meaney [2000] showed that DAI is function of distortional strain. In addition, the maximum principal strain was chosen by some researchers as predictor of DAI [Bain et al., 1996, Bain and Meaney, 2000, Galbraith et al., 1993, Gennarelli et al., 1989, Morrison III et al., 2003, Thibault et al., 1990]. Other local tissue injury measures have also been proposed and evaluated, such as von Mises stresses [Anderson et al., 1999, Miller et al., 1998, Shreiber et al., 1997], product of strain and strain rate [Goldstein et al., 1997, King et al., 2003, Viano and Lövsund, 1999], strain energy [Shreiber et al., 1997] and the accumulative volume of brain tissue enduring a specific level of strain, the Cumulative Strain Damage Measure (CSDM) [Bandak and Eppinger, 1994, DiMasi et al., 1995]. These and other predictors are presented and thoroughly reviewed in the next section.

Smith and Meaney [2000] hypothesized that brain tissue shear deformations coming from inertial loading conditions result in the stretching of neural axons and, when stretched beyond a critical threshold, normal biochemical processes in the cells are disrupted, leading to functional impairment of the neurons or even to cell death [Smith et al., 1999]. Later, Zhang et al. [2001b] compared brain responses between frontal and lateral impacts, and found higher shear stress at the brain core during a lateral impact. This agrees with the earlier results obtained by Gennarelli et al. [1982b, 1987]. However, a tied interface was again imposed between the skull and the brain leaving out any possibility of evaluating relative motion between the skull and the brain.

More recently, by using a detailed finite element head model (FEHM) and reconstructing real cases of neurotrauma, Zhang et al. [2003b] concluded that the strain rate and its product with strain are the best concussion predictors. Later, Zhang et al. [2004] concluded that both linear and angular accelerations are significant causes of TBI. Similarly, Franklyn et al. [2005] proposed that the localized strain and strain rate variables were the most relevant brain injury indicators for concussion and axonal injury.

Suh et al. [2005] considered the maximum relative displacement between skull and brain as the most dangerous factor to produce severe brain injuries, because it causes the rupture of the bridging veins, owing to the excessive tension. In this study, it was also concluded that HIC increased almost linearly with the impactor mass and impact velocity. Oehmichen et al. [2006] reported that when the skull remains intact after an impact, bleeding often occurs only at the opposite impact site. This may be interpreted as contrecoup contusion due to shearing or tensile forces that may also produce SDH.

Kleiven [2002] indicated that the increased risk of SDH in elderly people may be partly explained by the reduced brain size, resulting in a larger relative motion between the skull and the brain, with distension of bridging veins. He also concluded that larger relative mo-

tion between skull and brain is more pronounced for an occipital impact than for a frontal one. Later, for rotational impulses of short duration, Kleiven and von Holst [2003] found that the change in angular velocity best corresponds with the intracranial strains, which is in agreement with hypothesis suggested by Holbourn [1943]. Kleiven [2003] also observed that horizontal impulses produced almost exclusively DAI in the central parts of the brain, which endured higher stresses and strains than a translational impulse with the same impact power. This is one more study that supports the findings of Gennarelli et al. [1987]. Additionally, Kleiven [2003] stated that the use of either translation or rotation may underestimate the severity of an injury, as previously concluded by DiMasi et al. [1995] and Ueno and Melvin [1995].

Kleiven and von Holst [2002] and Kleiven [2003] found the largest strains for the centrally or frontally located bridging veins for all impact directions, supporting the experimental studies made by Hirakawa et al. [1972] and Jamieson and Yelland [1972], where SDH was found in the occipital region. It was also found that the influence of impact direction had a substantial effect in the prediction of SDH [Kleiven, 2003]. Later, Aare et al. [2004] compared the results from different simulated oblique impacts and concluded that the rotational effects have a major influence on the strain levels in the human brain, whereas the maximum strain was usually found at the white matter.

Kleiven [2005], in other numerical study, observed that low levels of strain can be seen in the vicinity of the ventricles, which supports the hypothesis of Ivarsson et al. [2000]. Kleiven [2005] also compared the influences of translational and angular impulses coming from lateral impulses, founding a tenfold increase in the intracranial strains when changing from translational to rotational motion. In the latter, the highest strain appeared at the cortex, corpus callosum and brainstem. The larger stresses and strains at the corpus callosum for lateral impulses, support the conclusions drawn by Gennarelli et al. [1982b, 1987]. In Kleiven [2005], it is also evident the high levels of strain nearby the skull vertex as well as close to the skull base irregularities, mainly due to the relative motion caused by rotation. Later, Kleiven [2007c] also demonstrated that both translational and rotational accelerations contribute to brain injury.

Fijalkowski et al. [2006b] indicated that injury severity is directly dependent of factors such as magnitude and duration of angular acceleration, brain mass, and rotation plane. One year later, Fijalkowski et al. [2007] demonstrated that angular acceleration duration is an influencing factor of DBI severity. In addition, other studies showed a correlation between angular acceleration magnitude and injury severity [Abel et al., 1978, Higgins and Schmall, 1967, Hodgson et al., 1983]. DBI determinants associated with injury severity include brain mass [Douglass et al., 1968, Ommaya et al., 1967], plane of rotation [Gennarelli et al., 1987, Ono et al., 1980, Shatsky et al., 1974], angular acceleration magnitude [Abel et al., 1978, Higgins and Schmall, 1967, Margulies and Thibault, 1992, Ommaya and Gennarelli, 1974, Ono et al., 1980, Unterharnscheidt, 1969] and angular velocity [Hirsch et al., 1968, Kleiven, 2007c, Meaney et al., 1993, Smith et al., 2000]. Studies demonstrate that coronal plane rotations are most injurious due to decreased inertial properties and geometric constraints [Gennarelli et al., 1987, Hodgson et al., 1983, Margulies and Thibault, 1992, Margulies et al., 1990, Thibault et al., 1990]. Furthermore, the duration of angular acceleration determines the type of injury, where short duration impacts result in focal injuries while longer impacts result in DBI [Margulies and Thibault, 1992, Ono et al., 1980, Shatsky et al., 1974, Stalnaker et al., 1973].

Mordaka et al. [2007] found that injury severity can be related - not to angular acceleration - but to peak change in angular velocity. The results showed that increased peak changes in angular velocity caused higher maximum principal strains in the brain and con-

sequently higher probability of DAI and ASDH. In addition, a three-fold increase at the brain strain levels was found when doubling the impact velocity. This variation is similar for the peak change in angular velocity, which corresponds to Holbourn's hypothesis [Holbourn, 1943], where strains are proportional to the change in angular velocity for rotational impulses of short durations.

In other numerical study, Zhang et al. [2008] indicated that different brain regions were susceptible to different strain responses, depending on direction of rotation. It was observed that coronal rotation induced multi-focal high strains at the midbrain and thalamus, indicating a plausible effect of the falx on the strain propagation. In the case of head rotation at the sagittal plane, the critical strain was mainly located in the hippocampus and upper brainstem region. According to Zhang et al. [2008], this strain localisation was likely dictated by the presence of the tentorium opening and its transverse orientation affecting the tissue deformation.

Yoganandan et al. [2008] studied the influence of angular-deceleration pulse shapes on specific brain strains. Principal strains were determined at the corpus callosum, the post-central sulcus base and the cerebral cortex of the parietal lobe, being the corpus callosum the one with highest strains. In this study, it was also suggested that angular velocity may be a better metric than peak acceleration. More recently, Post et al. [2012a] performed a study in order to analyse the predictors that most influence the loading curve shape in the brain and indicated that higher maximum principal strains and von Mises stresses are the predictors that most influence the curve shape.

More recently, Cloots et al. [2010] showed that the axonal strains cannot be trivially correlated to the tissue strain without taking into account axonal orientations, which indicates that heterogeneities at the cellular level play an important role on brain injury mechanisms and injury prediction. Later on, Wright and Ramesh [2012] showed that injury response of white matter is dependent on the primary orientation and on the angular distribution of axonal fibres.

Asiminei et al. [2011] observed that the high sensitivity of head acceleration/deceleration rate was the major determinant of bridging vein failure. No strain rate sensitivity could be observed up to 20 s^{-1}. In the same year, Krave et al. [2011] produced DAI by inducing rotational acceleration at the sagittal plane of some animals' head. Many of these studies have presented thresholds to assess injury occurrence. These predictors and other criteria are described in the next section.

2.3.4 Head injury predictors

Head injury typically results from either a direct impact to the head or from an indirect impact applied to the head-neck system, when the torso is rapidly accelerated or decelerated. For both cases, the head sustains a combination of linear and rotational acceleration [Aare, 2003]. As seen in the previous section 2.3.3, translational acceleration creates intracranial pressure gradients, while rotational acceleration rotates the skull relatively to the brain [Bandak, 1997a].

For over half a century, research has been undertaken to assess plausible injury mechanisms causing inertial head injury during impact and to establish associated human head tolerance levels. The development of injury criteria has been a major goal among researchers in order to accurately evaluate the risk of sustaining a head injury and to assess the effectiveness of potential protective head gear such as helmets.

In fact, this is still an active area of research and scientists are trying to relate this type of damage with impact forces or accelerations, mainly with kinematics. This may provide

a strong basis for improvements in restraint systems design. Currently, many studies have presented thresholds to assess injury occurrence. These predictors are described in this section. Head injury criteria can be roughly divided into three categories, as proposed by van den Bosch [2006]:

- Injury criteria based on translational or rotational accelerations of the head's COG,
- Injury criteria based on translational and rotational accelerations of the head's COG,
- Injury criteria based on stresses and strains in the brain tissue.

Each category is discussed in the following subsections. A thorough review on head injury predictors and their respective thresholds is presented in Fernandes and Alves de Sousa [2015]. This state-of-the-art review article is related with the development of this thesis.

All these referred classes of injury criteria were mainly developed to consider closed head injury. Localised loads, which could be considered suitable criteria for skull fracture, depend on the impactor shape and skull thickness at the impact site. Table 2.4 presents a summary of fracture peak forces at different regions of the skull.

Table 2.4: Peak force for fracture at different regions of the skull.

Impact area	Force [kN]	Reference
Frontal	4.0	Schneider and Nahum [1972]
	4.2	Nahum et al. [1968]
	4.3-4.5	Yoganandan et al. [1994]
	4.7	Allsop et al. [1988]
	5.5	Hodgson and Thomas [1971]
	6.2	Advani et al. [1975]
	15.6	Voo et al. [1994]
Temporal	2.0	Schneider and Nahum [1972]
	3.4-4.4	Yoganandan et al. [1994]
	3.6	Nahum et al. [1968]
	5.2	Allsop et al. [1991]
	6.2	Voo et al. [1994]
Occipital	11.7-11.9	Yoganandan et al. [1994]
	12.5	Advani et al. [1982]
Parietal	3.5	Hume et al. [1995]
Vertex	3.5	Yoganandan et al. [1994]

Hume et al. [1995] stated that a depressed skull fracture is likely to appear at the temporal area if the impacted area is less than 5 cm^2 and the pressure exceeds 4 MPa. McElhaney et al. [1970], Melvin et al. [1970] and Robbins and Wood [1969] have reported cranial bone stress thresholds. According to the mentioned references, a compact cranial bone breaks in tension at 48-128 MPa, while the cancellous bone breaks in compression at 32-74 MPa. Raul et al. [2006] proposed a global strain energy of 2.2 J as a 50% risk indicator for skull fracture. Recently, Monea et al. [2014] suggested an energy failure level of 22-24 J for the frontal site and 5-15 J for the temporal region.

Translational acceleration based injury criteria

In what concerns translational acceleration, several head injury criteria have been proposed.

Peak linear acceleration. The peak linear acceleration (PLA) is the maximum linear acceleration value. This method ignores the impact duration. Nevertheless, some studies present limits associated with the duration of an acceleration level. These and other thresholds are presented in table 2.5.

Table 2.5: PLA thresholds.

Injury	Tolerance	Reference
Head injury	a = 80 g for 3 ms	Got et al. [1978], Stalnaker et al. [1971]
	50% probability:	Peng et al. [2012]
	AIS 2+: 116 g	
	AIS 3+: 162 g	
	AIS 4: 200-250 g	Newman [1986]
	AIS 5: 250-300 g	
	AIS 6: $>$ 300 g	
Skull fracture	5% risk: a = 180 g	Mertz et al. [1997]
	40% risk: a = 250 g	
	50% risk: a = 135 g	Peng et al. [2012]
MTBI	25% probability: a = 559 m/s^2	King et al. [2003]
	50% probability: a = 778 m/s^2	
	75% probability: a = 965 m/s^2	
	50% probability: a = 762 m/s^2	Newman et al. [2000b]
	95% probability: a = 1131 m/s^2	
	85 g for an impact duration between 10$\leq$t$\leq$30 ms	Zhang et al. [2004]
Concussion	a = 81 g	Duma et al. [2005]
	60.51-168.71 g	Guskiewicz et al. [2007]
	105 $\pm$ 27 g	Rowson and Duma [2011]
	74 $\pm$ 21 g	McAllister et al. [2012]
	50% of probability: a = 65.1 g	McIntosh et al. [2014]
	75% of probability: a = 88.5 g	

The Abbreviated Injury Scale (AIS) was proposed in a effort to classify injuries according to its severity [Committee on medical aspects of automotive safety, 1971]. An AIS of 1 means a minor injury, while an AIS of 6 is attributed to lethal injuries. According to an updated AIS scale [Gennarelli and Wodzin, 2006], table 2.6 shows the meaning of each AIS code in terms of injury severity and type.

Head Injury Criterion. The most commonly acknowledged and widely applied head injury predictor is the head injury criterion (HIC), which is based on the assumption that head linear acceleration alone is a valid indicator. The HIC results from the evolution of the Wayne State Tolerance Curve (WSTC), developed in the pioneering work of Gurdjian and his co-workers [Gurdjian et al., 1953, 1955]. Further works were also developed [Gurdjian et al., 1963], until the final form of the WSTC was published in Gurdjian et al. [1966a], as shown in Fig. 2.42. This curve was presented as failure criterion for prediction of skull fracture and concussion. This relation between cerebral concussion and skull fracture was also observed by Melvin and Lighthall [2002], where 80% of all observed concussion cases also

Table 2.6: AIS head injury classification.

Code	Injury Severity	Injury description
0	No Injury	
1	Minor Injury	Scalp abrasion or superficial laceration, nose fracture
2	Moderate Injury	Vault and mandible fractures
3	Serious Injury	Basilar fracture, total scalp loss, single contusion cerebellum
4	Severe Injury	Brain damage: small EDH and SDH
5	Critical Injury	Penetrating injuries, brainstem compression, EDH, SDH, DAI
6	Fatal Injury	Massive destruction of both cranium and brain

had linear skull fractures. The final form of the WSTC was developed by combining results from a wide variety of pulse shapes, obtained from cadavers, animals, human volunteers and clinical research, among others.

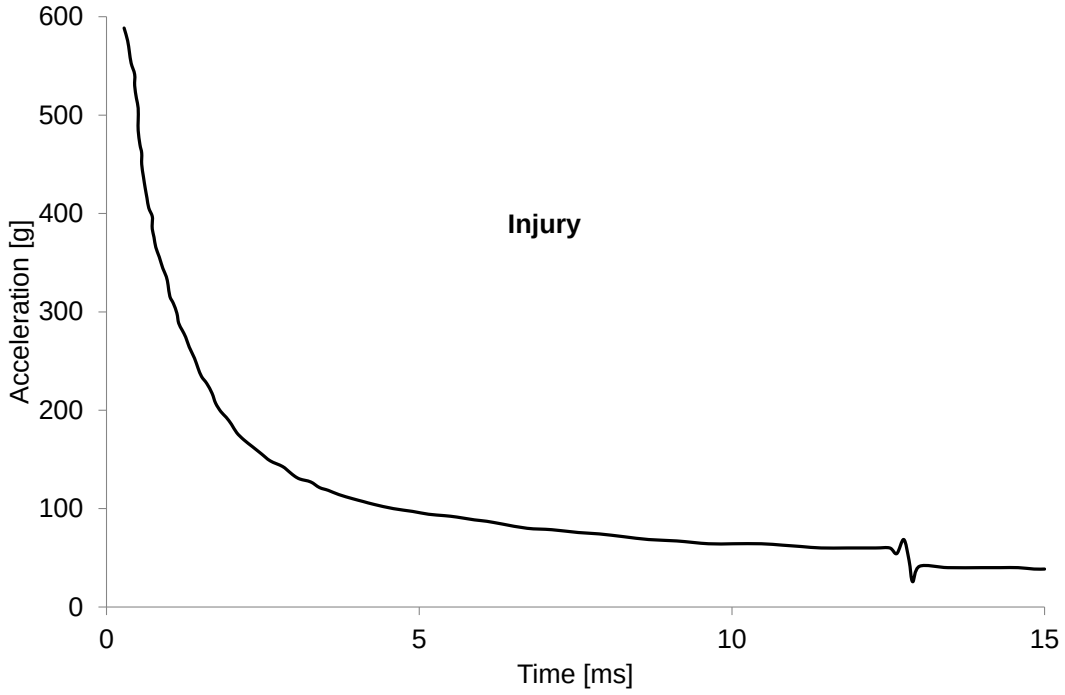

Figure 2.42: The Wayne State Tolerance Curve.

From observing the WSTC, it is possible to conclude that the head can withstand higher accelerations for shorter durations. Any exposure above the curve is considered an injury, while below it does not exceed human tolerance. The WSTC is also supported by experiments conducted by Ono et al. [1980] on primates and scaled to humans, which led to the Japan Head Tolerance Curve (JHTC), very similar to the WSTC. Nevertheless, the WSTC is based only on direct frontal impacts, and it is not applied to non-contact loading conditions nor to other impact directions.

By plotting the WSTC in a logarithmic scale, it becomes a straight line with a slope of -2.5, which was used by Gadd [1966] to propose a severity index called Gadd severity index (GSI). Gadd [1966] introduced the concept of a severity index to provide a rational and consistent basis for comparing the severity of various head impacts. It is based on the WSTC and on long pulse duration tolerance data from Eiband [1959]. The GSI is given by

the empirical expression 2.2, which was already presented together with some suggested thresholds in section 2.2.4.

Over the years, this criterion has been reviewed and several modified forms were proposed. One of those reviews was made by Versace [1971], who analysed the relationship between the WSTC and GSI and proposed a correction:

$$VSI = \left[\frac{1}{T}\int a(t)dt\right]^{2.5} \tag{2.3}$$

Later, the HIC was proposed by the NHTSA [1972], as a new criterion to identify the most damaging part of the acceleration pulse by finding the function's maximum value. The HIC is given by the expression 2.1, which was already presented in section 2.2.3.

Thus, the HIC approach claims that two parameters, acceleration and its duration over the time of impact are suitable for the definition of injury onset. However, other researchers have criticized the HIC use as a suitable predictor for head injury, due to being solely based on translational acceleration, with no consideration for rotational acceleration [Bellora et al., 2001, Feist et al., 2009, Gennarelli et al., 1982b, Kleiven, 2003, 2005, Newman, 1980, Ono et al., 1980, Viano, 1988]. Some authors also tried to predict head injuries with HIC and the results were not satisfactory [Deck et al., 2003a, Viano, 1988]. In Fig. 2.43, it is possible to observe the occurrence of head injuries almost independently of the HIC value. In table 2.7, some predicted HIC thresholds for head injuries are presented.

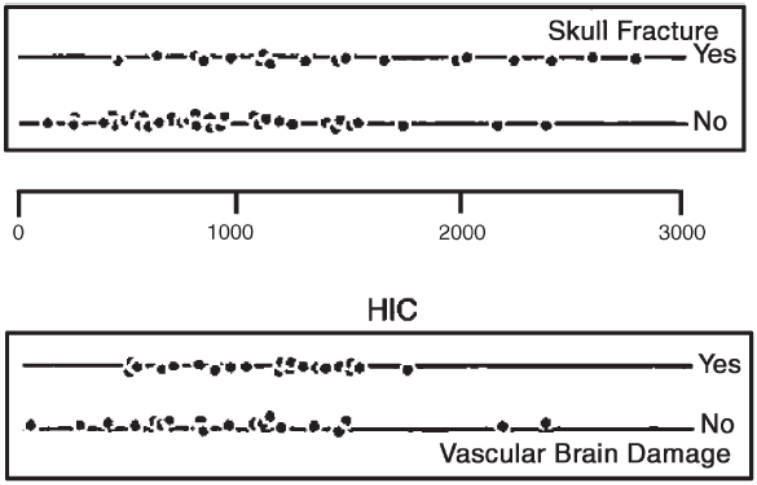

Figure 2.43: Relationship between HIC and the occurrence of skull fracture and brain damage (adapted from Bullock and Graham [1997]).

Nevertheless, HIC could be an useful predictor for qualitatively comparing energy absorbing safety devices, representing the global severity level of an impact and the potential head injury level [Deck et al., 2003a, Hopes and Chinn, 1989]. However, optimisation techniques based on biomechanical criteria are different from the ones linked with the HIC [Deck et al., 2003b, Deck and Willinger, 2006, Forero Rueda et al., 2011]. Other criticisms about HIC effectiveness can be found in Fenner Jr et al. [2005],Newman [1980] and Kleiven and von Holst [2002]. Overall, HIC is considered to be not enough to predict head injuries because it does not take into account the injury type, the head size, the rotational motion and the impact direction and also has nonsensical units [Newman, 1975]. As a consequence, the HIC validity has been intensively debated pointing to the necessity of taking into account these parameters. Nevertheless, HIC is the most disseminated injury

criterion, being used by some helmet safety standards.

Table 2.7: HIC thresholds.

Injury	Tolerance	Reference
Head injury	Severe but not life-threatening: 1000	Shuaeib et al. [2002a]
	8.5% probability of death: 1000	Hopes and Chinn [1989]
	31% probability of death: 2000	
	65% probability of death: 4000	
	16% probability of life threatening injuries: 1000	Horgan [2005]
	99% probability of life threatening injuries: 3000	
	50% probability of AIS 2+: 825	Peng et al. [2012]
	50% probability of AIS 3+: 1442	
MTBI	25% probability (for HIC_{15}): 136	King et al. [2003]
	50% probability (for HIC_{15}): 235	
	75% probability (for HIC_{15}): 333	
	50% probability (for HIC_{15}): 240	Newman et al. [2000b]
	95% probability (for HIC_{15}): 485	
	240	Zhang et al. [2004]
	50% risk: 533	Marjoux et al. [2008]
Severe TBI	50% risk: 1032	Marjoux et al. [2008]
Skull fracture	50% risk: 667	Marjoux et al. [2008]
SDH	50% risk: 1429	Marjoux et al. [2008]
Concussion	200	Duma et al. [2005]

Rotational acceleration and combined rotational and translational acceleration based injury criteria

The brain is composed of a natural viscoelastic material. Its mechanical response is dependent on the acceleration magnitude, rate and change of rotational velocity. However, purely translational or rotational loading to the human head is uncommon in reality, as these types of movements are not physiologically possible, mainly due to the head-to-neck kinematics. Rotation is reported as the most injurious loading mechanism to the brain, but in the vast majority of head impacts, it can be expected that both translational and rotational accelerations combined, cause brain injury [Pellman et al., 2006, Post et al., 2012b, Vezin and Verriest, 2004].

Injury criteria taking into account rotational kinematics or both rotational and translational kinematics have been proposed by some researchers. Global kinematic measures include magnitude in rotational and translational acceleration, change in rotational and translational velocity, and the predictors head injury power (HIP) and the generalized acceleration model for brain injury threshold (GAMBIT). These and other predictors as well as their thresholds are reviewed in this section.

Rotational acceleration thresholds. The relevance of rotational accelerations in brain injuries have been emphasized by many researchers, leading them to investigate thresholds to determine brain injury. This has already been discussed in section 2.3.3.

Löwenhielm [1978] showed that angular acceleration must be applied long enough to attain a critical angular velocity and excessive displacement between brain and skull.

Löwenhielm [1978] proposed an agular acceleration (α) of 5000 rad/s^2 together with an angular velocity (ω) of 50 rad/s to disrupt bridging veins. In previous studies, Löwenhielm [1974b, 1975] predicted similar values (α = 4500 rad/s^2 or ω = 50-70 rad/s). Fig. 2.44 shows tolerance curves for bridging vein disruption and gliding contusion determined by Löwenhielm [1978]. Gliding contusions are caused by displacement of the grey matter due to angular acceleration [Adams, 1992], occurring at the junction between the grey matter and the white matter. These are sometimes associated with DAI and ASDH [Oehmichen et al., 2006]. More recently, Monea et al. [2014] proposed an angular acceleration of 10 krad/s^2 for a duration of at least 10 ms to cause disruption of bridging veins.

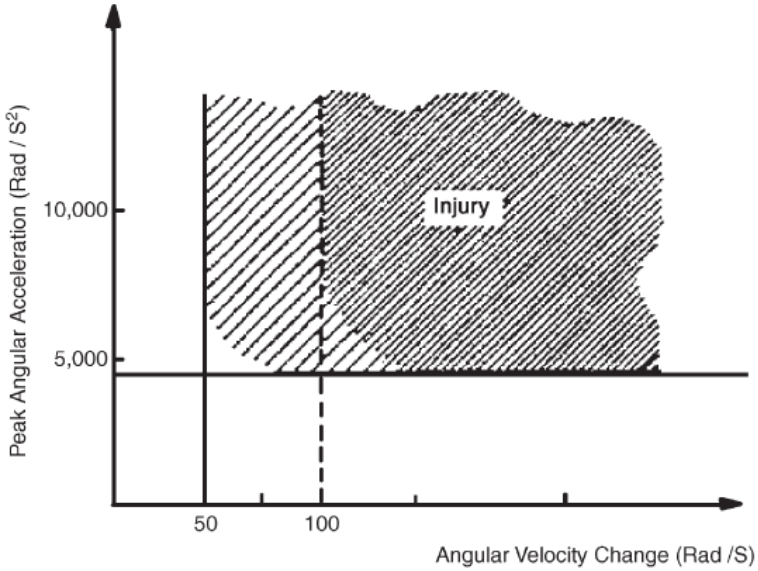

Figure 2.44: Tolerance levels for bridging vein disruption (solid lines) and for gliding contusions (dashed line) (adapted from Glaister [1997]).

COST327 [2001] suggested a limit for rotational acceleration of 5000 rad/s^2, together with a limit for rotational velocity of 40 rad/s. These values are close to the ones presented in Fig. 2.44 for bridging vein disruption. Ommaya [1984a] suggested a combination of rotational acceleration lower than 1700 rad/s^2 and a velocity higher than 30 rad/s to cause concussion.

More recently, Gennarelli et al. [2003] hypothesized the magnitude of angular acceleration required to induce concussion and DAI, proposing the injury levels given in table 2.8. The values in table 2.8 were obtained through this relationship for rotational acceleration [rad/s^2] = 2877.8 $\times$ AIS and through this for rotational velocity [rad/s] = 25 $\times$ AIS. Recently, Peng et al. [2012] predicted a 50% probability of AIS 2+ and AIS 3+ head injuries, for angular velocities and accelerations of 40 rad/s and 11368 rad/s^2, and 55 rad/s and 18775 rad/s^2, respectively.

A summary of more brain thresholds for rotational acceleration and velocity is presented in table 2.9. The great majority of these studies were performed by inducing rotational motion in the sagittal plane.

Zhang et al. [2004], using an advanced FEHM, suggested a tolerance for reversible brain injury levels as less than 85 g for translational acceleration and less than 60 krad/s^2 for a head exposed to combined translational and rotational acceleration (impact duration between 10 and 30 ms).

Earlier, Margulies and Thibault [1992] presented a criterion for DAI, developed using

Table 2.8: Thresholds based on angular acceleration and angular velocity for DBI prediction [Gennarelli et al., 2003].

AIS level	Injury Severity	Angular Acceleration [rad/s^2]	Angular Velocity [rad/s]
1	Mild Cerebral Concussion	2877.8	25
2	Classical Cerebral Concussion	5755.6	50
3	Sever Cerebral Concussion	8633.4	75
4	Mild DAI	11511.2	100
5	Moderate DAI	14389	125
6	Severe DAI	17266.8	150

experiments on primates in combination with gel physical models and analytical scaling procedures. This criterion is represented by curves delimiting equal strain levels in the analytical model, as a function of the angular acceleration and peak change of the angular velocity. Judging from Fig. 2.45, rotational accelerations exceeding 10 krad/s^2 combined with a rotational velocity of 100 rad/s or higher, give a risk of DAI for an adult (brain mass of 1.4 kg).

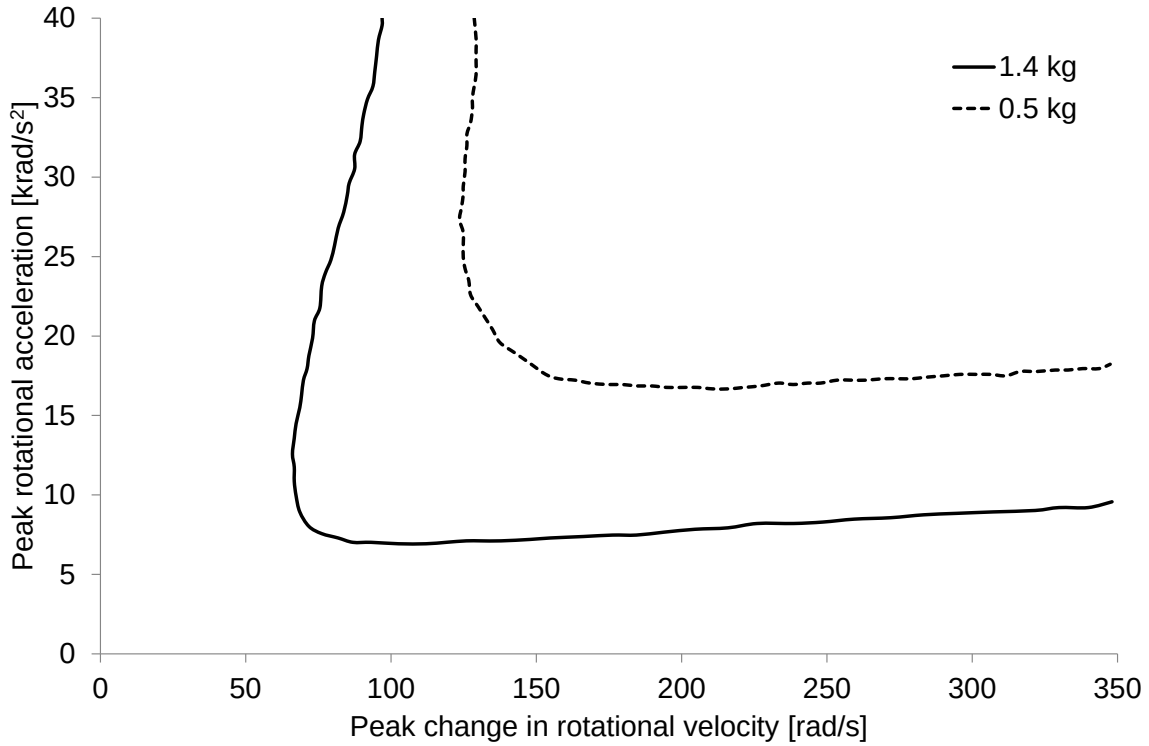

Figure 2.45: Angular criterion for DAI prediction based on the relation between peak rotational acceleration and the peak change in rotational velocity.

Gennarelli and Thibault [1982] performed tests on primates and scaled the results to humans. These are presented in Fig. 2.46. Interestingly, the SDH threshold seemed to increase with the impulse duration, oppositely to other head injuries such as skull fracture and concussion, as shown in Fig. 2.42. This phenomenon was also observed in experiments with human cadavers, as reported by Löwenhielm [1974b] and experiments on monkeys as reported by Unterharnscheidt [1969].

Table 2.9: Human brain tolerance to rotational acceleration and velocity.

Injury	Threshold	Reference
Contusion	α = 2000 - 3000 rad/s^2	Advani et al. [1982]
Concussion	50% probability:	Ommaya et al. [1967]
	α = 1800 rad/s^2 for t<20 ms	
	ω = 30 rad/s for t $\geq$ 20 ms	
	99% probability: α >7500 rad/s^2 for t>6.5 ms	Ommaya and Hirsch [1971]
	α = 14000 rad/s^2 for 11 ms	Unterharnscheidt [1969]
	α = 13000 rad/s^2 for 11 ms	Ono et al. [1980]
	α = 20 krad/s^2 for 18 ms	Gennarelli and Thibault [1982]
	α = 13600 - 16000 rad/s^2 and ω = 25 - 48 rad/s	Pincemaille et al. [1989]
	α = 18 krad/s^2 for 18 ms	Thibault et al. [1990]
	50% of probability: α = 6200 rad/s^2	Newman et al. [2000a]
	50% of probability: α = 6322 rad/s^2	Newman et al. [2000b]
	95% of probability: α = 9267 rad/s^2	Newman et al. [2000b]
	α = 6400 rad/s^2 and ω = 35 rad/s	Viano et al. [2005]
	α = 6200 rad/s^2	Fijalkowski et al. [2006a]
	α = 7600 rad/s^2 for 15 ms	Fijalkowski et al. [2007]
	α = 7300 rad/s^2 for 23 ms	
	α = 1800 rad/s^2	Kleiven [2007b]
	α = 6432 rad/s^2	Pellman et al. [2003]
	α = 5022 rad/s^2	Rowson et al. [2012]
	α = 5582.3 rad/s^2	Broglio et al. [2010]
	50% of probability: α = 1747 rad/s^2	McIntosh et al. [2014]
	75% of probability: α = 2296 rad/s^2	(coronal plane)
	α = 7912 rad/s^2	Duma et al. [2005]
	α = 5312 rad/s^2	Guskiewicz et al. [2007]
	α = 5025 rad/s^2	McAllister et al. [2012]
	50% of probability: α = 1747 rad/s^2	Patton et al. [2013]
DAI	α = 20 krad/s^2 for 18 ms	Gennarelli and Thibault [1982]
	α = 19 krad/s^2 for 20 ms	Gennarelli et al. [1987]
	α = 10000 rad/s^2 and ω = 100 rad/s	Margulies and Thibault [1992]
	α = 18000 rad/s^2	Ommaya et al. [2002]
	α = 8000 rad/s^2 or ω= 70 rad/s	Kleiven [2007b]
	α = 10000 rad/s^2 for t>4 ms or ω = 19 rad/s	Davidsson et al. [2009]
Mild DAI	α = 12500-15500 rad/s^2	Ommaya et al. [2002]
SDH	α = 32 krad/s^2 for 14 ms	Gennarelli and Thibault [1982]
	α = 10000 rad/s^2	Yoganandan et al. [2005]
	α = 10000 rad/s^2 for t>10 ms	Depreitere et al. [2006]
TBI	α = 1700 rad/s^2 and ω = 60 - 70 rad/s	Ewing et al. [1975]
	ω <30 rad/s and α < 4500 rad/s^2: safe	Ommaya [1984b]
	ω >30 rad/s and α = 1700 rad/s^2: AIS 2	
	ω >30 rad/s and α > 3000 rad/s^2: AIS 3	
	ω >30 rad/s and α > 3900 rad/s^2: AIS 4	
	ω >30 rad/s and α > 4500 rad/s^2: AIS 5	
	ω <30 rad/s and α > 4500 rad/s^2: AIS 5	
	α = 25000 rad/s^2 for short durations	Tarriere [1987]
	α >5000 rad/s^2	Thomson et al. [2001]
	4500< α <5000 rad/s^2 and ω = 60 rad/s	Shuaeib et al. [2002a]
MTBI	25% of probability: α = 4384 rad/s^2	King et al. [2003]
	50% of probability: α = 5757 rad/s^2	
	75% of probability: α = 7130 rad/s^2	
	α = 6000 rad/s^2 for 10<t<30 ms	Zhang et al. [2004]
	25% of probability: α = 4600 rad/s^2	
	50% of probability: α = 5900 rad/s^2	
	80% of probability: α = 7900 rad/s^2	

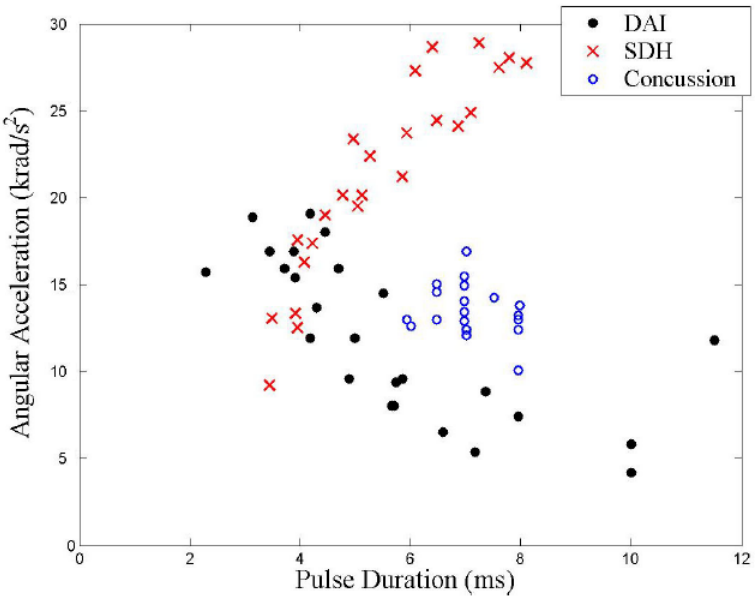

Figure 2.46: Angular threshold for injury prediction (adapted from Gennarelli and Thibault [1982]).

Generalized Acceleration Model for Brain Injury Threshold. Newman [1986] attempted to combine both translational and rotational responses into one injury criterion, considering that both cause the stresses generated in the brain. Assuming that translational and rotational acceleration equally and independently contribute to head injury, the GAMBIT expression is:

$$G(t) = \left[\left(\frac{a(t)}{a_c} \right)^n + \left(\frac{\alpha(t)}{\alpha_c} \right)^m \right]^{1/s} \tag{2.4}$$

where $a(t)$ and $\alpha(t)$ are the instantaneous values of translational and rotational acceleration expressed respectively in [g] and [rad/s^2]; n, m and s are empirical constants and a_c and α_c represent critical tolerance levels for those accelerations.

Some versions of $G(t)$ have been presented [Newman, 1986, Newman et al., 2000a, COST327, 2001, Mellor and StClair, 2005] as well as some values for the empirical constants (table 2.10). However, GAMBIT was never extensively validated as an injury criterion. Nevertheless, according to Kramer [1998], GAMBIT of value 1 represents a probability of 50% for an irreversible head injury. Some other thresholds were proposed and are presented in table 2.11.

Table 2.10: Empirical constants and critical tolerance values.

Reference	n	m	s	a_c [g]	α_c [rad/s^2]
Newman [1986]	2	2	2	250	25000
COST327 [2001], Mellor and StClair [2005]	2	2	2	250	10000

Although GAMBIT has some limitations, such as the lack of impulse duration dependency and directional sensitivity [Kleiven, 2002], this was a step in the right direction, combining both translational and rotational accelerations in the same criterion.

Table 2.11: GAMBIT thresholds.

Injury	Threshold	Reference
Concussion	50% probability: $G \geq 0.4$	Newman et al. [2000b]
	95% probability: $G \geq 0.56$	
Head injury	50% probability of AIS>3: G=1	
	1.5$\leq G \leq$2	COST327 [2001]

Head Injury Power. Newman et al. [2000b] reasoned that the translational and rotational kinetic energy rate could be a viable biomechanical function for head injury assessment. Newman et al. [2000b] proposed coefficients for the different directions that could be chosen to normalize the HIP with respect to some selected failure levels for a specific direction. Thus, Newman et al. [2000b] proposed a scaling of the impact power for different directions. However, coefficients values were not presented and information regarding directional sensitivity was lacking. HIP is expressed by an empirical expression:

$$\begin{aligned} HIP = Aa_x \int a_x\,dt + Ba_y \int a_y\,dt + Ca_z \int a_z\,dt + \\ + D\alpha_x \int \alpha_x\,dt + E\alpha_y \int \alpha_y\,dt + F\alpha_z \int \alpha_z\,dt \end{aligned} \tag{2.5}$$

Each term in this expression represents the change in kinetic energy for one degree of freedom, where the first half represents the linear contribution and the second one the angular contribution. The coefficients A, B and C represent the mass of the human head and D, E and F represent the appropriate moments of inertia for the human head I_{xx}, I_{yy} and I_{zz} respectively, which denote the injury sensitivity for each of the six head degrees of freedom.

Newman et al. [2000b] validated this criterion only for MTBI. The HIP$_{max}$ is not validated for severe head injuries. Nevertheless, some proposed injury thresholds are presented in table 2.12. The ones proposed by Newman et al. [2000b] are based on a 50^{th} percentile adult male head. In addition, Newman et al. [2000b] concluded that HIP better correlates with MTBI than HIC, probably due to incorporating directional sensitivity and both rotational and translational components. This was also concluded by Marjoux et al. [2008], although they also indicated that the difference between HIC and HIP, for severe cases, is negligible.

Table 2.12: HIP thresholds.

Injury	Threshold	Reference
Skull fracture	50% probability: HIP$_{max}$ = 38 kW	Marjoux et al. [2008]
SDH	50% probability: HIP$_{max}$ = 55 kW	
MTBI	50% probability: HIP$_{max}$ = 24 kW	
Severe TBI	50% probability: HIP$_{max}$ = 48 kW	
Concussion	50% probability: HIP$_{max}$ = 12.8 kW	Newman et al. [2000b]
	95% probability: HIP$_{max}$ = 20.88 kW	

Kleiven [2005], using a detailed FEHM, found that the change in angular velocity mirrored the strain level in the brain better than the HIP and the peak angular acceleration. An almost constant level of strain was found for a constant change in angular velocity, while for both the HIP and the peak angular acceleration an increasing strain level was obtained, for an increase in the impulse duration.

Rotational Injury Criterion. Kimpara and Iwamoto [2012] proposed the rotational injury criterion (RIC), which was derived by substituting the resultant linear acceleration of equation 2.1 for the resultant angular acceleration. Based on concussive NFL head impact data, Kimpara and Iwamoto [2012] proposed a RIC value of 1.03 $\times$ 10^7 to represent a 50% of MTBI probability.

Power Rotational Head Injury Criterion. Kimpara and Iwamoto [2012] also proposed the Power Rotational Head Injury Criterion (PRHIC), which is calculated as the integrated power of rotational head motion. The goal was to propose a new predictor for head injuries associated with angular head accelerations from datasets of six degrees of freedom at the head' COG [Kimpara et al., 2011]. The expression of this criterion is the same as equation 2.1, where the resultant linear acceleration is substituted by the HIP (only rotational components). The maximum integral time duration for PRHIC and also RIC was set to 36 ms, which was the original time duration set for the HIC. Kimpara and Iwamoto [2012] proposed a PRHIC value of 8.70 $\times$ 10^5 to represent 50% MTBI probability.

Strain correlated with both accelerations. Aare et al. [2004] have tried to develop a criterion correlating translational and rotational accelerations with strains in brain tissue. Previously, Kleiven and von Holst [2003] found that the change in angular velocity best corresponds to the intracranial strains. On the other hand, for translational impulses, HIC and HIP have shown the best correlations with the strain levels Kleiven and von Holst [2003]. Thus, Aare et al. [2004] suggested that following expression:

$$\varepsilon = k_1 \Delta\omega + k_2 HIC \tag{2.6}$$

where ε is the maximum strain component in the brain tissue, $\Delta\omega$ is the maximum change in rotational velocity, k_1 and k_2 are constants. These constants were obtained by regression analysis for each impact and are available in Aare et al. [2004]. More recently, Kleiven [2007c] found that a simple combination of rotational velocity and HIC shows a high correlation with the maximum principal strain in the brain.

No threshold was proposed by Aare et al. [2004]. Nevertheless, there are some works in the literature where thresholds were proposed for the maximum principal strain. These are presented in table 2.13.

Stress and strain based injury criteria

There is a tendency among researchers to use head injury predictors that are based on the head tissue level response, rather than on its kinematics.

Brain injury is reported to correlate well with stress, strain and strain rate [Lee and Haut, 1989, Viano and Lövsund, 1999]. However, strains and strain rates inside the brain are difficult to measure [van den Bosch, 2006]. This can be achieved using anatomical detailed and accurate FEHM, where stresses and strains are used to compute injury parameters in the skull and in the intracranial contents. Therefore, these models bring a detailed injury assessment closer to reality, since they enable stresses and strains to be examined.

DiMasi et al. [1995] and Bandak [1995, 1997b] developed three component-level injury predictors representing the general types of brain injuries: the cumulative strain damage measure (CSDM), the dilatation damage measure (DDM) and the relative motion damage measure (RMDM). Other predictors have been proposed, such as the brain pressure tolerance and the brain von Mises stress.

More recently, Takhounts et al. [2003, 2008] proposed the SIMon FE model based on the above-mentioned injury metrics proposed by DiMasi et al. [1995] and Bandak [1995, 1997b]. The Strasbourg University FEHM (SUFEHM) criteria is also reviewed in the this section.

Table 2.13: Strain thresholds.

Injury	Threshold	Reference
Contusion	50% risk: 0.19 (in the cortex)	Shreiber et al. [1997]
	0.15 (in the cortex)	Thibault et al. [1990]
DAI	0.1	Thibault [1993]
	0.21	Bain and Meaney [2000]
	0.18	Wright and Ramesh [2012]
	0.2	Morrison III et al. [2003],Kleiven [2007b]
	moderate-to-severe: 0.05-0.10	Margulies and Thibault [1992]
	50% probability of mild: 0.31	Deck and Willinger [2008]
	50% probability of severe: 0.4	
	50% probability:	Kleiven [2007c]
	0.21 (in the corpus callosum)	
	0.26 (in the grey matter)	
	0.16	Singh et al. [2006]
	0.22	Nakadate et al. [2014]
	50% probability: 0.22	Sahoo et al. [2016]
MTBI	0.35-0.45	Viano et al. [2005]
	25% probability:	Zhang et al. [2003b]
	0.26 (in the midbrain)	
	50% probability:	
	0.37 (in the midbrain)	
	75% probability:	
	0.49 (in the midbrain)	
Concussion	AIS1: 0.3 and AIS2: 0.35	Zhang et al. [2008]
	50% probability:	Zhang et al. [2004]
	0.19 (in the midbrain)	
	0.1	Kleiven [2007b]
	50% probability:	Patton et al. [2013]
	0.13 (in the thalamus)	
	0.15 (in the corpus callosum)	
	0.26 (in the white matter)	

Brain pressure. This is a head injury predictor based on the intracranial pressure. Several studies were published with thresholds for this predictor. Some are presented in table 2.14.

Liu and Fan [1998], using a FEHM, concluded that brain pressure has a better sensitivity for very short time impacts than the HIC. However, computed brain pressure does not correlate with some brain injuries. Kang et al. [1997] and Miller et al. [1998] criticized this criterion's capability to predict brain injuries, particularly DAI. In addition, Willinger and Baumgartner [2003b] established that computed brain pressure is not correlated with the occurrence of brain haemorrhages, whereas brain von Mises stress is.

Brain von Mises stress. This criterion assumes that the von Mises stress is the cause of brain damage. Some of the proposed thresholds are given in table 2.15.

Table 2.14: Brain pressure thresholds.

Brain injury	Pressure [kPa]	Reference
Moderate	172.3	Nahum et al. [1977]
Severe or fatal	234.4	
Minor or absent	$\leq$173	Ward and Chan [1980]
Severe (coup)	235	Ward et al. [1980], Chafi et al. [2009]
Severe (contrecoup)	-186	Ward et al. [1980]
Contusions, oedema and haematoma	200	Willinger et al. [1999b], Baumgartner [2001] and Raul et al. [2006]
Coup	180	Yao et al. [2006]
AIS3+ (coup)	256	Yao et al. [2008]
(contrecoup)	-152	
50% risk of MTBI (coup)	90	Zhang et al. [2004]
(contrecoup)	-76	

Table 2.15: Stress thresholds.

Injury	Stress [kPa]	Reference
TBI	11	Zhou et al. [1996a]
	12	Yao et al. [2006]
	8 (in the temporal lobes)	Willinger et al. [1999b]
MTBI	50% probability: 18	Willinger and Baumgartner [2003a,b]
Severe TBI	16	Kang et al. [1997]
	27	Anderson [2000]
	46	Baumgartner et al. [2001]
	50% probability: 38	Willinger and Baumgartner [2003a,b]
Concussion	22	Baumgartner et al. [2001]
	20	Willinger et al. [2000a]
	40	Deck et al. [2003a]
	Long duration: 20	COST327 [2001]
	Short duration: 10	
	50% probability: 8.4 (in the corpus callosum)	Kleiven [2007c]
	50% probability: 7.8 (in the brainstem)	Zhang et al. [2004]
	50% probability: 18	Willinger and Baumgartner [2003a]
Mild DAI	50% probability: 26	Deck and Willinger [2008]
Severe DAI	50% probability: 33	
DAI	50% probability: 61.6	[Sahoo et al., 2016]
AIS3+	14.8	Yao et al. [2008]

Cumulative strain damage measure. This method was presented by Bandak and Eppinger [1994] to evaluate the strain-related damage within the brain. The idea behind their hypothesis is the possibility to quantify the mechanical damage in the axonal components of the brain, once the responsible state of strain is characterized.

Therefore, a cumulative damage measure based on the brain's cumulative volume fraction calculation, which has experienced a specific level of stretch (maximum principal strain) is used as a possible predictor for deformation-related brain injury such as DAI [Marjoux et al., 2008, Takhounts et al., 2008, Zhang et al., 2007].

The CSDM is based on the hypothesis that DAI is associated with the cumulative volume fraction (%) of the brain matter experiencing tensile strains over a critical level. At each time increment, the volume of all elements that have experienced a principal strain above prescribed threshold values is calculated. The affected brain volume monotonically increases in time during conditions where the brain is undergoing tensile stretching deformations, and remains constant for all other conditions (compression, unloading, etc). Bandak et al. [2001] found that a CSDM level 5 corresponds to mild DAI and a CSDM level of 22 corresponds to moderate-to-severe DAI, which means that 5% and 22% represent respectively the brain volume experiencing strain in excess relative to the critical level of 15%, proposed by Thibault et al. [1990]. Takhounts et al. [2003] predicted a 50% probability of concussion for 55% of brain volume experiencing a 15% strain level. Later, Takhounts et al. [2008] predicted a 50% probability of DAI for 54% of brain volume experiencing a maximum principal strain of 0.25. Recently, as a 50% risk threshold for DAI,Sahoo et al. [2016] reported CSDM values of 0.85, 0.59 and 0.27 for strains of 0.10, 0.15 and 0.25, respectively.

Other proposed values of brain strain critical levels are presented in table 2.13. The CSDM is often considered the most promising stress and strain based injury criterion, since it is based on the brain's tissue strain. This is an important parameter, mainly when the brain is submitted to considerable rotations that cause large strains, causing brain injuries such as DAI [Aare et al., 2003].

Dilatation Damage Measure. The DDM is a pressure-based injury criterion proposed by Bandak [1997b], which evaluates brain injury caused by large dilatational stresses. It is supposed to correlate with contusions [Marjoux et al., 2008, Takhounts et al., 2008, Zhang et al., 2007], by monitoring the cumulative volume fraction of the brain experiencing specified negative pressure levels.

The DDM is similar to the brain pressure criterion presented previously. Nevertheless, this one focuses on the amount of dilatational damage caused by negative pressures, usually associated with contrecoup contusions. The probability of contusion is correlated with the brain volume fraction where negative pressures can produce damage [Vezin and Verriest, 2004].

Similarly to the CSDM calculation, at each time step, the volume of all elements experiencing a negative pressure level exceeding a prescribed threshold value is calculated. Bandak et al. [2001] suggested a DDM value of 5% at a threshold level of -101 kPa as an injury threshold. Takhounts et al. [2003] predicted a 50% probability of contusion for a DDM value of 7.2% for a pressure of -100 kPa.

Other researchers have been presenting tolerance values for negative pressures. Ward et al. [1980] proposed a value of -186 kPa in tension as a brain tolerance limit. Zhang et al. [2004] proposed a value of -76 kPa as a 50% risk of MTBI. Yao et al. [2006] proposed a critical value for contrecoup pressure of -130 kPa. More recently, Yao et al. [2008] presented

a critical value for contrecoup pressure of -152 kPa as a predictor for AIS3+ injuries.

Relative Motion Damage Measure. The RMDM was proposed by Bandak [1997b] to evaluate injuries related to brain movements located at the inner surface of the cranium. RMDM monitors the brain surface tangential motion resulting from combined rotational and translational head accelerations. Such motions are suspected to be the cause of SDH associated with large-stretch ruptures of the bridging veins [Marjoux et al., 2008], due to the brain motion relative to the skull.

The bridging veins have been described by Lee and Haut [1989] as having an ultimate strain of about 0.5 in tension, while Löwenhielm [1974b] observed failure at strain values ranging from 0.2 to about 1, depending on the strain rate. A smaller range of 0.3-0.6, but still within the range observed by Löwenhielm [1974b], was proposed by Monson et al. [2003] and Morrison III et al. [2003]. Takhounts et al. [2003] proposed rupture of the bridging veins for a tolerance limit of 1. More recently, Monea et al. [2014] presented a critical value of 5 mm elongation or 25% stretch limit for the occurrence of ASDH due to bridging veins rupture.

The majority of FEHMs do not have bridging veins. Nevertheless, RMDM does not require the modelling of the bridging veins, but rather the monitoring of the relative displacement between node pairs. Each pair represents a bridging vein tethered between the skull and the brain. Thus, RMDM relies heavily on the correct modelling of the interface between brain and skull. If the interface is modelled correctly, the RMDM is potentially a suitable injury criterion to predict SDH [Marjoux et al., 2008, Takhounts et al., 2008].

SIMon criteria. Head numerical models can be useful tools to improve the understanding of brain injury mechanisms. The simulated injury monitor (SIMon) proposed by Takhounts et al. [2003], is one of these models. It was originally developed by DiMasi et al. [1995] and later improved by Bandak et al. [2001]. More recently, this model was updated by Takhounts et al. [2008], presenting a new FEHM that comprised several parts represented in Fig. 2.47: rigid skull, cerebrum, cerebellum, falx, tentorium, combined pia-arachnoid complex with CSF, ventricles, brainstem, and parasagittal blood vessels. The model's topology was derived from human computer tomography (CT). The skull was assumed to be rigid, whereas the rest of the structures were considered as deformable, linear viscoelastic, isotropic, and homogeneous.

The SIMon crteria correspond to a set of thresholds obtained through reconstruction of real head impacts. These reconstructions were performed by Takhounts et al. [2003, 2008] and the predicted thresholds were already presented in the previous sections. For instance, a 50% probability of concussion was predicted for:

- a CSDM value of 55% of brain volume experiencing a 15% strain level;
- a DDM value of 7.2% for a pressure of -100 kPa;

In addition, Takhounts et al. [2003] proposed rupture of the bridging veins for a tolerance limit of 1. More recently, Takhounts et al. [2008] predicted a 50% probability of DAI for

- a CSDM value of 54% of brain volume experiencing a maximum principal strain of 0.25;
- any brain volume experiencing a maximum principal strain value of 0.87;

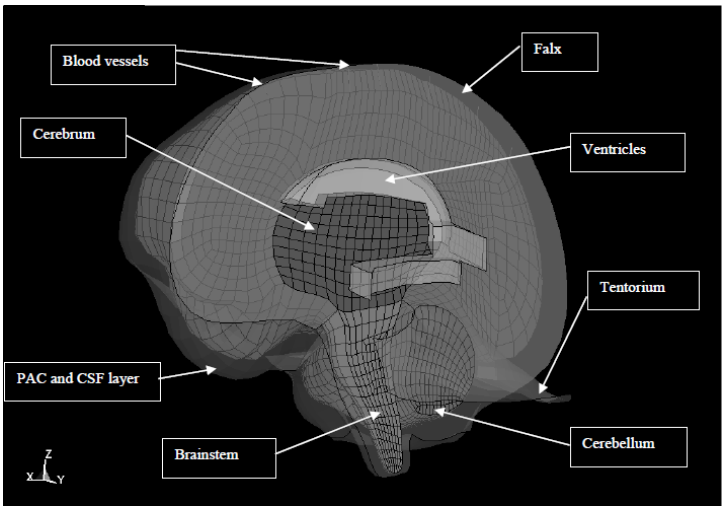

Figure 2.47: SIMon FEHM (adapted from [Takhounts et al., 2008]).

SUFEHM criteria Similarly to SIMon criteria, this one is based on a FEHM and on the thresholds predicted with it, by reconstructing real head impacts with injurious outcomes. As described in Willinger and Baumgartner [2003b], three injury criteria are computed with this model:

- The maximum von Mises stress value reached by a significant volume of at least 10 contiguous elements (representing about 3 cm^3 of brain volume) is proposed as a correlation to neurological injury occurrences. Marjoux et al. [2008], for a moderate and severe neurological injury, obtained von Mises stress values of 27 kPa and 39 kPa, respectively. More recently, Deck and Willinger [2009] updated these tolerance limits to 28 kPa and 53 kPa, respectively;
- The maximum value reached by the global internal strain energy of the elements modelling the space between the brain and skull is proposed as a correlation to SDH. This value represents the integral of $\sigma \times \varepsilon$ product over the whole domain between the brain and skull. Marjoux et al. [2008] found a maximum value reached by the global strain energy of the subarachnoidal space and proposed it as a correlation to SDH with a value of about 4211 mJ. This is higher than the 4J proposed by COST327 [2001] as strain energy in the CSF, for prediction of SDH. More recently, Deck and Willinger [2009] updated this tolerance limit to 4950 mJ and proposed a CSF pressure of 290 kPa as tolerance for SDH;
- The maximum value reached by the global internal strain energy of the deformable skull is proposed as a correlation to skull fracture occurrences. Marjoux et al. [2008] found an internal energy of 833 mJ. A lower value for strain energy magnitude (544 mJ) was proposed by Sahoo et al. [2013] as threshold for 50% risk of human skull bone fracture. More recently, this value was updated to 448 mJ [Sahoo et al., 2014b].

In addition, Deck and Willinger [2008, 2009] proposed a rational approach in order to evaluate the ability of head models to predict brain pressures and strains by using a statistical approach, predicting the following thresholds for DAI:

- Brain von Mises stress of 28 kPa for mild DAI and 53 kPa for severe DAI;

- Brain first principal strain of 33% for mild DAI and 67% for severe DAI.

All of these predictors are associated with an injury risk of 50%. More recently, the von Mises stress was updated to 61.6 kPa and the first principal strain to 0.93 for a 50% risk of severe DAI [Sahoo et al., 2016]. Marjoux et al. [2008] assessed and compared the injury prediction capability of the HIC, the HIP and the criteria provided by the SIMon FEHM and SUFEHM. Marjoux et al. [2008] found better injury predictions with SUFEHM criteria than SIMon criteria, justifying it with the simplicity of SIMon model, whereas SUFEHM geometry seems closer to the real head anatomy. This was also suggested by Franklyn et al. [2003], by comparing the results obtained with other state-of-the-art FEHM, the Wayne State University brain injury model (WSUBIM), with the SIMon model.

Throughout this section, it was evident that there is a wide range of tolerance levels for each injury criterion that can be justified by different models: physical head models, FE models, animal models, clinical and cadaver models [Hrapko et al., 2008, Wright and Ramesh, 2012]. Over the years, with the increasing CPU power, FEM appears to be one of the most useful tools for researchers in this field. Once a FEHM is validated and the proper criteria are settled, it may be used to predict accurately the injury outcome from head impacts. During the last decade, complex FEHMs have been developed. In the next section, these are reviewed.

2.3.5 Finite element human head modelling

Over the years, FEHMs have been used to understand and predict the head response under several impact conditions. These models allow an accurate computational-based prediction of brain injuries, by relating the results to medical investigations based on autopsies of corpses involved in real accidents [Kang et al., 1997]. Nowadays, with the huge development of CPU power, head modelling has evolved tremendously.

Nowadays, only 3D models are relevant for most impact analysis. Nevertheless, 2D models are still used for parametric studies of controlled planar motions [Darvish and Crandall, 2002, Wright and Ramesh, 2012]. Indeed, since a long time ago, there is a great interest in FE models for head injury research. One of the first 3D models was developed by Ward and Thompson [1975]. This is a simple model, with simplified geometries and linear material properties. Later, Shugar [1977] developed a 3D model, by upgrading a previous 2D version [Shugar and Katona, 1975]. In the same year, other simplified models were developed [Khalil and Hubbard, 1977, Nahum et al., 1977].

A few years later, a great step was made by Hosey and Liu [1982], presenting a geometric improved FEHM with brain and neck. Over the years, more FEHMs had been presented, always with complexer geometries [DiMasi et al., 1991b, Mendis, 1992, Ruan et al., 1991]. In fact, Krabbel and Müller [1996] and Hartmann and Kruggel [1999] developed a FEHM using CT and magnetic resonance imaging (MRI) scans to model the skull and brain geometries.

At this point, some of the current state-of-the-art FEHMs were firstly presented. For instance, the first version of WSUHIM [Ruan et al., 1993, Zhou et al., 1995, 1996a]. This one was already capable of differentiating the material properties between grey and white matter. The second version of WSUHIM was developed and upgraded by Al-Bsharat et al. [1999], by introducing a sliding interface between skull and brain.

More recently, the final version of WSUHIM (Fig. 2.48), was presented by Zhang et al. [2001a]. This includes scalp, skull, dura, falx cerebri, tentorium, CSF and brain with distinct

white and grey matter. Concerning the mechanical properties, the brain is characterised as viscoelastic and an elastic-plastic material model was used for bone.

This model was validated against cadaveric intracranial and ventricular pressure data [Nahum et al., 1977], relative brain/skull displacement data [Hardy et al., 2001], and facial impact data [Trosseille et al., 1992]. It was also validated against pedestrian accidents data [Dokko et al., 2003]. In addition, it was used to reconstruct 53 cases of sport accidents including 22 cases of concussion by King et al. [2003].

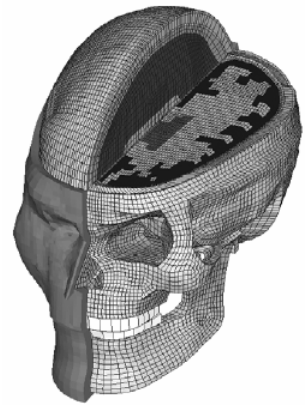

Figure 2.48: WSUHIM (adapted from Zhang et al. [2001a]).

Another model was developed by Claessens et al. [1997], which includes skull, brain and dura mater. This model was validated for intracranial pressure, by simulating the cadaver experiments of Nahum et al. [1977]. Later, Brands et al. [2002] upgraded this model, by incorporating nonlinear material behaviour on the brain response. Nevertheless, all structures were assumed to be rigidly connected to each other.

Also in the 90s, Kang et al. [1997] presented a FEHM that is currently considered a state-of-the-art model, called SUFEHM. The external geometry of the skull was digitised from a human adult male and the interior geometry was obtained from an atlas. This model also includes other anatomical features such as the scalp, dura matter and brain, as shown in Fig. 2.49. Viscoelastic properties were assigned to the brain and the other features were modelled as isotropic and homogenous [Khalil and Viano, 1982]. This model was validated [Willinger et al., 1999a,b, 2000c], with regard to cadaveric experiments [Hardy et al., 2001, Nahum et al., 1977, Trosseille et al., 1992, Yoganandan et al., 1994, 1995]. More details about the development and validation of this model are described in Willinger et al. [2000a,b], Willinger and Baumgartner [2003a] and Deck and Willinger [2009].

In addition, tolerance limits were identified by Marjoux et al. [2008] and Willinger and Baumgartner [2003a] through reconstruction of real accidents, being recognised as a good DAI predictor [Miller et al., 1998, Smith et al., 2003]. However, a well-defined correlation between mechanical loading and DAI using FEHM has not been achieved yet [Cloots et al., 2010]. A possible contribution to this is that the gyri and sulci in the brain, which are not included in the actual FEHM, can play an important role in the local tissue deformations [Cloots et al., 2008, Lauret et al., 2009]. Ho and Kleiven [2009] suggested that the inclusion of sulci should be considered in FEHM as it alters the strain and strain distribution.

More recently, Sahoo et al. [2013, 2014b] upgraded SUFEHM, by developing a more realistic skull geometry with a variable thickness, which is able to simulate skull fracture. This one was used to reconstruct real-world trauma accidents, developing a new skull fracture criterion [Sahoo et al., 2016b]. The brain mechanical properties were also improved,

focusing on high strain rates and nonlinear behaviour [Nicolle et al., 2004]. Later, Sahoo et al. [2014a] upgraded the model in order to be able to simulate axonal elongation in cases of head trauma. This was validated, showing the feasibility of integrating axonal direction information into FEHMs. This recently upgraded model was used to develop new predictors for DAI, by reconstructing 109 head trauma cases [Sahoo et al., 2016].

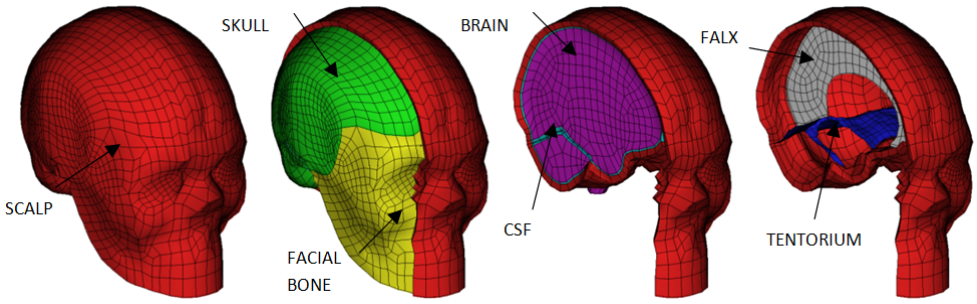

Figure 2.49: SUFEHM (adapted from [Fernandes et al., 2013]).

Another state-of-the-art model is the Kungliga Tekniska Högskolan (KTH) human head model presented in Fig. 2.50. This model was developed by Kleiven [2002] and comprises nonlinear viscoelastic, incompressible material modelling. It includes scalp, skull, brain, meninges, CSF and 11 pairs of parasagittal bridging veins. A simplified neck was also modelled.

The KTH model has been validated [Kleiven and Hardy, 2002, Kleiven and von Holst, 2001, 2002] against experimental pressure data [Nahum et al., 1977, Trosseille et al., 1992] and relative motion data [Hardy et al., 2001]. More recently, it was also validated against intracerebral acceleration experiments [Kleiven, 2006b] and skull fracture experiments [Kleiven, 2006a]. Kleiven [2007c] compared various predictors for MTBI, reconstructing real-world accidents.

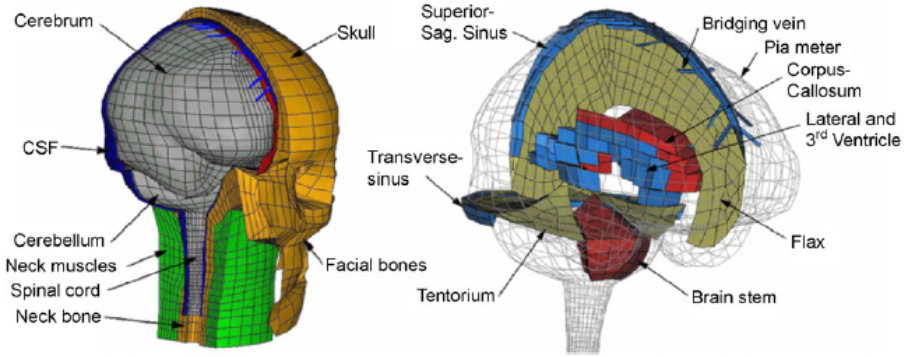

Figure 2.50: KTH FEHM (adapted from [Ho and Kleiven, 2007]).

Ho and Kleiven [2007] studied the influence of including vasculature in the KTH model by modelling a set of blood vessels and concluded that it could be useful for studying ASDH, since ruptures can be predicted by measuring the strain directly in the blood vessels. Later, Ho and Kleiven [2009] studied and suggested the inclusion of sulci in FEHMs, since it alters the strain and stresses distribution in an FE model. In other studies, it is also suggested that the folding structure of the brain surface and the non-uniform distribution of the CSF greatly influence both the distribution and the magnitude of the maximum stress and strains

in the brain [Cloots et al., 2008, Gilchrist and O'Donoghue, 2000, Lauret et al., 2009]. The KTH model suffered some modifications to be used in some specific studies, such as the changes done by Li et al. [2011] in order to model the ventricular system. More recently, the influence of anisotropy was included in this model [Giordano et al., 2014], by modelling the neural fibres and thus including the axonal orientation as in SUFEHM [Sahoo et al., 2014a, 2016].

Another model, the University College Dublin Brain Trauma Model (UCDBTM), based on CT and MRI data, was developed by Horgan and Gilchrist [2003a,b], being improved later by Horgan and Gilchrist [2004]. The model comprises a scalp, skull, dura, CSF, falx, tentorium and brain. This was validated against intracranial pressure data from Nahum et al. [1977] and brain motion data from Hardy et al. [2001]. Further validations were accomplished, comparing real-world brain injury events to model reconstructions [Doorly and Gilchrist, 2006]. More recently, Yan and Pangestu [2011] improved UCDBTM by including viscoelasticity in the material definition of almost all tissues. In addition, CSF was modelled as a hydrostatic fluid.

In the last decade, several new models were presented. After state-of-the-art models, such as WSUHIM, KTH, SUFHEM and UCDBTM, being developed, the majority of these new models did not improve or bring something new. Most of them have oversimplified geometries and material properties, being modelled with linear elastic models, with rigid connected parts or were not properly validated [Belingardi et al., 2005, Cardamone, 2005, Dirisala et al., 2011, Kim et al., 2005, Motherway et al., 2009, Suh et al., 2005, Ziejewski et al., 2009]. From this point, only some models are worth mentioning. For instance, the SIMon model developed by Takhounts et al. [2008] and already presented in section 2.3.4.

Canaple et al. [2003] developed a new model, focusing on the representation of the skull/brain interface and using a hyperelastic material to represent the CSF. Nevertheless, the material properties assigned to the other parts were isotropic and homogeneous. This model was validated for the cadaver impact tests of Nahum et al. [1977] and used in accidents reconstruction [Canaple et al., 2002].

A 3D model of the head-neck complex has been developed by Kimpara et al. [2006] including a detailed description of the brain and the spinal cord. According to the authors, the brain-spinal cord model was useful to investigate CNS injuries. This model was validated against three sets of brain test data [Hardy et al., 2001, Nahum et al., 1977, Trosseille et al., 1992]. In the same year, Yao et al. [2006] presented a FEHM that includes the main anatomical head structures, such as CSF, meninges and brain. This model was validated for Nahum et al. [1977] tests, and then used to reconstruct real-world pedestrian accidents [Yao et al., 2008, Yang, 2011].

Iwamoto et al. [2002] presented a FEHM that includes a skull, CSF, sagittal sinus, dura, falx cerebri, tentorium and brain with distinct white and grey matter, as shown in figure 2.51. This head was developed to incorporate the Total Human Model for Safety (THUMS), a FE model of the entire human body. The model was validated for head-neck motions, lateral bending and rear end impact [Iwamoto, 2003] and for experiments on cadavers [Hardy et al., 2001, Nahum et al., 1977, Trosseille et al., 1992]. THUMS was also tested with SUFHEM, showing comparable results [Ipek et al., 2009].

More recently, Mao et al. [2013] developed a new FEHM with precise geometries and validated it for several experimental cases. This head model was integrated into the full body model supported by the Global Human Body Models Consortium (GHBMC) [Schwartz et al., 2015]. This model is composed by scalp, skull, meninges, bridging veins and brain with distinct white and grey matter. Only the meninges were modelled as linear elastic. The others were modelled as viscoelastic or elastic-plastic materials. This model was

validated by Mao et al. [2013] for a huge number of experimental tests, such as brain pressure [Nahum et al., 1977, Trosseille et al., 1992], brain motion [Hardy et al., 2001], skull response [Hodgson et al., 1970, Yoganandan et al., 1995], among others. Nevertheless, significant discrepancies between simulated and experimental results were observed in a great number of different tests.

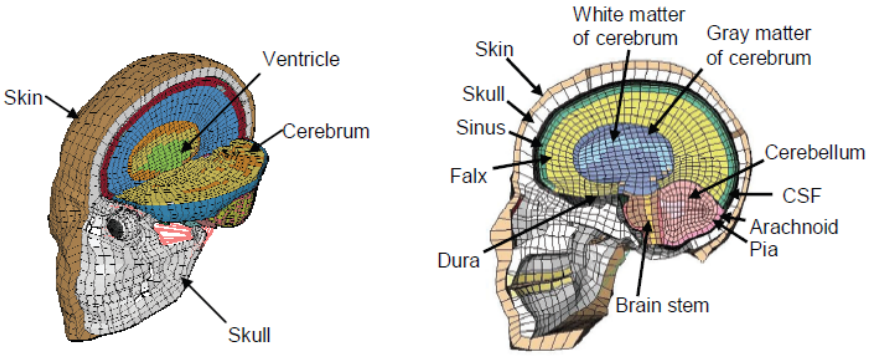

Figure 2.51: THUMS model (adopted from [Iwamoto et al., 2007]).

More information about these and other models can be found in Raul et al. [2008] and Tse et al. [2014]. At the point this work is written, models such as SUFEHM, WSUHIM, KTH, UCDBTM and GHBMC represent the cutting-edge state-of-art for FEHM. All of these use nonlinear material models to simulate brain's behaviour. Although a great number of FEHMs exist, gyri and sulci are absent in almost all these models. In these, brain's global geometry is usually similar to a ellipsoidal structure without sulci and gyri. Basically, a simplified volume resembling a brain with a smooth surface.

Cloots et al. [2008] reported that gyri and sulci had a significant effect on maximum von Mises stress value. Cloots et al. [2010] indicated that a well-defined correlation between mechanical loading and DAI using FEHM has not been achieved yet. A possible contribution to this is absence of gyri and sulci in brain models, which can play an important role in the local tissue deformations [Cloots et al., 2008, Lauret et al., 2009]. The folding structure of the brain surface and the non-uniform distribution of the CSF greatly influence both the distribution and the magnitude of the maximum stress and strains in the brain [Cloots et al., 2008, Gilchrist and O'Donoghue, 2000, Lauret et al., 2009]. In addition, Ho and Kleiven [2009] verified that strain and strain rates during impacts were both reduced in a model with sulci [Ho et al., 2009], especially for rotational accelerations in the sagittal plane. They also concluded that the presence of these structures should be considered in future models.

In addition, the relative motion between skull and brain is also important. The majority of these models have different components with shared or rigidly connected nodes, which influence the brain's intracranial motion. Little attention has been paid to the relative motion between structures. Excessive motion between skull and brain may injure brain's surface or even the bridging veins connecting them, which may rupture under excessive loading [Horgan and Gilchrist, 2003b, Tse et al., 2014]. This may cause damage on the brain's surface (sulci and gyri) and even in the brain tissue. Cerebral contusions usually involve the surface of the brain, especially the crowns of gyri [Gurdjian et al., 1966b, Ommaya et al., 1971].

Thus, in this thesis, it is developed a new FEHM with a brain model with sulci and gyri that also allows the brain to move inside the skull. This FEHM is a new contribution to the state-of-the-art FEHMs.

Chapter 3

Material characterisation and modelling

This chapter describes the experimental tests performed to characterize agglomerated cork and the simulations performed to validate the constitutive models. This same procedure was done for EPS and EPP.

This chapter comprises experimental tests performed at quasi-static and dynamic strain rates under uniaxial compressive loading. In addition, numerical simulations results are presented in order to test the validity of the developed material models. Finally, it is performed a comparison of the mechanical behaviour between agglomerated cork and synthetic foams in compression. In this work, the material testing and the numerical simulations were divided into three phases:

- Phase I - In the first phase, a few samples of agglomerated cork provided by a manufacturer were tested at quasi-static and dynamic strain rates. These were performed to assess the mechanical behaviour of agglomerated cork and mainly to have input data for the material model in order to assess its validity.

- Phase II - After checking the validity of the material model, more experiments were performed in several different agglomerates. These tests were intended to assess and compare the mechanical behaviour of these agglomerates in order to select the most promising ones. The referred tests include double impacts.

- Phase III - In the last phase, the constitutive strategy used to model agglomerated cork under one impact and validated in phase I, was adopted for simulating double impacts similar to those performed in phase II. In addition, the same experiments were performed in EPS and EPP foams, which are commonly used in helmets, in order to establish a comparison. Simulations were also performed for these foams, validating other material models for further use.

3.1 Phase I

In the last decades, many researchers have extensively studied the fundamental aspects of cork's mechanical behaviour under quasi-static compressive loading [Anjos et al., 2008, 2014, Fortes and Nogueira, 1989, Fortes et al., 2004, Gibson et al., 1981, 1982b, Mano, 2002, Pereira et al., 1992, Rosa and Fortes, 1988a]. However, few researchers studied cork's mechanical behaviour when subjected to dynamic compressions. At the moment this phase was under development, there was only one known publication where cork was subjected to dynamic loading. Gameiro et al. [2007a] studied cork's (natural and agglomerated) mechanical behaviour under impact loading at strain rates ranging from 200 to 600 s^{-1}.

Based on these experiments, Gameiro et al. [2005] also developed a numerical model for agglomerated cork. However, this was an elastic model with no type of damage included. Although cork is a material that recovers almost totally its initial dimensions, after compression, there is always some damage, which amount depends on the strains reached. Thus, it is necessary to model this damage in order to simulate multi-impacts. Regarding numerical simulations of cork, in all publications found in the literature [Gameiro et al., 2005, Sousa-Martins et al., 2013, Paulino and Teixeira-Dias, 2011, Alves de Sousa et al., 2012, Coelho et al., 2013, Alcântara et al., 2013], cork was always modelled as an elastic material without any type of damage.

The purpose of this research is to simulate agglomerated cork's dynamic compressive behaviour, including its relaxation. This phase also comprises experimental testing at quasi-static and dynamic strain rates. The quasi-static compression tests are performed in order to obtain the mechanical properties required to characterise agglomerated cork. On the other hand, the data from the impact tests is used to validate the numerical model. Thus, numerical simulations are performed using FEA, and the material model developed is validated against experimental results.

The same material model was also further validated by simulating the experiments performed by Gameiro et al. [2007a]. One advantage of this validation is the availability of the initial part of the relaxation in the compression curves obtained by Gameiro et al. [2007a]. It should be pointed out the difficulty to obtain experimental data regarding the material's relaxation at such strain rates. Thus, in phase I, it is presented a new strategy to develop a material model for agglomerated cork. The work developed in this first phase is already published in Fernandes et al. [2014].

3.1.1 Experimental tests

In this study, it is used agglomerated cork, which is produced on an industrial scale and available in many shapes and sizes. Other advantage is that its behaviour is less variable than natural cork. For instance, agglomerated cork made of bound cork granules between 0.5 mm and 2 mm, can be considered isotropic. On the other hand, such consideration cannot be made for natural cork. Also, natural cork has limited dimensions given its extraction process. The agglomerated cork used to perform both quasi-static and dynamic compression tests, was supplied by Granorte, a Portuguese company.

Quasi-static compression tests

The experimental work performed in this phase was carried out at University of Aveiro labs. These tests enabled a better and more complex validation of the material model used for

agglomerated cork. Quasi-static compression tests were performed in a Shimadzu universal testing machine (Fig. 3.1), as a first step in the characterisation of the agglomerated cork.

Figure 3.1: Shimadzu universal testing machine.

Seven rectangular samples of agglomerated cork were tested. The agglomerated cork samples dimensions, the amount of permanent deformation in the compression direction and the test configuration are shown in table 3.1. This type of agglomerated cork has a density of 180 kg/m^3.

A 10 kN constant force was used to compress the samples. The samples I to IV were compressed at a velocity of 2 mm/min and the remaining ones were compressed at 10 mm/min. Fig. 3.2 shows two curves obtained in the quasi-statics tests for two different compression velocities. These curves correspond to samples II and V, compressed at a velocity of 2 mm/min and 10 mm/min respectively. For the same velocity, the curves from different samples matched perfectly. These curves follow the typical pattern observed in cellular materials. There is a small linear elastic region for small strains, which corresponds to the elastic bending of the cell walls, followed by a plateau caused by the progressive buckling of the cell walls until the stress rises steeply.

During the compression of sample V, the measured stress was higher for the same levels of deformation of sample II. Nevertheless, this difference is very small. Thus, the compressive behaviour of agglomerated cork is almost strain rate independent between strain rates ranging from 9.62×10^{-4} s^{-1} to 4.82×10^{-3} s^{-1}. According to Gameiro et al. [2007a], agglomerated cork is strain rate independent when compressed at strain rates ranging between 10^{-3} s^{-1} and 600 s^{-1}.

At the end of these tests, it was observed that agglomerated cork's relaxation was faster when compressed at higher velocities. In the case, the recover was faster for the

compressive velocity of 10 mm/min. Also, the amount of permanent deformation was less in the samples tested with a compressive velocity of 10 mm/min. However, this difference was minimal.

In the specific case of the sample VII, the elastic return was higher than 90%. However, contrarily to the other samples, this one was compressed only to 48% of deformation, in order to determine what happens when an agglomerated cork sample is compressed to approximately half of its thickness. This shows the highly viscoelastic behaviour of cork. Fig. 3.3 shows a comparison between the compressed sample I (on the left), which exhibited more damage and a not tested sample.

Table 3.1: Agglomerated cork samples' dimensions and the amount of permanent deformation.

Sample	a [mm]	b [mm]	c [mm]	Permanent deformation [%]
I	30	28.5	34.65	14.29
II	30	29	34.65	13.56
III	29.55	28.75	34.9	14.18
IV	29.65	28.7	34.6	13.15
V	30.35	28.65	34.6	12.86
VI	30.75	30	34.4	11.92
VII	30.55	28.7	34.55	4.34

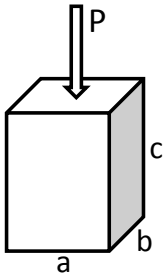

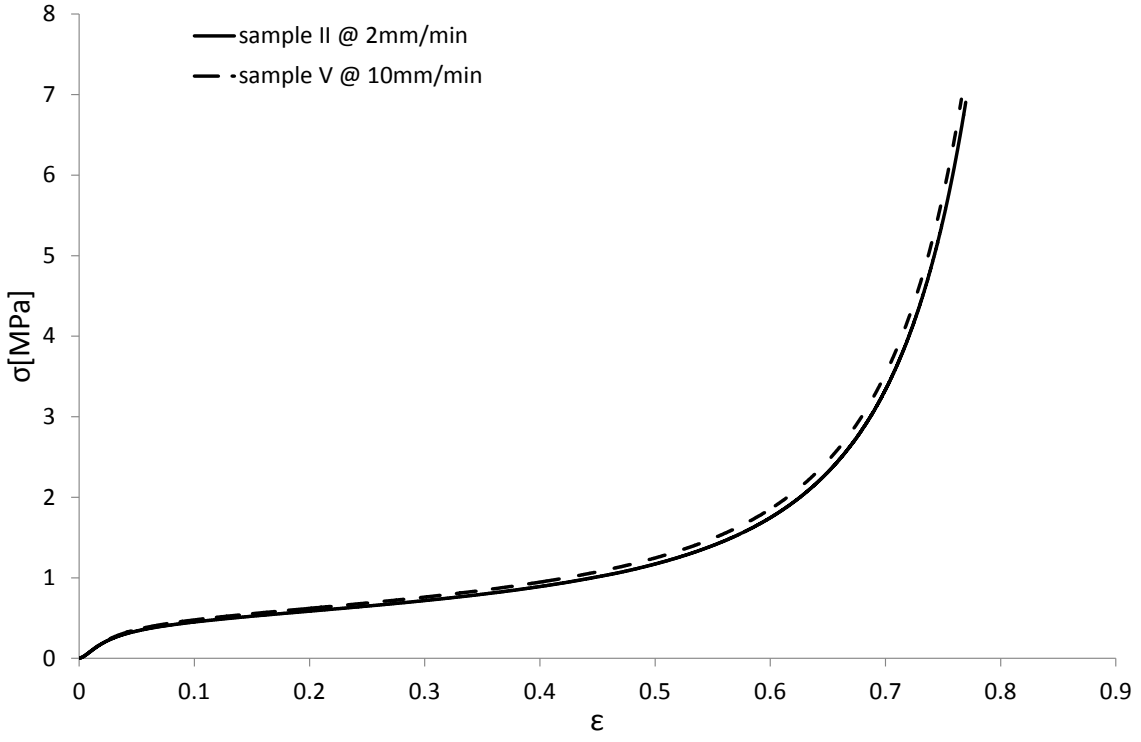

Figure 3.2: Stress-strain curve from quasi-static experimental tests.

In addition, the same findings reported in Rosa and Fortes [1988a] were verified in this work. They studied cork compression up to 80% of strain, and concluded that the recovery rate decreases appreciably with time and increases with the degree of deformation previously imposed. According to Anjos et al. [2008], when cell buckling occurs during cork

Figure 3.3: Agglomerated cork samples after and before being tested at quasi-static strain rates.

compression, the initial dimension recovery is associated with the unfolding of the buckled cell walls which occurs quickly.

In Anjos et al. [2014], cork samples were compressed to an approximate 50% strain and the results showed that only a small amount of permanent deformation remains (in the range of 3% to 9%), which corroborates the compression here performed to a strain of 48% where the permanent deformation was 4.34%. However, these experiments were performed in agglomerated cork and not in natural cork. Nevertheless, this small amount of permanent damage corroborates the capacity of the microstructural assembly of the cell walls to change in order to support that deformation by means of cell corrugation [Anjos et al., 2014]. According to the same author, it is possible that part of the permanent deformation is related to the deformation of pores. Regarding agglomerated cork, part of the permanent deformation may also be related to the plastic deformation of the thermosets.

Thus, cork's recovery is explained by the elasticity of its cells, and compression at strains in the plateau region only corresponds to an increase of corrugations in the cell walls, which is released immediately when the unloading starts. In fact, the recovery is done by the unfolding of the buckled cell walls, which must also involve relaxation processes at the molecular level in the cell walls [Anjos et al., 2008].

Impact tests

The dynamic tests were performed in a drop tower designed for this purpose. This tests apparatus consists of a 3 meters long steel tube, placed vertically with two position sensors at the bottom and separated by a constant distance in order to compute the impact speed. From the top, a 5 kg hemispherical steel impactor with an accelerometer placed in its centre was dropped from a height of 3 meters. The impactor's diameter is 94 mm. Fig. 3.4 shows the lower part of the tower after an impact. The samples were placed on top of a steel base made of the same steel used for the impactor.

The uniaxial accelerometer used was the model 1201 from Measurement Specialties and the model of the two objective reflector sensors was the OPB700ALZ from TT Electronics. An acquisition frequency of 2000 Hz was set using the acquisition card DT9816 from Data Translation. This was defined by developing an interface in MATLAB programming language, to process and set the acquisition conditions, computing the impact velocity and

the acceleration-time history.

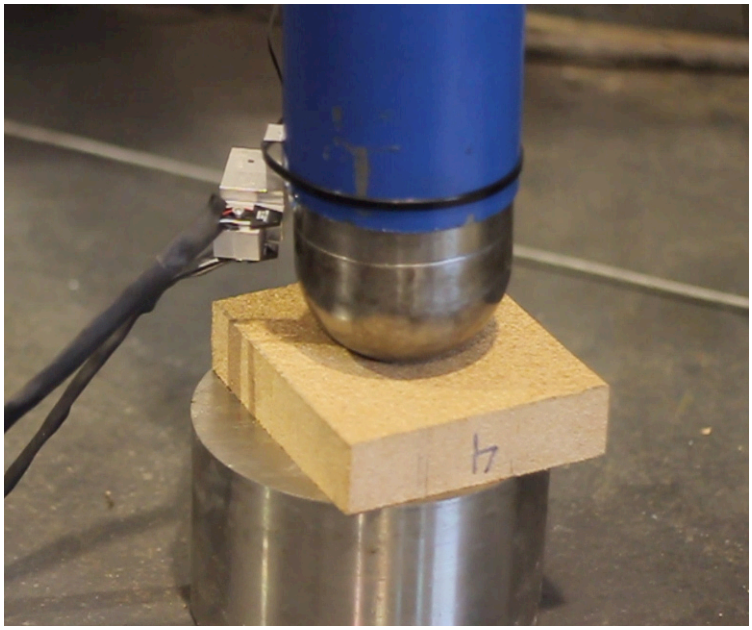

Figure 3.4: The lower part of the 3 meter drop-tower used for impact tests.

Impact tests were performed on seven samples of agglomerated cork. Table 3.2 shows the samples dimensions, the measured velocity at the moment of impact and the amount of permanent deformation. The amount of permanent deformation was minimal, observing a small and concentrated plastic deformation in the impact region, as shown in Fig. 3.5. In addition, this concentration of deformation in the impact region was possibly increased by the impactor geometry. In Fig. 3.5, it is also possible to see the small amount of permanent deformation, where half of the gap between the two samples in the impact region corresponds to the permanent deformation.

Table 3.2: Agglomerated cork samples' dimensions, impact velocity and the amount of permanent deformation.

Sample	a [mm]	b [mm]	c [mm]	Velocity [m/s]	Permanent deformation [%]
I	123	123	34.5	4.89	2.75
II	131.75	124	34.1	5.25	3.08
III	136	121.4	34.15	5.25	3.95
IV	137.8	123.35	34.2	4.5	2.49
V	140.1	129.2	34.2	5.25	3.7
VI	119.35	116.35	34.05	5.25	3.67
VII	119.8	116.7	34.4	4.5	2.63

Analysing the results in table 3.2 and Fig. 3.5, it is possible to conclude that samples thickness is almost the same before and after the impacts. The dimensional recovery was almost total, more than 95% of the initial dimension. These results show the great capability of agglomerated cork to continue absorbing energy after an impact. These values were measured immediately after impact, which proves the instantaneous recovery of agglomerated cork after being unloaded, stabilising at a very small value of permanent deformation. This makes it an optimal material for energy absorption applications where

multi-impacts will possibly occur. For instance in motorcycle helmets, since in road accidents multi-impacts may occur during 1 second.

In Fig. 3.10, it is shown the mean acceleration curve from the seven impacts. Since the results were similar, this curve is used in the next section to validate the numerical model.

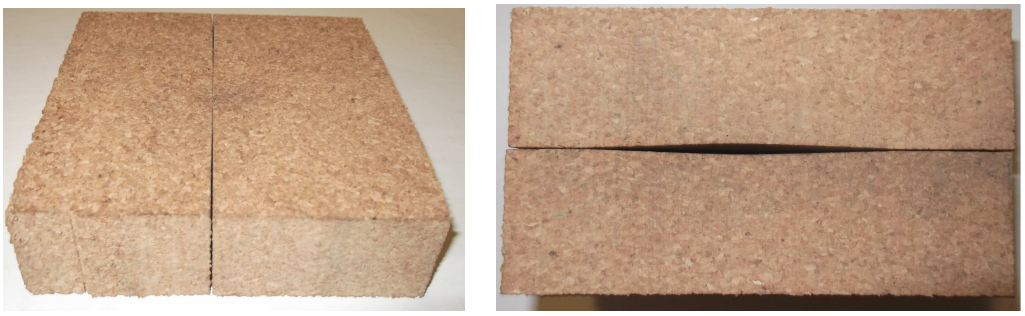

Figure 3.5: Cut sample at the centre of maximum deformation.

3.1.2 Agglomerated cork modelling

As already referred, several researchers attempted to model agglomerated cork under dynamic compression [Gameiro et al., 2005, Sousa-Martins et al., 2013, Paulino and Teixeira-Dias, 2011, Alves de Sousa et al., 2012, Coelho et al., 2013, Alcântara et al., 2013]. However, cork was always modelled as an elastic material without any type of damage. Although cork is a material that recovers almost totally its initial dimensions, there is always some amount damage after compression. This was evident in the experiments presented in the previous section.

In addition, the material models used in these studies were not properly validated. The majority of them used the quasi-static curves from Gameiro et al. [2007a] as validation for dynamic regimes and a few of them did not properly replicate the dynamic compressions performed in Gameiro et al. [2007a].

Constitutive laws

Abaqus FE code has several built-in material models that can be used to simulate the mechanical behaviour of a great variety of materials. Agglomerated cork exhibits predominantly an elastic behaviour, where the plastic behaviour represents a small part of cork mechanical characteristics, only reached at really high deformations. Doing so, Abaqus nonlinear elastic models seem to be a good initial approach to model agglomerated cork.

Agglomerated cork is primarily modelled as a hyperelastic material, using the hyperfoam model available in Abaqus material library. This is an isotropic and nonlinear model typically used to characterise elastomeric foams that present hyperelastic behaviour. It is valid for cellular solids whose porosity permits very large volumetric changes [ABAQUS, 2010]. It is also intended for finite-strain applications where it can deform elastically to large strains, up to 90% strain in compression. In addition, agglomerated cork has a Poisson's ratio of approximately zero, which means that a typical hyperelastic model is not suitable for agglomerated cork.

Hyperfoam is defined by a strain energy potential, also known as strain energy density function, which defines the strain energy stored in the material per unit of reference volume

(initial volume) as function of the strain in the material. In the hyperfoam material model, the elastic behaviour of the foams is based on the following strain energy function or potential:

$$\tilde{U} = \sum_{i=1}^{N} \frac{2\mu_i}{\alpha_i^2}[\lambda_1^{\alpha_i} + \lambda_2^{\alpha_i} + \lambda_3^{\alpha_i} - 3 + \frac{1}{\beta i}((J)^{-\alpha_i\beta_i} - 1)] \tag{3.1}$$

where N is an integer (the polynomial order), λ_i are the principal stretches, J is the elastic volume ratio ($J = \lambda_1\lambda_2\lambda_3$), μ_i are the shear moduli, α_i and β_i are curve-fitting material parameters. The latter are related to the material compressibility, where the initial bulk modulus, K_0, is given by the following expression:

$$K_0 = \sum_{i=1}^{N} 2\mu_i \left(\frac{1}{3} + \beta_i\right) \tag{3.2}$$

For each term in the energy function, the coefficient β_i determines the degree of compressibility. The coefficient β_i is related to Poisson's ratio, ν_i, by the expressions:

$$\beta_i = \frac{\nu_i}{1 - 2\nu_i} \tag{3.3}$$

$$\nu_i = \frac{\beta_i}{1 - 2\beta_i} \tag{3.4}$$

Thus, if β_i is the same for all terms, there is a single effective Poisson's raio, ν. The coefficients μ_i are related to the initial shear modulus, μ_0, by:

$$\mu_0 = \sum_{i=1}^{N} \mu_i \tag{3.5}$$

The principal stretches, λ_i, are related to the principal nominal strains, ε_i, by:

$$\lambda_i = 1 + \varepsilon_i \tag{3.6}$$

This hyperelastic model for elastomeric foams can be combined with other material model that provides a mechanism to include permanent energy dissipation and stress softening effects in elastomeric foams. In order to model correctly the permanent energy dissipation and stress softening effects in agglomerated cork, the Mullins effect model is used together with the hyperfoam material model, providing an extension to the isotropic elastomeric foam model. Thus, this material model is used to include the damage present in elastomeric foams, modelling energy absorption in foam components subjected to dynamic loading, under deformation rates that are high when compared to the characteristic foam time relaxation. In such cases, it is acceptable to assume that the foam material is damaged permanently and the stress softening is interpreted as being due to damage at the microscopic level [ABAQUS, 2010].

In the case of using just the hyperfoam model, the curve path for unloading is exactly the same for loading. This means that no energy was dissipated by permanent damage. With the inclusion of Mullins effect, the path of the unloading will not be the same and will happen for lower stresses, which means that some energy was dissipated. Fig. 3.6 shows a typical stress-stretch response of an elastomeric foam with energy dissipation. For instance, considering the primary loading path abb' of a previously unstressed foam,

with loading to an arbitrary point b'. On unloading from b', the path b'Ba is followed. When the material is loaded again, the softened path is retraced as aBb'. If further loading is then applied, the path b'c is followed, where b'c is a continuation of the primary loading path (which is the path that would be followed if there were no unloading). If loading is now stopped at c', the path c'Ca is followed on unloading and then retraced back to c' on reloading. If no further loading beyond c' is applied, the curve aCc' represents the subsequent material response, which is then elastic. For loading beyond c', the primary path is again followed and the pattern described is repeated. The shaded area represents the energy dissipated by damage in the material for deformation until c'. More information about this model and its implementation in Abaqus is available in Ogden and Roxburgh [1999].

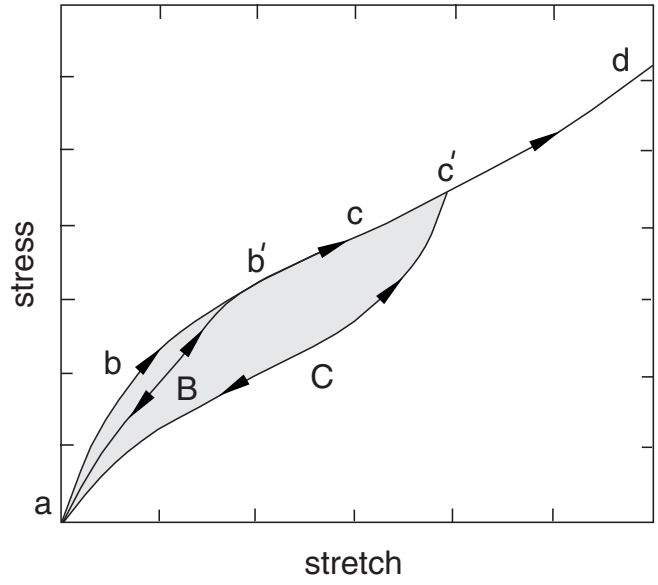

Figure 3.6: Typical stress-stretch response of an elastomeric foam with energy dissipation (adapted from ABAQUS [2010]).

In this model, the energy dissipation effects are accounted for by introducing an augmented strain energy density function of the form:

$$U\left(\lambda_i, \eta\right) = \eta \tilde{U}\left(\lambda_i\right) + \phi\left(\eta\right) \tag{3.7}$$

where λ_i (i = 1, 2, 3) represent the principal mechanical stretches and $\tilde{U}\left(\lambda_i\right)$ is the strain energy potential for the primary foam behaviour described by equation 3.1. The function $\phi\left(\eta\right)$ is a continuous function of the damage variable, η, and related to the damage function [ABAQUS, 2010]. The damage variable, η, varies continuously during the course of the deformation and always satisfies $0 < \eta \leq 1$, with $\eta = 1$ on the points of the primary curve (described by the hyperfoam model). When the damage function $\phi\left(\eta\right)$ satisfies the condition $\phi\left(1\right) = 0$, the deformation state of the material relies on the curve representing the primary foam behaviour, $U\left(\lambda_i, 1\right) = \tilde{U}\left(\lambda_i\right)$ and the augmented energy function reduces to the strain energy potential for the primary foam behaviour and thus, the material model responsible for mimicking the mechanical behaviour is only the hyperfoam.

Accounting with Mullins effect, the stresses are computed by:

$$\boldsymbol{\sigma}\left(\eta, \lambda_i\right) = \eta \tilde{\boldsymbol{\sigma}}\left(\lambda_i\right) \tag{3.8}$$

where $\tilde{\boldsymbol{\sigma}}$ is the stress corresponding to the primary foam behaviour at the current deformation level λ_i. Thus, the stress is obtained by simply scaling the stress of the primary foam behaviour with the damage variable, η. From any given strain level, the model predicts unloading/reloading along a single curve (that is different, in general, from the primary behaviour) that passes through the origin of the stress-strain plot. The model also predicts energy dissipation under purely volumetric deformation [ABAQUS, 2010].

The damage variable, η, varies with the deformation according to:

$$\eta = 1 - \frac{1}{r} erf\left(\frac{U^{max} - \tilde{U}}{m + \beta U^{max}}\right) \tag{3.9}$$

where U^{max} is the maximum value of $\tilde{U}$ at a material point during its deformation history; r, β and m are material parameters and $erf(x)$ is the error function. While the parameters r and β are dimensionless, the parameter m has the dimensions of energy. These material parameters are subject to the restrictions $r > 1$, $\beta \geq 0$ and $m \geq 0$ (the parameters β and m cannot both be zero). In general, these parameters do not have direct physical interpretations. The parameter m controls whether the damage occurs at low strain levels. On the other hand, a nonzero m leads to little or no damage at low strains levels. The parameter r controls the amount of damage, the larger the value of r, the less the damage is. The parameter β has a similar effect, the higher it is, the lower is the damage. The qualitative effects of parameters r and β, while others are fixed, are shown in Fig. 3.7

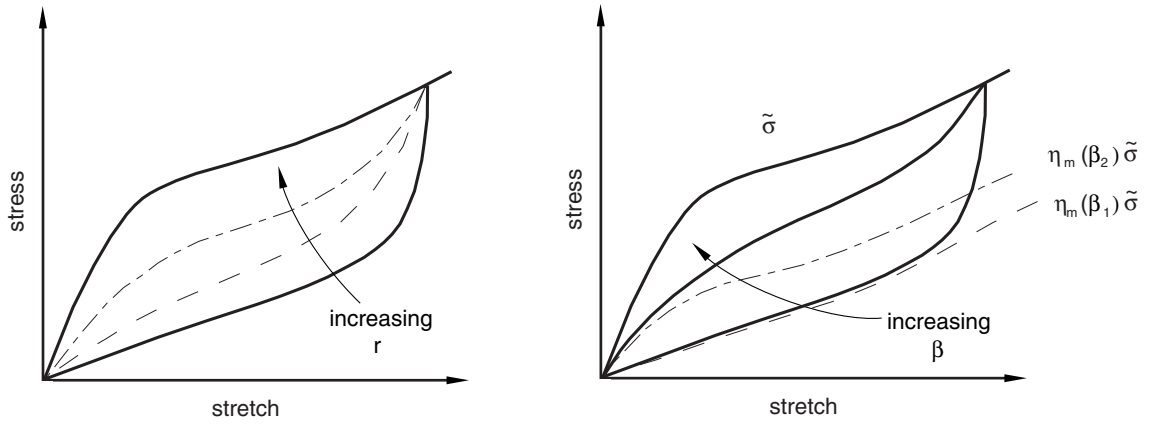

Figure 3.7: Qualitative dependence of damage on material parameters (adapted from ABAQUS [2010]).

When $\tilde{U} = U^{max}$, corresponding to a point on the primary curve, $\eta = 1$. On the other hand, upon removal of deformation, when $\tilde{U} = 0$, the damage variable, η attains its minimum value, η_{min}, given by:

$$\eta_{min} = 1 - \frac{1}{r} erf\left(\frac{U^{max}}{m + \beta U^{max}}\right) \tag{3.10}$$

For all intermediate values of $\tilde{U}$, η varies monotonically between 1 and η_{min}. The recoverable part of the energy is obtained by subtracting the dissipated energy from the augmented energy as:

$$U_{recoverable} = \eta \tilde{U}\left(\lambda_i\right) - \phi\left(\eta_{min}\right) \tag{3.11}$$

where the residual value of the augmented energy function, $\phi\left(\eta_{min}\right)$, represents the

energy dissipated due to damage in the material, upon complete unloading. The damage energy accumulates with progressive deformation along the primary curve and remains constant during unloading. During unloading, the recoverable part of the strain energy is released. The latter becomes zero when the material point is completely unloaded. Upon further reloading from a completely unloaded state, the recoverable part of the strain energy increases from zero. When the maximum strain that was attained earlier is exceeded upon reloading, further accumulation of damage energy occurs.

Impact tests

Agglomerated cork was modelled as a nonlinear elastic material, including energy dissipation and stress softening effects. This was considered valid due to the small amount of damage observed in the experimental tests. In order to model such behaviour, a combination between hyperfoam and Mullins effect material models was used. The quasi-static compression curve obtained from a sample compressed at 2 mm/min and shown in Fig. 3.2, was multiplied by a scale factor of value 3.1 in order to incorporate the dynamic effects, since the S-shape of the stress-curve of agglomerated cork is constant [Dart and Eugene, 1946]. Gameiro et al. [2005] used a slightly lower value of 3 in a different FE code. The final multiplied curve used as input is presented in Fig. 3.8.

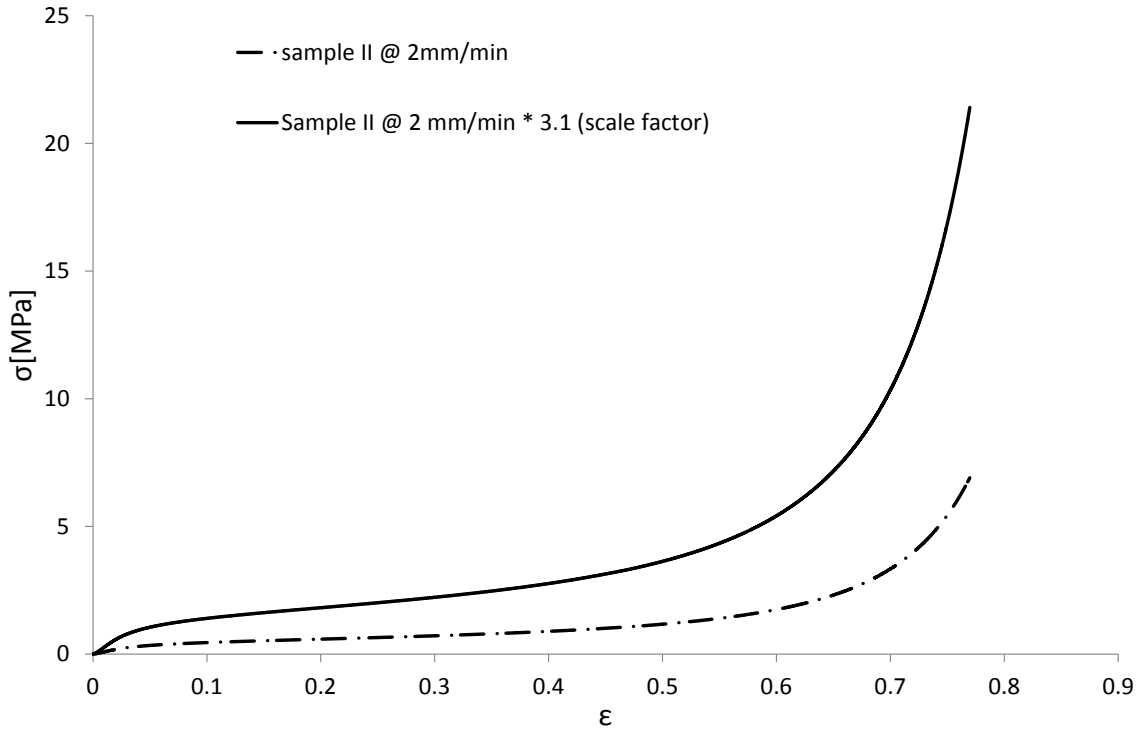

Figure 3.8: Quasi-static curve from compression experimental tests and the imported curve after multiplication by a scale factor of 3.1.

The material density, ρ, of 180 kg.m^{-3}, a null Poisson's ratio, ν, and the strain energy potential order, N, of value 3 were also used as input. The latter was concluded as the best value to model agglomerated cork with the hyperfoam material model, because this value makes it more stable. It is believed that at least at larger strains, the Poisson's ratio is approximately zero during compression. Probably because the buckling of the cell walls

does not result in any significant lateral deformation. This is one of the main reasons why it is used the hyperfoam model and not a typical hyperelastic model. The parameters used as input for this model are presented in table 3.3.

Table 3.3: Parameters introduced in Abaqus material law to characterise agglomerated cork.

ρ [kg.m^{-3}]	ν	N	r	m	β	a [mm]	b [mm]	c [mm]
180	0	3	1.1	0.5	0.1	129.69	122	34.23

In order to reproduce numerically the guided drop tests, a rectangular sample with mean dimensions from the seven samples shown in table 3.2 was modelled. The dimensions of the sample modelled are shown in table 3.3. Two rigid bodies were also modelled, a fully constrained bottom plate that represents a steel base and half a sphere that represents the steel impactor. This setup is shown in Fig. 3.9.

The rigid impactor has just one degree of freedom in the direction of compression, as in the experiments. The interaction between the sample and the rigid bodies was modelled with a "hard" surface-to-surface type of contact (Explicit). A friction coefficient of 0.64 was used to model such interaction. Vaz and Fortes [1998] indicated this value to be the friction coefficient between cork and smooth steel. A velocity of 5.25 m/s was prescribed to the top plate. The Abaqus Explicit solver with the large deformation option was used to simulate the impact.

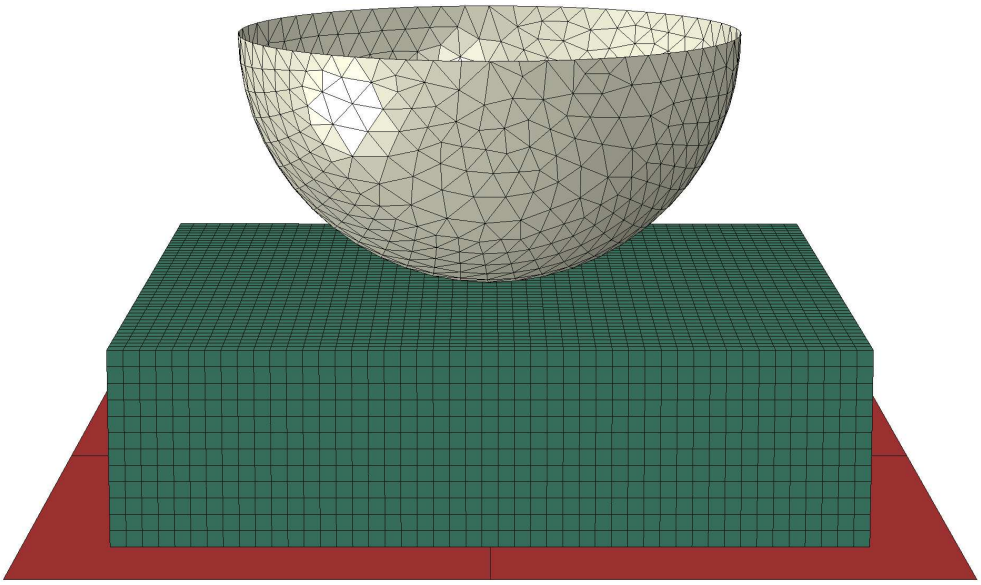

Figure 3.9: Guided drop test - numerical setup.

In order to create the FE model, the sample was modelled with eight-node linear brick fully integrated elements. The rigid plate was modelled with rigid quadrangular elements. The hemispherical impactor was modelled with rigid triangular elements. More details about the mesh are presented in table 3.4.

The meshes of each part were created always avoiding distorted and warped elements and special attention was given to the elements size, in order to have reliable results that were not influenced by mesh elements size but at the same time to have a reasonable computational time. Regarding the sample's mesh, several simulations were performed,

increasing the number of elements until the results converged, defining the optimal number of elements.

Table 3.4: Mesh properties of the guided drop test parts.

Part	Element type	Abaqus element	N° of elements	N° of nodes
Hemispherical impactor	Rigid triangular shell	R3D3	1142	602
Bottom plate	Rigid quadrangular shell	R3D4	4	9
Sample	Eight-node linear brick	C3D8	24816	28080

The results from the simulations were compared with the experiments. Fig. 3.10 shows this comparison in terms of uniaxial acceleration measured during the impact. It is possible to verify that the results obtained in FEA are close to the ones measured experimentally. In addition, and given the good validation, Figs. 3.11 and 3.12 show some results computed numerically. In the last figure, it is plotted the amount of energy dissipated by viscous effects. In Fig. 3.11, it is plotted:

- The amount of energy dissipated by damage;
- The amount of energy dissipated through frictional effects;
- The model's internal energy;
- The model's kinetic energy;
- The model's strain energy.

Regarding these results, the model was capable of dissipating 24.45 J through damage, which represents 35.48% of the initial kinetic energy. An amount of 5.25 J is dissipated by frictional effects. The kinetic energy reached its minimum at 4.35 s, which means that the impactor velocity at this moment was zero and the rebound just started. When the kinetic energy reached its minimum (maximum deformation, but not permanent, of 15.16 mm), the strain energy and the energy dissipated by damage reached its maximum as expected. The internal energy also reached its maximum because in this model, the internal energy is computed by the sum between the strain energy and the energy dissipated by damage. Although, the frictional energy dissipation was small compared to the others, it contributed to the dissipation of impact energy in this model.

In this model, the energy dissipated by viscous effects is very small, reaching a maximum of 22.67 mJ. This represents viscous regularization, not including the energy dissipated by automatic stabilization and viscoelasticity [ABAQUS, 2010]. Although this combination between hyperfoam and Mullins effect provides a mechanism that is similar to material relaxation, the model here used does not account with the viscoelastic model. Thus, the energy dissipated by viscous effects can be neglected for this model.

After the minimum kinetic energy, the rebound started and the impactor velocity increased until the impactor lifts off the sample. At this moment, the velocity in FEA remained constant and this explains why the kinetic energy remained constant after 8$\sim$9 milliseconds. Comparing Figs. 3.10 and 3.11, it is possible to see some similarities. For

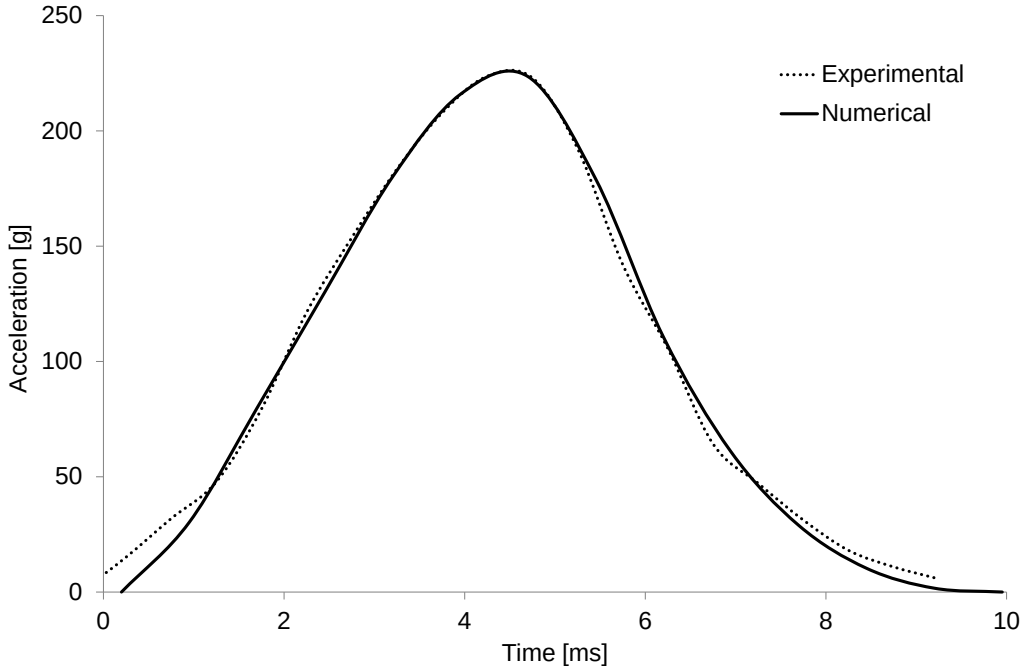

Figure 3.10: Acceleration measured during the impacts - results from FEA and experiments.

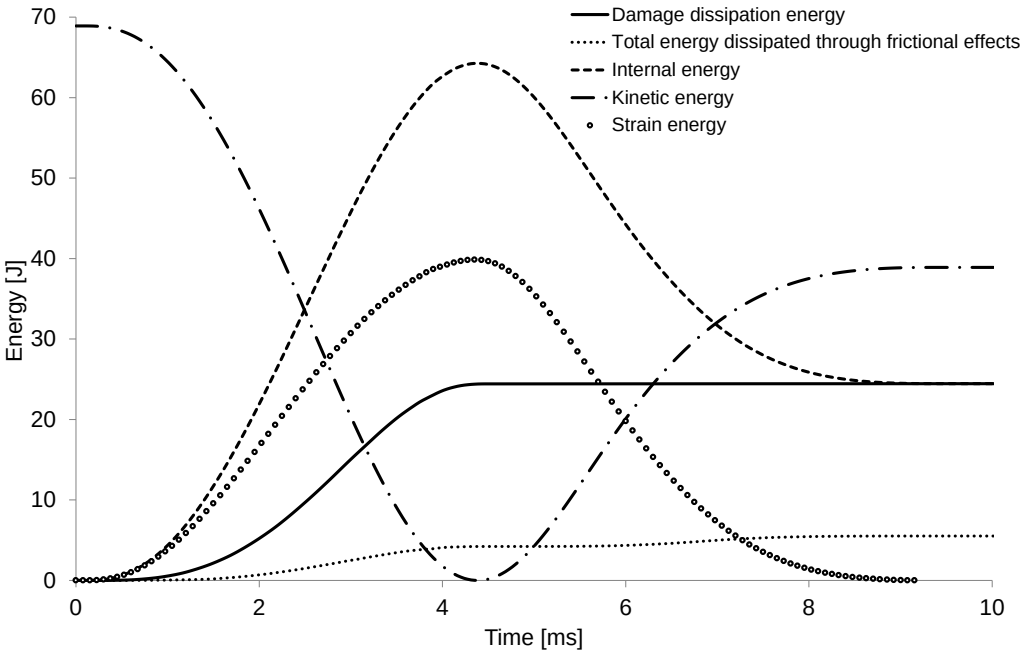

Figure 3.11: Energies measured during the impact - results from FEA.

example, when maximum deformation is reached, the kinetic energy is at its minimum and the acceleration and strain energy are at their maximum.

In Fig. 3.13, it is possible to see the region of the sample where the energy dissipated by damage is greater for the moment of maximum deformation. The curve that represents this energy in Fig. 3.11 is computed by summing the total energy dissipated in all ele-

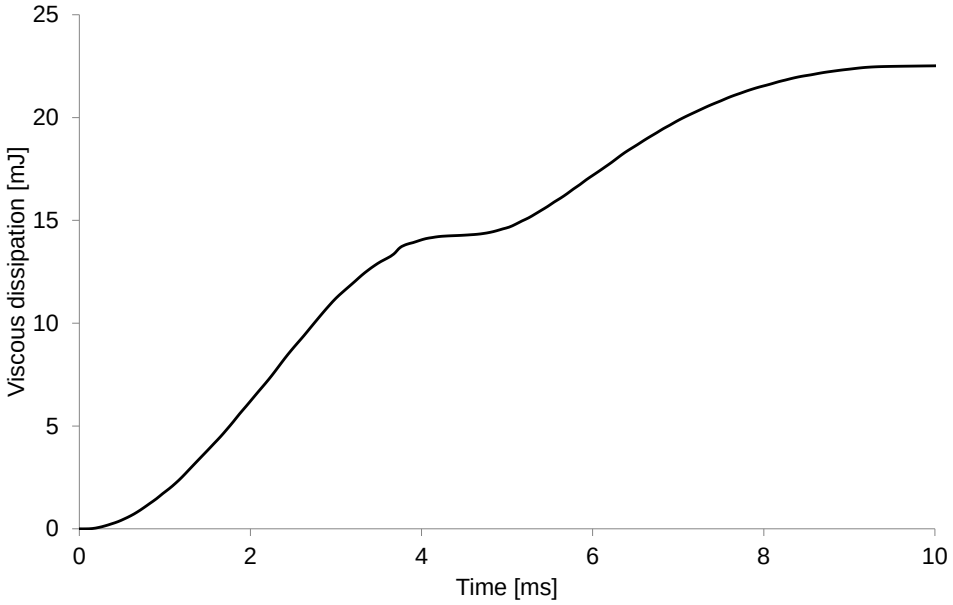

Figure 3.12: Energy dissipated by viscous effects during the impact - results from FEA.

ments of the model. This procedure is also done to obtain the strain energy and a similar illustration of Fig. 3.13 is presented in Fig. 3.14 for the strain energy case. According to ABAQUS [2010], when the Mullins effect is modelled with hyperelastic materials, this quantity represents the recoverable part of energy in the element.

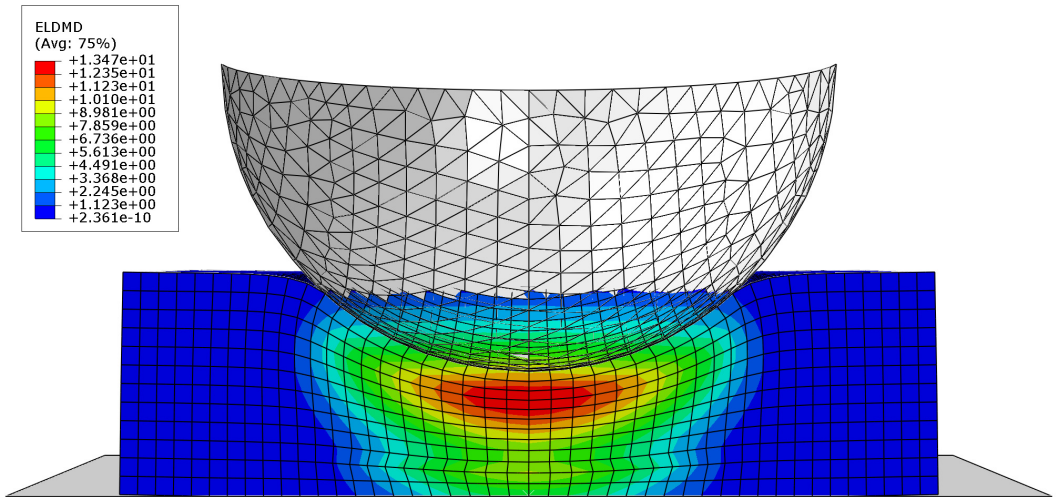

Figure 3.13: Illustration of a sample half-cut - total energy dissipated in the element by damage in mJ.

This nonlinear elastic model represented well the behaviour of agglomerated cork under dynamic compression. The inclusion of Mullins effect seems to represent the energy dissipation of cork and its recovery. Thus, this material model was considered valid for further use in cork modelling.

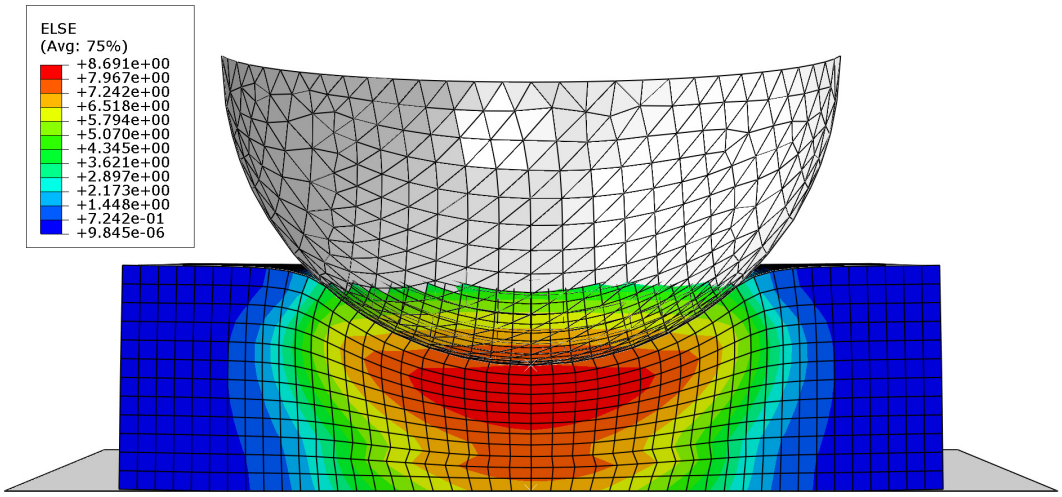

Figure 3.14: Illustration of a sample half-cut - total elastic strain energy in the element in mJ.

Modelling based on the literature data

In order to further validate the previously presented numerical model for cork modelling, experiments performed in Gameiro et al. [2007a] were replicated. It was the only work available in the literature that presents experimental data regarding the dynamic compression of agglomerated cork. In addition, the initial part of the unloading curve is present. The lack of complete data can be justified in part due to the difficulty of measuring the material recovery at dynamic rates. Thereby, these data were taken into consideration in order to model agglomerated cork's dynamic compression and its recovery.

Gameiro et al. [2007a] studied the mechanical behaviour of agglomerated cork under impact, using the Split Hopkinson Pressure Bar (SHPB) to perform the experimental tests. In order to reproduce this test in FEA, a cylindrical sample with a diameter of 23 mm and a length of 25 mm was modelled. Two circular rigid plates were also modelled and a mass of 4.70 kg and 2.76 kg was attributed to the top plate and the bottom plate, corresponding to the mass of the SHPB test input bar and output bar, respectively. These plates were placed next to the base and upper section of the cylindrical sample. This setup is shown in Fig. 3.15.

These plates have just one degree of freedom in the direction of compression, as in the SHPB test. The interaction between the sample and the plates was modelled with a "hard" surface-to-surface type of contact (Explicit). A velocity of 3.9 m/s was prescribed to the top plate. The Abaqus 6.13 Explicit solver with the large deformation option was used to simulate the impacts.

In order to create the FE model, the sample was modelled with eight-node linear brick elements. The two rigid plates were modelled with rigid quadrangular elements. More details about the mesh are presented in table 3.5. The meshes of each part were created always avoiding distorted and warped elements. Special attention was given to the elements size, in order to have reliable results that were not influenced by it, but also to have a reasonable computing time. Several simulations were performed, increasing the number of elements over the thickness from 7 to 25 and the seeding over the circumference from 32 to 66 to check convergence of results. Finally, the sample was meshed with 32 elements over the circumference and 7 elements along the length, resulting in a total of 791 elements.

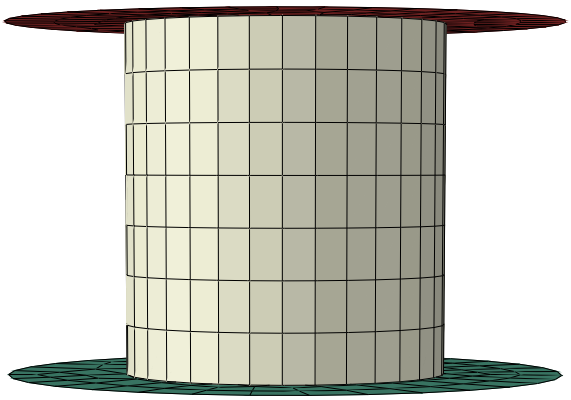

Figure 3.15: Split Hopkinson Pressure Bar test - numerical setup.

Table 3.5: Mesh properties of the SHPB test parts.

Part	Element type	Abaqus element	N° of elements	N° of nodes
Plates	Rigid quadrangular shell	R3D4	162 (each plate)	183 (each plate)
Cylindrical sample	Eight-node linear brick	C3D8	791	1040

In order to define the strain energy function parameters, data from uniaxial compression tests (also performed in Gameiro et al. [2007a]) were specified. This enables Abaqus to compute the hyperfoam material parameters, using a least square method fitting technique. The stress-strain curve imported into Abaqus is the result of a multiplication between the experimental compressions tests performed at quasi-static rates by Gameiro et al. [2007a] and a scale factor (function of the strain rate). This multiplication makes it possible to take into account the effect of the strain rate increase. This was already done in the previous validation.

The multiplication by a scale factor is valid for agglomerated cork due to the shape of the stress-strain curve, which is always the same [Dart and Eugene, 1946, Gameiro et al., 2007a]. The scale factor used has a value of 3.1 which is slightly superior to the scale factor of value 3 used by Gameiro et al. [2005] in a different FE code (LS-DYNA). The curve from quasi-static tests and its multiplied version are presented in Fig. 3.16.

In addition, a density of 293 kg.m^{-3}, a null Poisson's ratio, and the strain energy potential order, N, of value 3 were also used as input. The latter was again the best value to model agglomerated cork. These and the parameters of the Mullins effect material model are presented in table 3.6.

Table 3.6: Parameters introduced in Abaqus to characterise agglomerated cork.

ρ [kg.m^{-3}]	ν	N	r	m	β
293	0	3	1.01	0.1	0.1

The FEA and experimental results are shown in Fig. 3.17, where σ and ϵ are the nominal stress and strain, respectively. This graph shows the amount of stress measured during the compression and also a part of the unloading. Numerical and experimental results show quite good agreement. Thus, it is concluded that the combination of hyperfoam

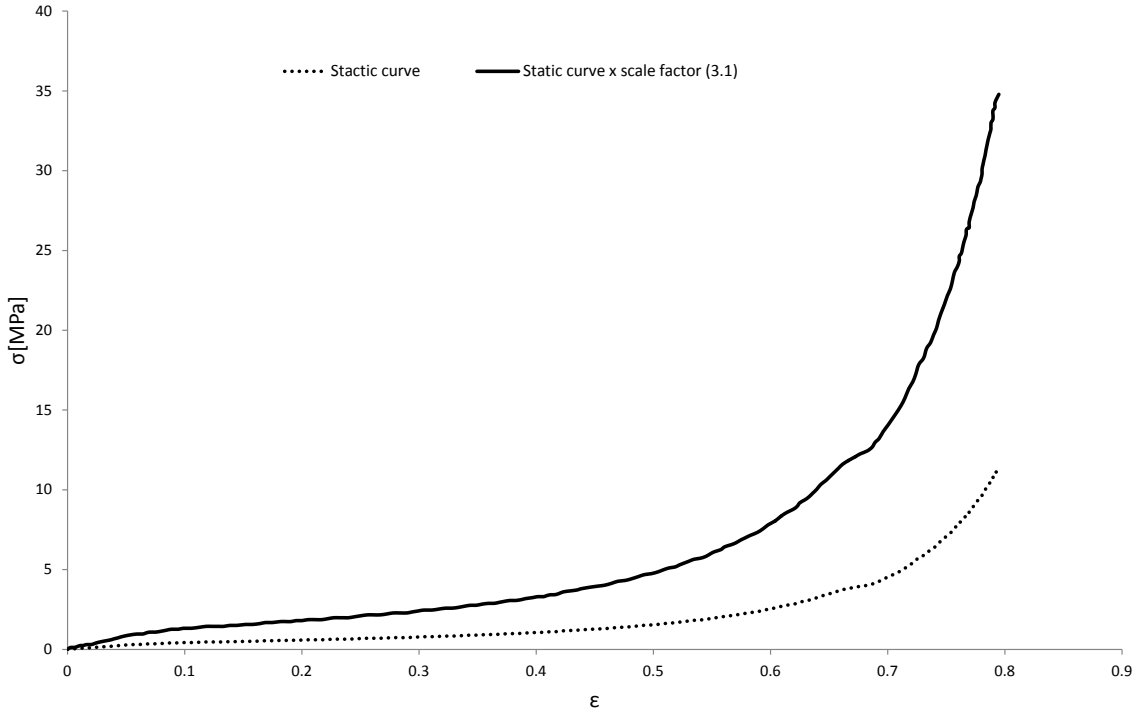

Figure 3.16: Quasi-static curve from the experimental tests performed by Gameiro et al. [2007a] and the imported curve after multiplication by a scale factor of 3.1.

and Mullins effect material models is capable of reproduce the mechanical behaviour of agglomerated cork under dynamic compressions.

However, there is a small deviation between the experimental and the numerical results at the moment of maximum compression. In the experimental one, the maximum stress value is 5.3 MPa, for a strain value of 0.52. On the other hand, in FEA, a maximum stress value of 6.1 MPa was measured for a strain of 0.54. Nevertheless, this is the only observable deviation. During almost all loading and unloading, the numerical and experimental results are similar.

In general, the combination of hyperfoam and Mullins effect material models was able to reproduce the mechanical behaviour of agglomerated cork during compression and also its recovery. Although the material model is nonlinear elastic, it was able to dissipate energy by damage. In addition, the amount of permanent deformation seen in the experiments was minimal. Thus, the material model is considered valid for simulating agglomerated cork compressions at dynamic strain rates and possibly for multi-impact simulations.

3.2 Phase II

Different agglomerates have different mechanical properties. Depending on their composition, the mechanical behaviour may be significantly distinct. For instance, by varying the granule size, it is possible to change the material properties of the agglomerate. This is also valid for the binder used to agglomerate the cork granules. In addition, it is possible to create agglomerated cork products without using a binder. This is the case of expanded cork, also known as black agglomerate, which is a 100% natural material. There is interest on study this agglomerate and on evaluating its suitability as impact energy absorber, since

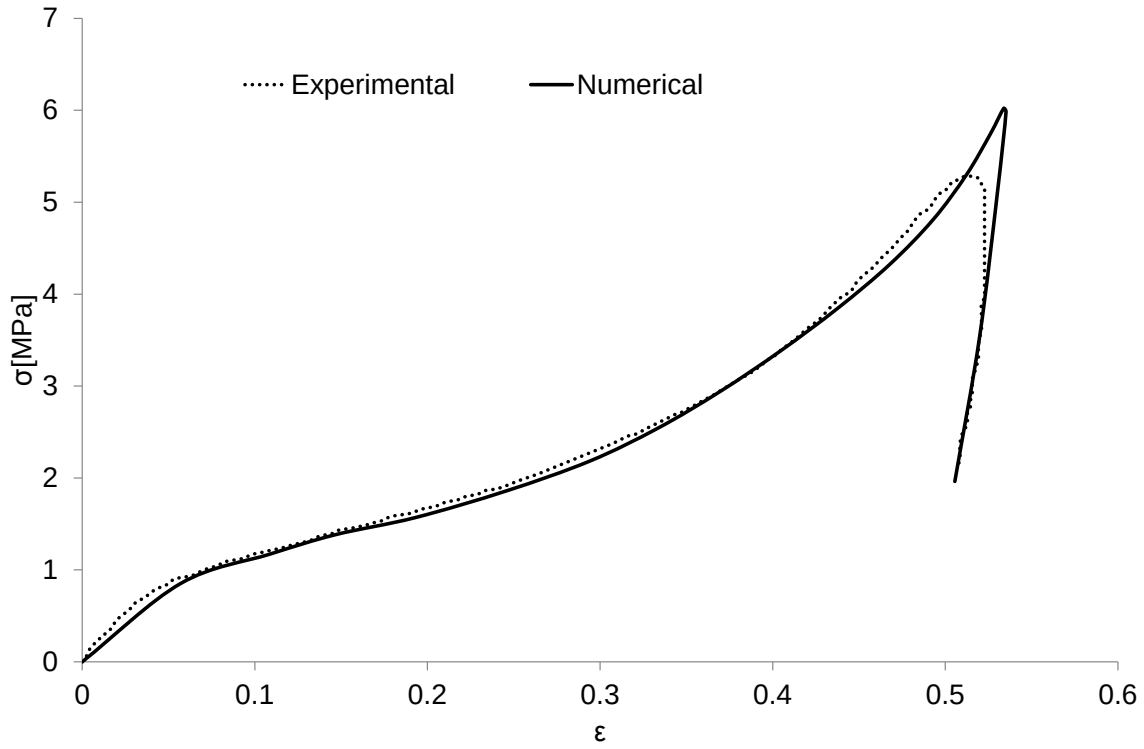

Figure 3.17: Comparison between experimental and numerical stress-strain curve obtained for agglomerated cork.

there is a lack of info about it in the literature.

Thus, in this second phase, more agglomerates are tested, including the expanded ones. The main goal of this stage is to test a great number of different agglomerates in order to select the most promising ones to be used as helmet liner. Therefore, the criterion is based on the capacity to withstand considerable amounts of energy and on the capacity to withstand further successive impacts.

In summary, several agglomerates are submitted to double impacts. These are higher energy impacts (approximately double) than the ones performed in the previous phase. In addition to dynamic testing, the samples are also tested under quasi-static loads. This is important in order to obtain the material properties of each agglomerate. The work developed in this phase is already published in Jardin et al. [2015].

3.2.1 Experimental tests

In this phase, the behaviour of different types of agglomerates, including expanded cork, are tested under quasi-static and multiple dynamic loading. Seven distinct types of agglomerated cork were tested. These were chosen in order to analyse a wide range of distinct solutions with different densities, granule sizes and agglomerate type. The agglomerated and the expanded cork samples were provided by CORKSRIBAS and Sofalca, respectively. Fig. 3.18 shows the different types of agglomerated cork provided by CORKSRIBAS.

Table 3.7 presents the density values and the range of granule sizes. Exact mixture ratios and the quantity of binder are commercial well kept secrets. In addition, the specific composition of the binders was not revealed by the company. It was just indicated that is a PU based binder.

Figure 3.18: Agglomerated cork provided by CORKSRIBAS.

Table 3.7: Information about the tested materials.

ρ [kg.m^{-3}]	Adopted designation	Granule size [mm]	Binder
157.0	AC157	2-4	PU
178.0	AC178	2-4	PU
199.1	AC199	0.5-2	PU
216.2	AC216	2-4	PU
122.9	EC122	4-10	Suberin
159.4	EC159	4-10	Suberin
182.8	EC182	4-10	Suberin

In addition to table 3.7, Fig. 3.19 depicts the granule size of some samples. In the case of the expanded agglomerate, the grain size is much larger than the typical agglomerate. This difference is explained by the manufacturing process already presented in section 2.1.2. The manufacturing process also explains the lower density of expanded cork, which is composed by expanded granules without externally added binder.

Quasi-static compression tests

The quasi-static compression tests were performed using a Shimadzu AG 50 KN testing machine, as in the previous phase. In addition, the video extensometer presented in Fig. 3.20 was also used. The samples are cubes with a size of 60 mm. These were carefully placed at the centre. The compression tests were carried out at a velocity of 5 mm/min. The uniaxial compression tests were stopped when a stress of 6.5 MPa was reached. At this value, all the samples were already densified, as shown in Fig. 3.21.

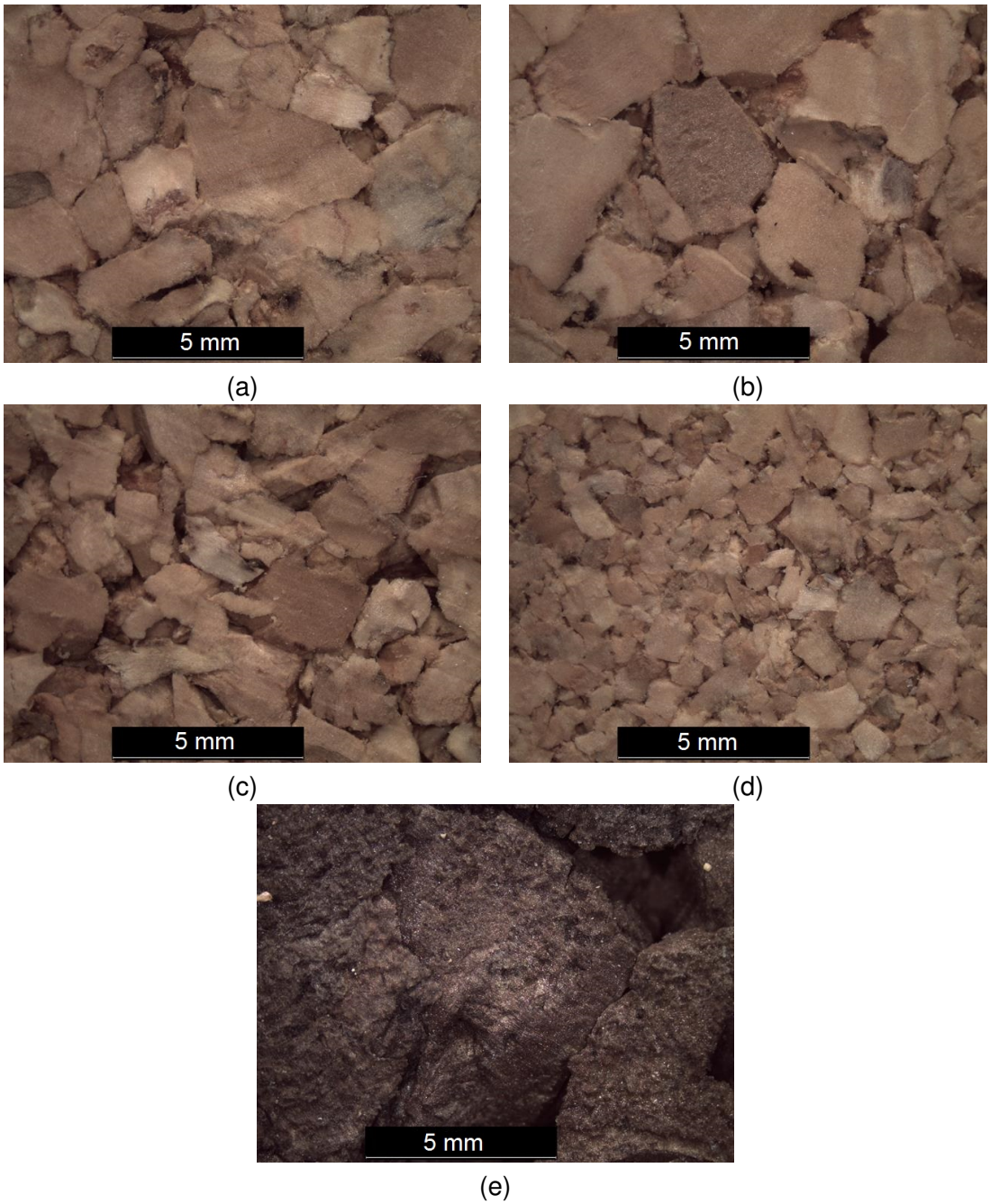

Figure 3.19: Macrostructure of some agglomerates: (a) AC216; (b) AC157; (c) AC178; (d) AC199; (e) EC159.

Figs. 3.21 and 3.22 show the stress-strain curves and the absorbed energy per unit volume, respectively. A total of 5 samples per each material were tested and the average result is presented. As expected for a cellular material, it is possible to observe a small and linear increase of stress for small strains. Then, all the agglomerates exhibit a low stress plateau for a wide deformation range (approx. up to 60%). This plateau is the key responsible for the energy absorption capacity of cellular materials. Finally, the materials reach densification, an accentuated increase of stress occurs for small strain variations.

Once the goal is withstanding large amounts of energy, the mechanical response should

(a)

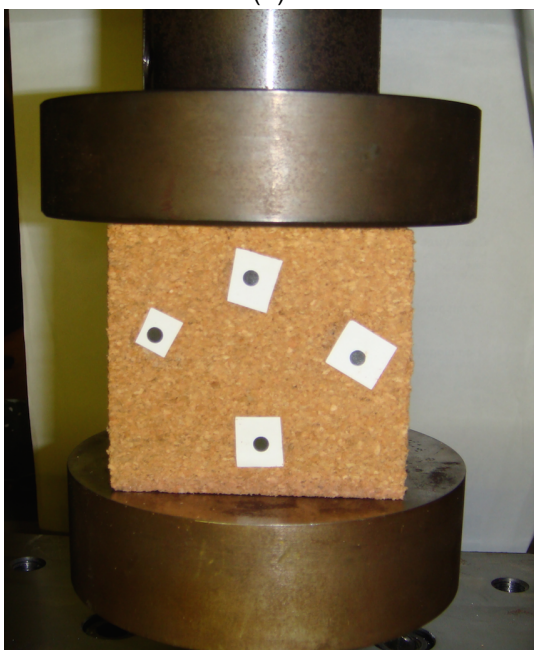

(b)

Figure 3.20: Uniaxial compression tests with video extensometer: (a) Messphysik video extensometer; (b) Experimental testing setup.

include a long plateau with moderate stress values, followed by densification only reached for high strain values. From this point of view, the AC216 exhibits the highest plateau, although reaching densification sooner than the other materials. The AC178 presents densification only for high strains but the plateau is characterised by low stress values. The other agglomerates present plateaus and densification strains between the values measured for AC216 and AC178. In the end, the agglomerate choice will depend on the desired application.

Fig. 3.21 shows three lines crossing the stress-strain curves, which indicate the amount of strain energy per unit volume. The energy density levels are 250, 500 and 750 kJ/m^3. For the lowest energy density level, the material with lower density stores energy at a lower stress level, reaching a larger deformation. This is the ideal situation for any kind of protection system, promoting gentle decelerations. For the intermediate level of energy, the denser material is still not fully compressed, being at the end of the stress plateau, while the others are already on the densification stage. For the highest level of energy, the denser material (AC216) provides the best result once the stress level reached is lower compared to the remaining ones, which present full densification.

In addition, Fig. 3.22 shows the energy per unit volume at the end of the compression, when a stress level of 6.5 MPa was reached. The trend is not linear but shows a proportional relationship between material density and energy density. Thus, AC216 and EC122

are respectively the upper and lower bounds in terms of strain energy under quasi-static compression. Although density seems to play a major role, other factors such as granule size and binder may also influence the results, explaining why the energy density is not purely proportional to the material density.

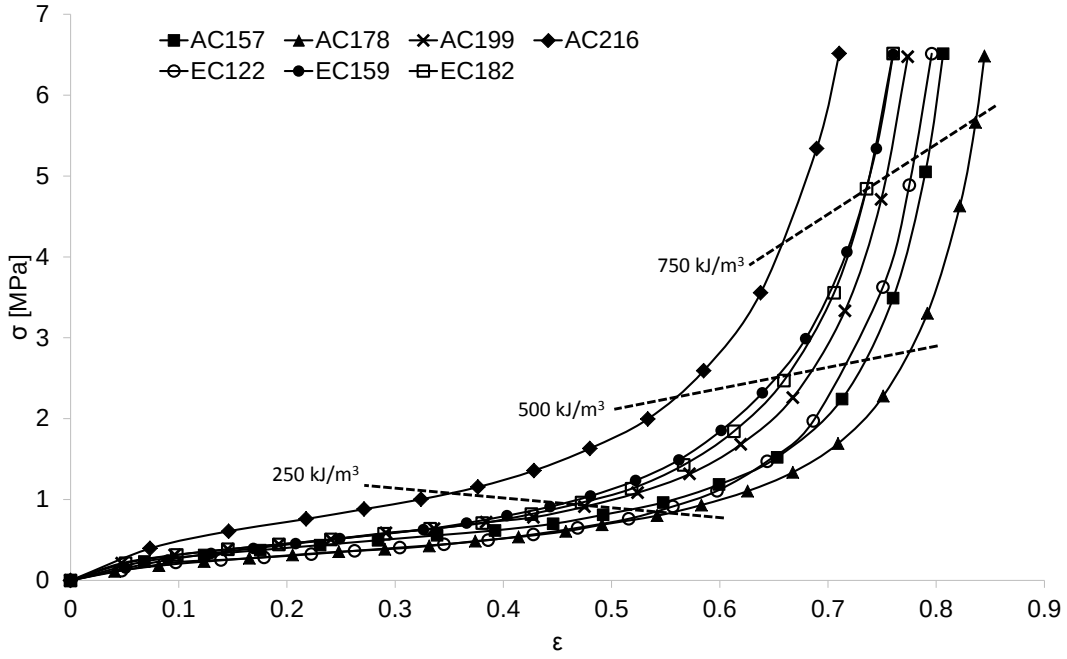

Figure 3.21: Stress-strain curves of all agglomerates subjected to uniaxial compressions at quasi-static strain rates.

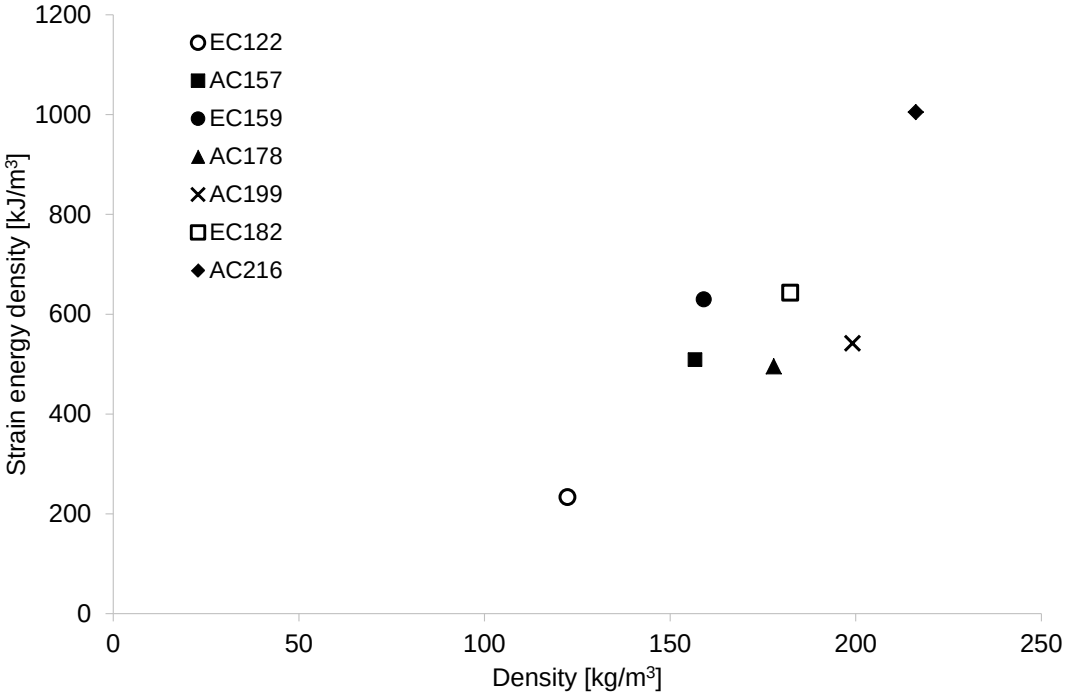

Figure 3.22: Strain energy density of each agglomerate for a stress level of 6.5 MPa.

Table 3.8 gives another quantitative insight, presenting the energy density at 60% of strain. These values were also calculated from the curves shown in Fig. 3.21. This value was chosen for being an average strain value for the densification onset. It is interesting to compare two agglomerates with very similar densities but different binders, for instance, AC178 and EC182, and also EC159 and AC157. The expanded agglomerates seem to have a slight advantage over the non-expanded ones. On the other hand, recalling Fig. 3.21, it is possible to verify that expanded agglomerates tend to reach densification earlier than non-expanded agglomerates bound with PU resin.

Table 3.8: Energy density at the end of compression and at 60% of strain.

Specimen	kJ/m^3 (at 6.5 MPa)	kJ/m^3 (at 60%)
AC157	854.5	322.8
AC178	849.2	344.8
AC199	871.2	341.3
AC216	1101.3	633.5
EC122	715.2	210.1
EC159	914.9	406.3
EC182	921.2	385.1

Additionally, the Young's modulus and the Poisson's ratio were also calculated. The Young's modulus ranged from about 2.5 MPa for the material with lower density to 6 MPa for the denser AC216. The remaining agglomerates showed values between 2.7 MPa (EC159) and 4.3 MPa (AC199). However, a significant deviation was observed for some agglomerates. This is indicated in Fig. 3.23

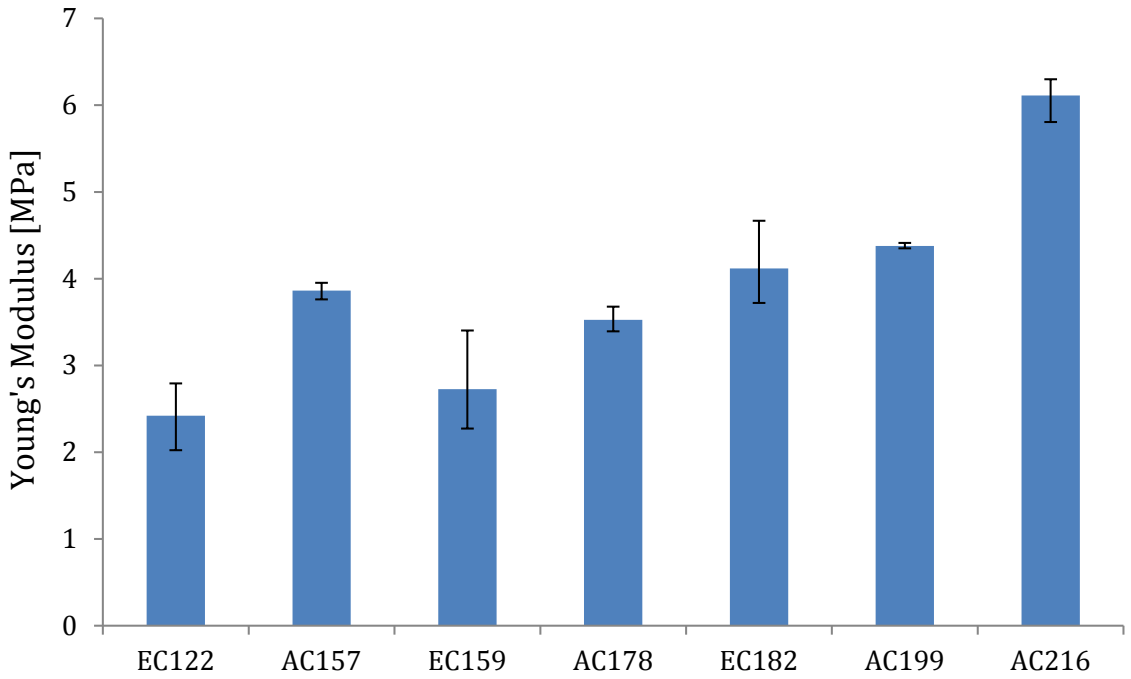

Figure 3.23: Young's modulus of each agglomerate.

Regarding the Poisson's ratio, an interesting evolution of it with strain is presented in Fig. 3.24. Similar tests were carried by Fortes and Nogueira [1989] regarding natural

cork. The Poisson's ratio, ν, was calculated considering $\nu = -\epsilon_x/\epsilon_y$, where ϵ_x and ϵ_y are the transverse and longitudinal strain, respectively. Fig. 3.20 shows the setup used to continuously record x and y coordinates of the four dots on the specimen at an acquisition rate of 5 Hz. Then, the transverse and longitudinal strains were computed by the following expressions:

$$\epsilon_x = \frac{\Delta L_x}{L_{x0}} \tag{3.12}$$

$$\epsilon_y = \frac{\Delta L_y}{L_{y0}} \tag{3.13}$$

where ΔL is the change in length and L_0 is the initial length. Given the experimental difficulties found to analyse the agglomerates, and for the sake of clearness, the results of only three materials are shown in Fig. 3.24. At the beginning of compression, the Poisson's ratio rises to approximately 0.15 for all agglomerates. As deformation takes place, and at a microscopic scale, cell walls start to buckle. Immediately, the ratio value decreases significantly. At some point, approaching densification, the ratio rises again, but is still considered a low value. In this sense, it is possible to state that there is no constant Poisson's ratio concerning cork agglomerates, as it varies with the level of deformation imposed. In addition, it can be considered that Poisson's ratio of cork agglomerates is somewhere between 0 an 0.1.

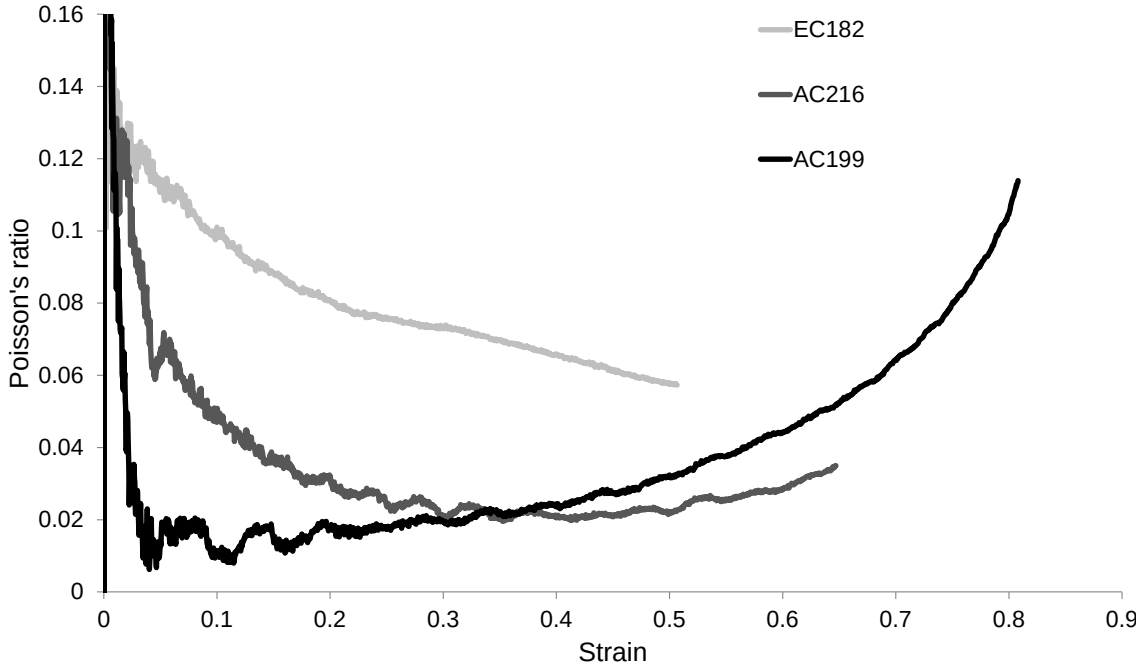

Figure 3.24: Poisson's ratio of three agglomerates.

Dynamic tests

Double impacts were also performed with the same test apparatus and conditions used in the previous phase (Fig. 3.4). The only difference is the impactor's mass. In this phase, a 10 kg steel impactor with the same geometry is used. The mass was doubled in order to

analyse the capacity of the agglomerates to withstand higher impact energies. In addition, each sample is tested twice for the same impact energy.

The average impact speed was 4.8 m/s. The samples dimensions are 120x120x25 mm. Each specimen was subjected to two impacts (with approximately 20-30 seconds interval) in order to assess the capacity of cork to keep its impact resistance during multiple impacts. This is one of the main advantages of cork relatively to EPS, which is the most used material in energy absorption applications.

However, the samples of EC122, which is the lighter agglomerate, failed to withstand second impacts. This expanded agglomerate was completely crushed after the first impact. In order to prevent damaging the accelerometer, no second impact was carried out for EC122. Thus, the results from impacts on this material were excluded. Fig. 3.25 presents the accelerations measured during both impacts for each agglomerate.

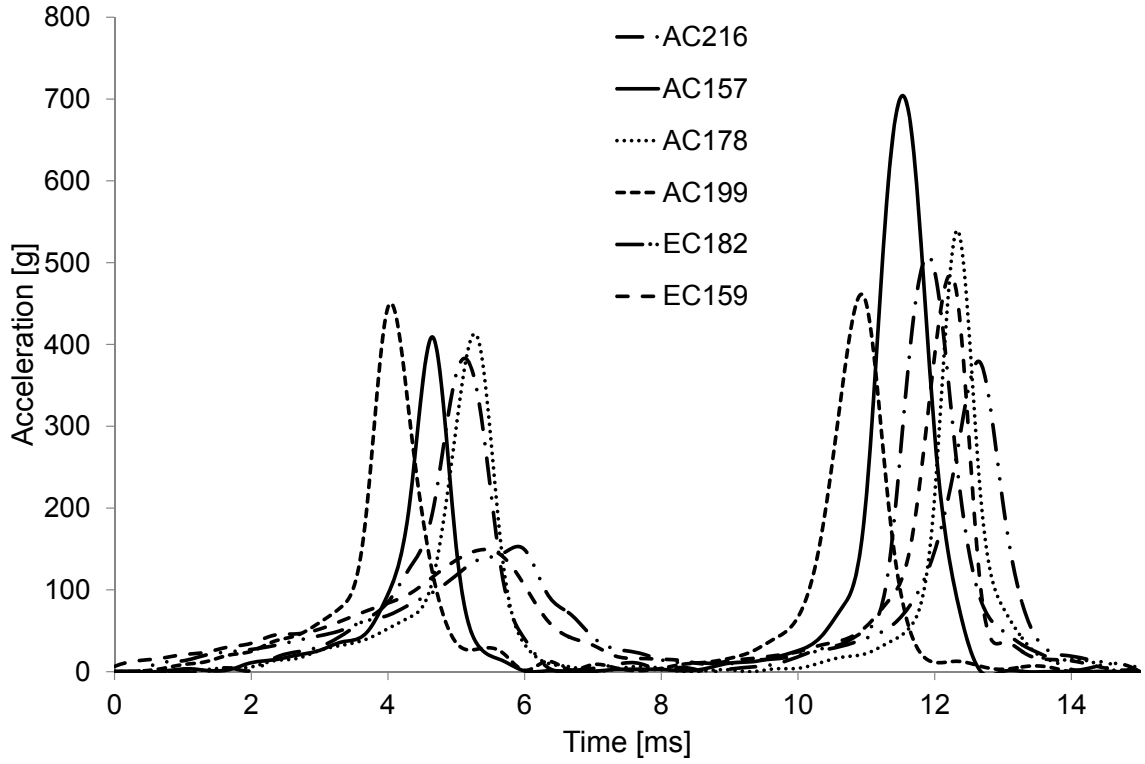

Figure 3.25: Double impact responses.

In safety applications, besides keeping its properties after multiple impacts, it is desirable that the peak acceleration remains as low as possible and the rate of deceleration is not too severe. This would imply impact curves with low peaks and large bases. From analysing Fig. 3.25, it becomes evident that expanded agglomerates performed better, having lower peak accelerations and lower deceleration rates. From this point of view, EC159 and EC182 have the best response for both the first and the second impacts. Nevertheless, it must be recalled that these conclusions hold for the specific impact energy level sustained in the performed tests.

Although the expanded cork performed better, after two impacts, the samples of this type of agglomerate were completely degraded while the non-expanded ones were intact and with an excellent recover. Thus, the number of impacts is extremely important in the case of expanded agglomerates. On the other hand, the number of impacts is almost

negligible for the agglomerated cork, as shown in table 3.9. This was the reason why EC122 was discarded from the impact tests, since it was completely destroyed after one impact.

This difference between the two types of agglomerates is explained by the manufacturing process. As already referred, no binder is added to the granules during the manufacturing of expanded cork. In addition, the high temperatures associated with its manufacturing originate some carbonized matter, typically some pieces of burnt wood, which contribute negatively to the impact performance of the material. This makes white agglomerates much more promising in applications dealing higher impact energy levels, especially if multi-impacts are expected. From this viewpoint, AC199 displays the lowest degradation in properties and the better performance during the second impact. Among these agglomerates, AC216 presents the best performance for a first impact.

Table 3.9: Mean peak acceleration during both impacts impacts.

Material	Impact	Peak acceleration [g]	Increase of peak acceleration [%]
AC157	First	408	73
	Second	703.5	
AC178	First	403.5	34
	Second	539	
AC199	First	445	2
	Second	452.5	
AC216	First	364	35
	Second	493	
EC159	First	148.5	172
	Second	404.6	
EC182	First	148.2	155
	Second	377.5	

The reported results showed that cork agglomerates can exhibit diverse material properties depending on the granule size, on the binder and even on the manufacturing method. In literature, agglomerated cork is usually referred as a single type of material. In this work, a range of agglomerated variations was studied and it was shown that its properties can indeed have significant variations and even be tailored to fit a particular application, for instance a crashworthiness application.

In a general sense, it was shown that: i) less dense agglomerates have lower Young modulus and a lower stress plateau. So, they store lower levels of energy per unit volume; ii) however, they reach densification stages later than denser samples; iii) specimens with larger granule size are much more prone to damage mechanisms; doing so, their performance during multiple solicitations (e.g., double impact) is severely compromised.

3.3 Phase III

In this last phase, the constitutive strategy used to model agglomerated cork under one impact and validated in phase I, was adopted to simulate double impacts similar to those experimentally performed in phase II. In addition, the same experiments were performed in EPS and EPP foams, which are commonly used in helmets, in order establish a comparison. Double impacts on EPS and EPP were also simulated in order to validate other material models for further use.

Thus, in this phase, it is compared the mechanical performance of cork agglomerates against synthetic materials typically used as impact energy absorbers, particularly EPS and EPP. Firstly, quasi-static compression tests are performed in order to assess the energy storage capacity and to characterise the stress-strain behaviour of the cellular materials under study. Secondly, guided drop tests are performed to study the response of these materials when subjected to multiple dynamic loading (two impacts). Thirdly, FEA is used to simulate the compressive behaviour of the studied materials under multiple dynamic loading. The work developed in this phase is already published in Fernandes et al. [2015].

3.3.1 Experimental tests

In this last phase, EPS, EPP, agglomerated cork and its expanded version were tested. EPS and EPP were tested because they are among the most popular synthetic foams employed in energy absorption applications, for instance in helmets. Thus, it is possible to carry a comparison between the most used synthetic materials in energy absorption applications and cork solutions.

In order to perform this comparison, compression tests were performed at quasi-static and dynamic strain rates. As in the previous phases, the latter are guided impact tests, using a drop tower.

Since the aim is to compare cork agglomerates against synthetic materials typically used for energy absorption in helmets, EPS with a density value of 90 kg/m^3 and EPP with densities of 60 and 90 kg/m^3 were selected. These are the density values commonly found in protective helmets. The synthetic foams were provided by Petibol company. Regarding the cork samples, considering the previous analysis, three types were selected: AC199, AC216 and EC159.

These agglomerates were selected based on their impact performance analysed in phase II. The agglomerated cork samples were chosen due to their relatively low degradation. Although AC199 has the worst impact performance for the first impact, it displays the lowest degradation in properties and the better performance during the second impact. Among these agglomerates, AC216 presents the best performance for a first impact and the second best performance in the last impact.

Overall, the expanded agglomerates presented a better performance regarding the measured accelerations. However, these were completely degraded after two impacts. Nevertheless, and since a helmet should be as light as possible, the EC159 was also selected. Overall, this was the material with best impact performance at the first impact. The cork agglomerates selected for the last testing phase are presented in Fig. 3.26.

Quasi-static compression tests

Uniaxial quasi-static compression tests were again carried out using a Shimadzu AG 50 KN testing machine with video extensometer (Figs. 3.1 and 3.20). The test conditions are exactly the same as the quasi-static compression tests performed in phase II: compression velocity of 5 mm/min, 5 samples per agglomerate with an average size of 60x60x60 mm and a stopping criterion of 6.5 MPa. Thus, in this phase, only the synthetic materials are tested. The results from these are then compared with the ones obtained in the previous phase for the selected cork agglomerates,

The output force-displacement curves allowed to compute the Young moduli and to plot the average stress-strain curves. The latter are presented in Fig. 3.27. As expected, these cellular materials exhibit a linear increase of stress for very small strains. Then, these

Figure 3.26: Cork agglomerates selected for a last round of tests.

materials exhibit a wide plateau, keeping a small stress. This plateau is the key responsible for the energy absorption capacity of cellular materials. Finally, the materials reach densification, characterised by a stress increase that occurs for a small strain variation.

The uniaxial quasi-static stress-strain curves of all the materials tested can now be compared. From a first look, it can be stated that synthetic materials have a higher Young's modulus than cork agglomerates. Also, synthetic foams present a lower slope in plateau region and a densification for higher strain values.

Once the goal is absorbing large amounts of energy, the mechanical response preferably should include a long plateau with moderate stress values, followed by densification only reached for high strains. From this point of view, and focusing only on the agglomerated cork, the AC216 is interesting because exhibits a moderate plateau stress. Nevertheless, it reaches densification sooner than the other agglomerates. On the other hand, AC199 densificates for higher strains but the plateau region has low stress values. Finally, EC159 presents a behaviour somewhere between the AC216 and the AC199. In the end, as already referred, the choice depends on the desired application and on the allowed stress level.

Regarding the synthetic foams, these exhibit high stress plateaus and densification only occurs for high strains. However, synthetic foams do not recover so well as agglomerated cork. This is demonstrated in the next section, where the response to double impacts is analysed.

Fig. 3.28 shows the average value of Young's moduli and its dispersion. These values were measured experimentally by computing the slope in the linear elastic region. According to Gibson and Ashby [1997], the most dominant factor of Young's modulus is the relative density. This is clear by analysing the different densities of the same type of material. Nevertheless, when the agglomerated cork with higher Young's modulus (the AC216)

is compared with synthetic foams, it can be seen that the latter show a much higher Young's modulus, despite having lower densities. EPS shows a higher Young's modulus and stress plateau, which indicates more energy absorbed per unit volume under quasi-static conditions.

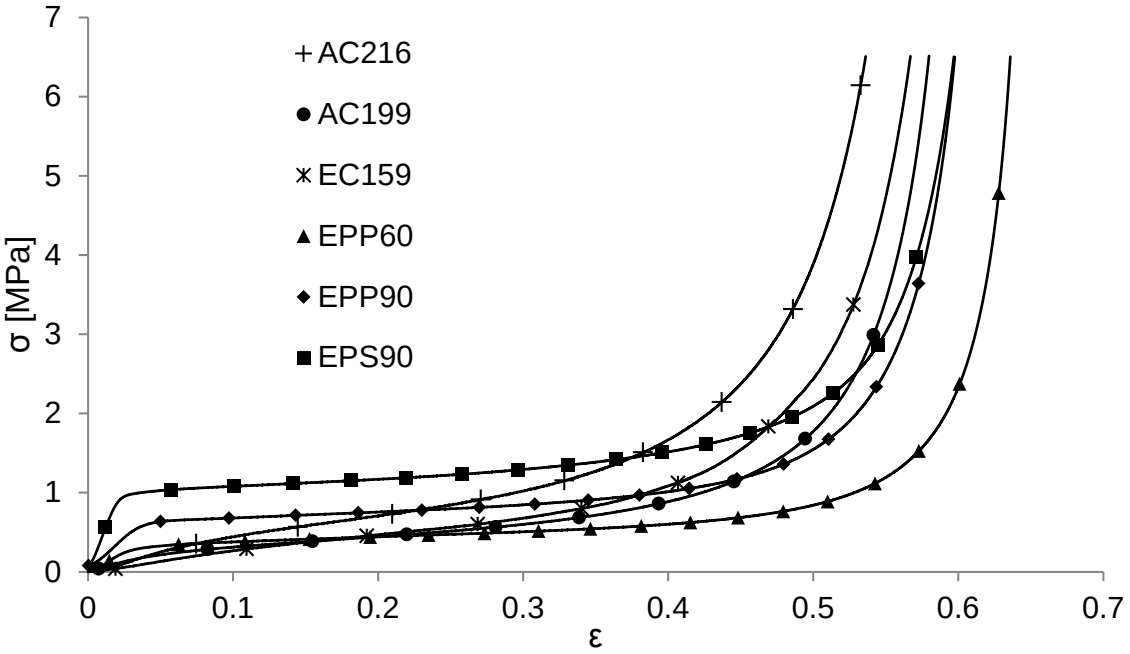

Figure 3.27: Synthetic foams and cork agglomerates stress-strain curves.

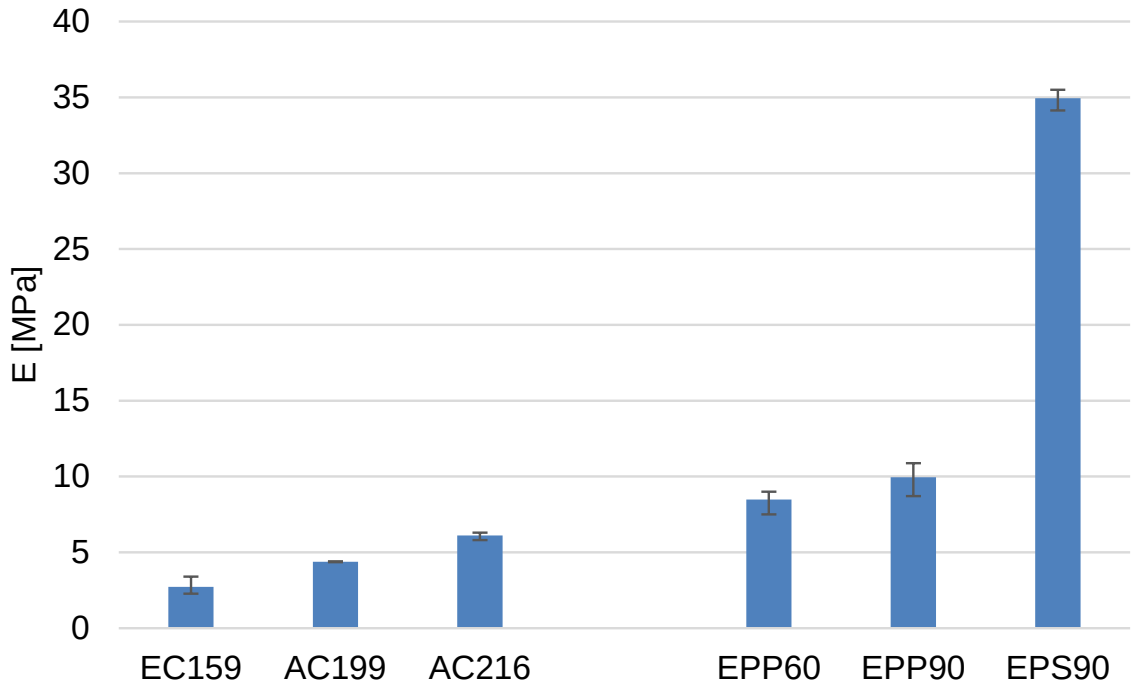

Figure 3.28: Young's modulus of cork agglomerates and synthetic foams.

Impact tests

Impact tests similar to the ones carried out in the previous phase are performed. The results from these impacts are used to further validate the material model developed in phase I. In addition, in order to compare the impact performance of cork agglomerates against the commonly used synthetic materials in helmets, EPP and EPS are also subjected to double impacts. The results from these will also be used to validate material models. These models are necessary in a following chapter.

The impacts are similar to the ones performed in phase II. However, the energy level of the impacts performed in the current phase is similar to the ones performed in the first phase. This is justified with the insecurity of testing some synthetic materials, believing that they may fail and damage the measuring system. Thus, a 5 kg impactor is used.

This is the only exception, since the test apparatus and the other test conditions are the same. The same drop tower is used and the average impact speed and the impactor's geometry are the same. In addition, the samples dimensions are also the same. These conditions are well described in section 3.2.1.

The main goal of these tests is the comparison of the agglomerated cork and the referred synthetic materials behaviour under dynamic loading. In other words, the capacity of these materials to absorb energy when continuously subjected to dynamic loading.

Fig. 3.29 presents the acceleration curves measured during both impacts. As in Fig. 3.25, the time between impacts is not real. This makes it easier to be analysed, making the plot clear and has no influence on the results. The real time between impacts is around 20 to 30 seconds. It is worth noting that the EPP60 second impact is missing in Fig. 3.29 and in table 3.10, since the first impact was more than enough to completely destroy the samples.

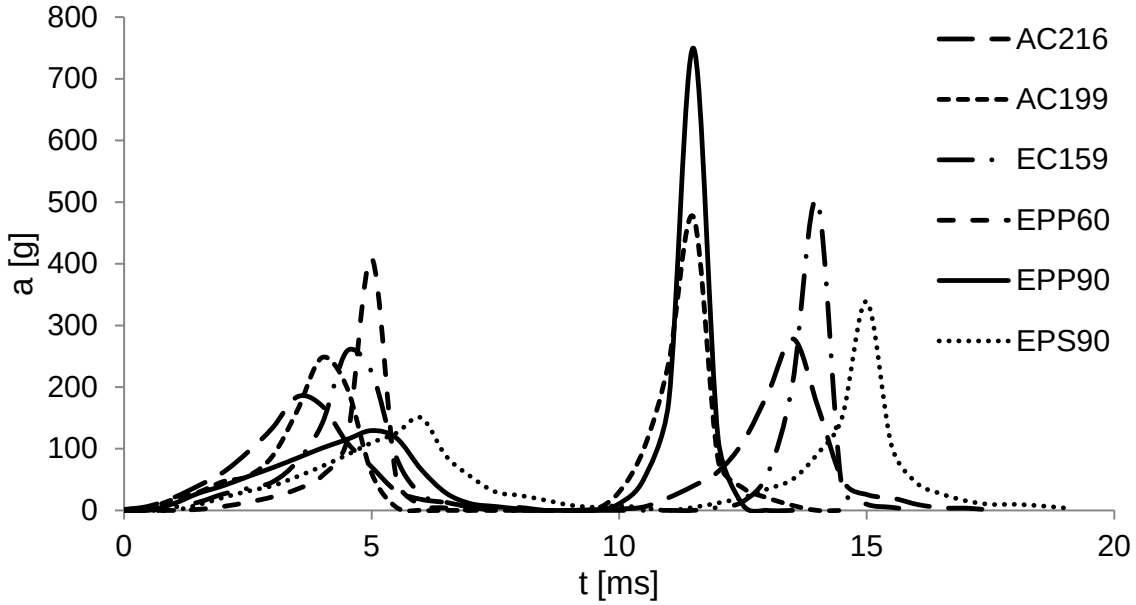

Figure 3.29: Double impacts acceleration-time history.

Fig. 3.30 and table 3.10 show that synthetic materials clearly have a higher degradation of their properties. Although it was possible to visually verify that EPP has a recovery mechanism, this is not linked to its mechanical properties, being the material with worst performance for a second impact. Thus, EPP recovery does not bring any advantage over

EPS, which has a perfectly plastic deformation outside the linear elastic zone. Nevertheless, EPP90 was the material with best response in the first impact.

EPP started to be used as liner in American football helmets due to its recovery after impact [Shuaeib et al., 2007]. However, for two impacts with an energy of 58 J, it only performed well in the first one. For the second impact, the EPS samples with the same density performed even better. Actually, this level of energy is not that severe. For instance, the single impact required from ECE 22.05 motorcycle standard is superior to 100 J. Nevertheless, the impactor used in the current experiments causes a more localised load in contrast to a helmet impact, where the shell spreads the impact over a superior area of the liner.

Table 3.10: Increase in peak acceleration between both impacts.

Material	Increase of peak acceleration [%]
AC199	85.4
AC216	34.3
EC159	37.1
EPP60	-
EPP90	491.5
EPS90	114.6

By visually comparing the tested cork samples, it is possible to conclude that there is almost none degradation of the AC216 properties, even after 4 or 5 impacts. In addition, table 3.10 indicates that this is the material with lower increase in its peak acceleration for a second impact. Further tests with different masses showed that cork agglomerates can be employed in applications with a wide range of impact energies. In the previous impact tests with a 10 kg impactor, AC199 agglomerate had a much reduced degradation of its properties, 1.7%. Also, in both second impacts with a 5 kg and a 10 kg impactor, the peak acceleration values were approximately the same.

In addition, the EC159 agglomerate presents again a noticeable degradation of its properties, but also a good first impact performance. Thus, analysing the results presented in Figs. 3.29 and 3.30 and in table 3.10, it can be concluded that AC216 was the agglomerate with best performance in both impacts. It was only slightly surpassed by EPP90 and EPS90 in the first impact. In the second impact, AC216 was by far the material with a better response. This allied with the fact that this material accumulates low amounts of damage after several impacts, makes it a promising material for application in protective helmets.

The results from quasi-static compressions performed in the previous section indicate a larger amount of energy absorbed by EPS. However, when impact situations are evaluated, some agglomerates, especially the AC216, show a much better compromise between performance and endurance under several impacts. It should be noted that helmet standards are evolving in the sense of requiring multiple impacts for certification. This can be the definitive key (along with environmental aspects) to drive a higher usage of natural cellular materials such as cork.

Thus, these results show that agglomerated cork is an excellent alternative to synthetic materials. Not only for being a natural and sustainable material but also for withstanding large amounts of energy continuously. In addition, its capacity to keep some of its initial properties after loading (regarding mechanical properties and dimensions) makes this material highly desirable for multi-impact applications.

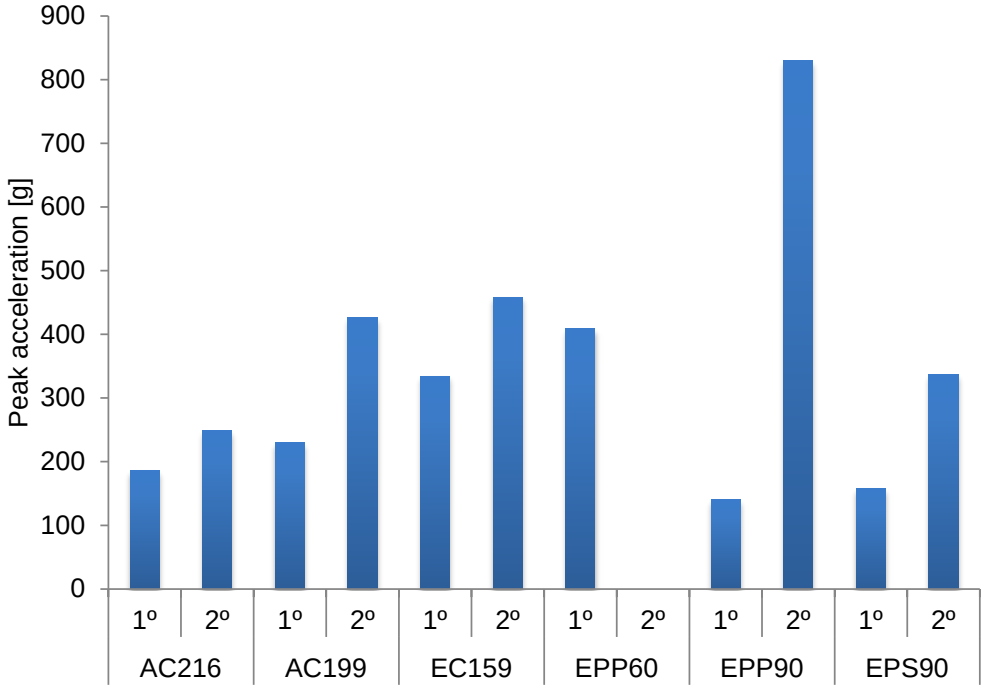

Figure 3.30: Peak acceleration from both impacts.

3.3.2 Numerical simulations

In this last phase, the validated constitutive strategy used to simulate agglomerated cork subjected to a single impact in phase I, was adopted for simulating the double impacts performed in the previous section. In addition, EPS and EPP samples, which are materials commonly used in helmets, were also tested. Thus, in order to model a material such as EPS, which presents a different behaviour from cork and EPS, a new material model must be used. This may be useful to assess helmets in an incoming chapter.

The double impacts performed were simulated using Abaqus Explicit solver. The test conditions indicated in the previous section were used as input. A friction coefficient of 0.75 was used to model the interaction between steel and EPS, as in the study carried out by Masso-Moreu and Mills et al. [2003]. The friction coefficient between steel and cork is the same one used in phase I.

As in phase I, two rigid parts were modelled, a fully constrained bottom shell that represents a steel base and a half sphere that represents the steel impactor. On the other hand, the samples were modelled as deformable bodies. The rigid impactor has just one degree of freedom, as in the experiments. The setup is shown in Fig. 3.9.

The sample was modelled with eight-node fully integrated linear brick elements. The rigid plate was modelled with rigid quadrangular elements. The hemispherical impactor was modelled with rigid triangular elements. More details about the mesh are given in table 3.11.

The meshes of each part were created always avoiding distorted and warped elements. Special attention was given to the elements size, in order to have reliable results that were not influenced by it, but at the same time to have a reasonable computational time. Regarding the mesh of the sample, several simulations were performed by increasing the number of elements until the results converged, defining the optimal number of elements.

Table 3.11: Mesh properties.

Part	Element type	Abaqus element	N° of elements	N° of nodes
Impactor	Rigid triangular shell	R3D3	1142	602
Base	Rigid quadrangular shell	R3D4	4	9
Sample	Eight-node linear brick	C3D8	17424	20250

Material modelling

Agglomerated cork and EPP were modelled as nonlinear hyperelastic materials. This simplification was considered valid due to the recovery observed experimentally. On the other hand, EPS was modelled as a nonlinear plastic material. Agglomerated cork was modelled by combining both hyperfoam and Mullins effect material models, as in phase I. This same combination was used to model EPP under compression. Parameters were optimized for each material. More information about this constitutive strategy can be found in section 3.1.2.

The EPS foam was modelled as an elasto-plastic material. The elastic part is specified as linear isotropic elasticity, basically defined by Hooke's law. In order to simulate the plastic behaviour, the crushable foam material model was employed. This model is intended for the analysis of crushable foams that are typically used as energy absorption structures. In addition, this model is typically used for foam materials that deform by developing permanent deformation.

In this plastic model, the yield surface is a von Mises circle in the deviatoric stress plane and an ellipse in the meridional (p-q) stress plane [ABAQUS, 2010]. The crushable foam model with volumetric hardening uses a yield surface with an elliptical dependence of deviatoric stress on pressure. A point on the yield ellipse in the meridional plane that represents hydrostatic tension loading is fixed and the evolution of the yield surface is driven by the volumetric compacting plastic strain [ABAQUS, 2010]. Thus, it assumes that the evolution of the yield surface is controlled by the volumetric compacting plastic strain experienced by the material. The yield surface for the volumetric hardening model is defined as:

$$F = \sqrt{q^2 + \alpha^2 (p - p_0)^2} - B = 0 \tag{3.14}$$

$p = -\frac{1}{3}\mathrm{tr}(\boldsymbol{\sigma})$ is the pressure;
$q = \sqrt{\frac{3}{2}\boldsymbol{S} : \boldsymbol{S}}$ is the von Mises stress;
$\boldsymbol{S} = \boldsymbol{\sigma} + p\mathbf{I}$ is the deviatoric stress and **I** is the identity matrix;
$B = \alpha A$ is the size of the (vertical) q-axis of the yield ellipse;
$A = \frac{p_c + p_t}{2}$ is the size of the (horizontal) p-axis of the yield ellipse;
$\alpha = B/A$ is the shape factor of the yield ellipse;
$p_0 = \frac{p_c - p_t}{2}$ is the center of the yield ellipse on the p-axis;
p_c is the yield stress in hydrostatic compression (always positive);
p_t is the strength of the material in hydrostatic tension.

The yield surface represents the von Mises circle in the deviatoric stress plane and is an ellipse on the meridional stress plane, as depicted in Fig. 3.31.

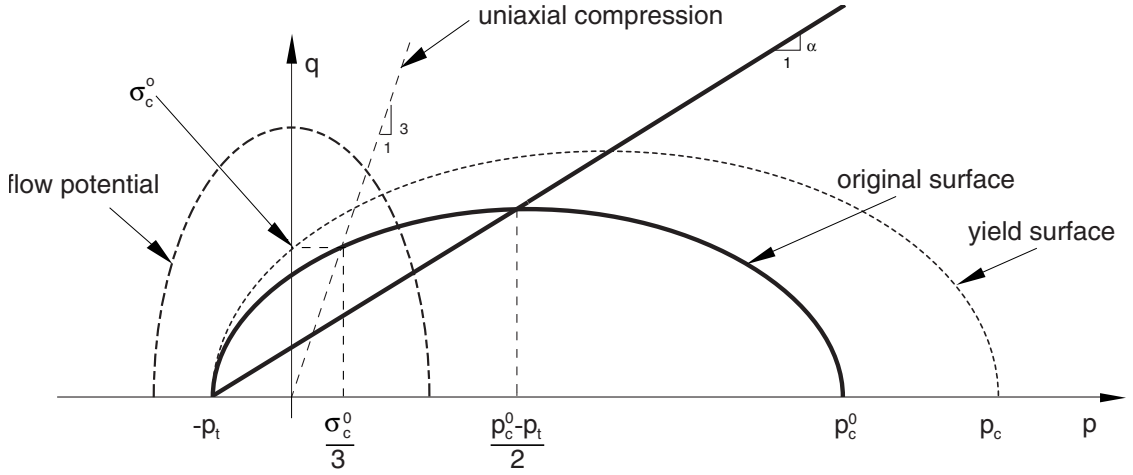

Figure 3.31: Crushable foam model with volumetric hardening: yield surface and flow potential in the p-q stress plane (adapted from ABAQUS [2010]).

The yield surface evolves with a constant α and thus, α can be computed using the initial yield stress in uniaxial compression, σ_c^0, the initial yield stress in hydrostatic compression, p_c^0 (the initial value of p_c), and the yield strength in hydrostatic tension, p_t, by:

$$\alpha = \frac{3k}{(3k_t + k)(3 - k)} \tag{3.15}$$

$$k = \frac{\sigma_c^0}{p_c^0}; k_t = \frac{p_t}{p_c^0} \tag{3.16}$$

For a valid yield surface the choice of strength ratios must be such that k has a value between 0 and 3 and k_t is positive. In order to define the shape of the yield surface, values are provided to k and k_t as input for the material model and thus, the necessary σ_c^0, p_c^0 and p_t are defined. The values here used are based in the ones determined by Mills et al. [2009a]. In addition, it is used the plastic part of the stress-strain curve obtained for EPS in a quasi-static uniaxial compression and plotted in Fig. 3.27. p_t usually have a weak effect on the numerical results unless the foam is stressed in hydrostatic tension [ABAQUS, 2010].

The other stress-strain curves presented in Fig. 3.27 were also used as input in the hyperfoam model. The strain energy potential order, N, used in hyperfoam material model was 3. This was concluded as the best value to model agglomerated cork and EPP. These and other important material properties used as input in the models are given in table 3.12.

Table 3.12: Material properties used as input in Abaqus material models.

Material	E [MPa]	ν	k_t	k	r	m	β
AC199	-	0	-	-	1.8	0.01	0.1
AC216	-	0	-	-	1.1	0.5	0.1
EC159	-	0	-	-	1.01	0.3	0.1
EPP60	-	0.04	-	-	1.01	0.01	0.1
EPP90	-	0.03	-	-	1.01	0.01	0.1
EPS90	36	0	0.1	2.5	-	-	-

Results

The results from FEA were compared against the experiments. Figs. 3.33 to 3.38 compare the impactor's acceleration-time history between experiments and simulations, for both natural and synthetic materials. An illustrative example of the difference between the two material models used is given in Fig. 3.32, showing a cut of the samples for AC216 and EPS90 at the end of simulation.

In general, the results obtained in FEA are close to the ones measured experimentally. The acceleration peaks in the simulations with AC199, AC216 and EC159 agglomerates and with both EPP60 and EPP90 are very close to the ones measured experimentally. Among these referred materials, the worst approximation was obtained in the first impact with EPP90. Regarding the impacts duration in the simulations, generally these are very similar to the ones measured experimentally, being slightly higher in some simulations. Thus, as concluded in phase I, the combination between hyperfoam and Mullins effect material models is capable of representing, with very good reliability, the behaviour of materials such as agglomerated cork and EPP.

The worst results were obtained in the simulation of EPS90. The numerical curve during both impacts is wider than the experimental one. Nevertheless, the impact duration is approximately the same for both impacts. In addition, the acceleration peaks of both impacts are reasonably represented. Thus, the results were considered good enough for further use. For instance, these validated models can be used for testing of protective helmets, saving material and time.

Therefore, it is important to consider the strain rate independence of agglomerated cork and EPS. According to Gameiro et al. [2007a], agglomerated cork is strain rate independent when compressed at dynamic strain rates, especially between 200 s^{-1} and 600 s^{-1}. Regarding EPS, there are also studies indicating its strain rate independence for dynamic regimes [Di Landro et al., 2002, Ouellet et al., 2006]. For instance, Ouellet et al. [2006] concluded that strain rate effects become pronounced only at rates above 1000 s^{-1}.

In general, the results obtained in FEA are close to the ones measured experimentally. In this sense, an accurate and reliable framework to simulate the mechanical response of natural and synthetic cellular materials was established. From the results of this chapter, agglomerated cork appears to be a completely plausible solution for protective helmets.

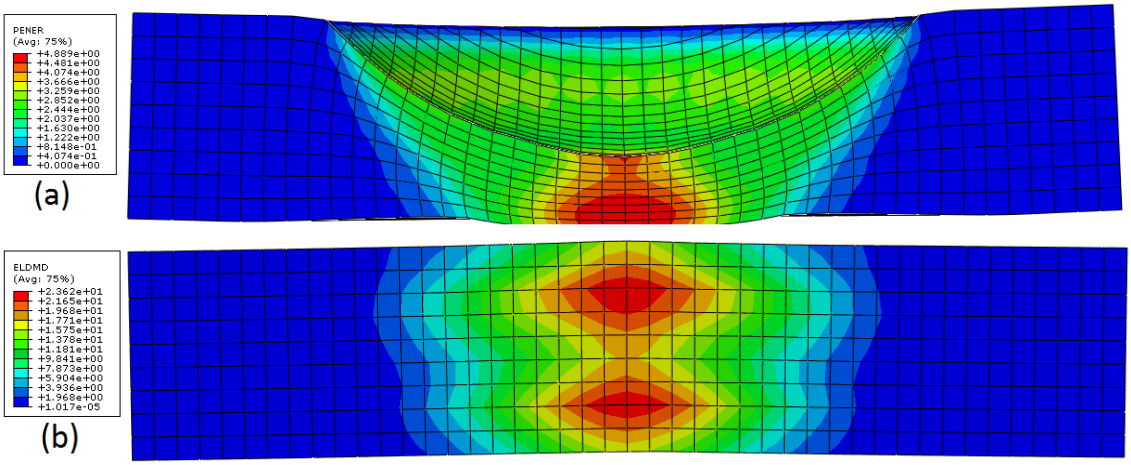

Figure 3.32: Illustration of a cut sample after two impacts: (a) EPS90 - Plastic work [mJ]; (b) AC216 - total energy dissipated in the element by damage [mJ].

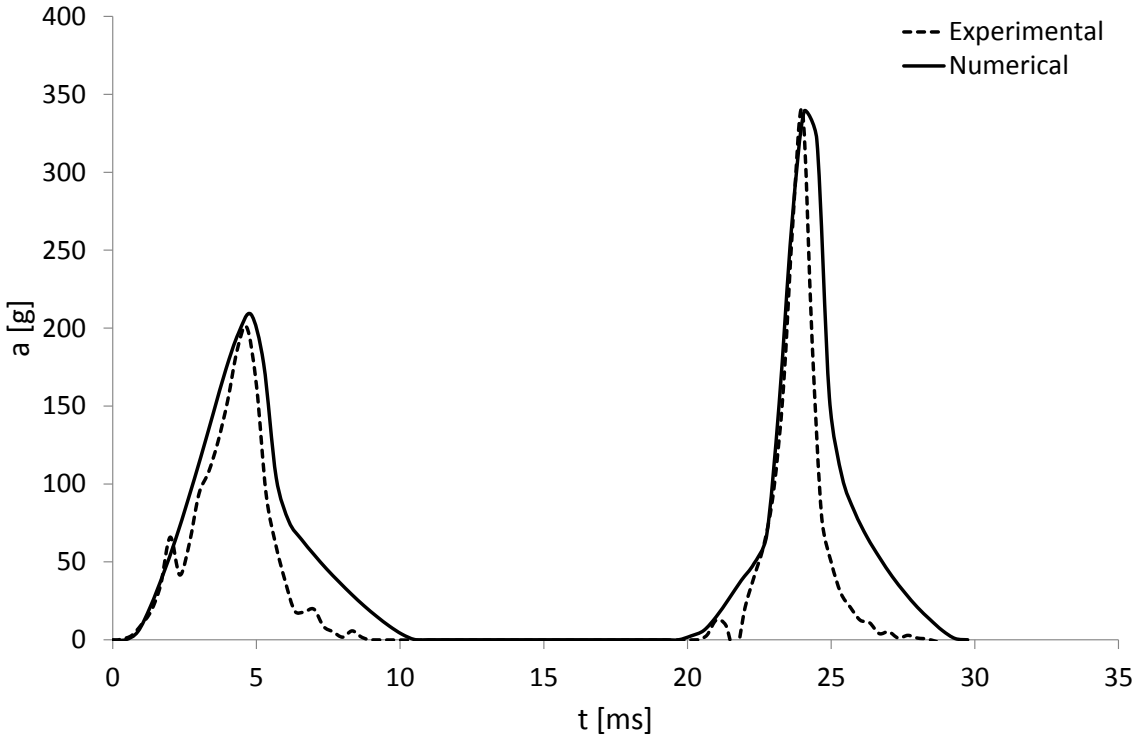

Figure 3.33: Comparison between numerical and experimental results - AC199.

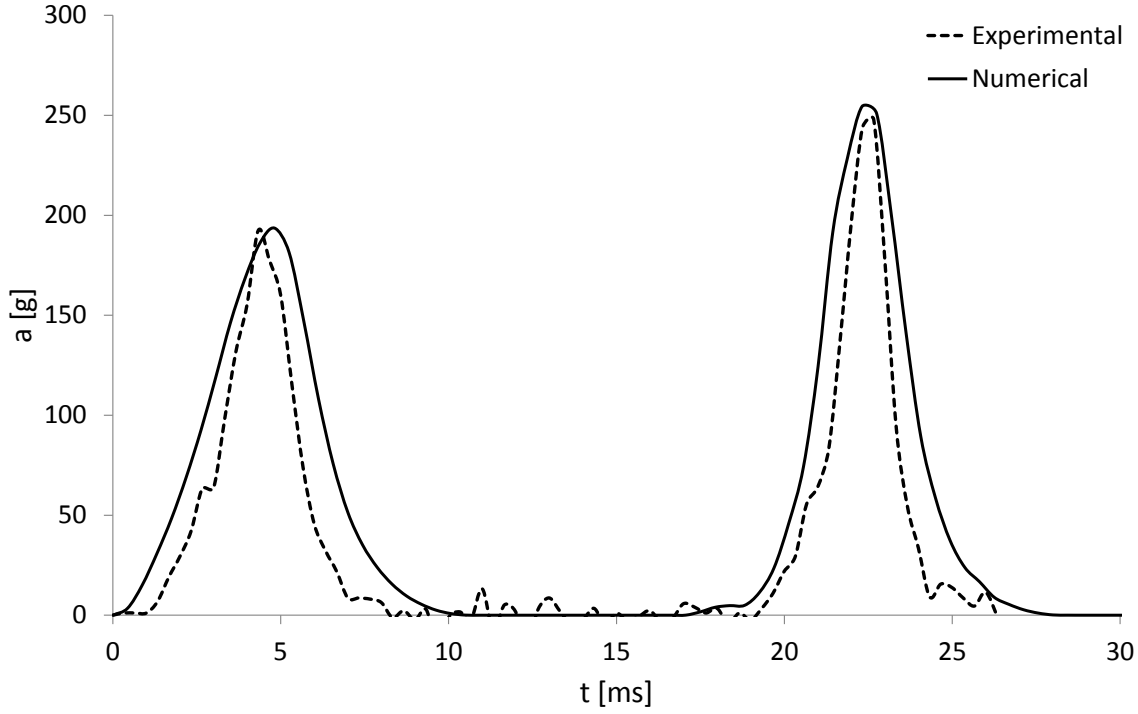

Figure 3.34: Comparison between numerical and experimental results - AC216.

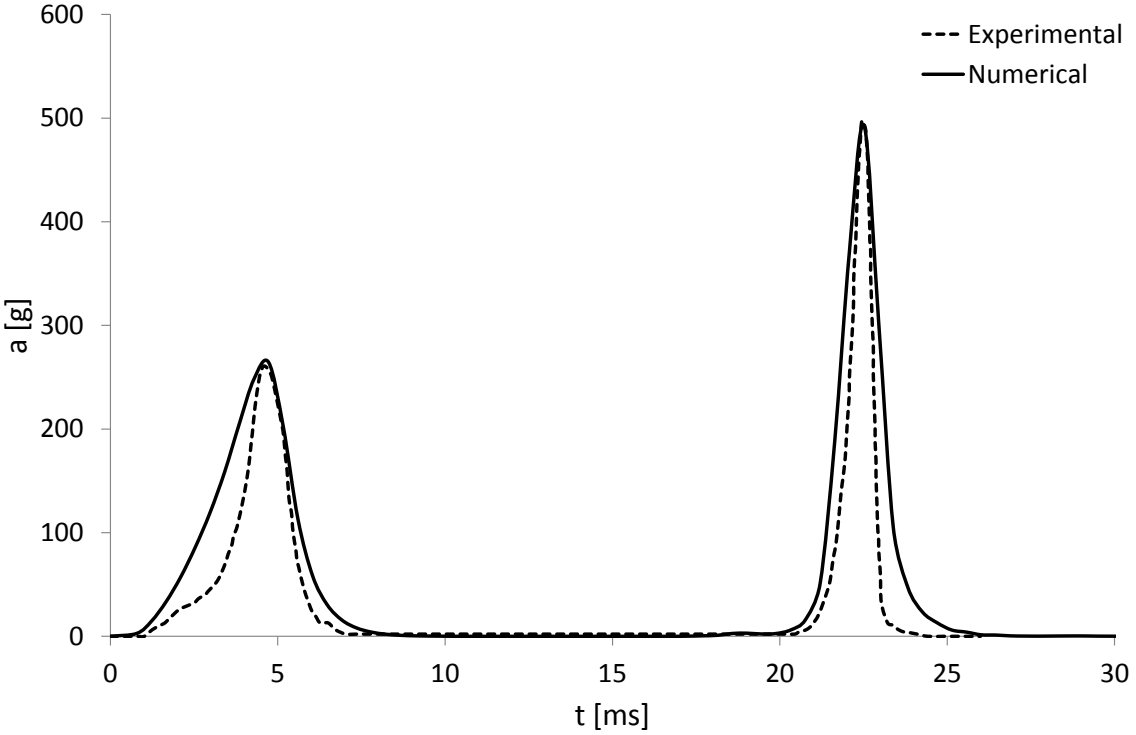

Figure 3.35: Comparison between numerical and experimental results - EC159.

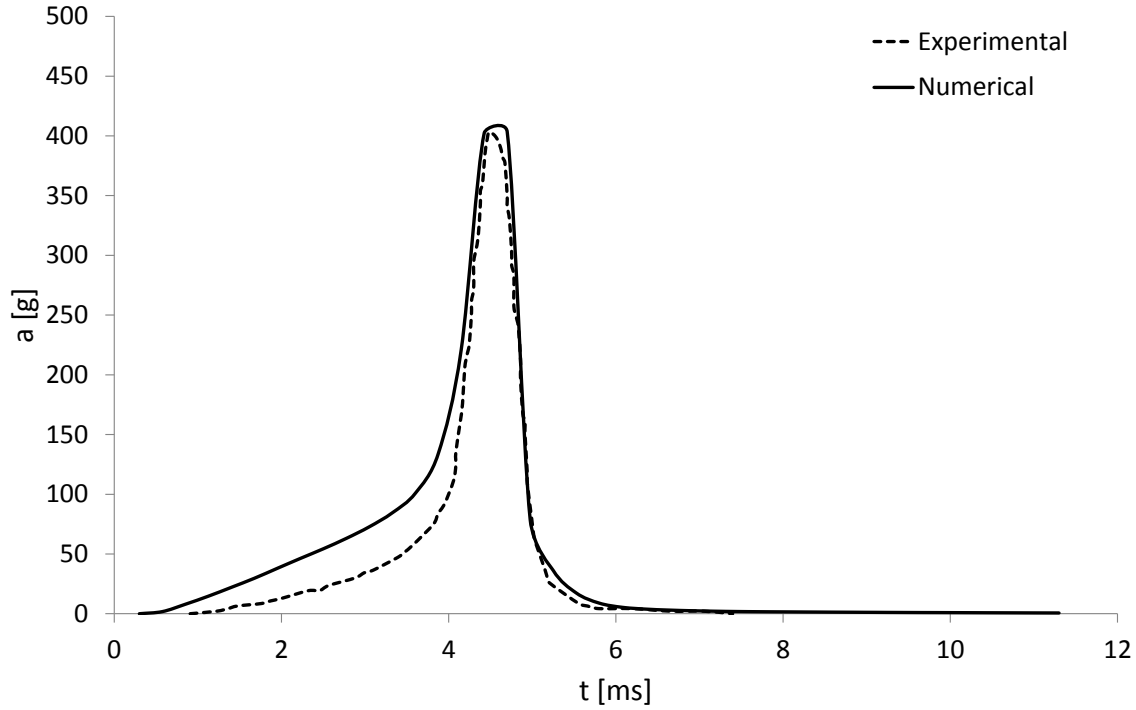

Figure 3.36: Comparison between numerical and experimental results - EPP60.

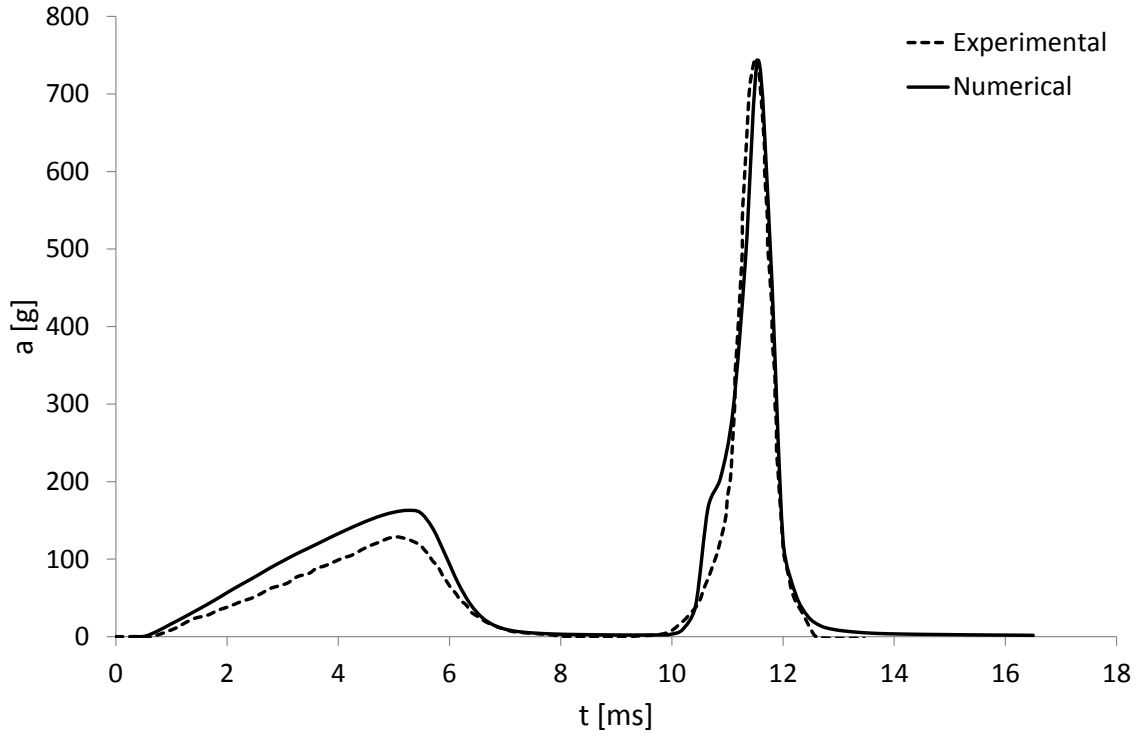

Figure 3.37: Comparison between numerical and experimental results - EPP90.

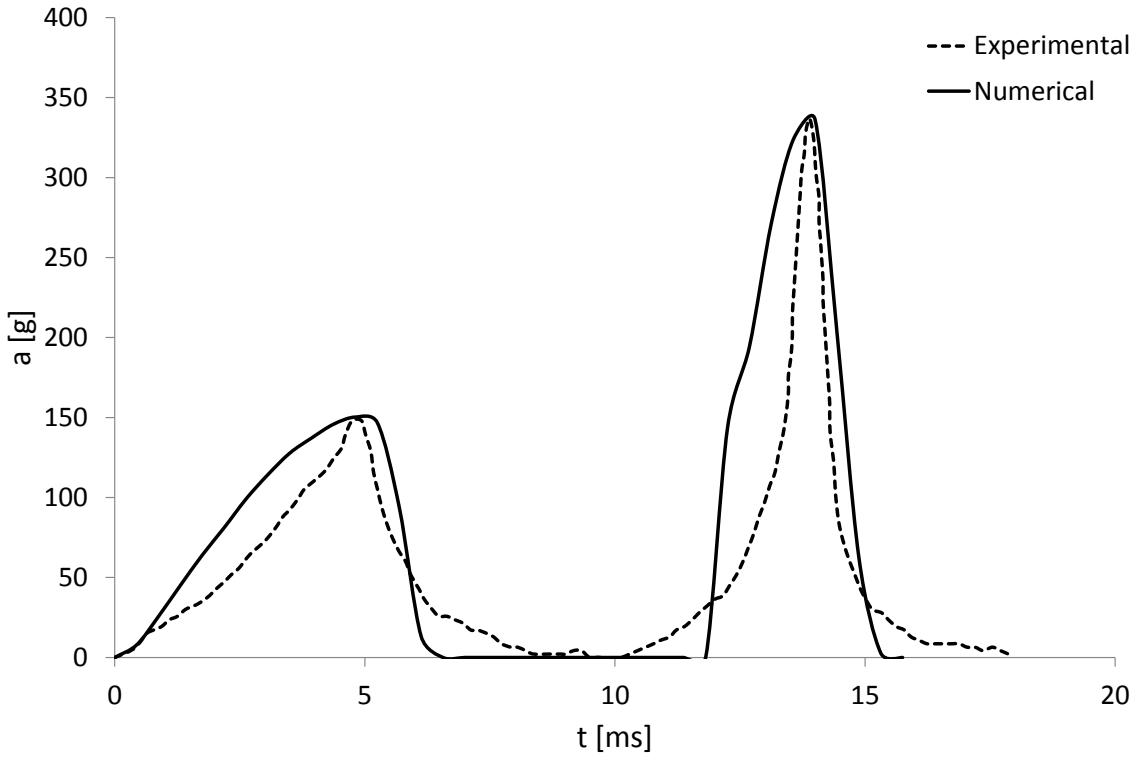

Figure 3.38: Comparison between numerical and experimental results - EPS90.

Chapter 4

Finite element head modelling

This chapter presents the modelling of a new and geometrically detailed FEHM. It is also described its validation against experimental data from impact tests on cadavers.

Traumatic brain injury (TBI) is one of the main causes of death and disability. TBI occurs when a load exceeds the brain tissue tolerance level [Fernandes and Alves de Sousa, 2015]. Road traffic accidents, sports, assaults and work and home accidents are the major sources. In some of these, the evolution of protective head gear is extremely important. One way of biomechanically optimising head protective devices is by using a finite element head model (FEHM).

Once properly validated, a FEHM is a valuable tool. It can be used in protective gear design and in the reconstruction of injurious events, by predicting brain injuries under several impact conditions. FEA allows to compute variables such as stress and strain, which would be infeasible experimentally (measuring in-vivo). Variables such as strain have been pointed out as better injury indicators than externally measured linear or angular acceleration (section 2.3.4). Due to legal and ethical reasons as well as the risk of injury, obtaining data from living human subjects is impossible. In the late 1970s, Nahum et al. [1977] performed impact experiments on cadavers. Currently, the results from this publication are still being used as reference in FEHM's validation.

In order to better understand the mechanisms of TBI, several research groups have developed FEHMs, some of them with detailed geometric descriptions of anatomical features and different material properties [Horgan and Gilchrist, 2003b, Kleiven, 2007c, Ruan and Prasad, 1995, Sahoo et al., 2014a, Takhounts et al., 2008, Yang, 2011, Zhang et al., 2011]. Detailed information about these models and the evolution of FEHMs is presented in section 2.3.5.

The first FEHMs appeared between the late 1970s and early 1980s. These were simple 2D models with some questionable results. Since then, the biomechanics of the brain for injury analysis and prevention has been a very active area of research [Miller, 2011]. With the increasing CPU power, more complex models have been developed.

More realistic 3D models were only possible in the 90s and further with the advances in computing [Horgan and Gilchrist, 2003b, Kleiven, 2007c, Mao et al., 2013, Sahoo et al., 2014a, Takhounts et al., 2008, Yang, 2011, Zhang et al., 2001a]. These are the more complex ones found in the literature. There are a great number of other models, but these

are oversimplified or not validated.

Although a great number of FEHMs exist, gyri and sulci are absent in almost all these models. In these, brain's global geometry is usually similar to spheroidal/ellipsoidal structures, without sulci and gyri. Basically, a simplified volume resembling a brain with a smooth surface. Cloots et al. [2008], using a 2D FE model, reported that gyri and sulci had a significant effect on von Mises stress maximum value. Additionally, Cloots et al. [2010] indicated that a well-defined correlation between mechanical loading and DAI using FEHM has not been achieved yet. A possible contribution to this is absence of gyri and sulci in brain models, which can play an important role in the local tissue deformations [Cloots et al., 2008, Lauret et al., 2009]. The folding structure of the brain surface and the non-uniform distribution of the CSF greatly influence both the distribution and the magnitude of the maximum stress and strains in the brain [Cloots et al., 2008, Gilchrist and O'Donoghue, 2000, Lauret et al., 2009]. In addition, Ho and Kleiven [2009] verified that strain and strain rates during impacts were both reduced in a model with sulci, especially for rotational accelerations in the sagittal plane. They also concluded that the presence of these structures should be considered in future models. Fig. 4.1 shows in detail sulci and gyri structures.

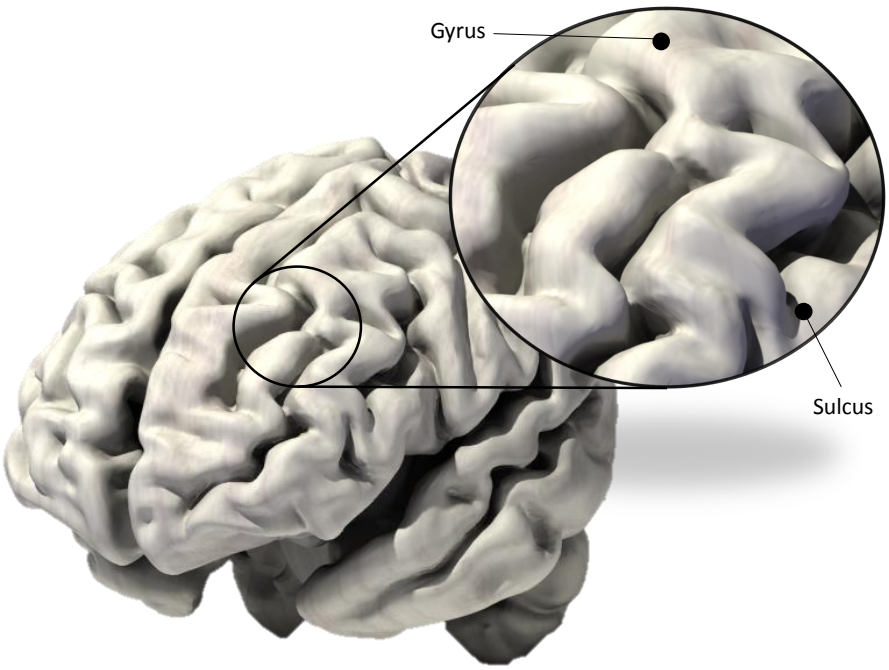

Figure 4.1: Illustration of the structures gyri and sulci.

The relative motion between skull and brain is also important to model. The majority of these models have shared or rigidly connected nodes, which influence the brain's intracranial motion. Little attention has been paid to the relative motion between structures. Supported on this, Claessens et al. [1997] created a geometrically simple FEHM where structures inside the head have the ability to move relative to one another.

Excessive relative motion between skull and brain may injure brain's surface or even the bridging veins connecting them, which may rupture under excessive loading [Horgan and Gilchrist, 2003b, Tse et al., 2014]. In addition, excessive relative motion may cause damage on the brain's surface (sulci and gyri) and even inside the brain. Cerebral contusions usually involve the surface of the brain, especially the crowns of gyri [Gurdjian et al., 1966b, Ommaya et al., 1971].

Thus, in this chapter, it is presented the modelling and validation of a FEHM with a brain model with sulci and gyri. This model will also allow the brain to move inside the skull. The model developed and validated in this work can give a great contribution in predicting brain injuries, using also proper criteria. For instance, cerebral contusions due to the geometrical detail of the brain surface. The work developed in this chapter was already accepted for publication [Fernandes et al., 2017].

4.1 Methods and Materials

In this work, a FEHM is developed. Different steps were necessary to model it: geometric modelling, material modelling, contact definition and validation. In order to validate it, the experiments performed by Nahum et al. [1977] and Hardy et al. [2001] in cadavers were simulated. These are important to validate the brain response in terms of pressure and motion, respectively.

4.1.1 Geometric modelling

In this work, the head modelled is based on medical images. These are typically used to correctly model the human body. Computer tomography (CT) and magnetic resonance imaging (MRI) are usually used to observe what is happening inside our bodies. The first technique, CT, is normally employed to observe bone structures, whereas MRI technique is suitable for soft tissues. Thus, in this work, CT and MRI were used to generate the skull's and brain's geometry, respectively.

In order to accurately generate skull's geometry, 460 images spaced 1.5 mm and obtained from CT scans were used. From this set of slices, the skull's geometry was extracted by creating a region of interest (ROI) with the Osirix software [Osirix, 2003]. This skull's ROI was created by automatic segmentation using Osirix's plug-in, MIA. Afterwards, this ROI was manually adjusted in some slices at the sagittal and coronal planes in order to improve the skull's geometry,as shown in Fig. 4.2.

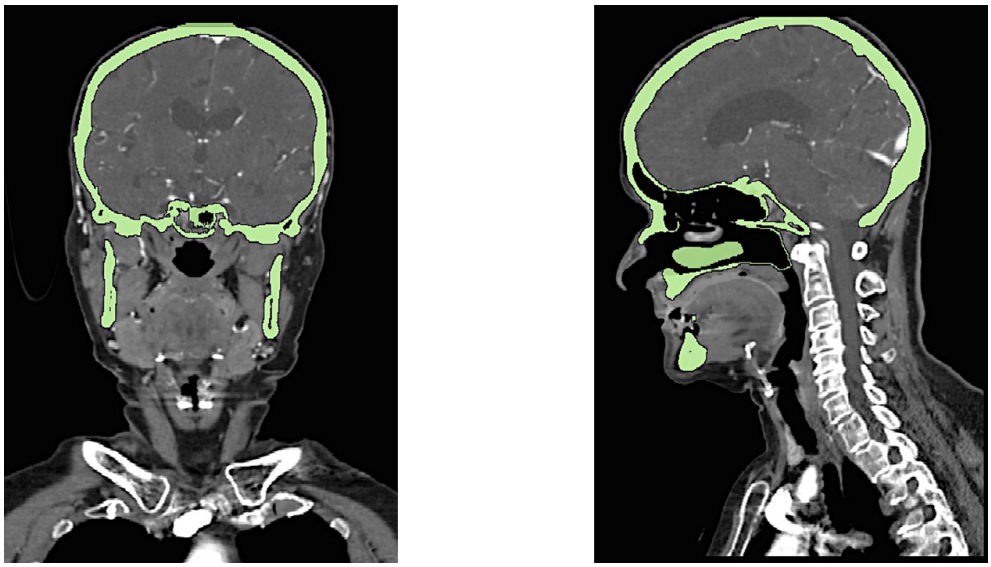

Figure 4.2: CT scans used to model the skull geometry.

Brain's geometry was generated from segmentation of MRI data, employing the same technique used for the skull. The MRI data consisted of 181 T2-weighted slices taken at 1 mm intervals in a human male head. With T2 weighted images, it was possible to distinguish the brain from the other intracranial contents. Some manual adjustments were applied at all the three planes, sagittal, coronal and axial, in order to improve the skull's geometry. Nevertheless, after manual segmentation and geometry generation, some irregularities and deviations were still present. These were lightly smoothed using Meshmixer software [Meshmixer, 2012], without compromising the model's global geometry. In addition, a software named Meshlab was also used in order to close any existing gaps in the triangular mesh of the geometric model (STereoLithography (STL) model) [Cignoni et al., 2008]. Both STL meshes have a suitable amount of triangles, generating precise geometries without overloading the computer.

These STL models were then imported to CATIA in order to create 3D solid computer-aided design (CAD) models. After successfully generating skull and brain CAD models, the space between skull and brain was used to model the cerebrospinal fluid (CSF). On other words, brain and skull models acted as "sculpting moulds" in the modelling of CSF, as shown in Fig. 4.3. Finally, these CAD models were imported into Abaqus 6.13, creating the FE meshes. Fig. 4.3 shows a summary of the methodology used to create the geometry of the YEt Another Head Model (YEAHM).

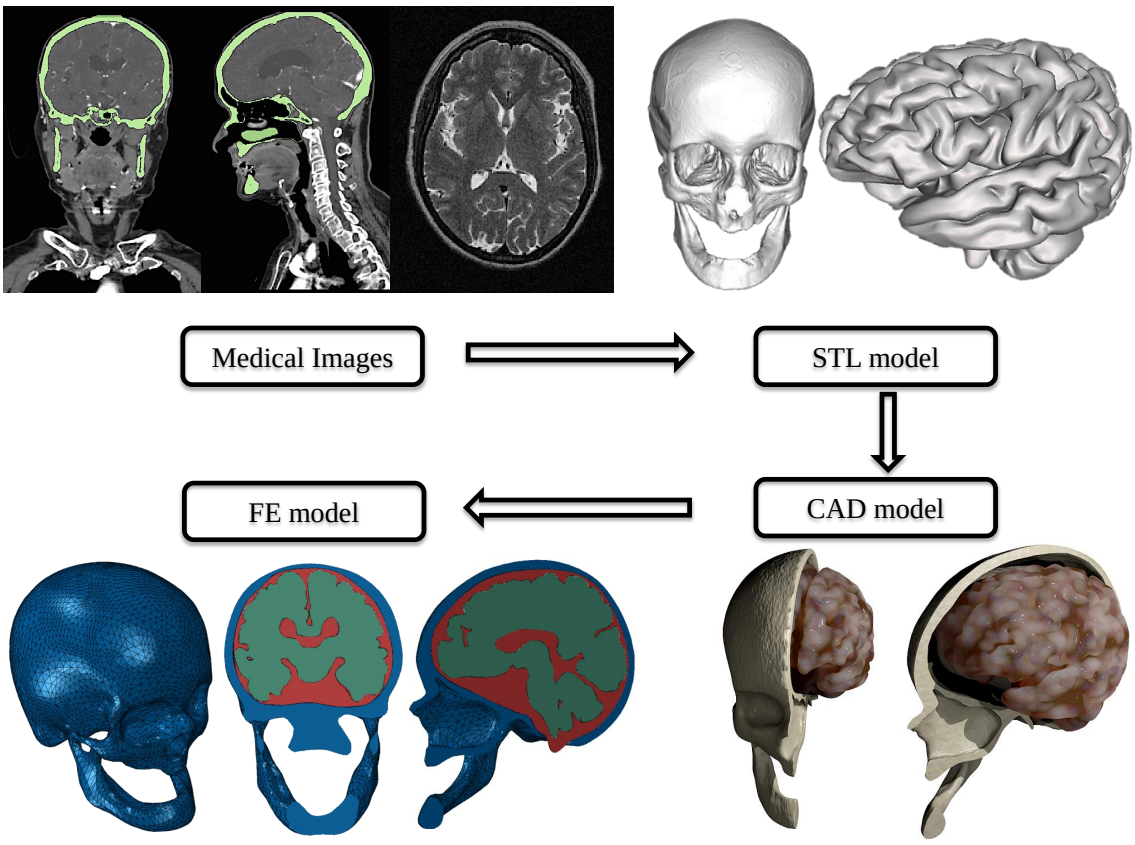

Figure 4.3: Methodology used to model YEAHM geometry.

4.1.2 Description of the YEAHM

The human brain can be simply described as a soft highly metabolically active tissue, floating in CSF within the rigid cranium [Bilston, 2011]. These protect the brain from external mechanical loads experienced by the head during normal daily life. Thus, YEAHM consists of skull, CSF and brain as shown in Fig. 4.4. This shows a cross section of the model and illustrates the anatomical features of the head.

The brain model has all important sections: frontal, parietal, temporal, and occipital lobes, both hemispheres, cerebrum, cerebellum, corpus callosum, thalamus, midbrain, and brain stem. It was not possible to separately segment CSF and structures such as membranes and bridging veins because of the resolution of MRI data. Then, a volume was created to represent all these parts between skull and brain. It was named as CSF due to its larger volume. Also, there is no consensus if cerebral vasculature should be included or not in head modelling [Ho and Kleiven, 2007, Zhang et al., 2002].

In addition, the cerebral ventricular system was also modelled and filled with CSF. The CSF is described using solid elements with a low shear modulus, as in other publications [Yang, 2011]. The global CSF model is a combination of the CFS and the meninges. For instance, the inner surface of the CSF model acts as the pia mater, surrounding the brain and dipping down into sulci and fissures and thus, acquiring the brain shape.

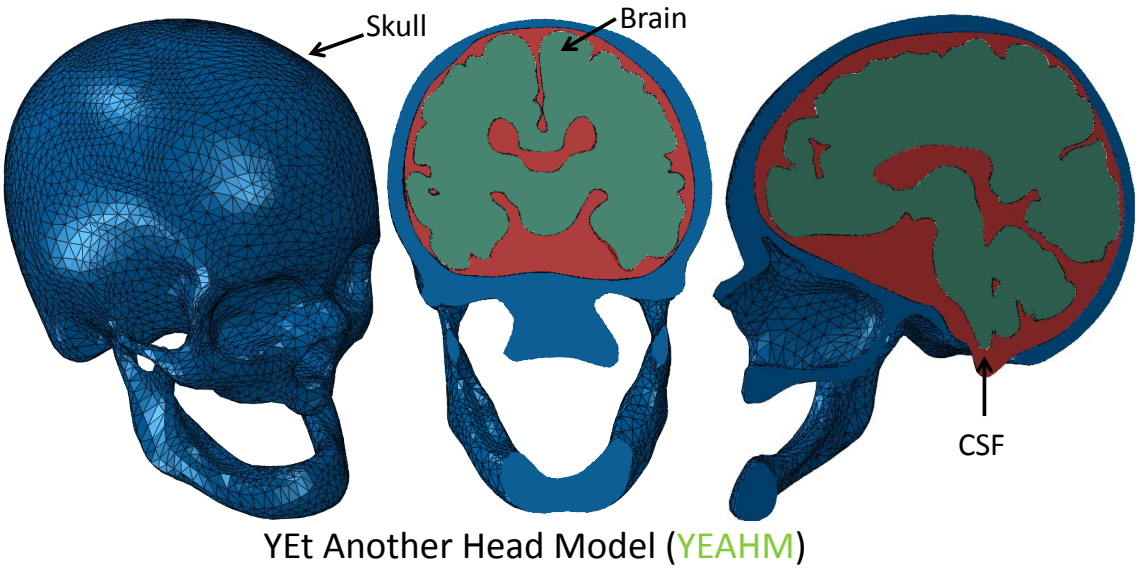

Figure 4.4: YEAHM consists of skull (blue), CSF (red) and brain (green).

The adult human skull is made up of eight bones that are rigidly connected by sutures. For this reason, there is no need to model them as separate bones. It has been reported that the skull thickness can vary from 4 to 9 mm [Kleiven, 2002, Ruan and Prasad, 2001]. YEAHM's skull has a variable thickness in this range, being geometrically accurate. In addition, most FEHMs developed so far have a skull with uniform thickness [Yang and King, 2011].

In addition to the ventricles and the skull with a variable thickness, the latter was also modelled with some of its real irregularities at the base. Ivarsson et al. [2002] indicated that the ventricles and the irregular skull base are necessary in modelling head impact, since the latter protects nerves and vessels passing through the cranial floor by reducing brain displacement. Ivarsson et al. [2002] also concluded that CSF relieves strain in regions

inferior and superior to the ventricles. This is supported by Kleiven [2005], observing also low levels of strain in the vicinity of the ventricles, probably due to strain relief around them.

All parts were modelled as solid. Due to the complex geometry of skull, brain and CSF, these were meshed with tetrahedral elements. The YEAHM is constituted by a total of 991617 elements. All YEAHM was modelled with four-node linear tetrahedron with one integration point. More details about the mesh are presented in table 4.1.

Table 4.1: YEAHM's mesh info.

Part	Number of elements	Number of nodes
Skull	57257	14443
CSF	98032	27499
Brain	836328	153749

In order to verify the mesh influence, a mesh convergence analysis was carried out by varying the mesh density. Mesh convergence is used to check how small the element size should be to ensure that simulation results are unaffected by a further refinement. Basically, ensuring the best solution and consuming the minimal computational resources as possible. The mesh was considered converged when there was a negligible change in the numerical solution with further mesh refinement. In addition, some quality mesh measures were also assessed by tools available in ABAQUS, including the aspect ratio, shape factor, tri-face corner angles and edge size. Stable time increment was always used a criterion when verifying the elements.

Special attention was also given to volumetric locking. Tetrahedral elements may show volumetric locking, especially in case of soft tissues such as the brain, which are modelled as almost incompressible materials [Miller and Chinzei, 2002]. Thus, artificial stiffening due to incompressibility was always a concern. Therefore, a very refined mesh was used.

Modelling of YEAHM is a nonlinear problem, which involves finite deformations, nonlinear material models, complex loading and boundary conditions and geometric nonlinearity. In order to perform a feasible numerical simulation, a correct geometry must be used but that is not enough. Material properties should be previously assigned to the model and special attention must be taken regarding the boundary conditions and the interactions between the various structures of the model.

4.1.3 Material modelling

Most biologic materials have nonlinear behaviour. In order to accurately simulate the brain response to loading conditions, accurate constitutive models must be used. Experimental data to identify the parameters for the constitutive models are also necessary.

The fidelity of FEHM models is highly dependent on the accuracy of the material properties used to model biological tissues [Rashid et al., 2012a]. Depending on the application, viscoelastic and even purely elastic models have been used by various research groups. The most appropriate constitutive model that can be used to describe brain tissue will depend heavily on the topic of interest [Bilston, 2011].

The characteristic time scale is very important when choosing a material model [Rashid et al., 2012a]. In the case of head impact, the duration is usually of the order of milliseconds. Therefore, brain tissue must be characterized with properties over the expected range of loading rate appropriate for potentially injurious circumstances [Rashid et al., 2012a]. Strain rates in the range of 10 - 100 s^{-1} and compressive strain levels of 10 - 50%

are the ones of direct relevance to impact injury [Bayly et al., 2006, Margulies et al., 1990, Meaney and Thibault, 1990, Morrison et al., 2006]. These are the ones used by Rashid et al. [2012a] to characterize brain tissue and used in this work to model the brain. Although the brain tissue samples tested by Rashid et al. [2012a] were from porcine, Nicolle et al. [2005] and Thibault and Margulies [1998] observed no significant difference between the mechanical properties of human and porcine brain matter. Thus, the properties of porcine brain tissue may be used in the modelling of the human brain.

Rashid et al. [2012a,b] determined the mechanical properties of fresh brain tissue by performing unconfined compression tests and tensile tests at strains rates up to 90 s^{-1} and strains up to 30% and also relaxation tests to determine the time dependent material parameters. Although these tests were performed at 23°C, the mechanical properties of brain tissue in unconfined compression are not affected significantly by variations in test temperatures (22-37°C) [Rashid et al., 2012c].

Rashid et al. [2012a] found a significant increase in elastic moduli with the increase in strain rate, which confirms rate dependency. Cheng and Bilston [2007], Tamura et al. [2007] and Pervin and Chen [2009] covered a broad range of loading rates and also found that brain tissue was strain-rate sensitive.

Failure or tissue yield in shear appears to begin at approximately 100-200% strain at low-to-moderate loading rates [Bilston et al., 2001]. This is a significantly higher strain than the one brain can withstand in tension and compression [Bilston, 2011]. Reports indicate failure for peak strains up to 30-50% and 20-60% for compression and tension, respectively [Bilston, 2011]. Thus, in this work, experimental data from compression and tensile tests were used to model the brain.

In summary, brain tissue is a very soft, strain rate sensitive, nonlinear viscoelastic material. It is usually assumed to be incompressible, or nearly incompressible, due to its very high water content [Brands et al., 2004, Miller and Chinzei, 1997]. Franceschini et al. [2006] subjected brain tissue to different conditions of hydration and verified brain's tissue incompressibility.

In this research, it is used a hyperelastic model to describe the nonlinear elasticity, combined with a viscoelastic model to describe the time-dependent behaviour. Both hyperelastic and viscoelastic material laws were already used to describe the brain's behaviour [Horgan and Gilchrist, 2003b, Miller et al., 2000, van Dommelen, 2011]. Thus, a hyper-viscoelastic material model is used to simulate brain tissue.

As for the hyperfoam model, the generic hyperelastic model is defined by a strain energy potential, also known as strain energy density function, which defines the strain energy stored in the material per unit of reference volume (initial volume) as function of the strain in the material. Each hyperelastic model has their own strain energy potential, W, from which the relationship between stress and strain tensors is derived. The strain energy function, W, is usually defined in terms of the invariants (I_1,I_2,I_3) of the strain tensor, which is itself defined by the deformation gradient tensor, $\boldsymbol{F}$. This relation is established by the left Cauchy-Green deformation tensor, $\boldsymbol{B}$:

$$\boldsymbol{B} = \boldsymbol{F}\boldsymbol{F}^T \tag{4.1}$$

The invariants of $\boldsymbol{B}$ are defined as:

$$I_1 = \mathrm{tr}(\boldsymbol{B}) = \lambda_1^2 + \lambda_2^2 + \lambda_3^2 \tag{4.2}$$

$$I_2 = \frac{1}{2}[\mathrm{tr}(\boldsymbol{B})^2 - \mathrm{tr}(\boldsymbol{B}^2)] = \lambda_1^2\lambda_2^2 + \lambda_2^2\lambda_3^2 + \lambda_1^2\lambda_3^2 \tag{4.3}$$

$$I_3 = \det\boldsymbol{B} = J^2 = (\det(\boldsymbol{F}))^2 = \lambda_1^2\lambda_2^2\lambda_3^2 \tag{4.4}$$

where λ_i are the principal stretches and J is the total volume ratio given by the determinant of the deformation gradient. The Ogden model [Ogden, 1972] has been used in the past to describe the nonlinear mechanical behaviour of the brain, as well as of other nonlinear soft tissues [Brittany and Margulies, 2006, Lin et al., 2008, Miller and Chinzei, 2002, Prange and Margulies, 2002, Velardi et al., 2006]. Soft biological tissue is often modelled with success by the Ogden hyperelastic function:

$$W = \sum_{i=1}^{N} \frac{2\mu_i}{\alpha_i^2}(\bar{\lambda}_1^{\alpha_i} + \bar{\lambda}_2^{\alpha_i} + \bar{\lambda}_3^{\alpha_i} - 3) + \sum_{i=1}^{N} \frac{1}{D_i}(J-1)^{2i} \tag{4.5}$$

where $\bar{\lambda}_i$ are the deviatoric principal stretches, which can be obtained through the relation between the total volume ratio J and the the principal stretches λ_i,

$$\bar{\lambda}_i = J^{-1/3}\lambda_i \tag{4.6}$$

N, μ_i, α_i and D_i are material parameters. The initial shear modulus can be obtained through the equation 3.5. The bulk modulus for the Ogden form is given by:

$$K_0 = \frac{2}{D_1} \tag{4.7}$$

Thus, the one-term Ogden hyperelastic function is given by:

$$W = \frac{2\mu_0}{\alpha_1^2}(\bar{\lambda}_1^{\alpha_1} + \bar{\lambda}_2^{\alpha_1} + \bar{\lambda}_3^{\alpha_1} - 3) + \frac{1}{D_1}(J-1)^2 \tag{4.8}$$

If a material is incompressible, the third strain invariant has a value of 1, and the strain energy function is only a function of the first two invariants. Thus, an isotropic hyperelastic incompressible material is characterized by a strain-energy density function W which is a function of two principal strain invariants only. The stress-strain relationship is then obtained from a partial derivative of the strain energy potential with respect to deformation gradient tensor $\boldsymbol{F}$.

The elastic and viscoelastic behaviour of brain tissue can be characterized using an Ogden based nonlinear viscoelastic model [Rashid et al., 2012a]. The relaxation response is based on a Prony series and the strain energy function is developed in the form of a convolution integral, already used by some research groups [Rashid et al., 2012a, Miller and Chinzei, 2002, Prange and Margulies, 2002].

Thus, in order to model the brain's nonlinear elasticity and the time-dependent behaviour, the one-term Ogden hyperelastic model and a Prony-series are combined:

$$W = \frac{2}{\alpha_1^2}\int_0^t [\mu(t-\tau)\frac{d}{d\tau}(\bar{\lambda}_1^{\alpha_1} + \bar{\lambda}_2^{\alpha_1} + \bar{\lambda}_3^{\alpha_1} - 3)]d\tau + \frac{1}{D_1}(J-1)^2 \tag{4.9}$$

Hence, the relaxation of the time-dependent shear modulus $\mu(t)$ to describe the viscous

response of the tissue is:

$$\mu(t) = \mu_0[1 - \sum_{k=1}^{n} g_k(1 - e^{-t/\tau_k})] \tag{4.10}$$

where μ_0 is the initial shear modulus, τ_k are the characteristic relaxation times and g_k are the relaxation coefficients, which can be determined from the experimental data.

Rashid et al. [2012a,b] estimated optimal parameters for one-term Ogden model and for Prony series, which provided an excellent fitting to the experimental data. The parameters used in this research are based on the ones determined by Rashid et al. [2012a,b]. Table 4.2 presents the values used to model the brain.

Table 4.2: Properties used to model the brain.

ρ [kg/m^3]	μ [MPa]	α_1	D_1 [MPa]	g_1	g_2	τ_1 [s]	τ_2 [s]
1040	0.012	5.0507	0.04	0.5837	0.2387	0.02571	0.02570

Mechanical properties of grey and white matter are expected to be different. Unfortunately, data reported in literature are not consistent in terms of which brain matter is stiffer than the other [Yang and King, 2011]. There is a lack of data about the mechanical properties on axonal directional dependency to justify the use of such a computationally expensive representation [Yang and King, 2011]. Limited by CPU power, it is also not practical to model individual cells and axons at this stage. As a result, most head models assume the brain to be homogeneous and isotropic [Miller et al., 2011], as in this work.

Simulations with CSF modelled as fluid were performed, but the required computational resources to simulate it were excessive. CSF was modelled as a solid with a very low shear modulus and as a hyperelastic material, using the Mooney-Rivlin strain energy potential:

$$W = C_{10}(\bar{I}_1 - 3) + C_{01}(\bar{I}_2 - 3) + \frac{1}{D_1}(J - 1)^2 \tag{4.11}$$

where W is the strain energy per unit of reference volume; C_{10}, C_{01}, and D_1 are material parameters; and $\bar{I}_1$ and $\bar{I}_2$ are the first and second deviatoric strain invariants defined as:

$$\bar{I}_1 = J^{-2/3} I_1 \tag{4.12}$$

$$\bar{I}_2 = J^{-4/3} I_2 \tag{4.13}$$

The bulk modulus can be obtained through the equation 4.7. The initial shear modulus is given by:

$$\mu_0 = 2(C_{10} + C_{01}) \tag{4.14}$$

Table 4.3 gives the values used to model the CSF. The CSF density used is the same as water since the two are similar. Regarding the values used for the C_{10}, C_{01} and D_1, these are higher than the ones typically used in the literature. This is normal since YEAHM's CSF global model needs to account for all the internal contents, except the brain. Nevertheless, the relation $C_{10} = 0.9\ C_{01}$ used by Gilchrist [2003] was here adopted.

Skull bone is usually modelled as linear elastic and isotropic material, which is considered a reasonable approximation [Kleiven, 2002]. In this work, it was also modelled as an

Table 4.3: Properties used to model the CSF.

ρ [kg/m^3]	C_{10} [MPa]	C_{01} [MPa]	D_1 [MPa]
1000	0.9	1	0.9

isotropic linear elastic material. Table 4.4 gives the values used to model the bone, where ρ, E and ν are the density, Young's modulus and Poisson's ratio, respectively.

Table 4.4: Properties used to model the skull.

ρ [kg/m^3]	E [MPa]	ν
1800	6000	0.21

Given the complexity and strong nonlinearity of brain tissue mechanical response, it is unrealistic to expect that one constitutive model will fit all circumstances. Depending on the loading regimes, specific brain tissue properties may be necessary to capture the correct response of brain tissue. Fortunately, the following tests performed in cadavers and used for validation were designed to replicate road accidents.

4.1.4 Contact and boundary conditions

During a head impact, CSF makes it possible for brain to move relatively to the skull. A great number of researchers fix the brain surface to the skull, sharing the nodes or even creating a rigid connection. This is not biofidelic and the best alternative is to allow the motion between brain and skull.

In order to correctly simulate the brain response upon impact and mimic experimental test conditions, appropriate boundary conditions must be applied. The relative motion between the skull and brain is simulated by the sliding interface between the skull and CSF and between the CSF and brain. Finite sliding formulation and kinematic contact method were used with a friction coefficient for tangential behaviour of 0.2 as used in Horgan and Gilchrist [2004] and proposed by Miller et al. [1998].

4.2 Validation of YEAHM - cadaver experiments

Over the decades, a few studies were made on human cadavers. Some of these, which are considered benchmark tests, were used in this study to validate YEAHM. Experiments from Nahum et al. [1977] and Hardy et al. [2001] were used to assess YEAHM's intracranial pressure response and brain motion, respectively.

4.2.1 Nahum et al. [1977] experiments

Nahum et al. [1977] performed impacts by submitting rigid masses travelling at a constant velocity against stationary seated unembalmed cadavers. These type of tests and data are rare due to the nature of it. Nevertheless, these tests performed by Nahum et al. [1977] are today's reference for FEHM validation.

Careful storage of this type of experimental material together with testing soon after death were necessary in order to gather useful information [Fallenstein et al., 1969, Nahum

and Smith, 1976]. Since the impacts were performed on cadavers, the authors of these experiments performed static fluid pressurization of the cranial vascular network and cerebral spinal fluid space to in vivo pressure levels at impact. According to Nahum and Smith [1976], the inability to study pathophysiologic changes and therefore, questions concerning the mechanisms of concussion are some of the disadvantages of using post mortem material. Nevertheless, the unembalmed cadaver could supply information regarding tissue changes that would be considered either lethal or reversible over an extended period of time in vivo and might be correlated with intra-operative or post mortem observations. In addition, in Nahum and Smith [1976], all of the tissue changes produced in the experimental specimens were observed in post mortem examination of in vivo head injury cases [Lindenberg et al., 1960].

In these tests, the head was not supported and it was not constrained. Thus, the head motion during impact was not influenced. The blow was delivered to the frontal bone in the mid-sagittal plane in an anterior-posterior direction. The skull was rotated forward so that the Frankfort anatomical plane was inclined 45° to the horizontal. Various padding materials were interposed between the skull and impactor to obtain the proper impact duration.

The experiment selected to validate YEAHM, experiment 37, is the most used in the literature to validate FEHMs. In addition, the subject of this experiment has the closest cranial anthropometric measurements to YEAHM. These measurements are described in table 4.5. Both, the experiment 37 and the volunteer from who the medical images were obtained, are male subjects. A lateral view of an adult human skull, indicating the Frankfort anatomical plane and the cranial landmarks used in the anthropometric measurements, is shown in Fig. 4.5.

Table 4.5: Cranial anthropometry comparison between experiment 37 and YEAHM.

Subject	Age	A[mm]	B[mm]	C[mm]	D[mm]	E[mm]	F[mm]	G[mm]	H[mm]
Exp.37	42	145	167	192	136	223	560	372	355
YEAHM	65	145	169	186	133	223	559	349	351

A - Head breadth (maximum above ears)
B - Head length (inion to glabella)
C - Head length (ophistocranon to glabella)
D - Head height (tragus to top of head)
E - Head height (gnathion to vertex)
F - Head circumference (max. forehead, over ears)
G - Head midsagittal arc length (inion to glabella)
H - Head coronal arc length (tragus to tragus)

In experiment 37, a cylindrical mass of 5.59 kg hit the subject at 9.94 m/s. Fig. 4.5 illustrates the configuration for simulation of the head impact test. The boundary conditions of simulation were defined based on test configurations. The impactor was defined as rigid, and the padding material in its front end was modelled as a linear elastic material with a Young's modulus of 6 MPa and a Poisson's ratio of 0.16.

The impact duration is so short that the neck has no effect on head response in this time window. Nahum et al. [1977] observed that dynamic pressure changes within the skull had ceased before significant rotation of the skull had occurred. Thus, a free boundary condition was assumed. ABAQUS 6.13 Explicit solver with the large deformation option was used to simulate the impacts.

The validation consists in the simulation of experiment 37 performed by Nahum et al. [1977], which is the reference for FEHMs validation. In these experiments, the input force and the intracranial pressure-time histories were recorded. Transducers were placed in the frontal bone adjacent to the impact contact area, immediately posterior and superior to the coronal and squamosal sutures respectively in the parietal bone, and inferior to the

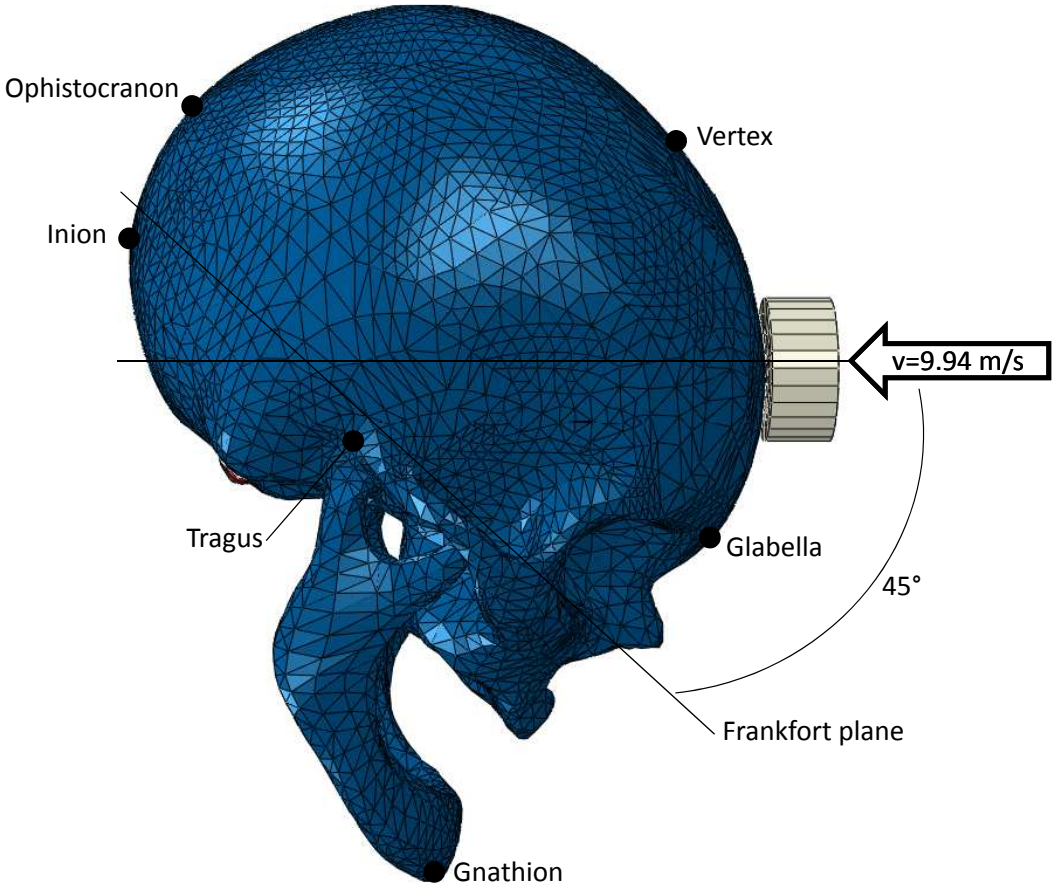

Figure 4.5: Configuration of Nahum experiment for model validation. Anatomic landmarks used in craniometric measurements.

lambdoidal suture in the occipital bone. Additionally, transducers were placed in the occipital bone at the posterior fossa. In the selected experiment, bilateral occipital pressures were also monitored. Thus, the contact force between the impactor and the head, and the pressure in five different positions were used in YEAHM's validation. An illustration of the regions used by Nahum et al. [1977] to measure the pressure is shown in Fig. 4.6.

In order to validate YEAHM, the results from simulation and from experiment 37 are compared in Figs 4.7-4.12. Figs 4.7, 4.8, 4.9, 4.10, 4.11 and 4.12 show the contact force between the impactor and the head, frontal pressure, parietal pressure, occipital pressures and posterior fossa pressure, respectively.

Nahum et al. [1977] recorded high positive peak pressures beneath the impact site in the frontal region. The same was observed in the simulations with YEAHM. The pressure decreased and eventually became negative as the area opposite to the blow was approached, which was also observed in the results of the simulations. The greatest negative pressures were generated at the posterior fossa, which due to the inclination of the skull, was the point opposite the impact site. This was also observed in the simulations with YEAHM.

There is a reasonable agreement between the results computed with YEAHM and the ones reported by Nahum et al. [1977]. In this simulation of a blunt impact to a stationary head, it was clear the faster movement from skull relatively to the brain, which originated a

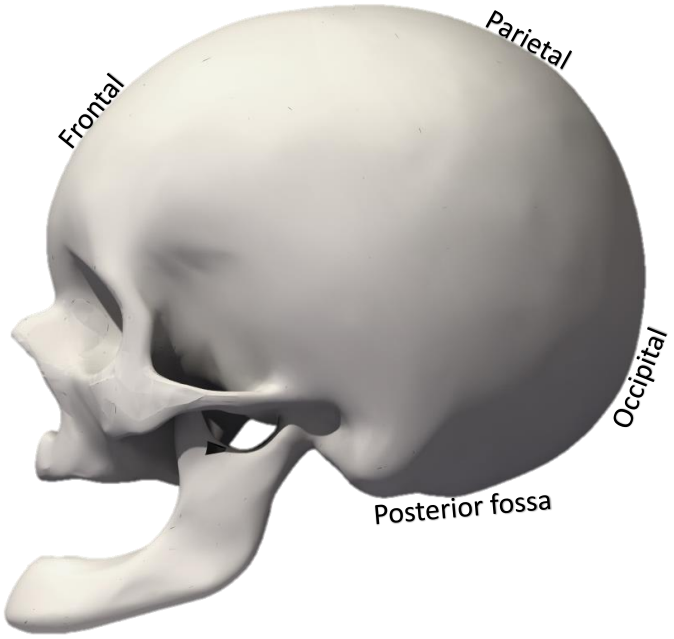

Figure 4.6: Regions where pressure was measured by Nahum et al. [1977].

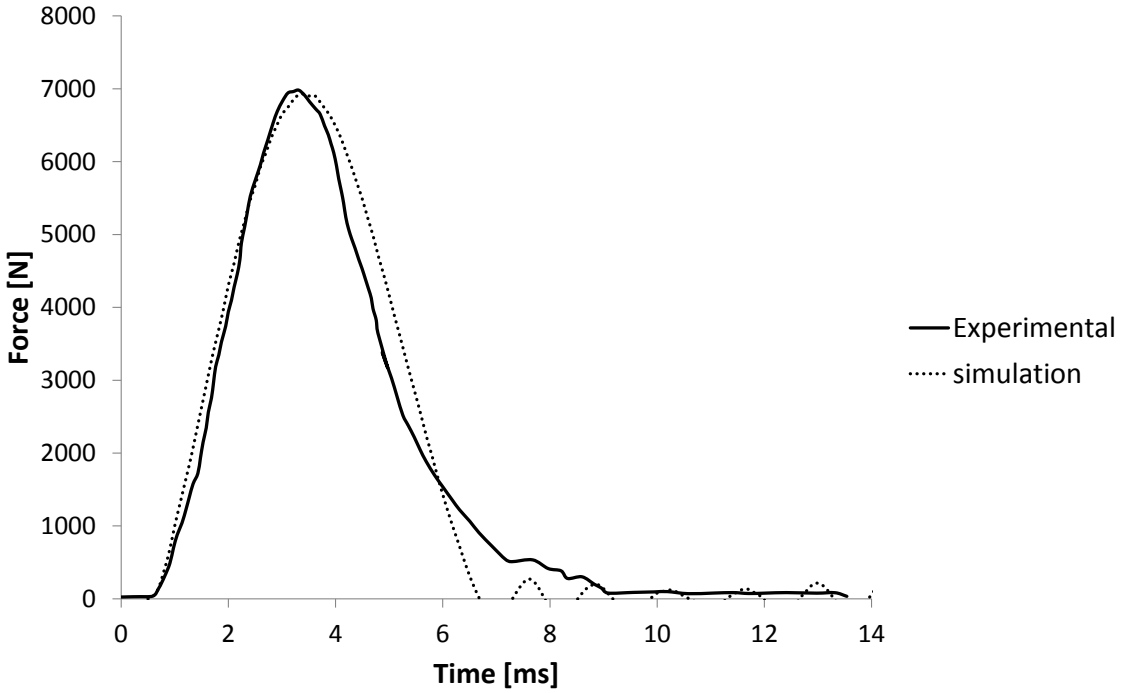

Figure 4.7: Comparison of input force between experimental and simulation results.

pressure gradient. Upon the impact, the skull and the brain tend to relatively move towards the impact site creating an area of elevated pressure where the intracranial tissues are compressed. This is known as coup and opposite to it, where brain tissues are stretched and under negative pressures, is known as contrecoup contusion [Chinn and Hynd, 2009]. Figs 4.13 and 4.14 illustrate pressure gradients across the brain, showing the coup and contrecoup phenomenons during the simulation of Nahum's experiment.

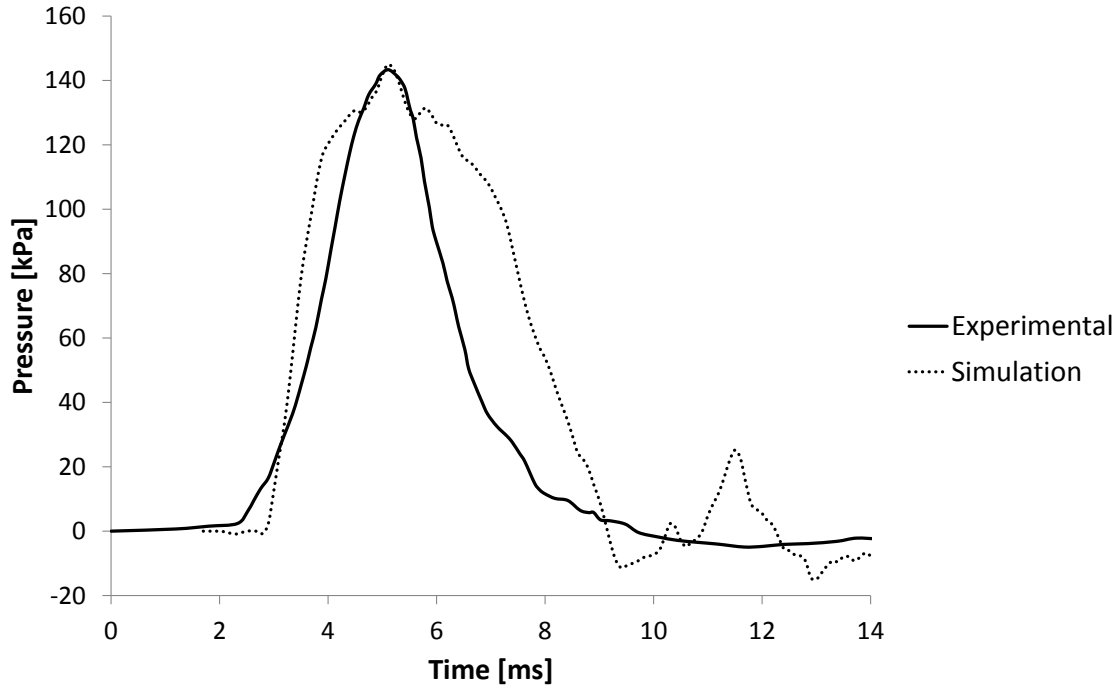

Figure 4.8: Comparison of frontal pressure between experimental and simulation results.

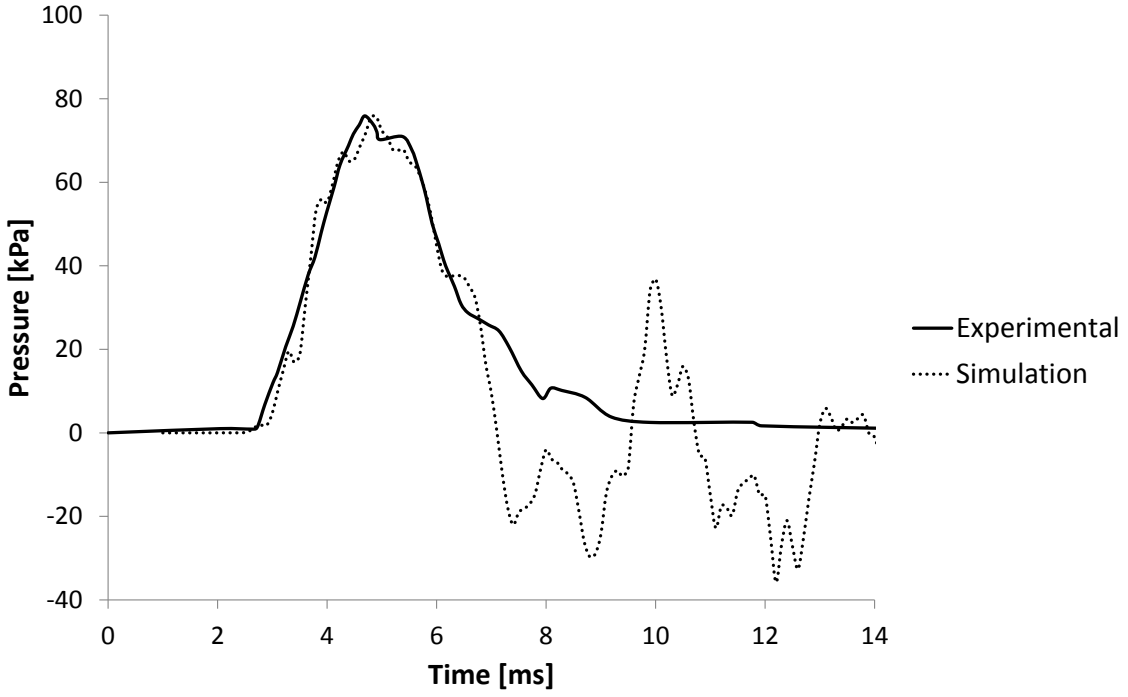

Figure 4.9: Comparison of parietal pressure between experimental and simulation results.

Some discrepancies observed in the previous figures may be explained by several factors. According to Bilston [2011], tests with fresh and post-mortem tissues may give different results. Also, some internal contents, such as the meninges, were not modelled separately, which may have influenced the results. Nevertheless, the results from the simu-

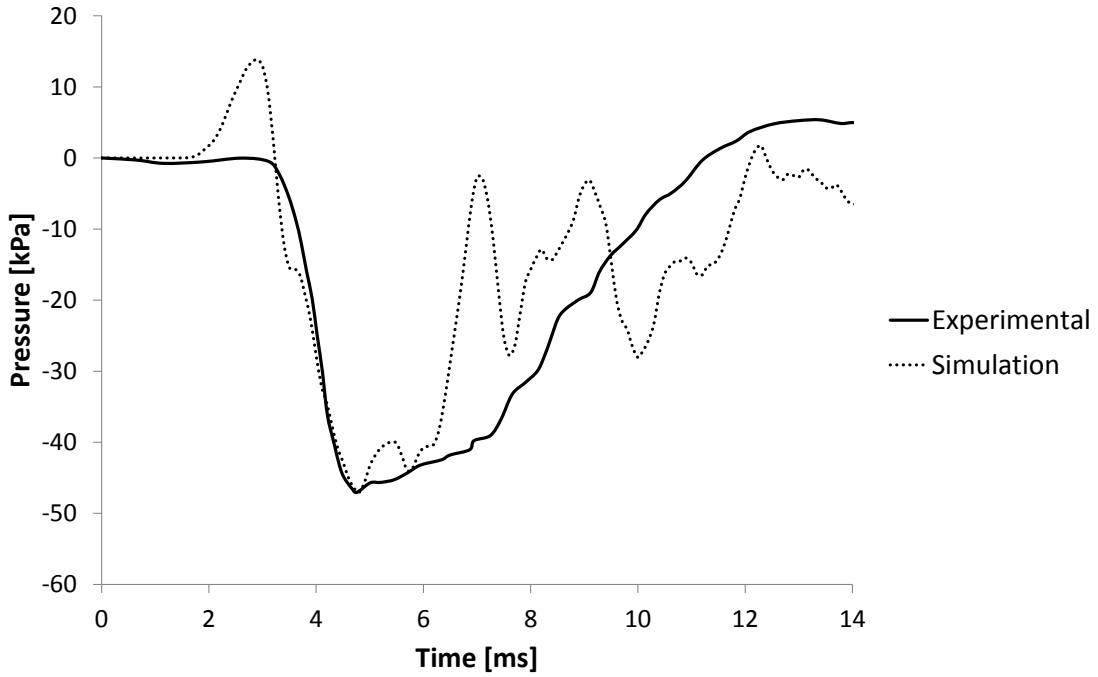

Figure 4.10: Comparison of occipital pressure between experimental and simulation results.

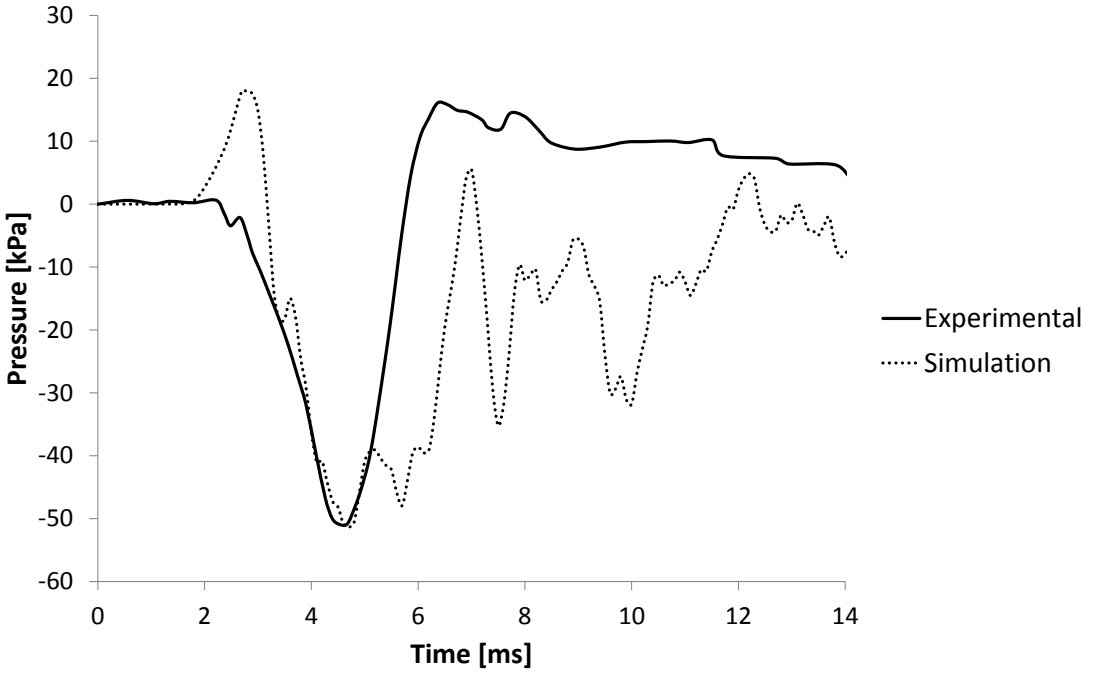

Figure 4.11: Comparison of occipital pressure between experimental and simulation results.

lations were good enough to consider YEAHM validated. Actually, comparing these results with the ones from state-of-the-art models available in the literature, the YEAHM results are quite good. Thus, the intracranial pressure of YEAHM is considered validated.

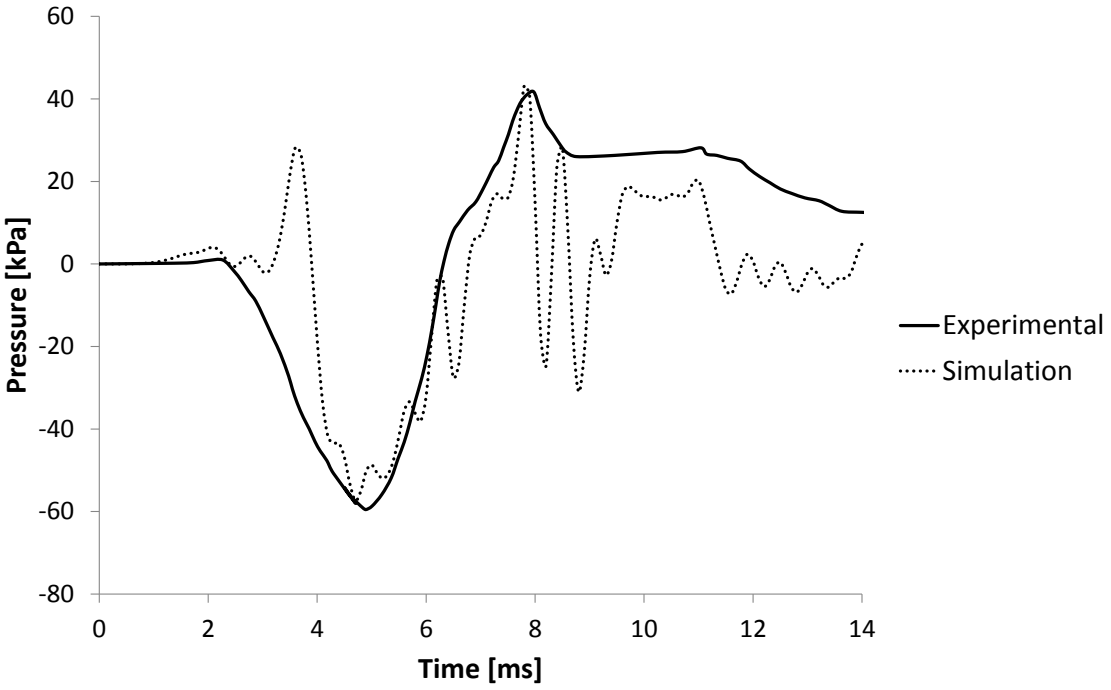

Figure 4.12: Comparison of posterior fossa pressure between experimental and simulation results.

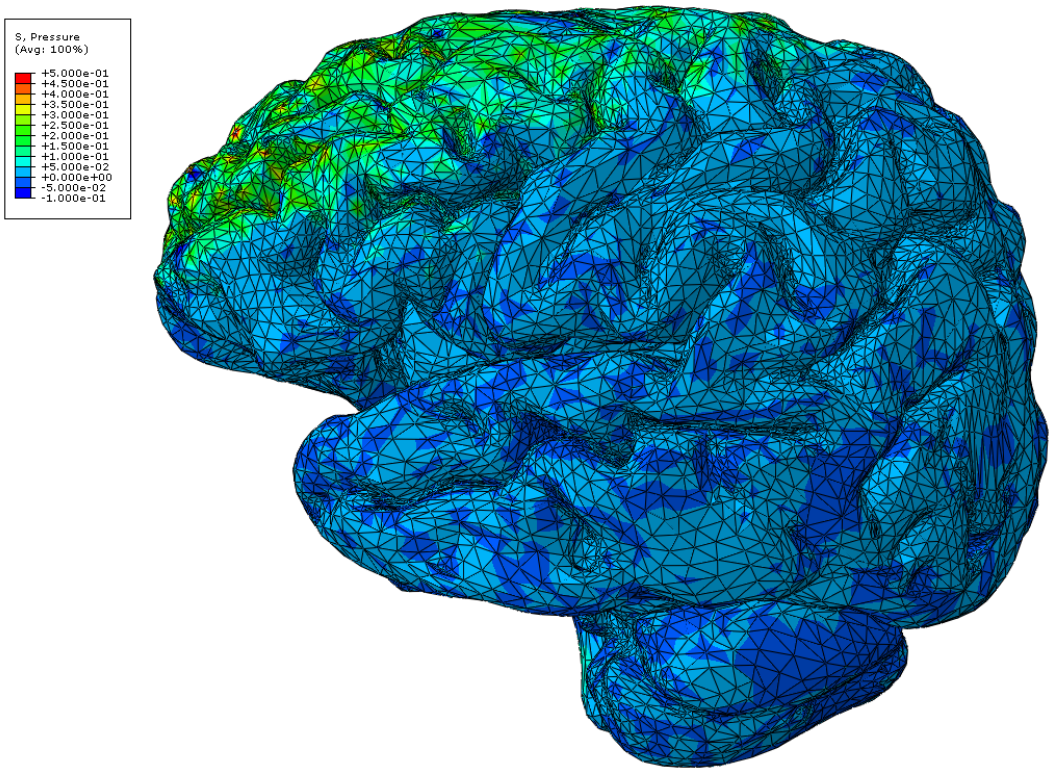

Figure 4.13: Coup phenomenon (hydrostatic pressure [MPa]).

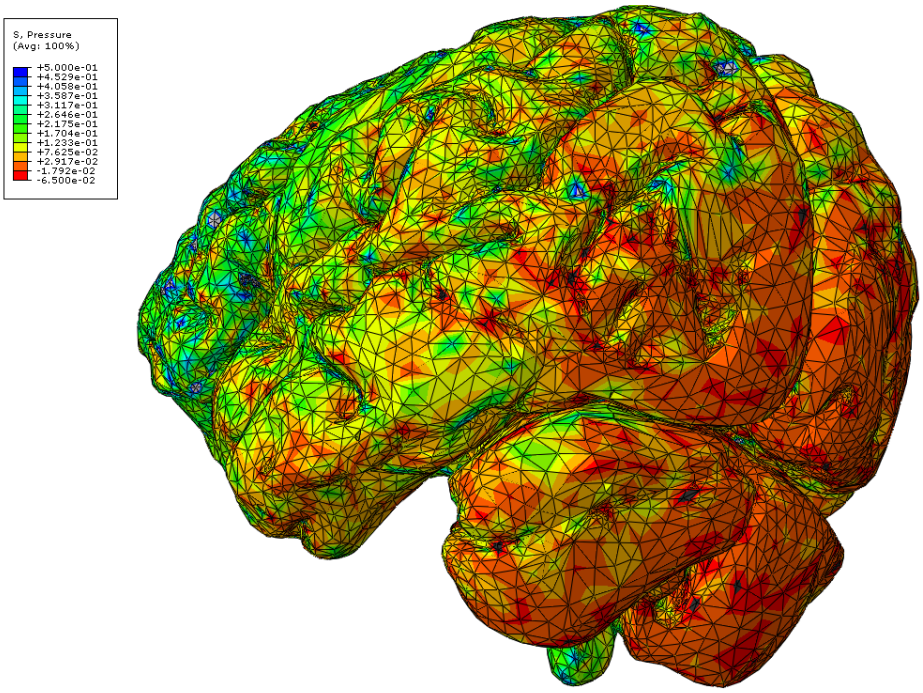

Figure 4.14: Contrecoup phenomenon (hydrostatic pressure [MPa]).

4.2.2 Hardy et al. [2001] experiments

In addition to the experiments performed by Nahum et al. [1977], experiments from Hardy et al. [2001] are also used by other authors to validate their models. This is usually done to validate the motion of the brain model. One of these experiments is the C755-T2. It is an occipital impact with a velocity of 2 m/s. In these experiments, the local brain motion was measured by tracking neutral-density targets (NDTs), using a high-speed biplanar X-ray system during different impact conditions. The NDTs were implanted in two vertical columns, a posterior and an anterior columns located at the occipito-parietal and the temporo-parietal regions respectively, as shown in Fig. 4.15. In the coronal plane, the two columns were approximately aligned with the right eye.

The head model nodes nearest located to the position of the NDTs were used to validate the brain response during numerical replication of the test. In addition, Hardy et al. [2001] measured the head kinematics (all six degrees of freedom, three components of translational and rotational acceleration) during impact. The exactly same kinematics measured by Hardy et al. [2001] during the C755-T2 experiment, were applied to the local coordinate system attached to the YEAHM's COG, which is the origin and a reference point of the skull. The latter was modelled as rigid for this validation and the local coordinate system moves with it. Modelling the skull as a rigid part in this specific case, it is considered a feasible simplification due to the absence of skull fracture and considerable deformations. In addition, the skull bone is much stiffer than brain matter and thus, modelling it with a much higher Young's modulus or as a rigid part is reasonably the same. Additionally, it is not simulated a direct impact. Instead, the translational and rotational accelerations measured by Hardy et al. [2001], were used as input for simulation of C755-T2 experiment. The data used to drive YEAHM are shown in Figs. 4.16 and 4.17.

The simulation for experiment C755-T2 was conducted and the brain motion data of the selected nodes were compared with experimental NDTs displacement. The simulation was

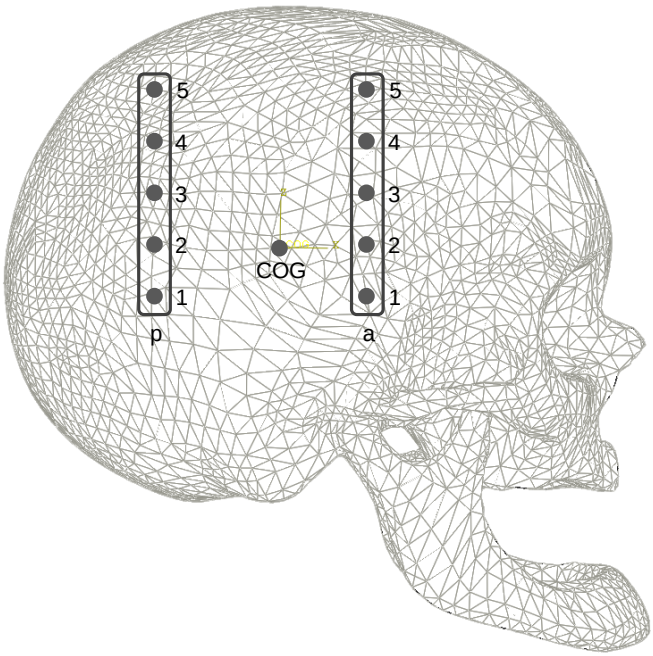

Figure 4.15: Illustration of the NDTs columns location used to track brain motion.

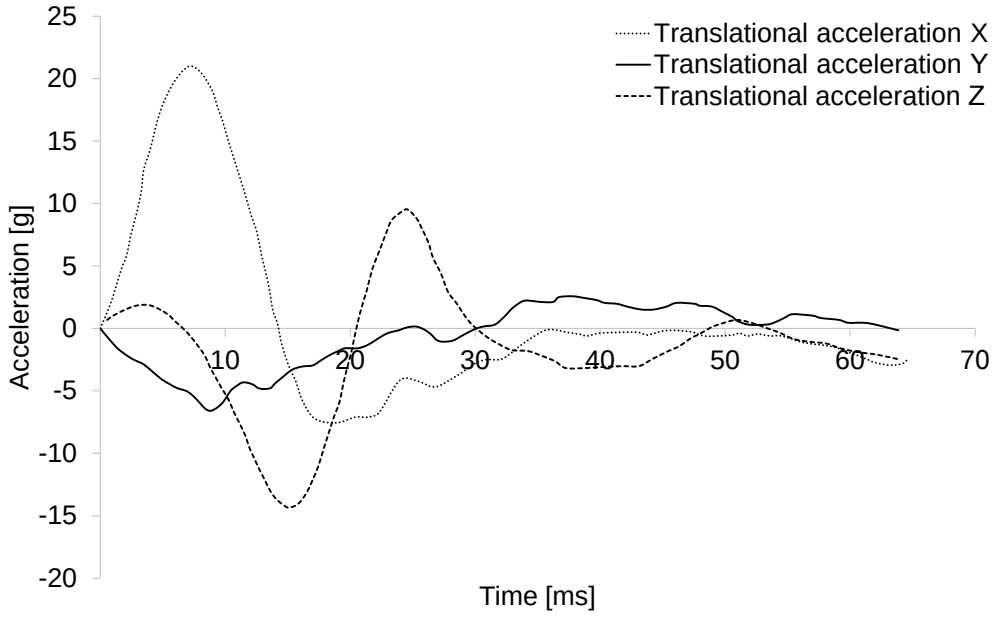

Figure 4.16: Translational acceleration used as input for simulation of C755-T2 experiment.

conducted up to a duration of 60 ms, which is the duration of the experiments performed by Hardy et al. [2001].

YEAHM has been validated against the pressure data provided by Nahum et al. [1977]. In order to further validate this model, validations were performed regarding brain motion from the experimental impacts performed in Hardy et al. [2001]. The experiment C755-T2 from Hardy et al. [2001] was replicated with YEAHM.

The brain model nearest nodes to the position of NDTs were chosen to analyse the brain motion during the simulation. The simulation for experiment C755-T2 was conducted

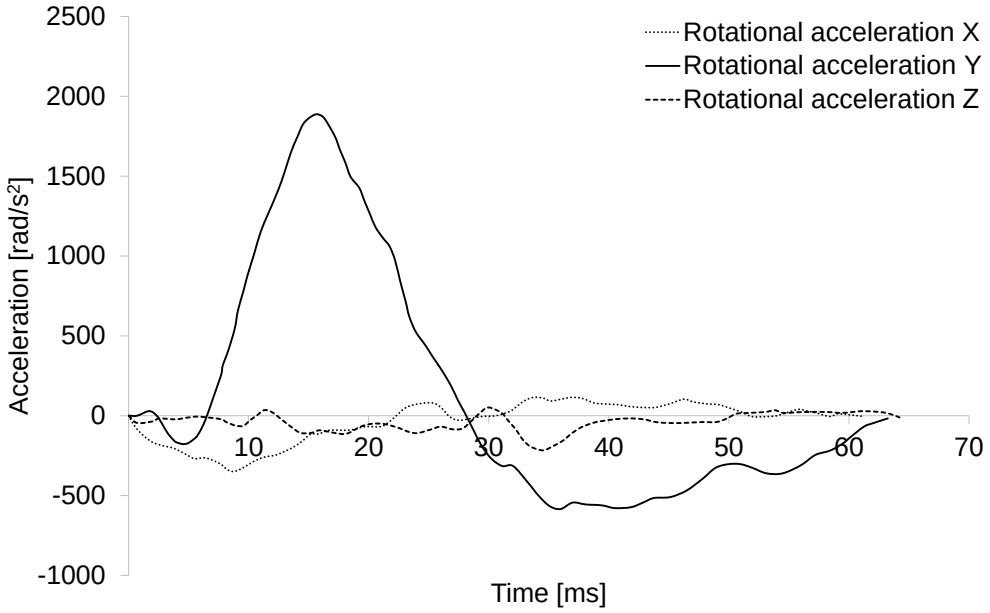

Figure 4.17: Rotational acceleration used as input for simulation of C755-T2 experiment.

and the brain motion data of selected nodes were compared with experimental NDTs relative displacement.

The simulation results for the relative displacement of five NDTs locations in X and Z directions for the occipital impact test C755-T2 and its comparison with experimental data are illustrated in Figs. 4.18 and 4.19. Fig. 4.18 shows the displacement-time history for NDTs at the temporo-parietal region. Fig. 4.19 shows the NDTs motion at the occipito-parietal location. In both figures, the left and right plots represent the NDTs relative displacement in the X and Z directions, respectively. The motion pattern of the NDTs is typically characterized by maximum and minimum displacements which lay between 20 and 40 ms.

Although there are some differences between the experiments and the results from the simulations, Figs. 4.18 and 4.19 show that simulations are in accordance with the experimental data from the NDTs. In general, the simulated relative displacements are close to the experiments or at least follow the same trend. The major discrepancies found in these simulations with YEAHM were the maximum displacements in X direction for NDTs 1 and 2 in both anterior and posterior columns. In other words, the worst results computed with YEAHM were the relative displacements in X direction for NDTs a1, a2, p1 and p2. The source of this discrepancy could be the absence of a singular model for falx cerebri and cerebelli and tentorium cerebelli, instead of modelling everything as a CSF global model.

Nevertheless, these results were considered good enough to trust on YEAHM's brain motion response. In addition, by comparing the results of YEAHM with other FEHMs available in the literature and cited as state-of-the-art models in chapter 2, excellent results were computed with YEAHM. Probably because the majority of these FEHMs have simplified brain geometries and a fixed brain surface to the skull.

In conclusion, in this chapter, a new FEHM was developed and validated against the cadaver impacts performed by Nahum et al. [1977] and Hardy et al. [2001]. This model has a geometric accurate brain model, where sulci and gyri are present. In addition, relative motion between brain and skull is also possible with this model. YEAHM, associated with suitable head injury criteria, can be used in many applications, for instance in accidents reconstruction and in the design of helmets.

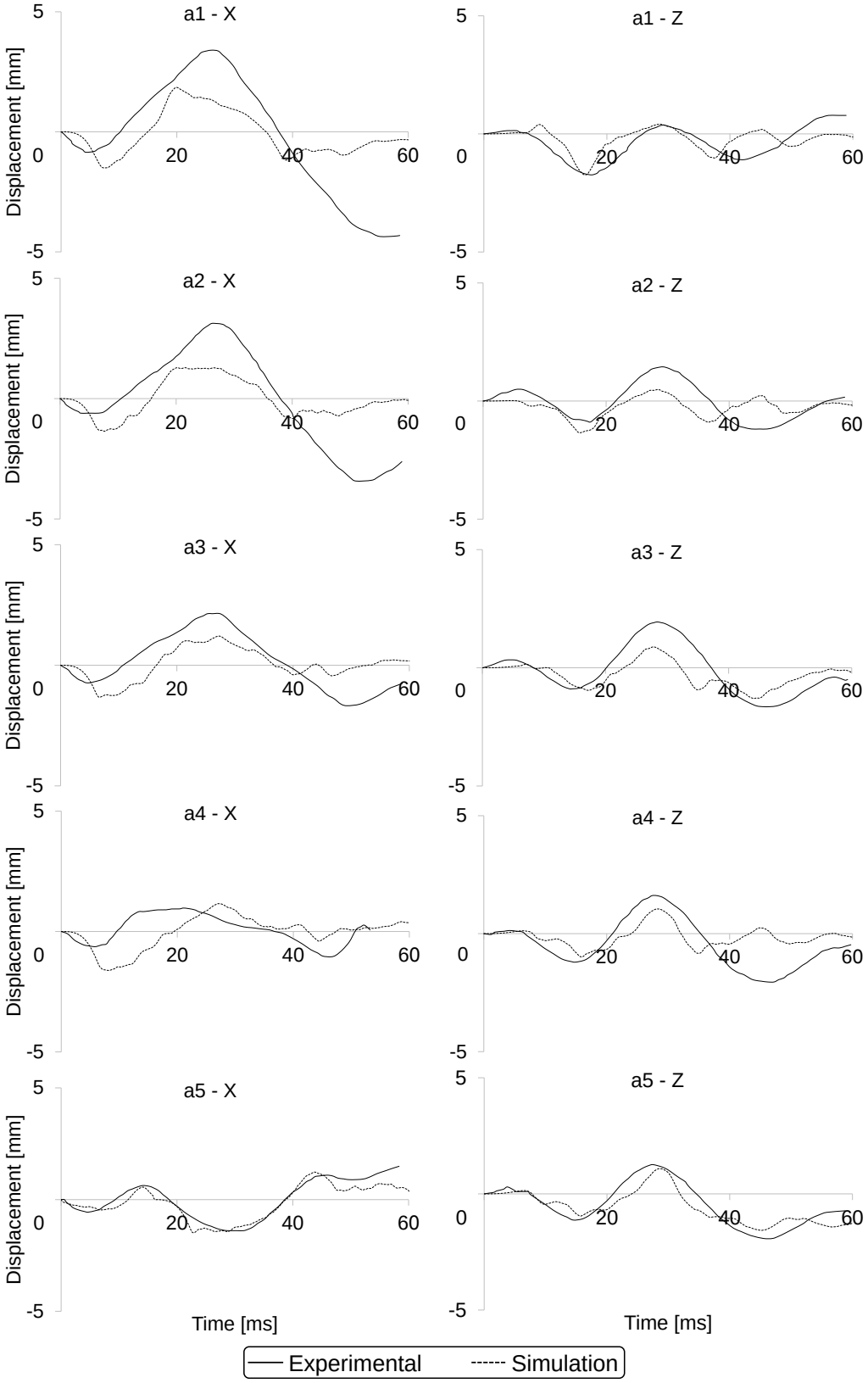

Figure 4.18: Comparison of displacement-time histories, measured by the anterior column of NDTs located at the temporo-parietal region, between C755-T2 experiment and its simulation with YEAHM.

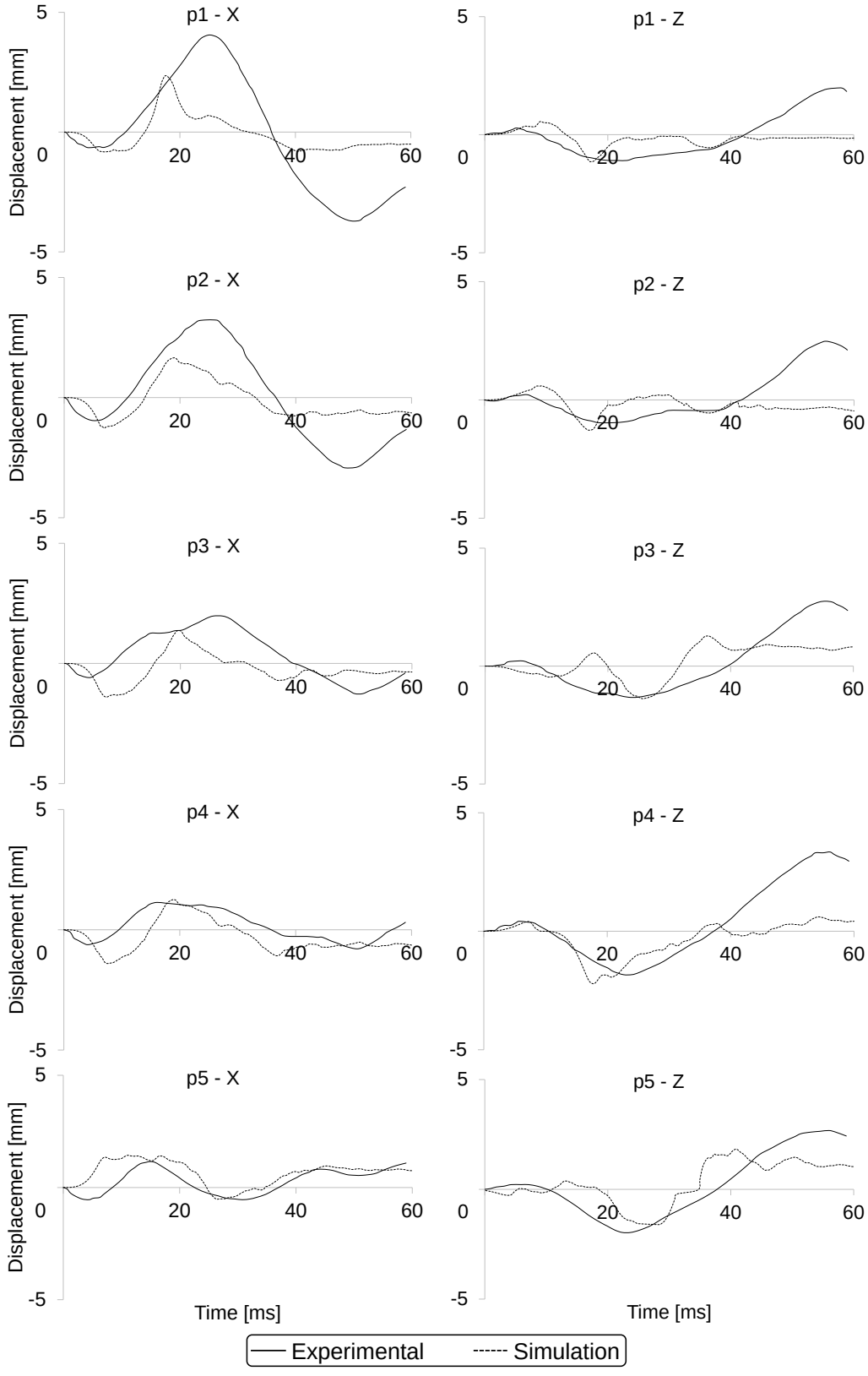

Figure 4.19: Comparison of displacement-time histories, measured by the posterior column of NDTs located at the occipito-parietal region, between C755-T2 experiment and its simulation with YEAHM.

Chapter 5

Finite element modelling and evaluation of a helmet available on the market

In this chapter, a helmet available on the market was modelled and validated in order to assess its safety performance. Additionally, a preliminary analysis is performed, by establishing a direct comparison between liners made of EPS and cork agglomerates.

In this chapter, a motorcycle helmet already certified by some standards is assessed with YEAHM. A FE model of this helmet is created and validated. The validation is performed by simulating the ECE standard impacts, the same ones used to certify the helmet. The materials used in these simulations were already validated in chapter 3. This validation regards to the acceleration measured at the headform's COG during the linear impacts defined in the ECE 22.05 standard. Additionally, the HIC values for each impact were also compared.

Nowadays, the majority of helmets standards are targeted with criticism involving their test methods and certification criteria. Some of these issues were already addressed specifically in subsection 2.2.3 and throughout the entire section 2.2. Some of these criticisms are related to the fact of only assessing linear acceleration, establishing criteria that depend on the maximum value of linear acceleration (PLA) or on the linear acceleration-time history (HIC).

For instance, motorcycle accidents involving helmeted impacts and usually resulting in severe injuries are frequently associated with rotational forces [Aare et al., 2004, Gennarelli, 1983, Otte et al., 1999]. When these forces act on the head, the results are large strains in the brain, which have been proposed as a cause of severe TBI, for instance DAI and SDH due to the tear of neuronal axons in brain tissue and the rupture of bridging veins, respectively [Gennarelli, 1983, Margulies and Thibault, 1992].

With the development of FE helmet models, it is possible to assess the influence of a large number of parameters in a way that would be extremely expensive and inflexible for experimental testing. For instance, the evaluation of different materials, if the models of these were already validated. In this study, after validating the helmet model and assessing it with YEAHM, cork agglomerates were used as liner, keeping the same conditions such

as helmet geometry and impact conditions, only changing the liner material.

These models can even be optimised according to a specific criterion. For instance, Tinard et al. [2012b] evaluated the real injury risk of a certified motorcycle helmet with a validated FEHM. In order to do this, a FE motorcycle helmet was also developed and validated [Tinard et al., 2012a]. Tinard et al. [2012b] assessed the helmet model with a FEHM and concluded that a standard-approved helmet has a significant injury risk associated. This prediction was performed by simulating the impact tests required by the ECE 22.05 standard. Then, the helmet model was optimised against biomechanical criteria, by using the FEHM rather than the standard criteria. These results showed that even if a helmet passes the impact tests required by the ECE 22.05 standard, there is a high risk of injury associated with these same impacts. Thus, from this study, it was possible to confirm the potential of FEHMs in helmet design and the problems associated with the standards criteria.

Additionally, Tinard et al. [2012b] optimised the helmet by improving the shell's geometry and changing the material, based on the FEHM predictions. A similar analysis is done in this chapter, by evaluating a standard-approved motorcycle helmet. If a significant injury risk is identified, the helmet's liner will be optimised in terms of geometry and material according to YEAHM's predictions.

Summing up, in this chapter, a commercially available helmet approved by the ECE 22.05 standard is assessed with a FEHM. In order to do this, a FE motorcycle helmet model is created. This numerical model is validated by simulating the energy absorption tests prescribed by the ECE 22.05 standard. Then, results from simulations and from experimental impact tests used to certify this helmet are compared. In addition, cork agglomerates are evaluated as helmet liners in order to establish an additional comparison with EPS. Some parts of the work developed in this chapter are already published in Fernandes and Alves de Sousa [2013b], Fernandes et al. [2013] and Ptak et al. [2016].

5.1 Materials and methods

In this work, the modular motorcycle helmet presented in Fig. 5.1 was modelled. This commercially available helmet fully meets the ECE 22.05 regulation [ECE R22.05, 2002], the U.S. Regulation DOT [U.S. Department of Transportation, 2012] and also the Brazilian Regulation NBR-7471 [ABNT, 2001].

5.1.1 Motorcycle helmet modelling

A FE model of the helmet presented in Fig. 5.1 was created. Several steps were needed before reaching this final FE model. The overall geometry of the helmet was provided by the manufacturer. Nevertheless, an arduous stage of geometric modelling was still necessary in order to have a FE mesh with a still accurate geometry. The geometry of the different parts that compose the helmet was improved in CATIA software. The final result is presented in Fig. 5.2. Then, each of theses parts was imported into Abaqus in order to be meshed.

Figs. 5.1 and 5.3 show the developed FE helmet model, which includes the shell and the different parts of the liner. The latter is divided in three parts due to assembly constraints. These parts were considered the main and most important ones regarding the helmet impact performance.

Figure 5.1: Certified motorcycle helmet and the developed FE model.

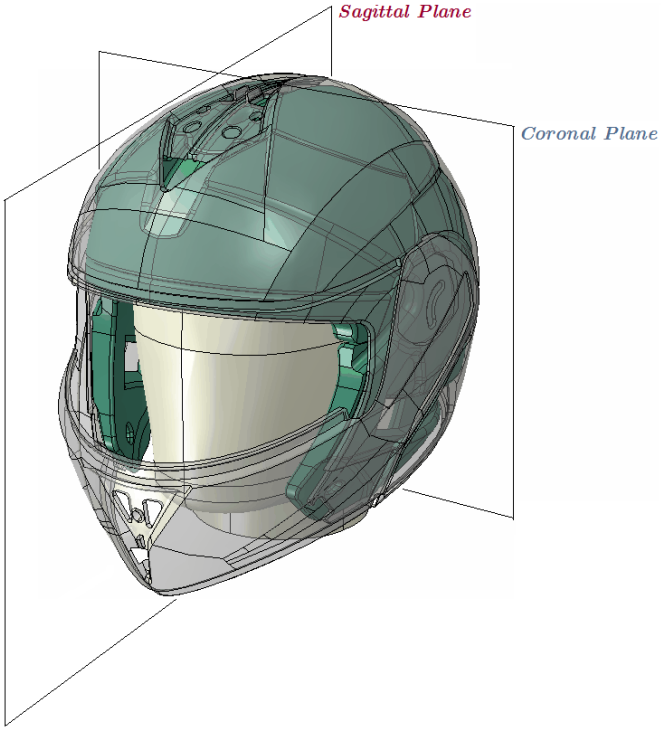

Figure 5.2: Final CAD model fitted with the test headform, which base is parallel to the axial plane.

In the literature, it is rare to find a study where the comfort padding was modelled. In one exception, Brands [1996] modelled the comfort liner and concluded that its effect is negligible. In addition, Pinnoji and Mahajan [2010] affirmed that this extremely soft foam does not contribute to energy absorption, being used only for fitting helmets to different head sizes. As a result of its low stiffness, the comfort foam deforms completely without absorbing any relevant amount of energy, and therefore, has no direct influence in impact protection [Beusenberg and Happee, 1993, Cernicchi et al., 2008]. Thus, comfort paddings do not have influence on the headform's response during an impact [Tinard et al., 2012a,b].

Therefore, from a cost-benefit ratio, the comfort padding was not modelled.

The liners thickness varies from 20 mm to 50 mm. The thickness of the green liner in Fig. 5.3 varies mostly between 40 and 50 mm, being only thinner at the low rear region. This represents a considerable thickness and a high EPS volume. Actually, this is becoming a tendency, since helmets are becoming thicker, probably due to updates in some standards, which are requiring higher energies or more than one impact. On the other hand, the white liner thickness varies from 20 to 40 mm, being also thinner at the low rear. The outer shell made of ABS has a thickness of 3 mm.

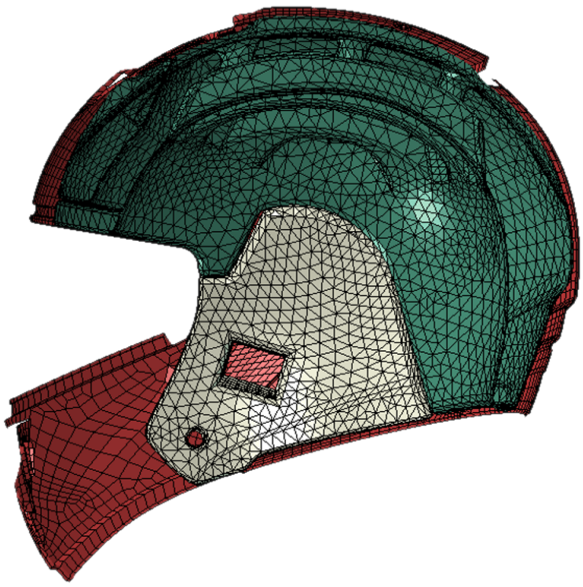

Figure 5.3: FE helmet model - A cut view at the sagittal plane.

According to ECE 22.05 regulation, for the size of this helmet, a 5.6 kg headform should be used (M size). The developed FE headform model is shown in Fig. 5.4 and its inertial characteristics are given in table 5.1. In addition, Fig. 5.4 shows the coordinate system used to apply the principal inertial moments. After assembling all the helmet components, the headform was fitted in the helmet as shown in Fig. 5.5.

Table 5.1: Headform mass and principal inertial moments.

Mass [kg]	I_{xx} [kg.cm^2]	I_{yy} [kg.cm^2]	I_{zz} [kg.cm^2]
5.6	370	440	300

5.1.2 Finite Element Mesh

The FE motorcycle helmet model was created using four-node linear tetrahedral elements to mesh the liner. This type of element was used to model it mainly due to its complex geometry. On the other hand, the shell was modelled with four-node linear shell elements with enhanced hourglass control. The headform and the flat anvil were modelled with rigid quadrangular elements. Although ECE 22.05 standard requires more than one anvil, only the flat anvil was modelled because it is the most impacted object (for instance, the road surface) in motorcycle crashes involving head impact [Shuaeib et al., 2002b, Vallee et al., 1984].

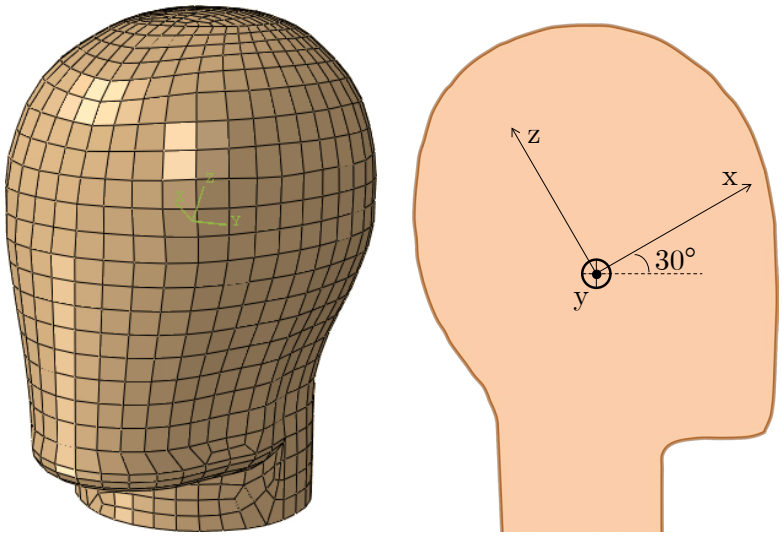

Figure 5.4: FE headform model and an illustration of the coordinate system used to apply the inertial moments.

The meshes were created always avoiding distorted and warped elements. Additionally, special attention was given to the time increment, not having very small elements in order to have a reasonable computation time but at the same time a mesh refined enough to obtain precise results. A summary of the meshes, including the element types, integration schemes and mesh density, is presented in the table 5.2.

Table 5.2: Mesh characteristics of the helmet model.

Part	Element type	Abaqus	N° of elements	N° of nodes
Shell	Four-node linear shell	S4	11954	12310
Liner	Four-node linear tetrahedron	C3D4	109872	24545
Headform	Rigid quadrangular shell	R3D4	1346	1348
Anvil			4	9

5.1.3 Material Modelling

In order to simulate the helmeted impacts, it was necessary to choose suitable constitutive material models to simulate the mechanical behaviour of each material. Two different materials were modelled, the EPS and the ABS. The constitutive law and material properties chosen to simulate the EPS mechanical behaviour under compression can be found in chapter 3. The material model used to simulate EPS was also validated (section 3.3).

The outer shell is made from ABS, a widely used material on motorcycle helmets. The ABS is a stiff thermoplastic material very resistant to penetration. The ABS material properties used to model the shell are listed in table 5.3. To simulate ABS mechanical behaviour, an isotropic linear-elastic material model was considered (Hooke's law). This choice is supported by the fact that during an impact the outer shell is mainly responsible for spreading out the impact's concentrated load and generally deforms elastically, which is an acceptable simplification for a shell made from a thermoplastic like ABS. In addition, in the literature (sections 2.2.1 and 2.2.5), all the authors modelled thermoplastic shells as linear elastic

materials, using only non-elastic models to simulate shells made of composites.

The material properties used to model ABS and given in table 5.3 are based on the same ones used by Pinnoji and Mahajan [2006]. In addition, based on the properties used in this thesis for both ABS and EPS and previously published in Fernandes and Alves de Sousa [2013b] and Fernandes et al. [2013], Mustafa et al. [2015] used the same properties to model a helmet, which was validated with success.

Table 5.3: Mechanical properties of ABS.

$\rho[kg/m^3]$	$E[MPa]$	ν
1200	4000	0.37

5.1.4 Boundary Conditions

In order to simulate the interactions between the headform and the liner and also the interactions between the anvil and the shell, a surface-to-surface type of contact with friction coefficients of 0.55 and 0.5 were used, respectively [Mills et al., 2009a]. Also, a tie was used to simulate the interaction between glued parts. This same type of contact was used to fully constrain the helmet's chin guard relatively to the main shell.

According to the ECE 22.05 standard, the helmet-headform system is dropped, without any restriction, against an anvil with a velocity of 7.5 m/s. Thus, the anvil is fully constrained and an impact velocity of 7.5 m/s was prescribed to the helmet-headform model. Fig. 5.5 shows the impact configurations according to the ECE 22.05 standard, the B, P, R and X impact points. The explicit solver of Abaqus was used to simulate the impacts, with the large deformation option activated. In order to reduce the computational time required, the helmet was placed very close to the anvil.

5.2 Validation

Numerical simulations of helmeted impacts were performed in order to validate the developed motorcycle helmet model, by comparing the numerical results against the experimental data from energy-absorption tests required by the ECE 22.05 standard. This comparison, which is based on the acceleration recorded at the headform COG, is shown in Fig. 5.6. The criteria PLA and HIC are compared as well. The PLA measured at the headform COG and the computed HIC values from numerical and experimental analyses are presented in table 5.4. The expression used to compute HIC is given by the equation 2.1.

Overall, there is a good agreement between experiments and simulations for all four impact points. The small differences between experimental and numerical results may be explained by the absence of some neglected components. For instance, the impacted area at point X has several parts that were not modelled such as the visor locking system, the chin strap, the fixation system between the two parts of the shell and the comfort padding that has a considerable thickness at this region. Despite some differences between experimental and numerical impact results, the helmet model was considered adequate enough for further analyses.

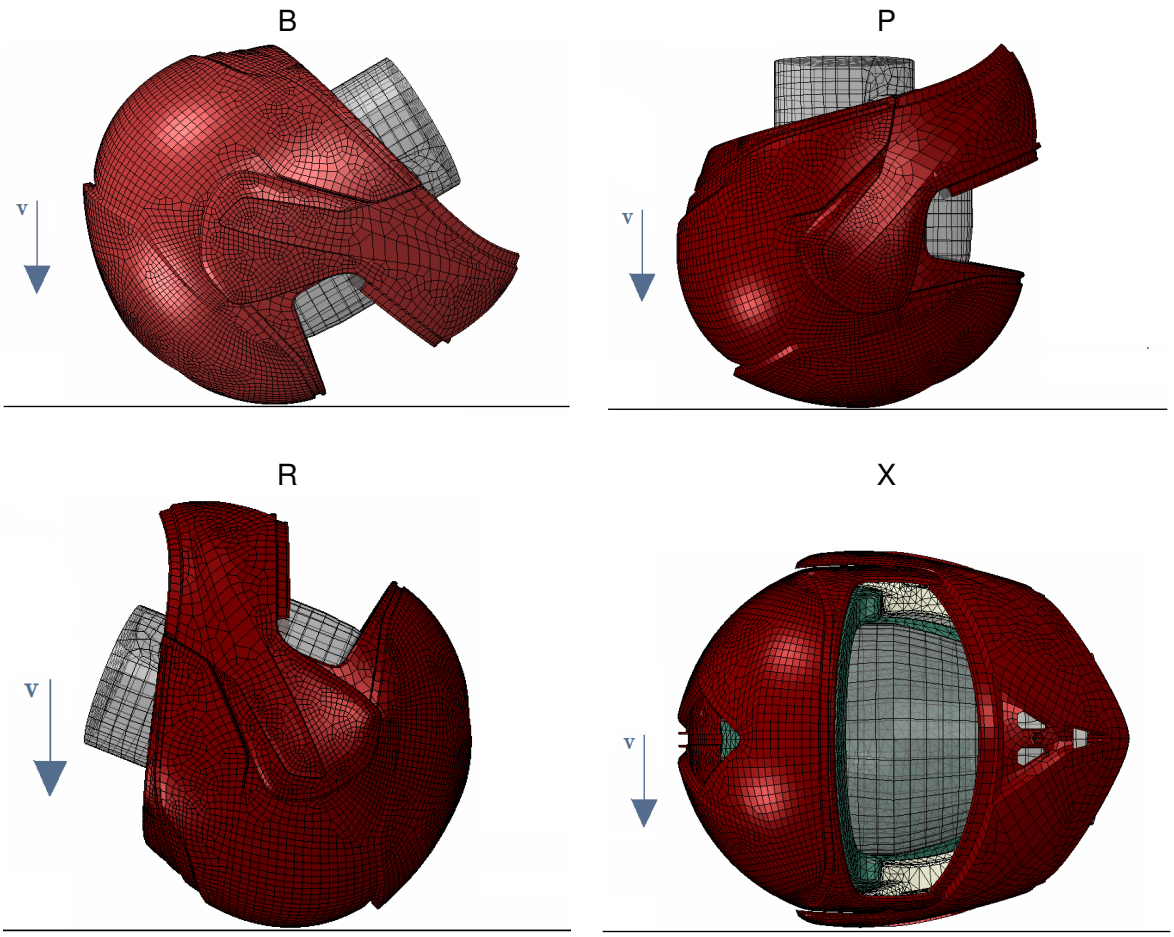

Figure 5.5: ECE 22.05 impact configurations.

Table 5.4: Headform maximum acceleration and HIC computed values for both simulations and experiments.

Impact point		a_{max} [g] ($\leq$ 275)	HIC ($\leq$ 2400)
Point B	experimental	208	1696
	numerical	213.9	1876.8
Point P	experimental	227	1903
	numerical	228.5	2161.7
Point R	experimental	234	2235
	numerical	221.2	2366.2
Point X	experimental	237	1714
	numerical	235.6	2018.6

5.3 YEAHM evaluation

Other objective of this chapter is to assess a certified helmet with a validated FEHM. This evaluation consists in determining the risk of head injuries that can possibly occur with a certified. In order to perform such analysis, the experimental data from the impact tests required by ECE 22.05 standard were used to drive YEAHM. These are the impact tests that were performed to certify this specific helmet.

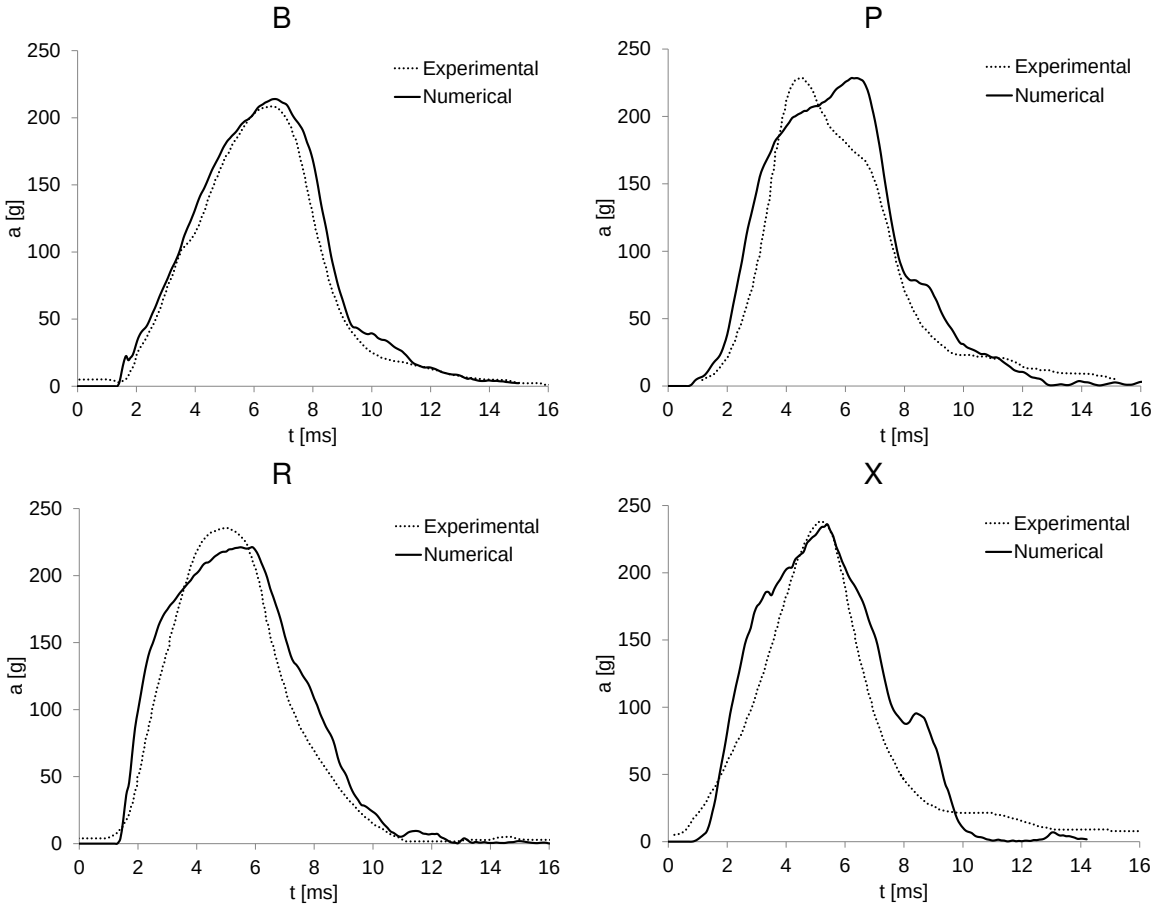

Figure 5.6: ECE 22.05 impact results - comparison between experimental and numerical accelerations.

Thus, the acceleration measured in these impacts and presented in Fig. 5.6 was induced to YEAHM's skull. This is exactly the same procedure used in the previous chapter for validating YEAHM's brain motion, based on the experiments performed by Hardy et al. [2001].

Additionally, it is necessary to establish the head injury criteria to be used with YEAHM. The criteria and respective thresholds previously reviewed in section 2.3.4, more specifically the stress and strain based injury criteria are used together with YEAHM to perform an injury risk analysis. This analysis was performed for four impacts: the B, P, R and X impact points required by the ECE 22.05 standard.

The use of detailed tools, such as FEHM, together with local tissue thresholds seems to be the best way to evaluate the influence of both translational and rotational motion in head structures [Mordaka et al., 2007]. It is possible that future methods used to assess head injury risk and protective head gear will rely on the predictions from numerical head models. This is the best way to study injury mechanisms, focusing on brain reaction to inputs of translational and rotational acceleration [Zhang et al., 2003b]. The brain response can be analysed in terms of several parameters, such as pressure and strain. This is the way for intelligent helmet design.

5.3.1 Impact point B

The acceleration measured during the impact at point B, and presented in Fig. 5.6, is used to drive YEAHM. The YEAHM definitions are the same ones presented in section 4.2.2. The output parameters used to assess the helmet are the same ones indicated as head injury criteria in section 2.3.4. For instance, brain pressure and the maximum principal strain.

Considering the maximum principal strain measured in the brain, a significant risk of injury was identified at the contrecoup region. In table 2.13, the maximum principal strain thresholds vary between 0.1 and 0.49. Fig 5.7 shows a considerable volume where the maximum principal strain value is ranging between 0.1 and 0.4. The dark region is characterised by maximum principal strain values inferior to 0.1. Thus, this corresponds to a uninjured region.

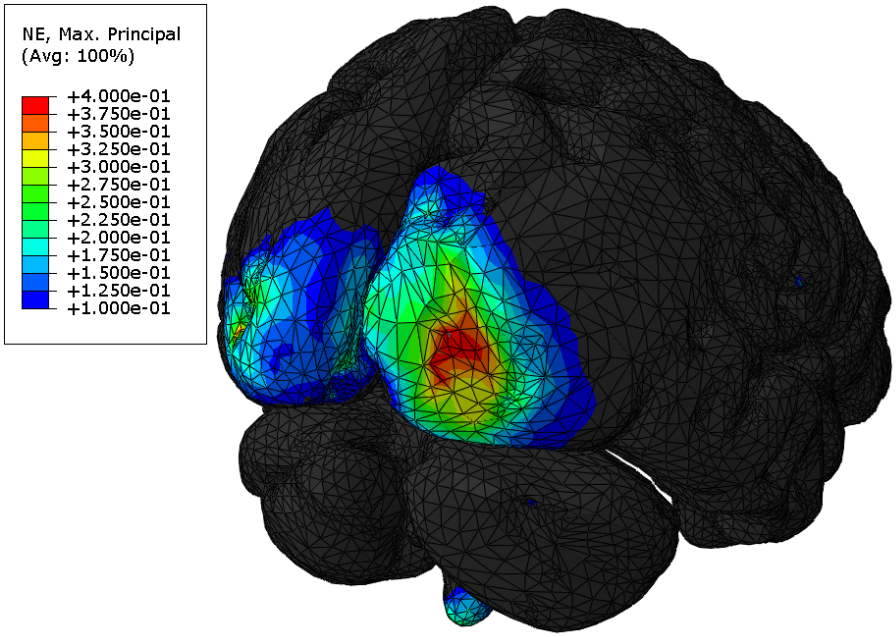

Figure 5.7: Maximum principal strain at the occipital lobe.

On the other hand, the coloured regions are associated with a relevant risk of injury. These represent brain regions where thresholds were exceeded. Regarding the colour scale, the red regions are the most probably ones to be injured. It is clear that almost the entire occipital lobe is under high strain values. Thus, from the thresholds presented in table 2.13, it is clear that at least mild brain injuries are an almost certain outcome. The majority of these thresholds were exceeded, including the ones for contusion, concussion and DAI.

In Fig. 5.7 the colour transition between blue and green represents an approximate maximum principal strain of 0.2, which demonstrates a considerable volume of brain tissue experiencing a significant strain. The strain values of 0.18 and 0.21 proposed by Wright and Ramesh [2012] and Bain and Meaney [2000] respectively, represent the most used thresholds for principal strain to predict DAI.

The CSDM, which is considered one of the most promising stress-strain based injury criteria, was also evaluated. Prior to the moment captured in Fig. 5.7, which corresponds to almost 10 ms, a larger brain volume was experiencing a strain higher than 0.15. A brain

volume of approximately 20% of its total volume experienced a maximum principal strain of 0.15. This volume is composed mainly by the corpus callosum, some internal regions of the parietal and temporal lobes and the entire occipital lobe. This corresponds to a CSDM level of 20, which is associated to an almost certain mild DAI and close to a moderate-to-severe DAI according to the values presented by Bandak et al. [2001].

The brain pressure was also evaluated. By comparing the brain pressure obtained with YEAHM with the threshold values given in table 2.14, a tremendous risk of injury was found. Regarding coup pressure, the limit values range between 90 and 256 kPa depending on the type of injury. In Figs. 5.8 and 5.9 the colour limits were defined between 100 and 500 kPa. The brain model is almost totally coloured, which means that almost the entire brain was subjected to a pressure higher than 100 kPa.

The dominant colour is light green which is equivalent to a pressure higher than 300 kPa. This is higher than any threshold value proposed in table 2.14. Therefore, a high risk of severe injuries is identified. Some small light grey areas are observed in the model with a unit pressure level in the order of MPa but these correspond to isolated peak pressures on the brain surface due to contact pressure with other parts of the model. Therefore, these were neglected. Nevertheless, even from the cut of the frontal lobe presented in Fig. 5.9, it is possible to conclude that brain is under dangerous pressure levels.

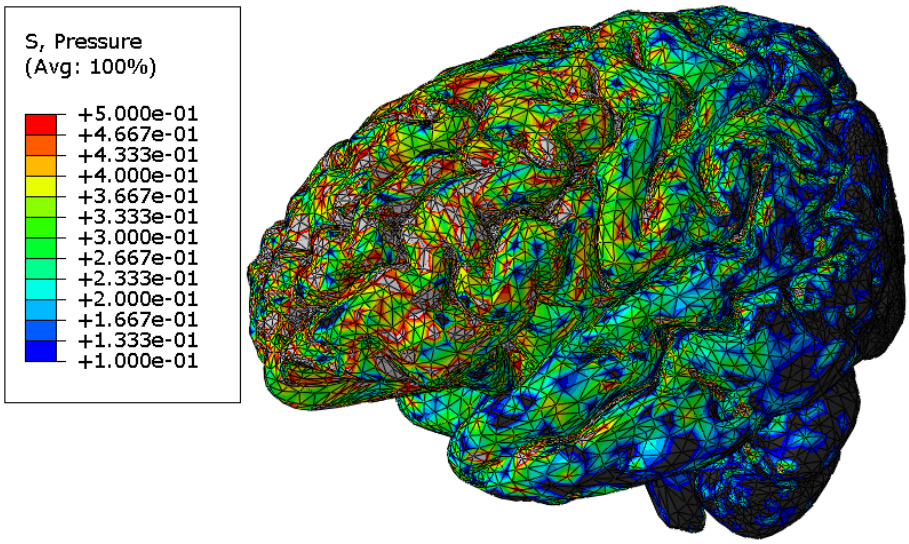

Figure 5.8: Global brain pressure in MPa at the moment of maximum acceleration.

The DDM was also evaluated, but the average negative pressure found at the countrecoup region was under -100 kPa (in absolute value), which is a safe value according to table 2.14 and the DDM levels indicated in section 2.3.4. Nevertheless, a small region with values near -100 kPa was found at the same area marked red in Fig. 5.7. This region presents the higher value for negative pressure. Thus, it is evident that exists a relation between these two parameters regarding the contrecoup. However, the volume that sustained a pressure of -100 kPa was small and did not reach any proposed threshold for DDM. Only, the -76 kPa proposed by Zhang et al. [2004] for a 50% risk of MTBI was exceeded.

Additionally, in this exact same region, it was found the maximum von Mises stress (Fig. 5.10). The maximum values of von Mises stress, maximum principal strain and negative pressure were found at this region and at the same time of impact, which is approximately 10 ms.

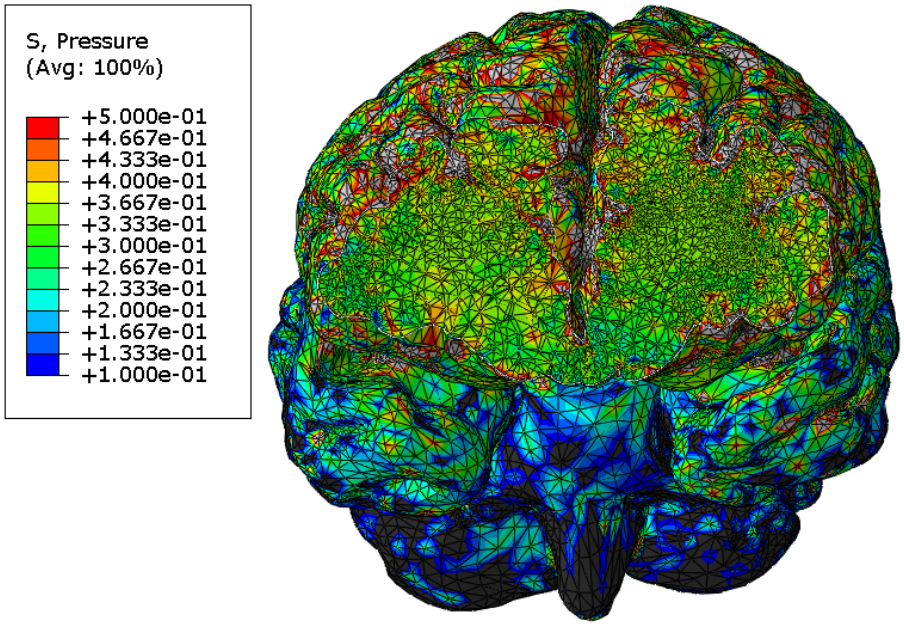

Figure 5.9: A cut view at the frontal lobe, showing the brain internal pressure in MPa.

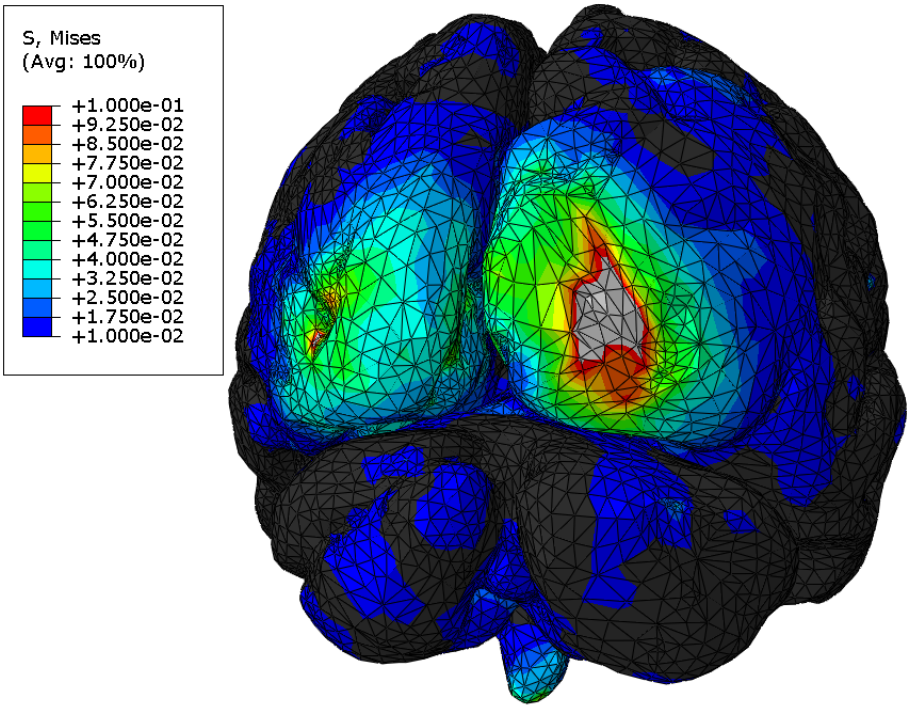

Figure 5.10: Maximum von Mises stress in MPa at the occipital lobe.

Fig. 5.10 shows the occipital lobe experiencing dangerous levels of von Mises stress. The transition between blue and green is characterised by a stress of approximately 40 kPa. In addition, the region where the maximum value was found exceeds 100 kPa (light grey volume), reaching a localised maximum of 260 kPa. This clearly exceeds any proposed value given in table 2.15. Therefore, severe forms of TBI are expected, including concussion and DAI.

In addition, the entire brain experienced an average stress higher than 10 kPa, as shown in Fig. 5.11. This demonstrates that the entire brain is at risk and not just the occipital lobe. In Fig. 5.11, the von Mises stress values are in MPa.

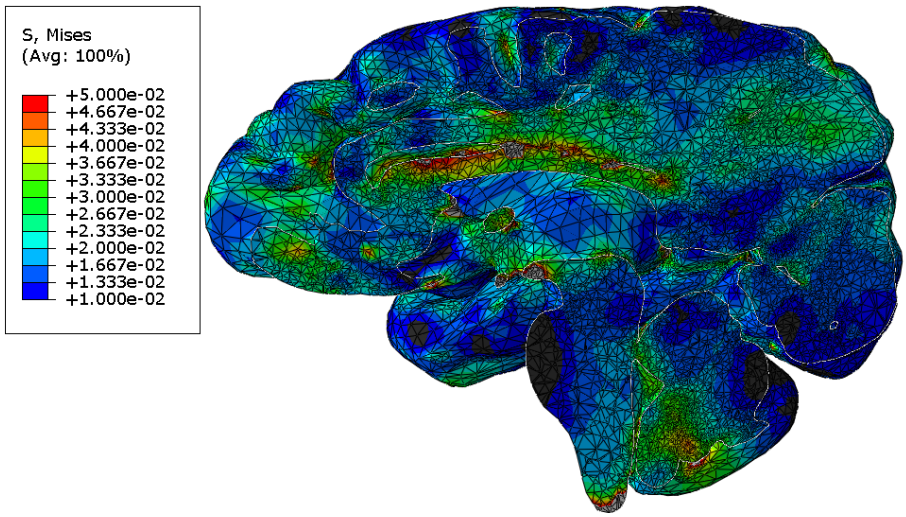

Figure 5.11: Sagittal cut view at the moment of maximum acceleration.

The brain motion was also monitored and a significant relative displacement was found at the occipital lobe between brain and skull. Fig. 5.12 shows a comparison between the initial state and the maximum displacement reached by the brain relatively to the skull. The CSF was removed from the Fig. 5.12 for the sake of clearness.

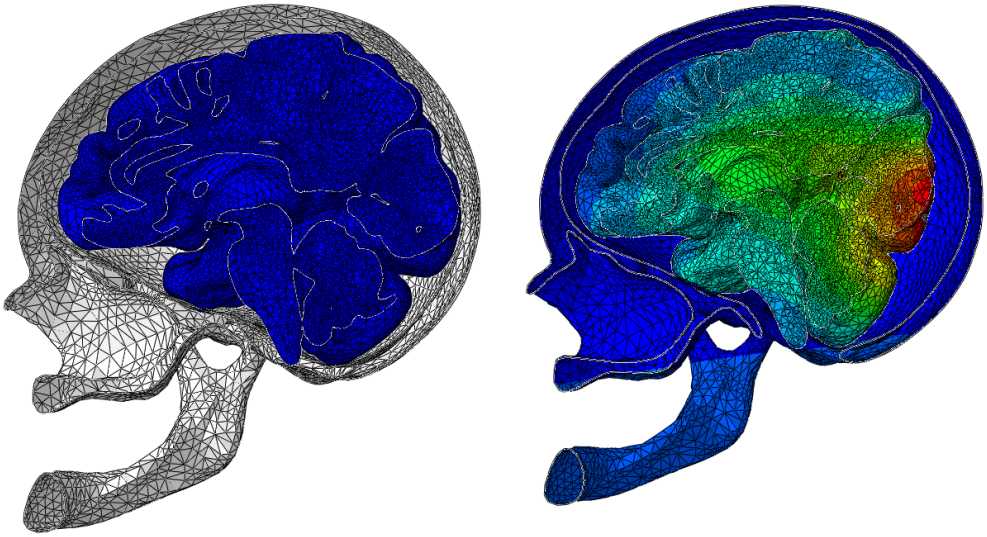

Figure 5.12: Brain motion relatively to the skull: left) before impact; right) at the moment of maximum acceleration.

This relative motion was possibly the main cause of the maximum values verified for von Mises stress and maximum principal strain at the occipital lobe. When the peak acceleration in Fig. 5.6 is reached, compression of the frontal lobe and the relative displacement between the occipital lobe and the skull are also maximums. Then, the rebound immedi-

ately starts and the occipital lobe impacts the skull, compressing the brain at the contrecoup region. This is most likely the cause of the maximum von Mises stress. Additionally, during the rebound, the brain tissue stretches at this region, causing the maximum principal strain value.

The CSF strain energy and its pressure were also analysed and compared with the values proposed in the literature regarding SDH prediction. The maximum strain energy found in the CSF was 6490 mJ, which is higher than the values proposed in the literature [COST327, 2001, Marjoux et al., 2008, Deck and Willinger, 2009]. For instance, the highest value was proposed by Deck and Willinger [2009], a limit of 4950 mJ. Nevertheless, the value computed with YEAHM may not be feasible to directly compare with injury thresholds, since the global model of CSF incorporates the properties of all the intracranial contents with exception of the brain. Nevertheless, this value may be useful to compare different helmets for the same impact conditions. Deck and Willinger [2009] also proposed a CSF pressure of 290 kPa as tolerance for SDH. This value was never exceeded, reaching a maximum pressure of 265.8 kPa next to the corpus callosum.

In conclusion, brain injuries are predicted with a certified helmet for the impact used to certify it. Although it is already concluded that a standard-approved helmet does not fully protect its user in the same impact used to certify it, the remaining three impacts (P, R and X) were also analysed in order to eliminate any dependence on the type of impact.

5.3.2 Impact point P

Similarly to impact point B, the impact at point P was also evaluated. As in the previous section, the acceleration presented in Fig. 5.6 is used to drive YEAHM. The same output parameters are used to assess the helmet impact performance at this point.

Regarding the von Mises stress, two different levels were observed in YEAHM. A lower stress level across the cerebrum reaching an average of 12 kPa, and a much higher level in cerebellum. In Fig. 5.13, considering that the transition between blue and green occurs for an approximate value of 25 kPa and that light grey is higher than 60 kPa, an injury at the cerebellum is most likely to occur.

Again, the maximum von Mises stress is experienced at the contrecoup region and at the moment of maximum acceleration. The von Mises stress values at the cerebellum and at the base of brainstem were higher than all values presented as thresholds in table 2.15. Actually, the brainstem seems to be one of the most sensitive regions to von Mises stress, due to the low values proposed as thresholds at this region. For instance, a 50% probability of concussion was proposed by Zhang et al. [2004] for von Mises stress values higher than 7.8 kPa in the brainstem. In addition, the value of 8.4 kPa in the corpus callosum, proposed by Kleiven [2007c] for a 50% probability of concussion, was largely exceeded. Thus, concussion is an almost certain outcome. Additionally, other forms of TBI are highly likely to occur based on the thresholds given in table 2.15.

As in case of impact point B, the maximum pressure occurred at the coup site. Additionally, almost the entire brain experienced enormous pressure values. In Fig. 5.14, the low limit of 90 kPa marked as blue is the lowest threshold in table 2.14. The medium green colour corresponds to a pressure of 295 kPa, which is much higher than any value given in table 2.14. Thus, a TBI is the most likely outcome.

The DDM was also evaluated, and the results are very similar to impact B. The average negative pressure found at the countrecoup region was under -75 kPa (in absolute value), which is a safe value according to table 2.14 and the DDM levels indicated in section 2.3.4.

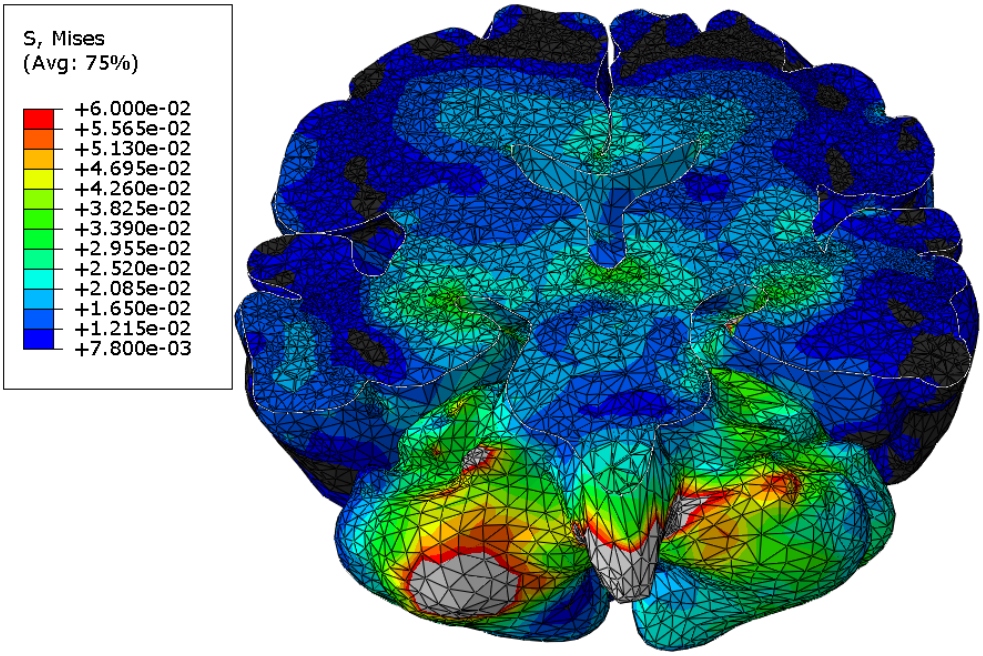

Figure 5.13: Coronal cut view at the moment of maximum acceleration, showing the von Mises stress in MPa.

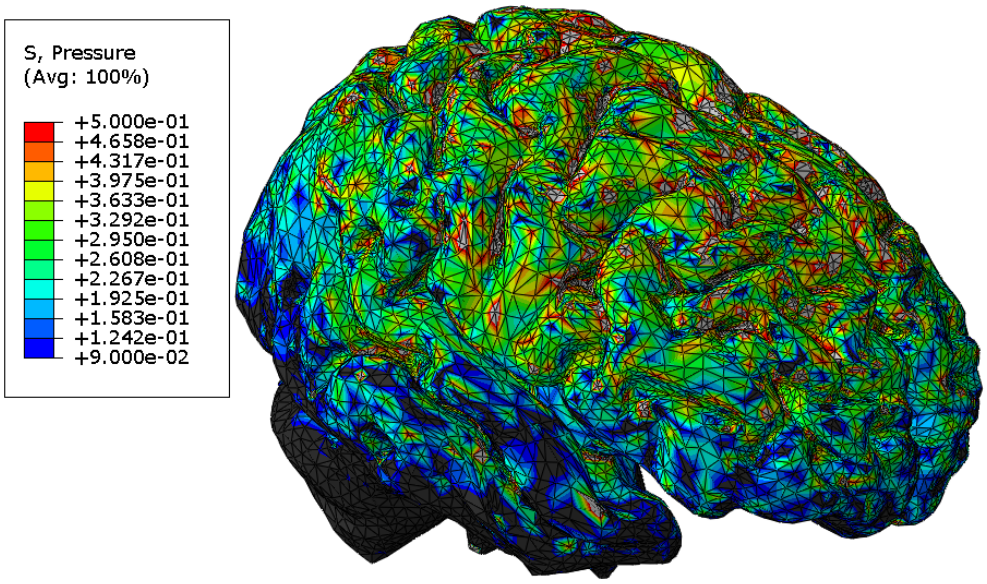

Figure 5.14: Brain pressure in MPa at the moment of maximum acceleration.

Additionally, the region where the higher negative pressure was found is the same volume (cerebellum and brainstem) where it was found the maximum von Mises stress.

The maximum principal strain was also assessed. Again, its maximum value was found at the same region where the maximum von Mises stress and negative pressure were found (Fig. 5.13). In other words, the maximum values for these were found at the contrecoup region, more specifically at the cerebellum and brainstem. Although the maximum principal strain observed at these regions reaches 0.38, the brain volume experiencing this strain is small. Additionally, the brain volume experiencing a maximum principal strain higher than

0.15 is less than 5%, which means this is lower than the injury thresholds proposed for CSDM in section 2.3.4.

Regarding the relative motion between brain and skull, the maximum was also observed at the cerebellum. However, this was not much significant. The pressure in the CSF was also monitored. This reached a maximum value of 193.3 kPa, which is much lower than the value proposed by Deck and Willinger [2009] as tolerance for SDH. In addition, a CSF strain energy value of 4322.6 mJ was computed. This is lower than the limit proposed by Deck and Willinger [2009]. However, it is higher than the SDH thresholds of 4211 mJ and 4000 mJ proposed by Marjoux et al. [2008] and COST327 [2001], respectively.

This same impact with this same helmet was previously assessed with other FEHM. The same conditions prescribed for YEAHM were applied to SUFEHM in Fernandes et al. [2013]. Strain energy in the CSF of 4097 mJ was found with SUFEHM, which is lower than YEAHM. The maximum von Mises stress was located between the brain and the cerebellum and between the cerebellum and the brainstem. This supports the findings obtained with the YEAHM model. Both models predicted the maximum von Mises stress at the same region. Nevertheless, SUFEHM predicted the maximum pressure in occipital area, while YEAHM predicted in the parietal lobe. YEAHM prediction regarding the maximum brain pressure seems more realistic since the impact was on the parietal area.

In addition, the average von Mises stress found with SUFEHM at the cerebellum was 39.7 kPa, which is in accordance with the values predicted with YEAHM at that region. This value corresponds to a 90.2% risk of moderate DAI, according to SUFEHM's criteria. Again, it is clear that an approved helmet does not protect its user in the same impacts in which it was validated.

5.3.3 Impact point R

The same impact used to certify the previously validated helmet at point R was used to assess it with YEAHM. The experimental acceleration-time history of impact R, shown in Fig. 5.6, was used to drive YEAHM. This impact at the back of the head originated high strains in the frontal lobes, opposite to the impact site. Figs. 5.15 and 5.16 show the maximum principal strain distribution.

The lower limit was set to 0.1, since it is the lowest injury threshold given in table 2.13. Fig. 5.15 shows the start of the rebound, being possible to observe a distribution resembling wave propagation. At the end of the rebound, the maximum principal strain was reached, with a relatively localised value of 0.53. This value and even the ones presented in Figs. 5.15 and 5.16 exceed the injury thresholds presented in table 2.13. Thus, several forms of TBI, including contusion, concussion and DAI are predicted for this impact. Fig. 5.16 shows the internal distribution of strains higher than 0.1. It is possible to observe the presence of these around the corpus callosum and midbrain. These figures show also the importance of modelling sulci and gyri structures. These make it possible to obtain some patterns in the results that are not possible to observe in a brain model with a smooth-spherical surface.

In addition, from the start of the rebound until the end of the acceleration-time history curve, approximately 36% of the brain experienced a strain of at least 15%. Comparing these values with the ones proposed in the literature (section 2.3.4), a CSDM level of 36 is enough to cause a moderate-to-severe DAI [Bandak et al., 2001].

Fig. 5.17 shows the pressure propagation across the brain, being higher at impact zone. In Fig. 5.17, some light grey and red small regions are observed. However, these high values might happen due to the influence of contact pressures. Internally, at the

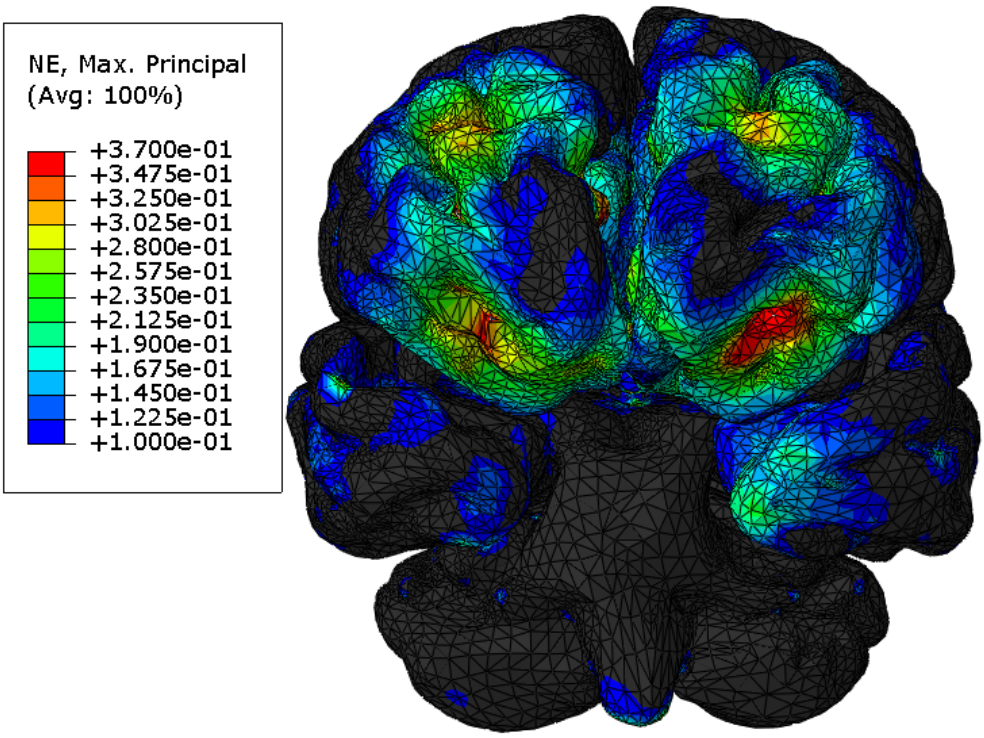

Figure 5.15: Maximum principal strain reached at the contrecoup site (frontal lobes).

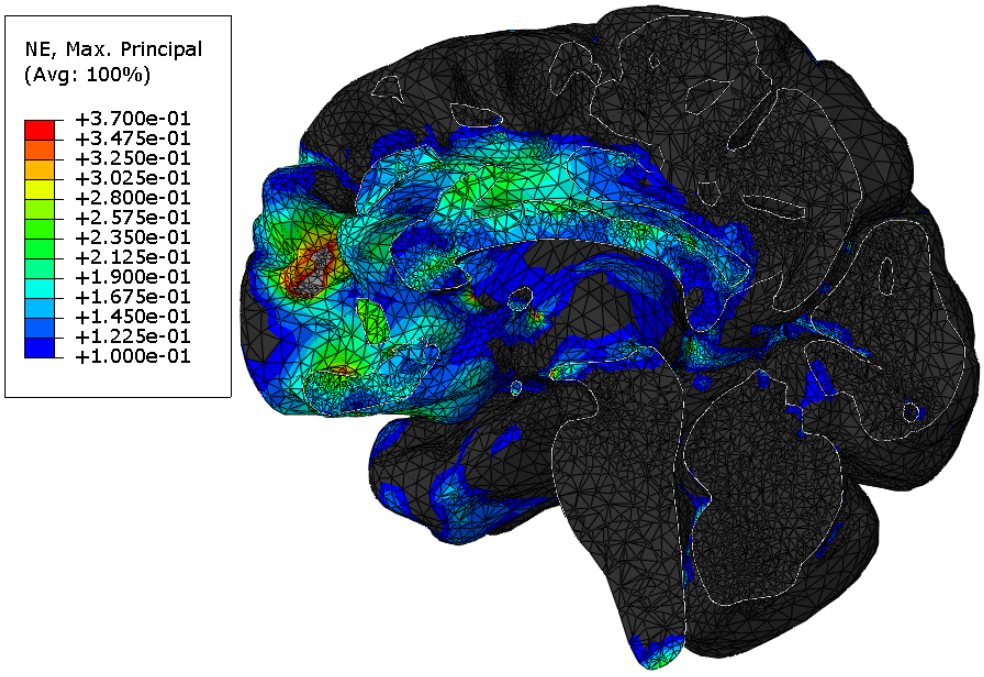

Figure 5.16: Sagittal cut view showing the internal distribution of the maximum principal strain.

impact zone (coup), pressures are lower than in these small regions at the brain surface but still higher than the injury thresholds presented in table 2.14, ranging between 329.2 and 363.3 kPa. Such pressures found in the occipital lobes are likely to originate a severe

injury. In addition, a great brain volume experienced pressures higher than 90 kPa, such as the occipital lobes, parts of the cerebellum and temporal and parietal lobes. Regarding the DDM, only safe values were observed.

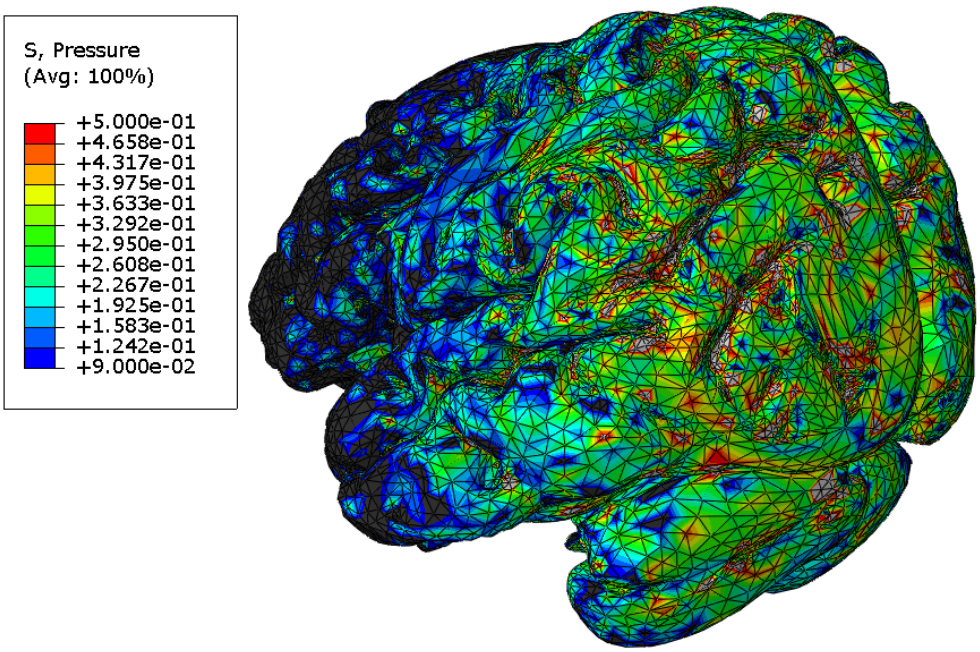

Figure 5.17: Brain pressure propagation in MPa.

The von Mises stress was also monitored. Its maximum values were observed in the frontal lobes (contrecoup site), with values exceeding all the thresholds presented in table 2.15. The light grey regions shown in Fig. 5.18 exceed any given threshold in this table, even the highest one. Thus, severe forms of TBI are likely to occur.

Regarding the CSF pressure, the tolerance value of 290 kPa proposed by Deck and Willinger [2009] as threshold for SDH was reached but not significantly exceeded. This high pressure was found in the CSF at the base of the occipital lobe. This region of the CSF also simulates the junction between falx cerebri and tentorium. The maximum CSF strain energy found was 6911.5 mJ which is higher than any proposed threshold for SDH. Thus SDH is a probable outcome.

5.3.4 Impact point X

Finally, the lateral impact was also assessed. Regarding the von Mises stress, as in other impacts, the maximum value was reached at contrecoup site, in this case the temporal lobe opposite to the impact point. Overall, almost the entire brain experienced a value higher than 7.8 kPa, which is the lowest injury threshold proposed in table 2.15. In addition, as shown in Fig. 5.19, the maximum value found in the brain model (light grey) exceeded the highest one proposed in table 2.15. Thus, brain injuries such as concussion and DAI are likely to occur.

As in the other impacts, the pressure reached its maximum at the coup site. Fig. 5.20 shows a coronal cut of the brain, showing the pressure wave propagation across the hemispheres. The low limit of 90 kPa (blue) is the lower injury threshold found in table 2.14 (with the exception of negative pressures). In addition, the higher pressure threshold given in

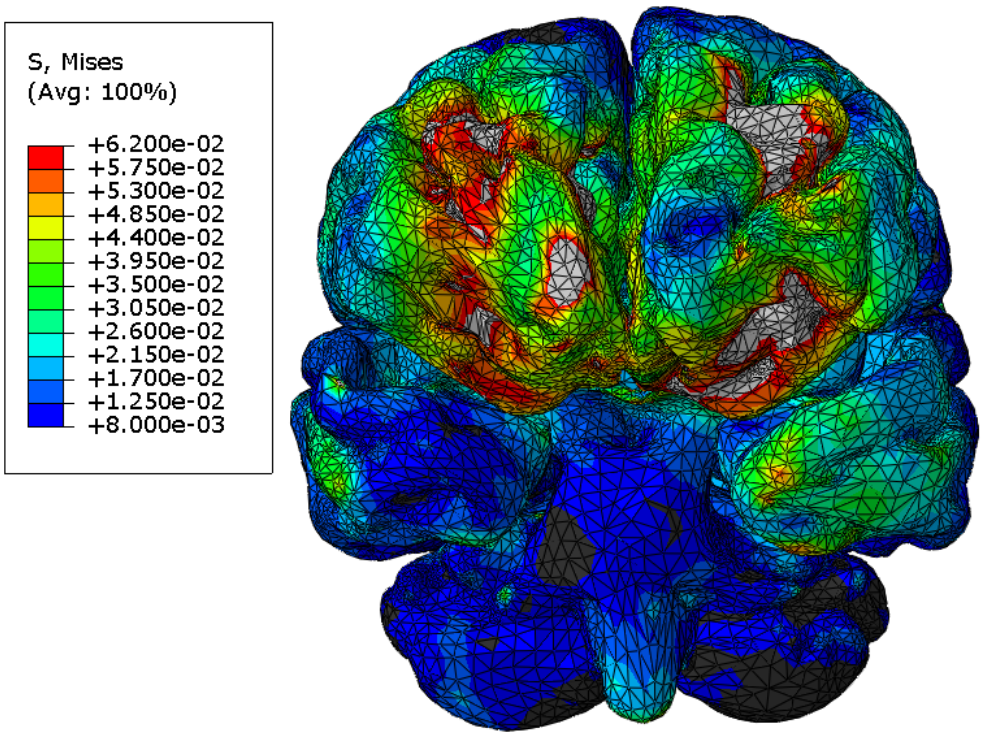

Figure 5.18: The von Mises stress across the brain in MPa.

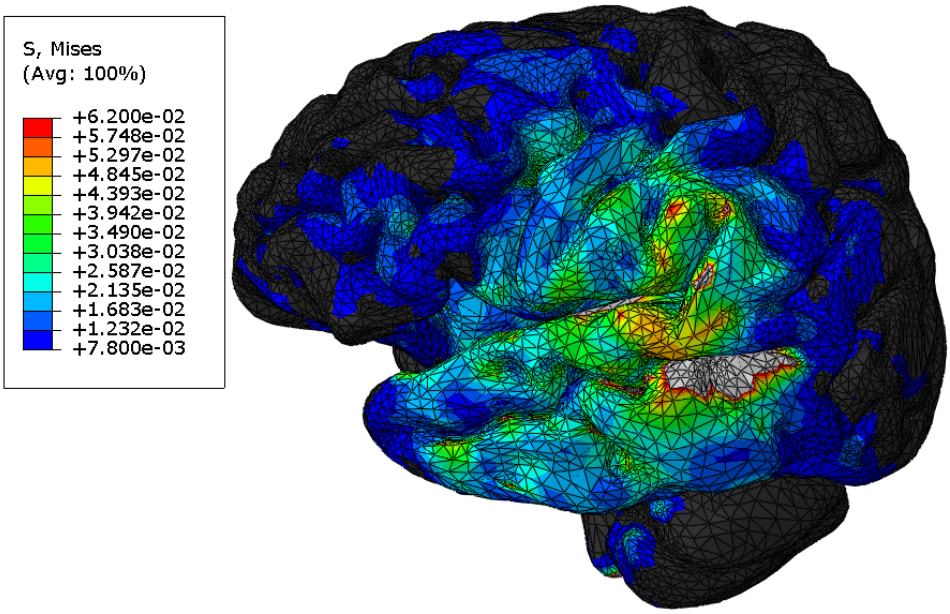

Figure 5.19: Maximum von Mises stress found at the contrecoup site (in MPa).

this table is 256 kPa, which was exceeded for almost an entire hemisphere. Again, several sorts of TBI are an almost certain outcome. Regarding the DDM, none of the limits were exceeded.

In this impact, the maximum principal strain was generally under the values indicated in table 2.13. However, around the contrecoup region, strains ranging between 0.1 and 0.17 were found. These are higher than some values proposed in 2.13. Additionally, exactly

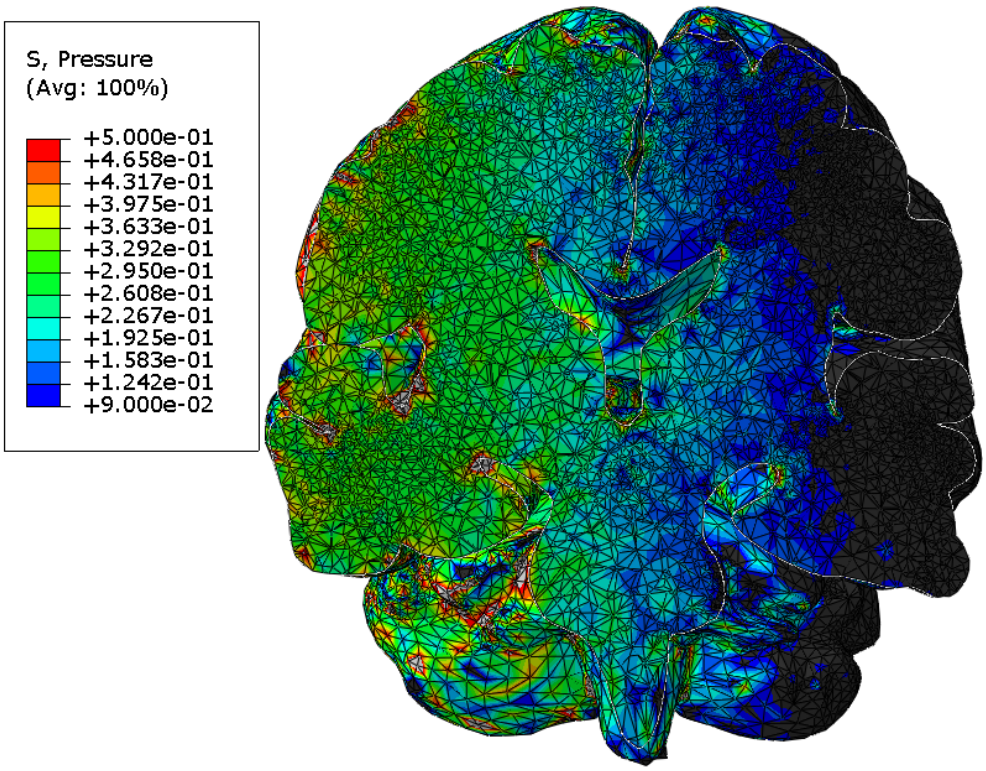

Figure 5.20: Coronal cut view of the brain showing the pressure wave propagation across the hemispheres (in MPa).

in same area of the temporal lobe where it was found the maximum von Mises stress, a localised strain of approximately 0.43 was found. Nevertheless, the brain volume experiencing such strain is small. Thus, the CSDM limits were not exceeded.

Regarding the SDH prediction, both CSF pressure and CSF strain energy were lower than the SDH thresholds proposed in the literature. A pressure of nearly 290 kPa was found at the skull base but did not surpass this value. A value of 3975.5 mJ was computed for the CSF strain energy, which is close to the threshold but still lower. Thus, SDH is an improbable outcome.

Several types of head injuries were predicted in these four impacts, since contusions, concussions and DAI. Some limitations of the standards are underscored from what was seen with YEAHM. This supports the premise that the current criteria for helmet standards are not optimal.

In conclusion, the analysis of these four impacts showed that by reproducing the same impacts that are assessed by the ECE 22.05 standard, it is evident that a certified helmet cannot protect its user from suffering brain injuries. This clearly shows that simple injury criteria such as PLA and HIC are not enough to assess the protection provided by helmets. Therefore, it can be concluded that a motorcyclist wearing an approved helmet can suffer brain injuries in the same impact that was used to certify the helmet. The conclusions here withdrawn are supported by other studies, for instance Fernandes et al. [2013] and Tinard et al. [2012b], where similar analyses led to the same conclusions.

5.4 Comparison with liners made of cork agglomerates

In the previous section, from an analysis performed with YEAHM, it was seen that a standard-approved helmet fails to protect its user in the same impacts used to test it and certify it. Thus, since the main objective of this work is to evaluate the applicability of cork agglomerates as helmet liners, the material models validated in chapter 3 were used together with the FE helmet model validated in this chapter.

Thus, exactly the same helmet, validated in this chapter, is used. Only the material of the liner is changed, keeping exactly the same geometry. The cork agglomerates AC199, AC216 and EC159, validated in chapter 3, are evaluated in the same impacts used to test the helmet with EPS liner. Thus, the four impacts required by the ECE 22.05 standard are simulated for each of these materials used as energy absorbing liner.

Figs. 5.21-5.24 show the results obtained for each material in terms of acceleration measured in the headform. Clearly, the EPS performed better in all the four impacts. Nevertheless, the results obtained from impact point X reveal a similar response between cork agglomerates and EPS. Still, the later presented a better response, managing lower peak accelerations.

One cork agglomerate that stood out from the others for all the four impacts was AC216. This agglomerated cork had a clear better performance than the other agglomerates. In all the four impacts, AC216 had larger acceleration-time curves with lower peak accelerations. In the phase III of the chapter 3, AC216 was also the better cork agglomerate in the impact tests, showing lower peak accelerations. Additionally, AC216 was the best material regarding the response to a second impact, even better than EPS90.

Although EPS90 had clearly a better response in all the impacts. From what was seen in chapter 3, AC216 has a greater capacity to withstand impact energy and to continuously doing it. Thus, it is believed that the helmet used in this analysis has a liner with a thickness higher than necessary for AC216. Actually, the better results with the cork liners were obtained for impact X, which is the region of the helmet where the liner is thinner (between 35-40 mm at the impact point). The larger area of the helmet has a thickness of 50 mm, which decreases in the areas next to the edges, especially at the rear end. This means a high volume and in the case of AC216, it means more weight, since it is the denser material. Thus, the impact energy is greater in the case of AC216.

Therefore, it is believed that a thinner liner made of AC216 will perform better, even when subjected to multi-impacts. Nevertheless, it is important to retain the fact that AC216 reaches the densification phase sooner than EPS90. The AC216 enters this region for nominal strains higher than 0.6 (at quasi-static regimes in Fig. 3.21).

Figs. 5.25 and 5.26 show the nominal strain at the moment of maximum deformation in the frontal impact (B), for both AC216 and EPS90. At the centre of the impacted region, the EPS liner, reached a maximum deformation of 76.9%, which is permanent. On the other hand, with the cork liner, a maximum deformation of 51.6% was found, which is recoverable. At the end of the rebound, this value dropped to 5.6%.

The results from the impact tests required by the ECE 22.05 standard and the ones from the impact tests performed in chapter 3 revealed AC216 as the best cork agglomerate for this application. Although this preliminary analysis of a helmet model with cork liners was performed only with the headform, not using the YEAHM model, this was useful to select one agglomerate for further analyses.

In the next chapter, it is developed a new helmet model composed of thinner liners made of AC216. This same model is optimised according to YEAHM response to double impacts.

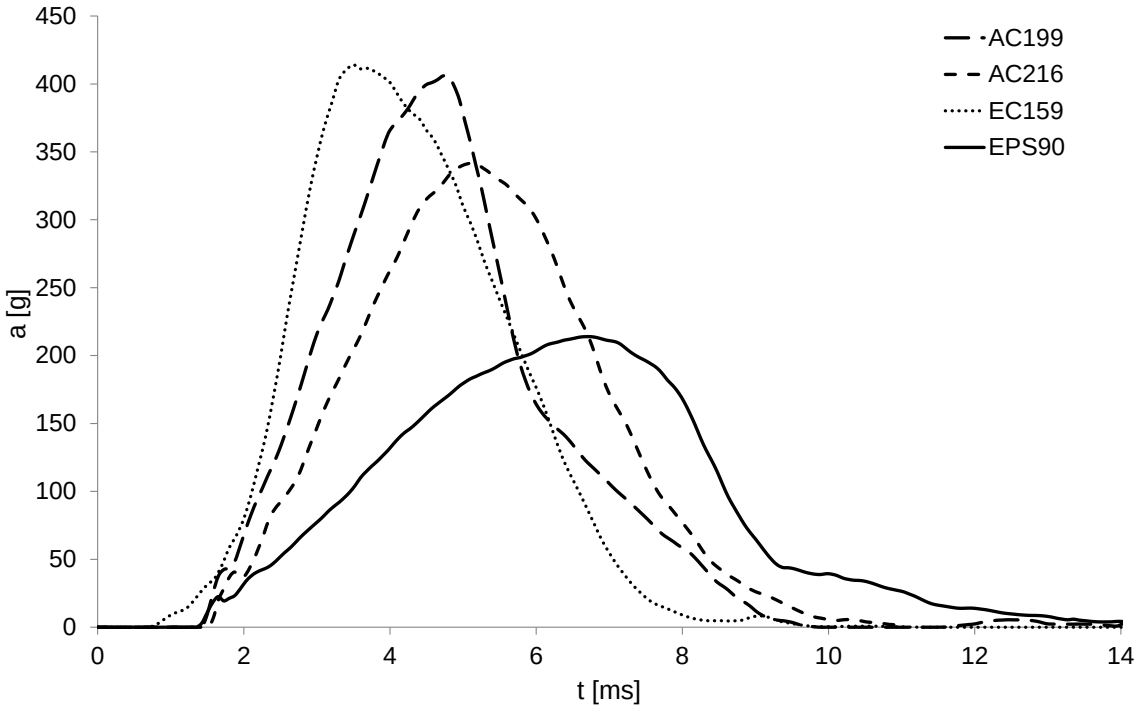

Figure 5.21: Impact point B.

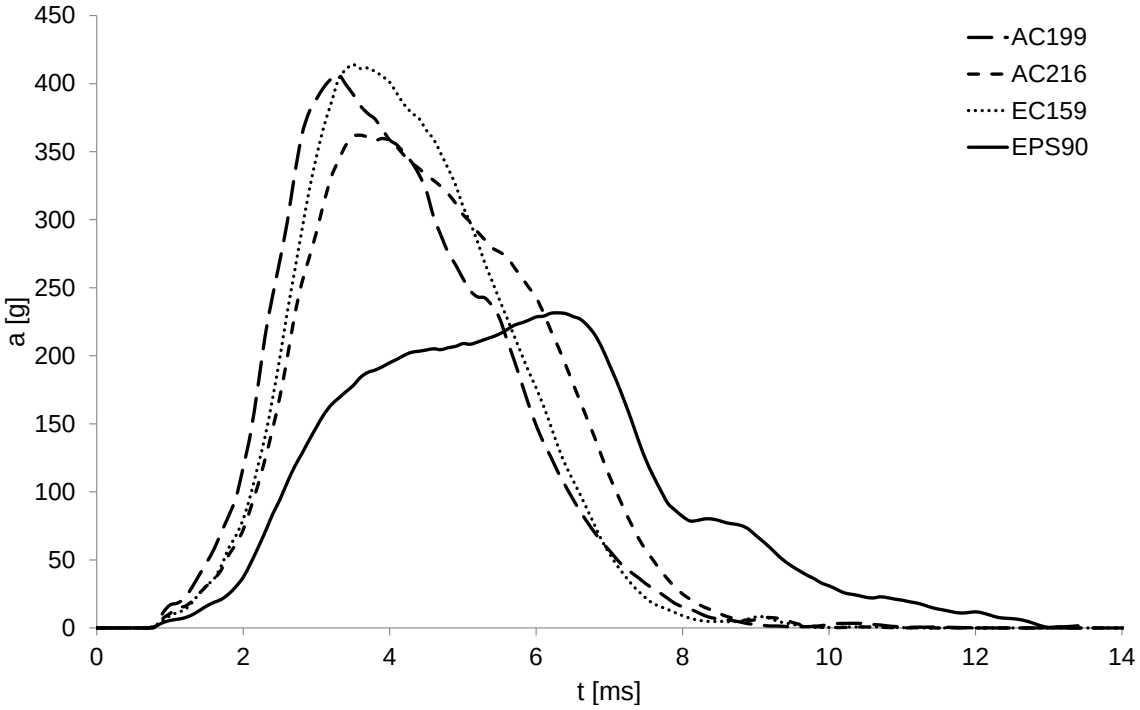

Figure 5.22: Impact point P.

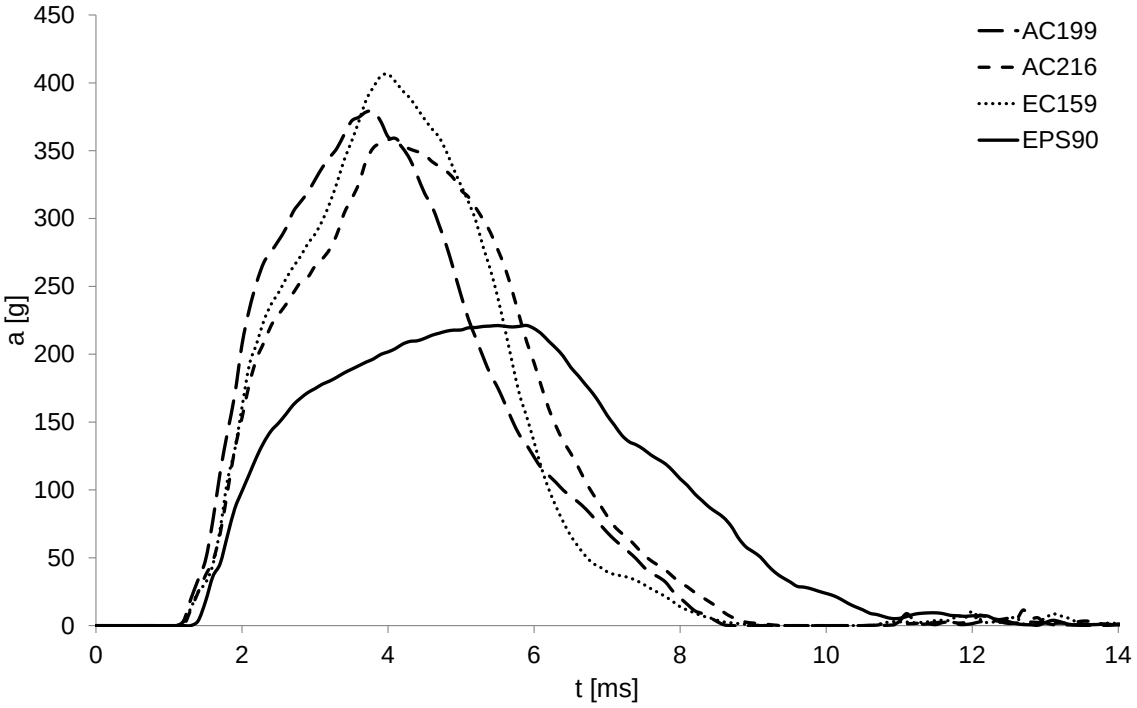

Figure 5.23: Impact point R.

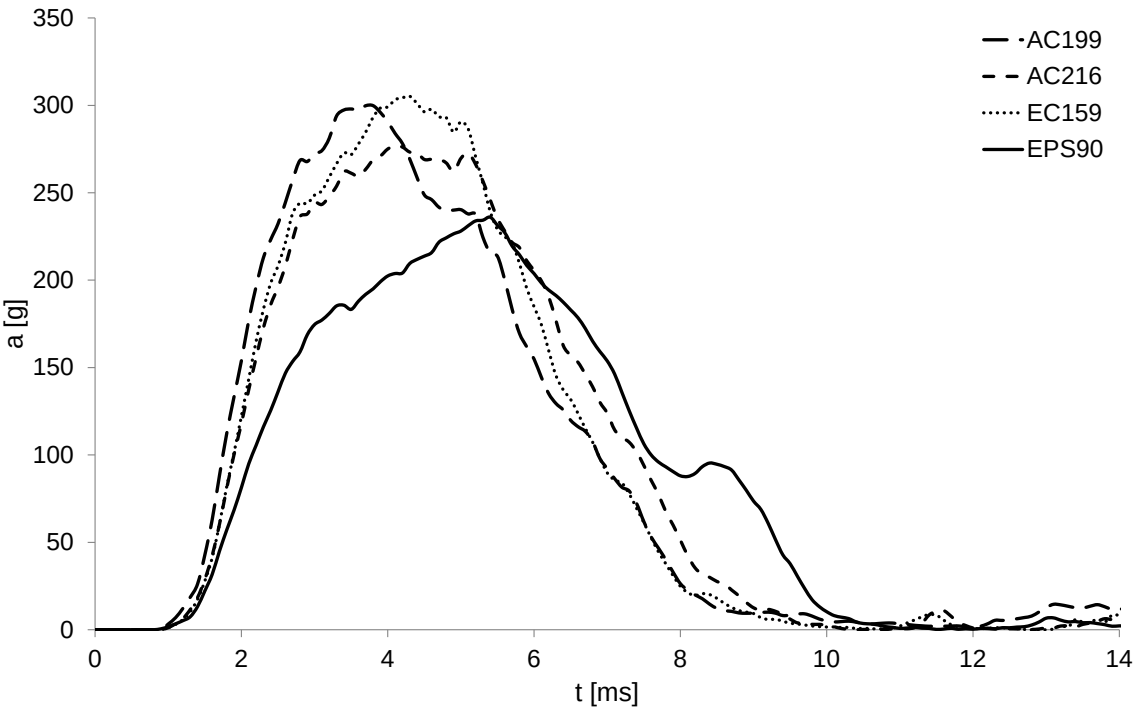

Figure 5.24: Impact point X.

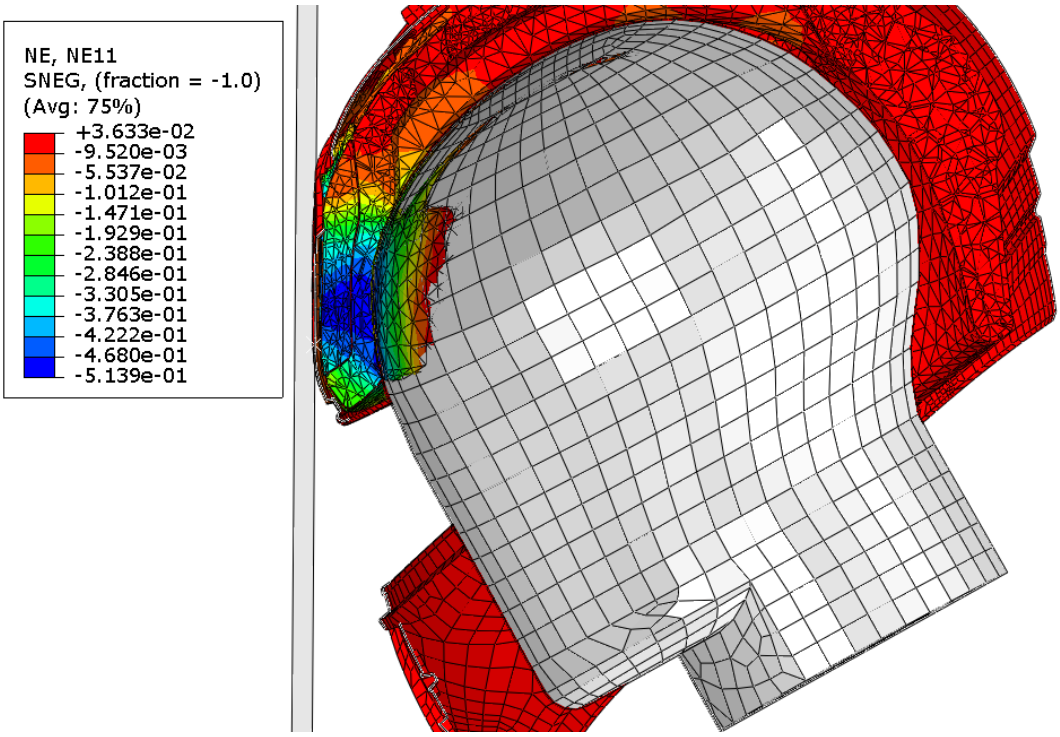

Figure 5.25: Sagitall cut view of the helmet-headform system at the moment of maximum deformation with a AC216 liner.

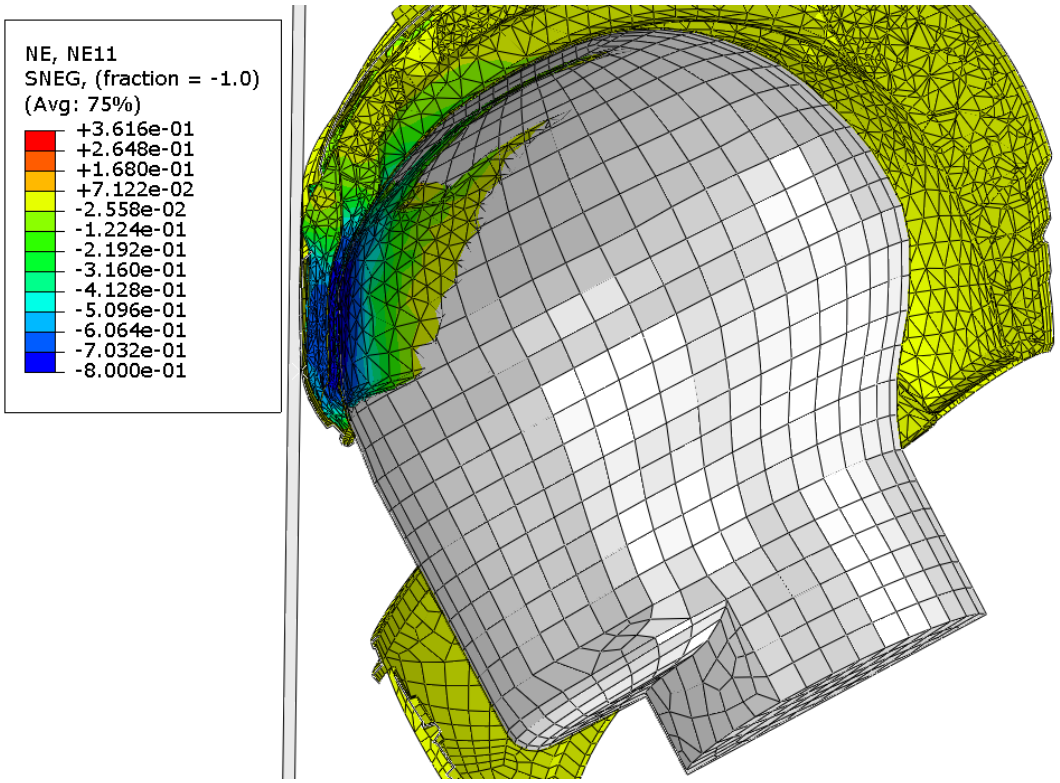

Figure 5.26: Sagitall cut view of the helmet-headform system at the moment of maximum deformation with a EPS90 liner.

Chapter 6

Biomechanical evaluation of a helmet composed of agglomerated cork liners

This chapter presents the development of a new helmet model and its assessment based on the head injury risk predictions by YEAHM. This evaluation is performed in order to verify if a helmet composed of agglomerated cork liners is an alternative to the ones made of EPS.

In this chapter, a new helmet model is developed and its impact performance is assessed based on the YEAHM predictions. In the previous chapter, the results indicated that AC216 is the most promising agglomerate to be used as helmet liner. Additionally, it was verified that the helmet validated in this previous section fails to protect its user in the same impacts in which it was certified. This was inferred by evaluating the impact performance of this commercially available helmet, composed of EPS liners, with YEAHM and the injury criteria presented in section 2.3.4.

This was a preliminary analysis to evaluate a modern helmet (with EPS liners) and the current criteria used by helmet standards. The same helmet was tested with cork liners and although lower peak accelerations were measured for EPS, the acceleration-time curves measured for the agglomerate AC216 are promising (Figs. 5.21-5.24).

This first helmet is composed by liners with a thickness around 50 mm in the impact points (B, P and R). From what was seen in chapter 3 and in the previous chapter, it is believed that a thinner liner of AC216 agglomerate is enough to absorb the impact energy, in the same tests required by the standard, without increasing the stress levels. For instance, Fig. 5.25 shows a 50% deformation for a thickness of 50 mm, not reaching densification (Fig. 3.21). In addition, more material means more weight, which increases the impact energy.

In the impact point X, the results between cork agglomerates and EPS were very close to each other. In this region, the liner has a thickness of approximately 40 mm. Another factor that may have contributed to the lower accelerations in this point (Fig. 5.24) is the larger impacted area.

Thus, considering the great capacity of AC216 shown in chapter 3 and its impact per-

formance in the standard tests, for instance in impact X (Fig. 5.24), a new helmet model is developed. The strategy with this helmet is based on the 40 mm thickness seen for impact X. This is already a significant thickness, which is usually exceeded in the current helmets. Considering that the last updates in standards are demanding more impacts or higher energies, helmet liners are becoming even thicker. In a technical report, Smith and Pomerening [2014] indicated that a helmet made of EPS needs a thickness between 75 and 90 mm to achieve an acceleration of 100 g for a 6.2 m/s impact, and to pass the standard criteria they indicated thicknesses ranging between 50 and 60 mm, which may increase up to 72 mm due to safety margins used by some manufacturers.

Thus, for the new helmet model, a maximum thickness of 40 mm was set for the liner. Several models were created by varying the thickness. Then, the impact performance of each one of these helmets is analysed with YEAHM, by comparing its predictions with the injury criteria presented in section 2.3.4 and therefore, evaluating the applicability of agglomerated cork as helmet liner.

6.1 Methods and materials

In this section, a new helmet model is created. Its style is based on jet helmets, also known as open face helmets. This style was chosen because it makes it easier to model the geometry and it is the most common style considering all types of helmets. It is used in a great variety of applications, for instance in contact sports such as American football and ice hockey, in urban activities, winter sports, by motorcyclists, among many other activities.

The geometry was created in CATIA V5 CAD software in a way that makes it simple to define a new thickness for the thickness of helmet model. Thus, different versions of it were created by varying the thickness. The entire liner is designed with a constant thickness, which maximum value was set to 40 mm. Fig. 6.1 shows a render of the final geometric model.

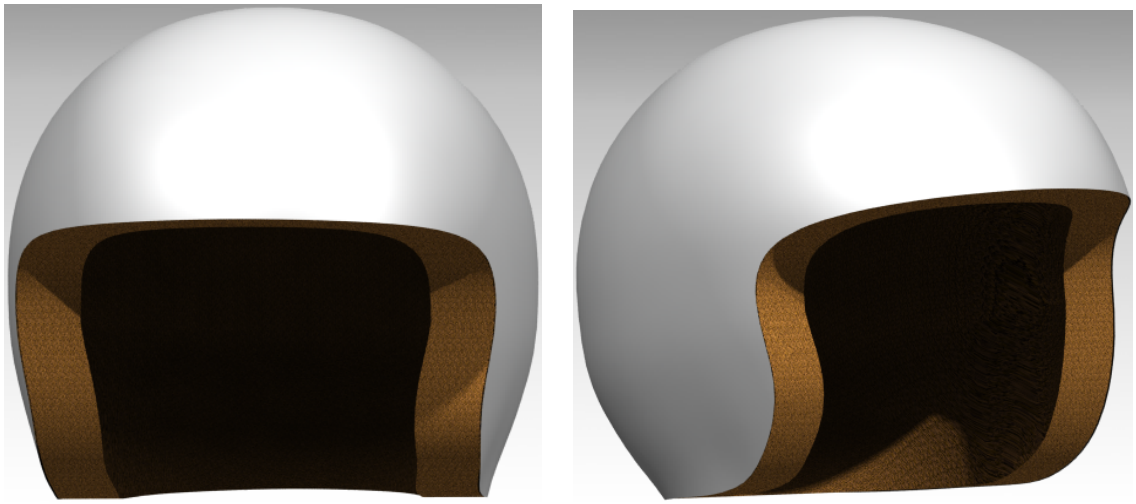

Figure 6.1: New jet helmet with constant thickness liners made of agglomerated cork.

Other versions with lower thicknesses were created. A 5 mm thickness variation was set between liners. Thus, four helmet models were created with a thickness of 40, 35, 30 and 25 mm. These were then imported into Abaqus FEA software in order to develop the FE versions of these helmets. As in the previous chapter, only the helmet's shell and

energy absorbing liner were modelled, being considered the main and most important parts regarding the helmet impact performance. The shells have a thickness of 3 mm, which is independent of the liner thickness.

The FE helmet models were created using four-node linear tetrahedral elements to mesh the liner. This type of element was used to model it mainly due to its complex geometry. On the other hand, the shell was modelled with four-node linear shell elements with enhanced hourglass control. The meshes were created always avoiding distorted and warped elements. Additionally, special attention was given to the time increment, not having very small elements in order to have a reasonable computation time but at the same time a mesh refined enough to obtain precise results. Fig. 6.2 shows the mesh of the FE helmet model.

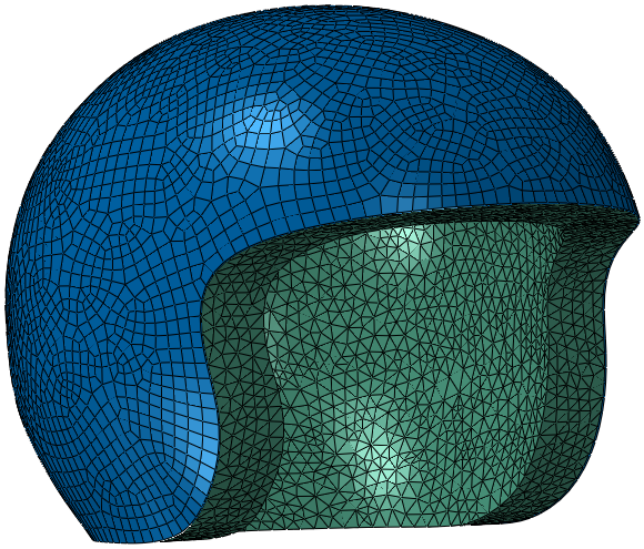

Figure 6.2: FE helmet model.

The helmets were tested according to the conditions required by the ECE 22.05 standard. Additionally, two impacts with the same conditions were performed. The impact point B was chosen because it is the most common impact. Statistics show that independently of the helmet type, this is the most impacted area [Becker et al., 2015, Brugger et al., 2010, DeMarco et al., 2016, Klug et al., 2015, McIntosh et al., 1998, Post et al., 2014, Rice et al., 2016, Richter et al., 2001, Rowson and Duma, 2011]. In addition, in the previous chapter, this was the impact point where the EPS helmet had lower accelerations (Fig. 5.21), although brain injuries were predicted with YEAHM. The one made of AC216 agglomerate presented at this point a 50% deformation for a thickness of 50 mm, not reaching densification (Figs. 5.25 and 3.21).

Thus, two impacts are consecutively performed at 7.5 m/s. Double impacts were defined with basis on another premise of this work and already verified in chapter 3. Generally, cork agglomerates are able to recover and withstand multi-impacts whereas synthetic foams absorb impact energy by deforming permanently.

The second impacts were performed immediately after the first, usually separated by 5 ms. This is challenging for agglomerated cork since its recover depends on the time. If a good behaviour is observed in such conditions, a helmet with this material could be an excellent alternative to the ones used in contact sports such as American football and ice hockey. The standards of these usually test helmets with low multi-impact energies and

with long recovering times between impacts.

The interactions between the different parts were the same ones defined in the previous chapter. Additionally, the same material models and properties used in the previous chapter to simulate ABS, EPS and the AC216 agglomerate were also used. Fig. 6.3 shows the impact at point B and a cut of the helmet revealing its constant thickness.

In order to evaluate the applicability of agglomerated cork as helmet liner, the performance of each helmet will be analysed with YEAHM, by comparing its predictions with the injury criteria presented in section 2.3.4. In other words, this can be considered a biomechanical optimisation of a helmet composed of agglomerated cork liners, by varying its thickness. The best one will be compared against an EPS helmet with the same geometry. Thus, the main goal is to determine if agglomerated cork is an alternative to EPS liners. In order to evaluate that, the liners are optimised in terms of thickness based on the YEAHM response to double impacts.

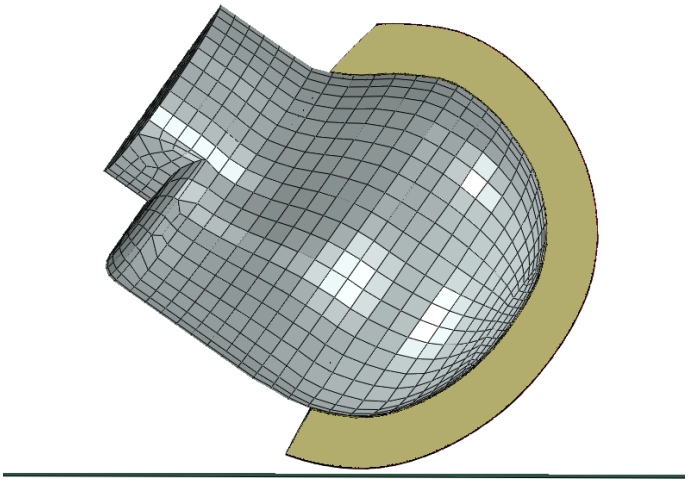

Figure 6.3: Sagittal cut view of the FE helmet model positioned for an impact point B.

In order to reduce the computational resources needed for a singular simulation, two different steps were performed in order to assess the helmet models with YEAHM. First, the headform was coupled to the helmet model and the impacts were simulated. Then, the measured kinematics were induced to YEAHM. This is also the procedure usually carried out in other studies. For instance, a similar analysis was performed by Tinard et al. [2012b], simulating two simpler simulations. In other others, it is better to simulate two simpler simulations, than a extremely complex one with a huge amount of computational resources consumed.

Tinard et al. [2012b] optimised a motorcycle helmet based on the predictions of a FEHM, which is very similar to the work performed in this chapter. Nevertheless, the focus was the helmet shell which was optimised by varying its thickness and shape. Thus, FEHMs can be used to optimise protective head gear, such as helmets.

The modelling of biomechanical human head models using FEM provides a strong basis for helmet design improvements, allowing a further accurate computational-based prediction of brain injuries. For instance, stress and strains are compared against proposed injury thresholds, and conclusions about possible brain injuries are inferred. By using YEAHM as a tool to optimise the thickness of the liner made of agglomerated cork, the objective is to find a configuration capable of not reproducing injuries, or with a injury risk as low as possible and lower than EPS.

After determining the best solution for agglomerated cork, exactly the same helmet will be tested with EPS in order to establish a further and direct comparison. This is important to verify if a helmet composed of agglomerated cork liners is an alternative to the ones made of EPS.

6.2 Results

The double impact simulations were performed using Abaqus Explicit solver. Four simulations were performed, one for each thickness of 25, 30, 35 and 40 mm. Fig. 6.4 shows the measured accelerations at the COG of the headform. These were obtained for liners with different thicknesses and made of AC216 agglomerate.

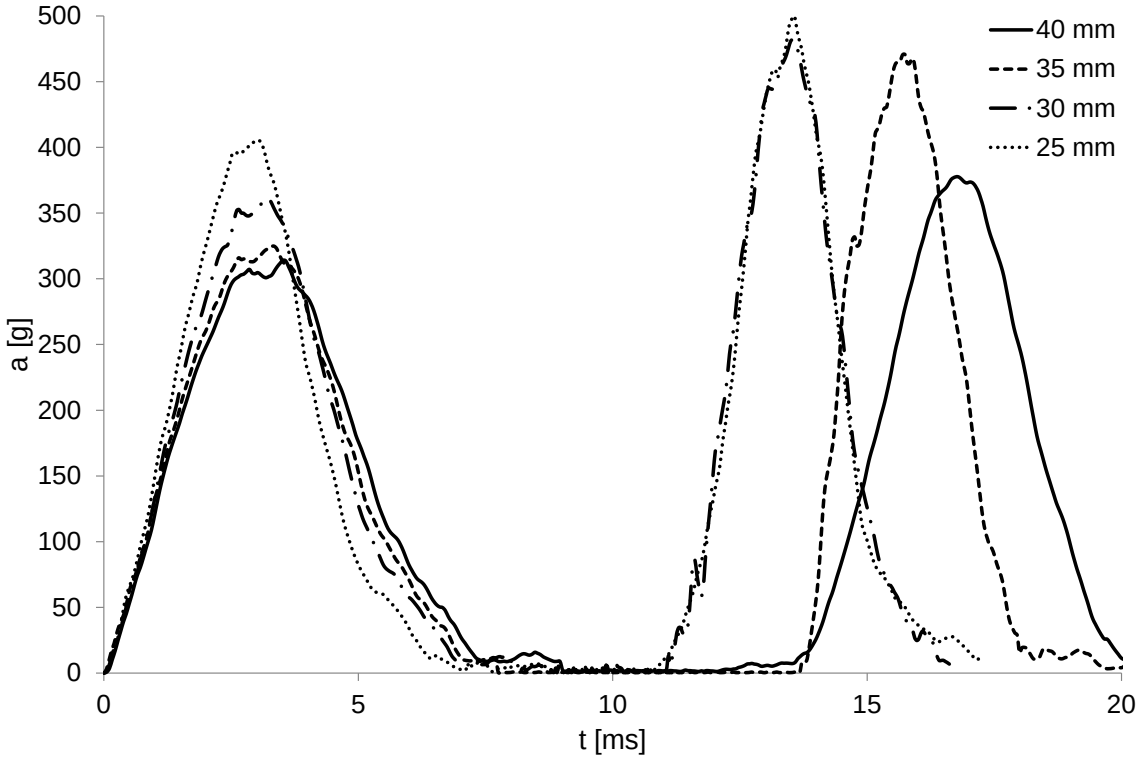

Figure 6.4: Acceleration-time history of double impacts performed with helmets composed of agglomerated cork liners with thicknesses ranging between 25 and 40 mm.

The results from the simulations of the double impacts show a better response in terms of maximum acceleration by the helmet with a liner thickness of 40 mm. This was slightly better than the one with 35 mm for the first impact, and in the second one, it was clearly better. In Fig. 6.4, the difference between peak accelerations seems to differ for the first and the second impacts. Table 6.1 gives precisely the peak accelerations measured for each impact.

Table 6.1: Peak accelerations measured for each impact [g].

Impact	25 mm	30 mm	35 mm	40 mm
First	405.5	361.5	324.7	314.1
Second	499.9	482.2	470.6	377.7

In the first impact, by decreasing the thickness, the variation of the peak accelerations increases. On the other hand, in the second impact, the opposite is observed. Lowering the thickness leads to a peak acceleration limit, since similar results were computed for liners with thicknesses of 35, 30 and 25 mm, reaching almost 500 g. This is explained by the amount of deformation imposed to the material, reaching the densification regime. The time between impacts is so small that the material does not recover in time from the previous impact, starting the second impact with stored deformations higher than 10%. This explains the similar results for the second impacts with thicknesses lower than 40 mm.

Figs. 6.5 and 6.6 show the maximum deformation in both impacts with liner thicknesses of 35 and 40 mm, respectively. In Fig. 6.5, although the densification regime is not reached during the first impact (maximum deformation of 50.2%), due to the stored strain energy that was not released in time for the next impact, this regime is reached by exceeding a strain of 60%. On the other hand, the maximum deformation of the liner with a thickness of 40 mm was lower than 50% for both impacts.

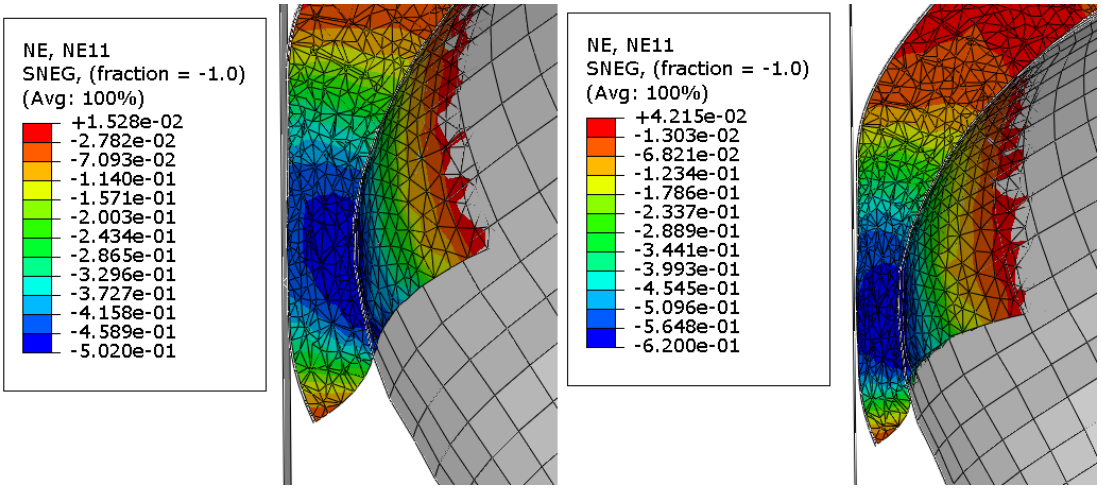

Figure 6.5: Maximum deformation of a liner with a thickness of 35 mm: left) first impact; right) second impact.

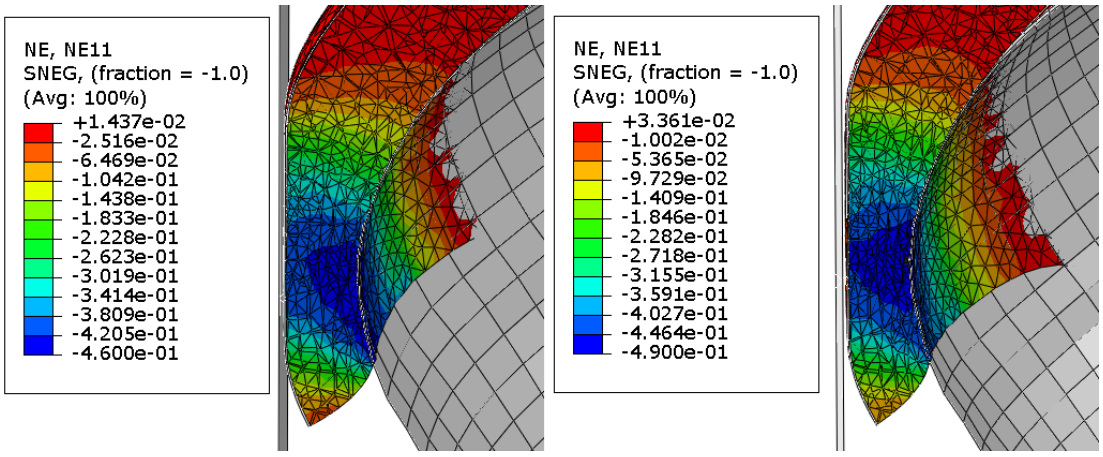

Figure 6.6: Maximum deformation of a liner with a thickness of 40 mm: left) first impact; right) second impact.

These results emphasise the applicability of agglomerated cork in multi-impact applications. In this section, severe impact conditions were imposed, by performing two impacts of 7.5 m/s separated by a time of approximately 5 ms. The helmet standards of more demanding applications, such as motorcycle standards, usually demand one impact at the same velocity used in these simulations, or two impacts but with lower impact velocities.

Helmet standards for multi-impact applications, such as contact sports, usually require at least three impacts, but with significant lower energies. Additionally, independently of the standard or application, the helmets are tested with minutes separating the impacts, which is more than enough for agglomerated cork to recover. Even in real impact scenarios, an agglomerated cork helmet will probably fully recover. The presence of some permanent damage will depend on the severity of the impact. However, as seen in chapter 3, a huge amount of impact energy is necessary to cause permanent deformation in the AC216 agglomerate.

6.2.1 Helmet evaluation and optimisation based on the YEAHM response

Although the helmet with a thickness of 40 mm presented a better response regarding the acceleration curves plotted in Fig. 6.4, an additional analysis was performed with YEAHM. This analysis is considered important in order to assess the helmet from a biomechanical point of view.

This evaluation consists in determining the risk of head injuries for each helmet thickness. Thus, it is possible to compare the helmets in order to determine which thickness makes it safer. In order to perform such analysis, the acceleration-time histories given in Fig. 6.4 were used to drive YEAHM, by inducing them to YEAHM's skull. The criteria and respective thresholds previously reviewed in section 2.3.4 are used together with YEAHM to perform an injury risk analysis. Table 6.2 summarises the maximum values computed for each criterion.

Table 6.2: Comparison of head injury criteria values computed for each helmet thickness.

Criterion	25 mm	30 mm	35 mm	40 mm
Strain	0.5125	0.5250	0.4917	0.3833
von Mises stress [kPa]	218.7	204.2	198.8	134.2
Pressure [kPa]	745.8	823.3	846.7	691.7
CSF pressure [kPa]	482.5	483.7	434.2	291.7
CSF strain energy [mJ]	15506.2	15488.2	16219.8	12481.2

The results presented in table 6.2 show a better performance by the thicker helmet. In the analysis with YEAHM, the lower values for the criteria given in table 6.2 were computed with the 40 mm thick helmet. There is a considerable difference between the results computed for this helmet and the results computed for the remaining ones. On the other hand, the latter were similar to each other. These results were expected since the impacts were linear and the significant lower accelerations were computed for the 40 mm thick helmet.

In addition to the results presented in table 6.2, the CSDM criterion was also evaluated (section 2.3.4). The helmet with a thickness of 40 mm was the only one with a CSDM level inferior to 22, contrary to the others with which strains over 0.15 were observed in the cerebellum, corpus callosum and occipital and temporal lobes. Nevertheless, a CSDM level of 5 was determined for the 40 mm thick helmet, with strains higher than 0.15 in the occipital lobes. Fig. 6.7 shows the affected region, where the colours indicate strains higher

than 0.15. Nevertheless, only this CSDM threshold proposed by Bandak et al. [2001] was exceeded.

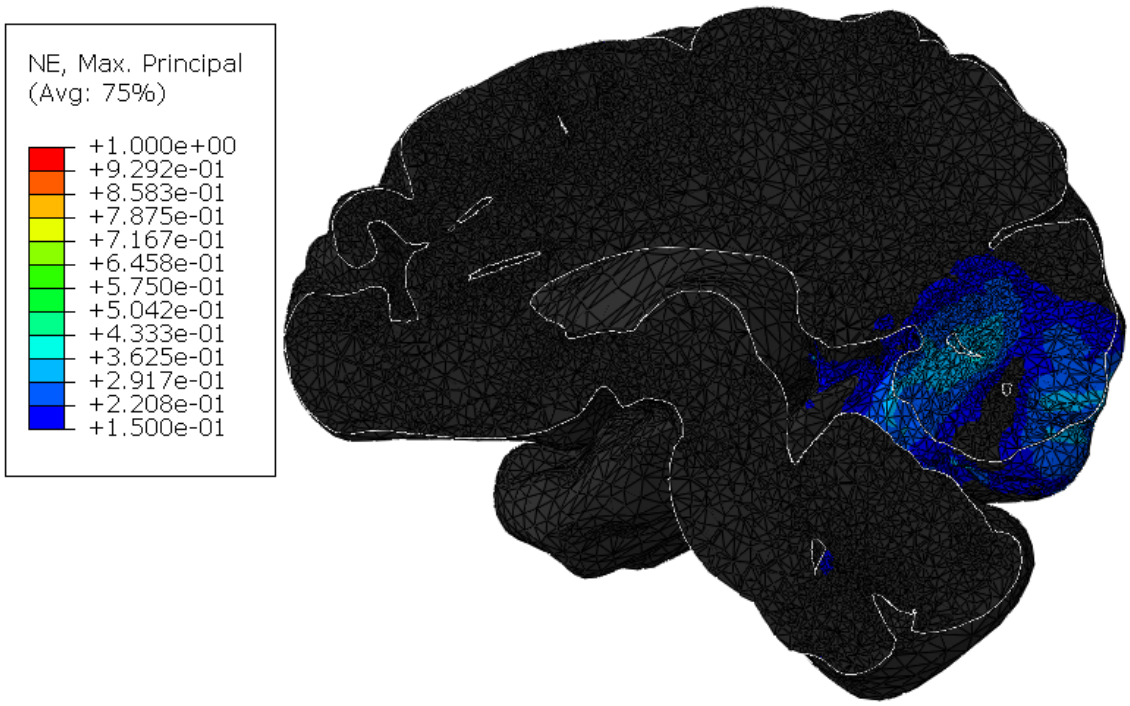

Figure 6.7: Sagittal cut of the brain showing the regions with strains higher than 0.15.

In general, the results given in table 6.2 correspond to very localised regions. In other words, the maximum values for each criterion were experienced in very small volumes, which may explain why some maximum pressure values are not linear with the peak accelerations, as other parameters are. The rest of the brain usually experiences much lower values for each criterion.

However, this difference is not so significant for brain pressure. A considerable volume of the frontal lobes is under pressures almost in the level of its maximum value. This was verified in all the impacts with these fours helmets and also in the ones performed in the previous chapter.

Additionally, by comparing the results in table 6.2 with the thresholds presented in the literature, injuries are predicted with all the helmets. The only one that did to exceed all the limits was obviously the 40 mm thick helmet. For some criteria, it has values in the range of given thresholds, between the lower and the higher ones. However, this was only verified for strain, CSDM, DDM and CSF pressure.

The levels of brain pressure and von Mises stress in the brain were much higher than the proposed thresholds in the literature. These high predicted values cannot be justified with just the helmet response. Contrary to the majority of strain thresholds experimentally measured and proposed in the literature, the pressure and von Mises stress thresholds were proposed based on predictions of FEHMs. This means that these values are inherent to the respective models. Additionally, the pressure response of all these FEHMs was validated by comparing their predictions with the experimental tests performed by Nahum et al. [1977], as it was performed for YEAHM in chapter 4.

However, the results used to validate these models were taken directly from the brain model, which does not correspond to what was really done in Nahum's experiment. In this,

the faces of the pressure transducers were placed aligned with the inner surface of the skull, without rupturing the dura mater. Thus, the pressure was measured directly at the outer surface of the dura mater and not in the brain. The same was done when validating YEAHM for Nahum's experiment. This fact may explain the higher values computed with YEAHM when compared with the ones proposed in the literature. Therefore, accident reconstructions must be done to develop the YEAHM's own criteria.

However, strain based injury criteria is considered valid for a direct comparison and injury prediction, since the YEAHM brain motion was validated against the tests performed by Hardy et al. [2001] in the same conditions of the other FEHMs used to propose the strain thresholds. Additionally, the pressure and stress predictions were considered good enough for further comparisons between the different helmets. In order to determine if agglomerated cork is truly an alternative to EPS as helmet liner, the exactly same helmet with a 40 mm thick liner made of EPS was subjected to the same impact conditions. The headform kinematic response in these impacts was then used to perform an additional analysis with YEAHM.

6.2.2 Comparison between agglomerated cork and EPS

In this section, the best solution found in the previous stimulations is now tested in the same conditions but with an EPS liner. This is performed in order to compare it against the best agglomerate solution. In other words, this new analysis is performed in order to verify if a helmet composed of agglomerated cork liners is truly an alternative to the ones made of EPS. Fig. 6.8 compares the acceleration-time histories measured at the headform's COG during double impacts performed for the same 40 mm thick helmet, between liners made of AC216 cork agglomerate and EPS90.

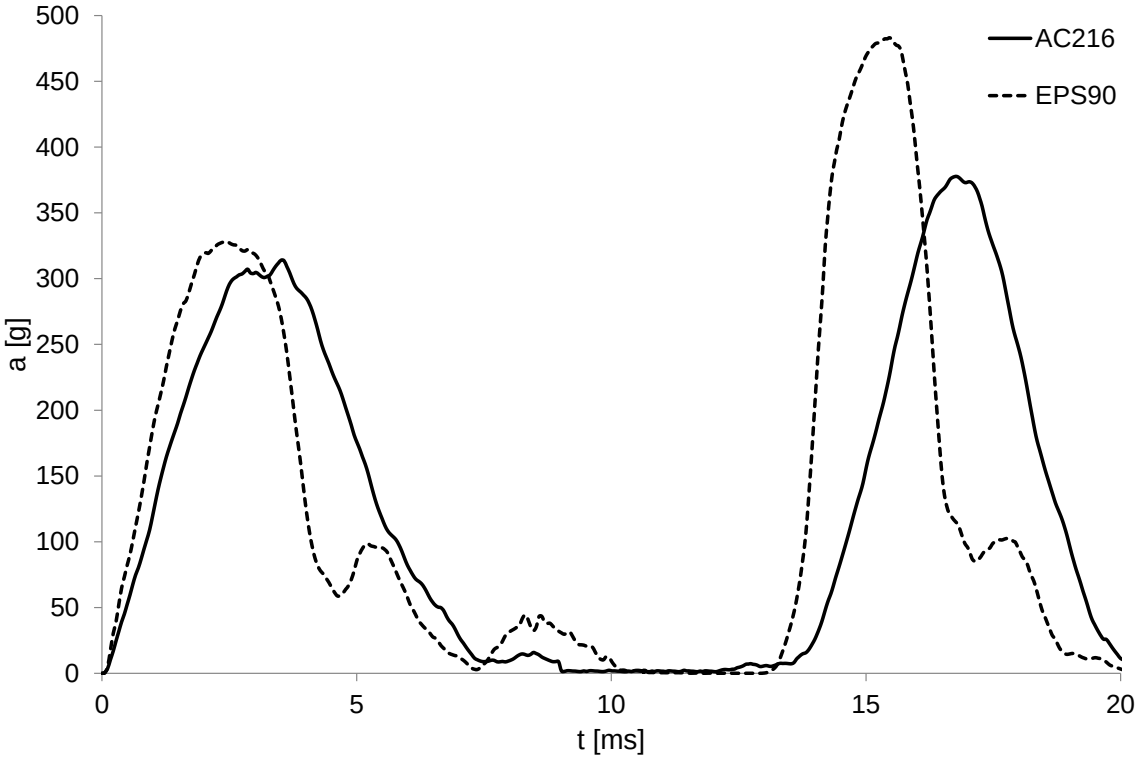

Figure 6.8: Acceleration-time history of 40 mm thick helmets subjected to double impacts.

Regarding the acceleration response of the headform, the helmet with an agglomerated cork liner performed better than the one with EPS. For the first impact, the acceleration curves are similar. Nevertheless, the helmet with the agglomerated cork liner managed to induce a slightly wider acceleration curve with a lower peak acceleration. The difference between peak accelerations was also very small, reaching 314.1 g and 328.3 g for AC216 and EPS90, respectively.

However, this difference increased considerably for the second impact. Acceleration peaks of 377.7 g and 483.1 g were measured for AC216 and EPS90, respectively. In Fig. 6.8, it is clear the different headform response between the helmets made of agglomerated cork and EPS. Actually, by analysing the curves in Figs. 6.4 and 6.8, it is possible to conclude that the results of the 40 mm thick helmet made of EPS and the 35 mm thick helmet made of AC216 agglomerate are very similar, regarding both the curves peak and width.

These results show a clear worst behaviour of the EPS helmet than the one with the same amount of AC216 agglomerate for a second impact. In addition, the results were better for a first impact. This was not the case for the first impact with the commercially available helmet modelled in the previous chapter. By comparing Figs. 5.21 and 6.8, it is possible to conclude that the results for AC216 improved slightly and the ones for EPS become worst. This difference was caused by two main factors: the thickness of the liner at the impact points and the overall geometry of the liners.

The liner of the helmet tested in the previous chapter has an average thickness of 50 mm at the impact point. In addition, the thickness is not constant and in some regions has channels, holes and ribbed protrusions. Some of these were designed together with the deformation mechanism of EPS, which makes it easier to absorb more energy by developing permanent deformation. On the other hand, the helmet developed in this chapter has a constant thickness of 40 mm, being at least 10 mm thinner at the impact points. This liner is also completely solid, a 40 mm thick layer covering the head. These are the reasons why the EPS behaviour was worst in the first impact.

Regarding the AC216 agglomerate, the results indicate the 40 mm thick solution as the best in the range of tested thicknesses (20, 25, 30, 35, 40 and 50 mm). Additionally, in the same conditions with the same helmet geometry, this solution performed better than the EPS alternative. Although some conclusions were already drawn from the comparison of headform acceleration responses, an additional analysis was performed. These acceleration-time curves were used to drive YEAHM in order to compare both solutions from a biomechanical point of view.

The same parameters used to compare the different thickness solutions for the AC216 liner and presented in table 6.2 were again computed in order to compare the 40 mm thick liners made of AC216 and EPS90. Table 6.3 summarises the maximum values computed for each criterion.

Table 6.3: Comparison of head injury criteria computed for helmets with liners made of AC216 and EPS90.

Criterion	EPS90	AC216
Strain	0.5067	0.3833
von Mises stress [kPa]	191.7	134.2
Pressure [kPa]	840.9	691.7
CSF pressure [kPa]	459.4	291.7
CSF strain energy [mJ]	12611.5	12481.2

The results presented in table 6.3 show a better performance by the agglomerated cork helmet. In the analysis performed with YEAHM, lower values for all the criteria were computed with the helmet composed with a liner made of AC216 agglomerate. There is a considerable difference between some of the results computed for this helmet and the one made of EPS.

Considering the tables 6.2 and 6.3, the results for the agglomerated cork helmet with a thickness of 35 mm are very similar to the ones computed with the 40 mm thick EPS helmet. This may be considered normal since input was also similar, especially considering the peak of the acceleration curves. Nevertheless, a significant difference was observed for the maximum CSF strain energy. Actually, the CSF strain energy computed with the EPS helmet was very similar the one computed with the 40 mm agglomerated cork version. This can be explained by the acceleration curve obtained with the EPS helmet, which is narrower than the one computed for the 35 mm cork version. This possibly leads to a lower storage of strain energy by the CSF, reaching a lower maximum value. Fig. 6.9 shows the variation of strain energy in the CSF during the impacts for both 40 mm helmet versions.

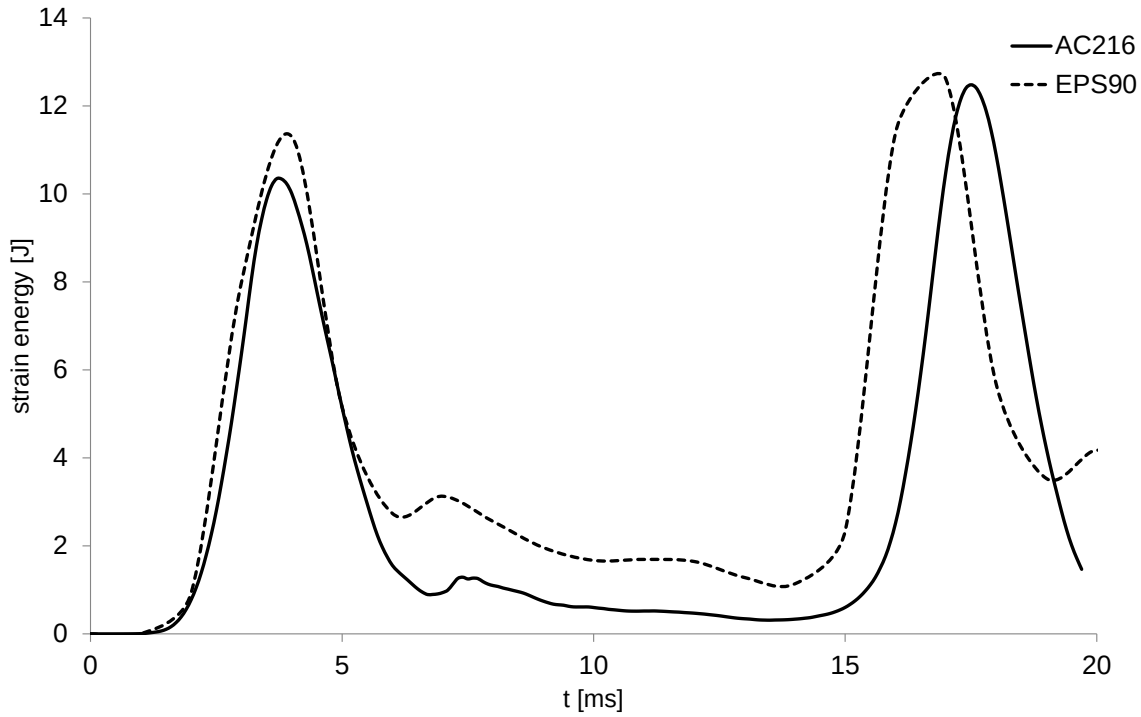

Figure 6.9: CSF strain energy variation during the impacts for both 40 mm helmet versions.

In addition to the results presented in table 6.3, the CSDM criterion was also evaluated. In the previous chapter, the agglomerated cork helmet with a thickness of 40 mm was the only one with a CSDM level inferior to 22. Nevertheless, a CSDM level of 5 was determined for it, with strains higher than 0.15 in the occipital lobes, as shown in Fig. 6.7. Even so, this was the only CSDM threshold exceeded. Regarding the EPS helmet, a CSDM level of 22 was found considering the strain limit of 0.15. This was found across the the cerebellum, corpus callosum and temporal and occipital lobes. Higher and concentrated values were found in the latter. Fig. 6.10 shows the strain distribution across the brain at the moment the maximum strain was found in the occipital lobes. Other dark regions in Fig. 6.10 exceeded the strain of 0.15 during the impact, which contributed to a CSDM level higher than 22.

In conclusion, the helmet composed by a 40 mm thick liner made of the AC216 cork

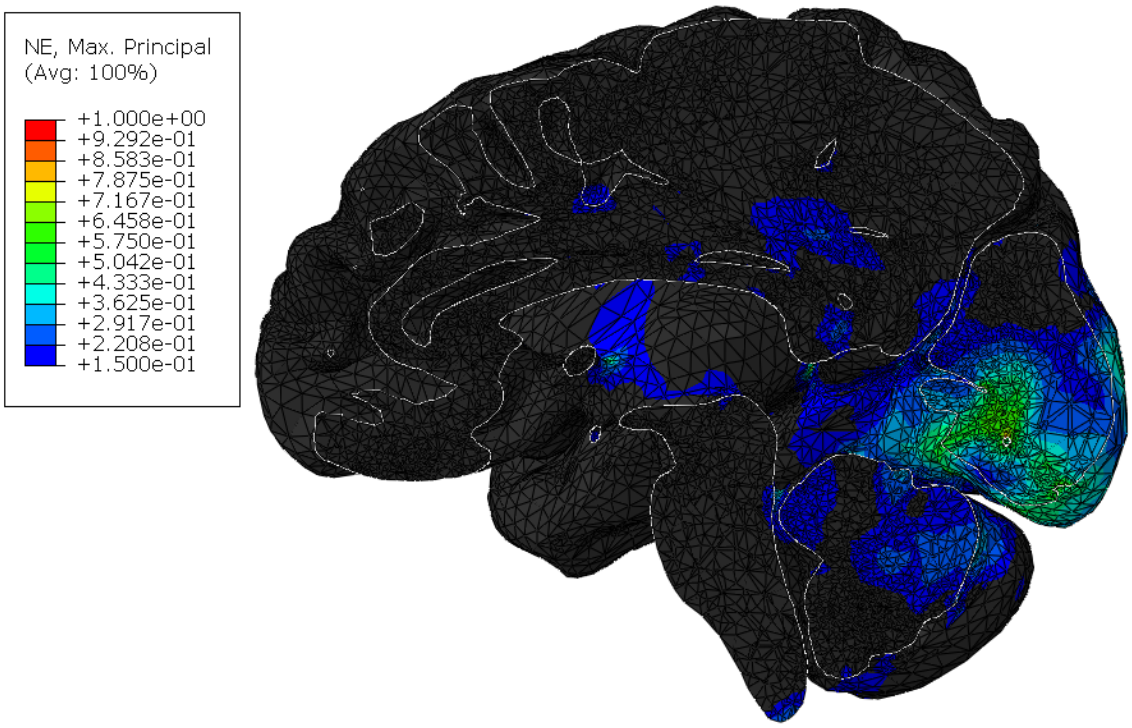

Figure 6.10: Brain strain distribution obtained with the EPS helmet.

agglomerate performed better than the EPS version. Thus, agglomerated cork can be considered a good alternative to EPS, especially for helmets typically subjected to multi-impact scenarios. In addition, the agglomerated cork helmet performed better for both impacts, although the difference was more significant in the second impact. Even so, it is considered that there is still a margin for improvement considering what was seen in this study regarding some injury predictions. However, this is a good starting point for a further optimisation of helmets made of cork. Here it was seen that with the right design, agglomerated cork can be used as a helmet liner with a better performance than other materials currently used on the market.

The model here developed is rather simple, considering its constant thickness. The thickness in some regions of the helmet can be reduced, for instance where the impacts are less likely to occur, such as the rear sides of the helmet. Thus, by reducing the liner volume, the helmet weight is also reduced, which means lower impact energies. In addition, the liner geometry may be upgraded with an innovative design that allied with the mechanism of cork deformation can optimise the general impact behaviour and hopefully improving the safety level of the helmet. This may also allow reducing even further the helmet thickness.

In addition, it is worth mentioning and recall that the double impacts performed in this study were severe, since there were two consecutive impacts separated by approximately 5 ms. These are more severe than most of the tests required by the helmet standards. These are usually one impact, with maximum velocities around 7.5 m/s for motorcycle helmets or even lower for other helmet types. There are also standards that require two impacts but these are lower energy impacts and the time between impacts is around minutes.

In applications where multi-impacts are often such as winter sports like skiing and snowboarding, contact sports such as American football and ice hockey and even urban activities such as roller skating and skateboarding, the impacts are spaced by enough time to

let agglomerated cork fully recover. In addition, in some of these, the impact velocities are much lower than 7.5 m/s causing none or just a small amount of permanent damage to cork.

Chapter 7

Conclusions and future work

This chapter presents the general and main conclusions, and discuss the results obtained in this work. In addition, some research ideas that may be implemented in related future works are suggested.

7.1 Conclusions

Nowadays, consumer awareness and go-green tendencies are pushing manufacturers to provide eco-friendly alternatives to current market solutions. Currently, goods based on natural materials are mostly designed to mimic the original synthetic product. Nevertheless, more than mimicking, the improvement of existing functionalities of products that resort to synthetic materials is also important.

Currently, a great variety of personal safety gear employs energy absorption liners. Examples are sport accessories, protective vests and helmets, among others. The vast majority of these liners are usually made of synthetic cellular materials, such as EPS. These materials are able to absorb reasonable amounts of energy by deforming permanently.

In a society continuously searching for new environmentally friendly and sustainable resources, a material such as cork can be a natural alternative to synthetic materials. Cork is a natural cellular material capable of absorbing great amounts of energy. In addition, cork recovers almost entirely after deformation, which is a desirable characteristic in multi-impact applications.

In general, helmets are subjected to significant multi-impact loads. Helmet liners are usually made of EPS, which absorbs impact energy by deforming permanently. Thus, helmet liners are an interesting application for cork. Therefore, the main objective of this work was to analyse the applicability of agglomerated cork as energy absorption liner in personal safety gear. More specifically, it was analysed if agglomerated cork is an alternative to EPS helmet liners.

Helmets are one of the most important types of personal safety gear. An impact to the head can have serious consequences and could even be fatal. Thus, head protection and safety helmets are a matter of extreme importance.

Currently, helmets are used in a large number of different applications, for instance in contact sports, in urban and winter activities and even by bicyclists and motorcyclists, among many others. Although each of these applications has different technical require-

ments, there is no substantial difference in the energy absorption between the different types of helmets. The material is almost always EPS and even the geometries are similar.

In order to assess the applicability of agglomerated cork as energy absorption liner and its capacity to be an alternative to current liners made of EPS, several steps were performed. First, experimental tests were performed on different types of agglomerated cork and EPS samples in order to characterise these materials. Quasi-static and impact tests were performed, including double impacts, which were important to select the most promising cork agglomerates.

The latter were performed in order to evaluate the behaviour of both materials when subjected to more than one impact, and to validate the numerical models for multi-impacts. Constitutive models with a proper set of mechanical properties were validated with success, by simulating the experiments performed in this work. Additionally, it was the first time that such a combination of constitutive models was used to simulate the mechanical behaviour of cork. Until this moment, agglomerated cork has been modelled as a pure hyperelastic model with no consideration for its recovery. The combination of a modified hyperelastic model such as hyperfoam with the Mullin's effect has made it possible to correctly model the recovery of cork, which is fundamental for a precise modelling of this material under multi-impact loads. It was also the first time that agglomerated cork was experimentally subjected to multi-impacts. In the end, the material models were validated with success for several impact tests performed in this study and even for some available in the literature. These were then used in the helmets modelling.

In order to assess the helmet models from a biomechanical point of view, a FEHM was developed and validated. Once validated, such a tool allows the evaluation of injuries that may be a possible outcome from head impact scenarios. The current FEHMs, presented in the literature, disregard the modelling of sulci and gyri structures, modelling a spherical-shaped brain with a smooth surface. The geometric modelling of YEAHM, the FEHM developed in this work, was carried out precisely, by modelling these structures according to medical images. Sulci and gyri structures should be included in every FEHM, since they influence the intracranial kinematics and probably the way brain deforms, as concluded by Ho and Kleiven [2009].

In addition to this innovative modelling of the brain, the interaction between the head parts was modelled differently from the majority of the FEHMs in the literature. These usually have the different parts connected by shared nodes or rigidly connected nodes, restricting the brain intracranial motion relatively to the skull. In this work, the interactions were modelled by sliding surfaces with a friction coefficient, allowing the brain to move relatively to the skull. Finally, YEAHM was validated against two different experiments, Nahum et al. [1977] and Hardy et al. [2001]. In these, the intracranial pressure and brain motion were the data used to perform the validation.

In this work, two FE helmet models were developed. The first one corresponds to a motorcycle helmet with EPS liner available in the market and certified by some standards, including the one that regulates the helmets in some European countries, such as the case of Portugal. The ECE 22.05 standard requires one impact with a helmeted steel headform at an impact velocity of 7.5 m/s, establishing as criteria the peak linear acceleration and HIC. These have been criticised by the research community as bad quality criteria for helmets approval. This was one of the motivations for YEAHM development. Nevertheless, these criteria are still considered good for comparisons, just not as approval criteria. Therefore, the helmets here developed were assessed with YEAHM, by comparing its predictions with the injury thresholds presented in the thorough state-of-the-art performed in this thesis.

This first helmet, the one certified by the ECE 22.05 standard, was modelled and validated by performing the same four impact tests used to certify it, by comparing the acceleration responses between simulations and experiments. Then, these curves were used to drive YEAHM in order to analyse the helmet from a biomechanical point of view. This methodology was adopted due to the high computational resources needed to perform a simulation with YEAHM coupled with the helmet model. In addition, this is the methodology used by the other researchers to drive their models. The skull is set as rigid in order to induce the kinematics to the model. This is valid if there is no skull fracture or other types of skull deformation, which is usually the case of helmeted impacts. In these, injuries to the intracranial contents are the common ones. From the analysis with YEAHM, in all the four impacts required by the ECE 22.05 standard, it was identified a risk of injury, showing that an EPS liner might not be enough to protect its user.

Thus, it was concluded that a certified helmet was not capable of protecting its user in the same impacts used to certify it. Based on this, a direct comparison was performed between EPS and agglomerated cork by evaluating the exactly same helmet with agglomerated cork liners. The same geometries and impact conditions were used, just the liner material was changed. The computed acceleration-time curves indicated the EPS helmet as the better one with a considerable difference for some of the impacts. Nevertheless, the agglomerate AC216 showed some promising results, even closer to the ones obtained with the EPS helmet for the impact points B and X. Considering this and the fact that this helmet is significantly thick, around 50 mm at the impact points, with exception of the point X where it has 40 mm, a new helmet model was developed.

In some of the last standards updates, the required impact energies become higher and in some, more impacts are required, which led to thicker EPS helmets. A thinner liner made of AC216 agglomerate is enough to absorb the impact energy in the same tests without increasing the stress level, since the liner maximum deformation in the previous helmet was around 50%. Thus, a new helmet model was developed, based on the 40 mm thickness seen for impact X. This is already a considerable thickness, which is usually exceeded in the current helmets. Considering that the last updates in standards are demanding more impacts or higher energies, helmet liners are becoming even thicker.

Thus, for the second helmet model, a maximum and constant thickness of 40 mm was set for the liner. Four other models were created by decreasing the thickness with intervals of 5 mm. These were assessed with YEAHM in order to optimise the helmet thickness according to biomechanical criteria. Then, double impacts were performed and the kinematic response of the headform was used to drive YEAHM. The helmet with a thickness of 40 mm computed the best results, having the best headform acceleration and YEAHM responses to the double impacts performed.

In order to determine if cork is truly an alternative to EPS as helmet liner, the same helmet with a 40 mm thick liner made of EPS was subjected to the same impact conditions. The results were clear, the helmet composed by a 40 mm thick liner made of the AC216 cork agglomerate performed better than the EPS version. Thus, agglomerated cork can be considered a good alternative to EPS, especially for helmets typically subjected to multi-impact scenarios. In addition, the agglomerated cork helmet performed better for both impacts, although the difference was more significant in the second impact. Even so, it is considered that there is still a margin for improvement considering what was seen in this study regarding some injury predictions. However, this is a good starting point for a further optimisation of helmets made of cork. Here it was seen that with the right design, agglomerated cork can be used as a helmet liner with a better performance than other materials currently used in the market.

In addition, it is worth mentioning and recall that the double impacts performed in this study were demanding, since there were two consecutive impacts separated by approximately 5 ms. These are more severe than most of the tests required by the helmet standards. These are usually one impact with maximum velocities raging between 4 and 8 m/s, depending on the helmet type. There are also standards that require two impacts but these are even lower energy impacts and the time between them is around minutes.

In applications where multi-impacts are common, for instance winter sports such as skiing and snowboarding, contact sports such as American football and ice hockey and even urban activities such as roller skating and skateboarding, the impacts are spaced by enough time to let agglomerated cork fully recover. In addition, in some of these, the impact velocities are lower than 7.5 m/s causing none or just a small amount of permanent damage to cork.

Cork application is not limited to helmets and has the potential to be applied in other types of personal safety gear or even in other applications where its characteristics are desirable. In a society constantly looking for natural and sustainable resources, substituting a synthetic material such as EPS by a natural material like cork is a good solution.

7.2 Future work

Considering the conclusions previously presented, the following future work is suggested:

- Development of new cork agglomerates, by controlling the granules size and the binder. Thus, creating guidelines for manufacturing cork for specific applications;
- Further optimisation of the best helmet solution found in this study;
- Modelling of more intracranial contents in order to make YEAHM more accurate;
- Development of a model capable of simulating skull fractures, which is necessary at least for non-helmeted impacts;
- Development of YEAHM's own specific injury criteria by reconstructing real accidents;
- Development of a new and environmentally friendly helmet, completely made of natural materials.

A helmet completely made of natural materials is possible if the first point is also considered, since a cork agglomerate such as AC216 is manufactured with a PU based resin. This means that in order to develop a 100% natural helmet, natural resins must be used to develop new and completely natural agglomerates. Nevertheless, the price of natural resins may be a problem. Another option is the development of new black agglomerates, better than the ones tested in this study, since no binder is added in its manufacturing. The other parts of the helmet may be accomplished with a combination of natural fibres, natural resins and even wood.

The helmet model here developed is rather simple, considering its constant thickness. The thickness in some regions of the helmet can be reduced, for instance where the impacts are less likely to occur, such as the rear sides of the helmet. Thus, by reducing the liner volume, the helmet weight is also reduced, which means lower impact energies.

In addition, the liner geometry may be upgraded with an innovative design that allied with the mechanism of cork deformation can improve the impact response and hopefully the

safety level of the helmet. This may also allow reducing even further the helmet thickness. Additionally, this design allied with new agglomerates can be used to optimise each helmet according to its type and application. The application of cork in other types of personal safety gear can also be explored.

In this study, it was verified that YEAHM's pressure predictions were always above the thresholds proposed in the literature. This was explained by the fact that the models used to propose these thresholds were validated differently from YEAHM. Therefore, accident reconstructions must be done to develop YEAHM's own injury criteria. In the future, data from real world head injury accidents must be collected and by reconstructing these same accidents, it is possible to compute specific head injury thresholds for YEAHM.

It is possible that future methods used to assess head injury risk and protective head gear will rely on the predictions from numerical head models, which should hopefully provide robust and accurate assessment of the head injury risk. This might be the way for intelligent helmet design.

References

Aare, M., 2003. Prevention of head injuries focusing specifically on oblique impacts. Doctoral Thesis, Technical Report 2003-26, School of Technology and Health, Royal Institute of Technology, Stockholm, Sweden.

Aare, M., Halldin, P., 2003. A new laboratory rig for evaluating helmets subject to oblique impacts. Traffic Injury Prevention 4(3), 240-248.

Aare, M., Kleiven S., Halldin, P., 2003. Injury criteria for oblique helmet impacts. Proceedings of IRCOBI Conference, Lisbon (Portugal), pp.349-350.

Aare, M., von Holst, H., 2003. Injuries from Motorcycle and Moped crashes in Sweden from 1987-1999. Injury Control and Safety Promotion 10, 131-138.

Aare, M., Kleiven, S., Halldin, P., 2004. Injury tolerances for oblique impact helmet testing. International Journal of Crashworthiness 9(1), 15-23.

ABAQUS 6.10 documentation. Hibbitt, Karlsson & Sorensen, Inc; 2010.

Abel, J.M., Gennarelli, T.A., Segawa, H., 1978. Incidence and severity of cerebral concussion in the rhesus monkey following sagittal plane angular acceleration. Proceedings of 22^{nd} Stapp Car Crash Conference, Society of Automotive Engineers, SAE Paper No. 780886.

ABNT, Associação Brasileira de Normas Tecnicas, 2001. Capacetes de motocicletas e similares. Technical Report NBR 7471:2001, Rio de Janeiro.

Accident Attorneys, 2016. http://accidentattorneys.org/ 26/09/2012

Adams, J. H., 1980. Brain damage in fatal non-missile head injury. Journal of Clinical Pathology 33, 1132-1145.

Adams, J.H., 1986. Gliding contusions in non-missile head injury in humans. Archives of Pathology & Laboratory Medicine 110(6), 485-508.

Adams, J. H., Doyle, D., Ford, I., 1989. Diffuse axonal injury in head injury: definition, diagnosis and grading. Histopathology 15, 49-59.

Adams, J.H., 1992. Head injury. Adams, J.H., Duchen, L.W., (eds) Greenfield's neuropathology. Edward Arnold, London, pp.106-152.

Advani, S.H., Powell, W., Huston, J., Ojala, S.J., 1975. Human head impact response - experimental data and analytical simulations. Proceedings of IRCOBI, Birmingham, pp.153-163.

Advani, S., Ommaya, A., Yang, W., 1982. Head injury mechanisms. In: D.N. Ghista (Ed.), Human Body Dynamics, Oxford University Press.

Aiello, M., Galvanetto, U., Iannucci, L., 2007. Numerical simulations of motorcycle helmet impact tests. International Journal of Crashworthiness 12, 1-7.

Al-Bsharat, A.S., Hardy, W.N., Yang, K.H., Khalil, T.B., Tashman, S., King, A.I., 1999. Brain/Skull Relative Displacement Magnitude Due to Blunt Head Imapact: New Experimental Data and Model. Proceedings of the 43^{rd} Stapp Car Crash Conference, pp.321-Ű332, Paper No. 99SC22.

Alcântara, I., Teixeira-Dias, F., Paulino, M., 2013. Cork composites for the absorption of impact energy. Composite Structures 95, 16-27.

Allsop, D., Warner, C., Wille, M., Schneider, D., Nahum, A., 1988. Facial impact response - a comparison of the Hybrid III dummy and the human cadaver. Proceeding of 32^{nd} Stapp Car Crash Conference, SAE 881719, Atlanta.

Allsop, D., Perl, T., Warner, C., 1991. Force/deflection and fracture characteristics of the temporo-parietal of the human head. Proceedings of 35^{th} Stapp Car Crash Conference, SAE 912907, San Diego, pp.139-155.

Alves de Sousa, R.J., Gonçalves, D.F.S., Coelho, R.M., Teixeira-Dias, F.M.V.H., 2012. Assessing the effectiveness of the use of a natural cellular material as safety padding in motorcycle helmet. Simulation: Transactions of the Society for Modeling and Simulation International 88(5), 579-590.

Amoros. E., Chiron, M., Thélot B., Laumon, B., 2011. The injury epidemiology of cyclists based on a road trauma registry. BMC Public Health 11(1), 1-12.

Anderson, R.W.G., Brown, C.J., Blumbergs, P.C., Scott, G., Finney, J.W., Jones, N.R., McLean, A.J., 1999. Mechanics of axonal injury: An experimental and numerical study of a sheep model of head impact. Proceedings of IRCOBI Conference, Sitges, Spain, pp.107-120

Anderson, R., 2000. A study of the biomechanics of axonal injury. PhD thesis, University of Adelaide.

Anderson, R.W.G., McLean, A.J., 2005, Biomechanics of closed head injury. Head injury: pathophysiology and management, 2^{nd} edition, Reilly, P.L., Bullock, R. (eds), pp.26-40.

Anjos, O., Pereira, H., Rosa, M.E., 2008. Effect of quality, porosity and density on the compression properties of cork. Holz als Roh-und Werkstoff 66(4), 295-301.

Anjos, O., Pereira, H., Rosa, M.E., 2010. Tensile properties of cork in the tangential direction: Variation with quality, porosity, density and radial position in the cork plank. Materials and Design 31, 2085-2090.

Anjos, O., Pereira, H., Rosa, M.E., 2011a. Tensile properties of cork in axial stress and influence of porosity, density, quality and radial position in the plank. European Journal of Wood and Wood Products 69(1), 85-91.

Anjos, O., Pereira, H. Rosa, M.E., 2011b. Characterization of radial bending properties of cork. European Journal of Wood and Wood Products 69, 557-563.

Anjos, O., Rodrigues, C., Morais, J., Pereira, H., 2014. Effect of density on the compression behaviour of cork. Materials and Design 53, 1089-1096.

APCOR, Associação Portuguesa da Cortiça, 2016. http://www.apcor.pt/ 28/07/2016

Aroso, I.M., Fernandes, E.M., Pires, R.A., Mano, J.F., Reis, R.L., 2015. Cork extractives exhibit thermo-oxidative protection properties in polypropylene-cork composites and as direct additives for polypropylene. Polymer Degradation and Stability 116, 45-52.

Asiminei, A.G., Baeck, K., Verbeken, E., Sloten, J.V., Goffin, J., 2011. Investigation on strain rate dependency in the biomechanical behaviour of the Superior Sagittal Sinus - Bridging Vein Complex. Proceedings of IRCOBI Conference, Warsaw, pp.36-39.

Ask Nature. http://www.asknature.org/ 26/02/2012

Bain, B.C., Billiar, K.L., Shreiber, D.I., McIntosh, T.K., Meaney, D.F., 1996. In vivo mechanical thresholds for traumatic axonal damage. Proceedings of AGARD AMP Specialists, Meeting, Mescalero, New Mexico, USA, published in CP-597.

Bain, B.C., Meaney, D.F., 2000. Tissue-level thresholds for axonal damage in an experimental model of central nervous system white matter injury. Journal of Biomechanical Engineering 122(6), 615-622.

Ball, C.G., Ball, J.E., Kirkpatrick, A.W., Mulloy, R.H., 2007. Equestrian injuries: incidence, injury patterns, and risk factors for 10 years of major traumatic injuries. The American Journal of Surgery 193(5), 636-640.

Bandak, F.A., Eppinger, R.H., 1994. A three-dimensional FE analysis of the human brain under combined rotational and translational accelerations. Proceedings of 38^{th} Stapp Car Crash Conference, Society of Automotive Engineers, pp.145-163.

Bandak, F.A., van DerVorst, M.J., Stuhmiller, L.M., Mlakar, P.F., Chilton, W.E., Stuhmiller, J.H., 1994. An imaging based computational and experimental study of skull fracture: finite element model development. Proceedings of the Head Injury Symposium, Washington DC.

Bandak, F.A., 1995. On the mechanics of impact neurotrauma: A Review and critical synthesis. Journal of Neurotrauma 12(4), 635-649.

Bandak, F.A., 1997a. Biomechanics of impact traumatic brain injury. In: Ambrosio, J.A.C., Seabra Pereira, M.F.O., Silva, P.F. (Eds.), Crashworthiness of Transportation Systems: Structural Impact and Occupant Protection, Dordrecht, pp.53-93, Springer Netherlands.

Bandak, F.A., 1997b. Impact traumatic brain injury: a mechanical perspective. In: Neurotraumatology - Biomechanic aspects, cytologic and molecular mechanisms, eds. Oehmichen, M., König, H.G.. Lübeck: Schmidt-Römhild, pp.59-83.

Bandak, F.A., Zhang, A.X., Tannous, R.E., DiMasi, F., Masiello, P., R. Eppinger, 2001. SIMon: a simulated injury monitor: application to head injury assessment. Proceedings of the 17^{th} International Technical Conference on the Enhanced Safety of Vehicles (ESV), Amsterdam, The Netherlands.

Baugh, A.D., Baugh, R.F., Atallah, J.N., Gaudin, D., Williams, M., 2013. Craniofacial trauma and double epidural hematomas from horse training. International Journal of Surgery Case Reports 4, 1149-1152.

Baumgartner, D., 2001. Mécanismes de lésion et limites de tolérance au choc de la tête humaine - Reconstruction numérique et expérimentale de traumatismes crâniens. Ph.D. dissertation, Université Louis Pasteur Strasbourg.

Baumgartner, D., Willinger, R., Shewchenko, N., Beusenberg, M., 2001. Tolerance limits for mild traumatic brain injury derived from numerical head impact replication. Proceedings of IRCOBI Conference, Isle of Man, UK.

Bayly, P.V., Black, E.E., Pedersen, R., et al, 2006. In vivo imaging of rapid deformation and strain in an animal model of traumatic brain injury. J. Biomech. 39, 1086-1095.

Becker, E.B., Anishchenko, D.V., Palmer, S.B., 2015. Motorcycle Helmet Impact Response at Various Levels of Severity for Different Standard Certifications. In: IRCOBI Conference, IRC-15-91

Belingardi, G., Chiandussi, G., Gaviglio, I., 2005. Development and validation of a new finite element model of human head. Politecnico di Torino, Dipartimento di Meccanica, Italy, Paper Number 05-0441.

Bellora, A., Krauss, R., Van Poolen, L., 2001. Meeting Interior Head Impact Requirements: A Basic Scientific Approach. SAE 2001-01-0469.

Besenski, N., 2006. Imaging of Head Injuries. Marincek, B., Dondelinger, R.F., (eds) Emergency Radiology: Imaging and Intervention, Springer, 99-124.

Beusenberg, M.C., Happee, R., 1993. An experimental evaluation of crash helmet design and effectiveness in standard impact tests. Proceedings of IRCOBI Conference, Eindhoven, The Netherlands.

Bilston, L.E., Liu, Z., Phan-Thien, N., 2001. Large strain behaviour of brain tissue in shear: some experimental data and differential constitutive model. Biorheology 38, 335-345.

Bilston, L.E., 2011. Brain tissue mechanical properties. In: K. Miller (Ed.), Biomechanics of the brain, pp.69-89, Springer-Verlag New York.

Blanco, D.H., Cernicchi, A., Galvanetto, U., 2014. Design of an innovative optimized motorcycle helmet. Journal of Sports Engineering and Technology 228(2), 95-110.

Blumbergs, P.C., Scott, G., Manavis, J., Wainwright, H., Simpson, D.A., McLean, A.J., 1995. Topography of axonal injury as defined by amyloid precursor protein and the sector scoring method in mild and severe closed head injury. Journal of Neurotrauma 12, 565-571.

Blumenfeld, H., 2002. Neuroanatomy through Clinial Cases. Sinauer Assoc. Inc, p.122.

Bourdet, N., Deck, C., Tinard, V., Willinger, R., 2012. Behaviour of helmets during head impact in real accident cases of motorcyclists. International Journal of Crashworthiness 17, 51-61.

Brands, D.W.A., 1996. Development and validation of a finite element model of a motorcycle helmet. Master's Thesis, Eindhoven University of Technology, The Netherlands.

Brands, D.W.A., Thunnissen, J.G.M., Wismans, J.S.H.M., 1996. Modelling head injury countermeasures: a 3D helmet model. AGARD Meeting on Impact Head Injury, New Mexico, AGARD conference proceedings, pp.26-1 - 26-8.

Brands, D.W., 2002. Predicting brain mechanics during closed head impact:Numerical and constitutive aspects. Ph.D. dissertation, University of Eindhoven, The Netherlands.

Brands, D.W., Bovendeerd, P.H., Wismans, J.S.H.M., 2002. On the potential importance of non-linear viscoelastic material modelling for numerical prediction of brain tissue response. Proceedings 46^{th} Stapp Car Crash Conference, SAE paper vol 2002-22-0006, pp.103-121.

Brands, D.W.A., Peters, G.W.M., Bovendeerd, P.H.M., 2004. Design and numerical implementation of a 3-D non-linear viscoelastic constitutive model for brain tissue during impact. J. Biomech. 37, 127-134.

Brittany, C., Margulies, S.S., 2006. Material properties of porcine parietal cortex. J. Biomech. 39, 2521-2525.

Broglio, S.P., Schnebel B., Sosnofff, J.J., Shin, S., Feng, X., He, X., Zimmerman, J., 2010. Biomechanical properties of concussions in high school footballbiomechanical properties of concussions in high school football. Medicine and Science in Sports and Exercise 42(11), 2064-2071.

Brown, C., Hejl, K., Bui, E., Tips, G., Coopwood, B., 2011. Risk factors for riding and crashing a motorcycle unhelmeted. The Journal of Emergency Medicine 41, 441-446.

Brugger, O., Bianchi, G., Schulz, D., Kisser, R., Rogmans, W., 2010. Snow-sport helmets: injury prevention, rate of wearers and recommendations. bfu - Swiss Council for Accident Prevention, EuroSafe Task Force Safety in Sports, Berne.

BS 6658:1985, British Standard Institution 1985. Protective Helmet for Vehicles Users. British Standard 6658, London. http://www.bsigroup.com/

Bullock, R., Graham, D.I., 1997. Non-penetrating Injuries of the Head. Section 2 of the Scientific Foundation of Trauma, in: Graham, J.C., Dudley, H.A.F., Gann, D.S., Little, R.A., Maynard (Eds.), Butterworths/Heinemann, London.

Caccese, V., Ferguson, J.R., Edgecomb, M.A., 2013. Optimal design of honeycomb material used to mitigate head impact. Composite Structures 100, 404-412.

Cairns, H., 1941. Head Injuries in Motor-Cyclists: The Importance of the Crash Helmet. British Medical Journal, No. 4213, pp.465-471.

Cairns, H., 1946. Crash Helmets. British Medical Journal, No. 4470, pp.322.

Caserta, G.D., Iannucci, L., Galvanetto, U., 2011. Shock absorption performance of a motorbike helmet with honeycomb reinforced liner. Composite Structures 93, 2748-2759.

Castro, O., Silva, J.M., Devezas, T., Silva, A., Gil, L., 2010. Cork agglomerates as an ideal core material in lightweight structures. Materials and Design 31(1), 425-432.

Canaple, B., Rungen, G., Markiewicz, E., Drazetic, P., Happian-Smith, J., Chinn, B., Cesari, D., 2002. Impact model development for the reconstruction of current motorcycle accidents. International Journal of Crashworthiness 7(3), 307-320.

Canaple, B., Rungen, G., Drazetic, P., Markiewicz, E., Cesari, D., 2003. Towards a finite element head model used as a head injury predictive tool. International Journal of Crashworthiness 8(1), 41-52.

Cardamone, L., 2005. Analisi numerica del trauma cranico da impatto. Technical report, Bioengineering Laboratory, University of Salerno, Italy.

CATIA V5 (2008). User Manual. Dassault Systems.

CEN, 2012. EN 1078:2012+A1:2012 - Helmets for pedal cyclists and for users of skateboards and roller skates. European Committee for Standardization, Brussels.

Cernicchi, A., Galvanetto, U., Iannucci, L., 2008. Virtual modelling of safety helmets: practical problems. International Journal of Crashworthiness 13(4), 451-467.

Chafi, M.S., Karami, G., Ziejewski, M., 2009. Biomechanical assessment of brain dynamic responses due to blast pressure waves. Ann Biomed Eng 38(2), 490-504.

Chamard, E., Théoret, H., Skopelja, E.N., Forwell, L.A., Johnson, A.M., Echlin, P.S., 2012. A prospective study of physician-observed concussion during a varsity university hockey season: metabolic changes in ice hockey players. part 4 of 4. Neurosurgical Focus 33(6), E4.

Chang, L.T., Chang, C.H., Chang, G.L., 1999a. Experimental evaluation of chin bar on head injury in facial impact. JSME International Journal 42, 294-300.

Chang, L.T., Chang, C.H., Huang, S.C., Chang, G.L., 1999b. A dynamic analysis of motorcycle helmet by finite element methods. Proceedings of IRCOBI Conference, Sitges, Spain, pp.371-382.

Chang, C.H., Chang, L.T., Chang, G.L., Huang, S.C., Wang, C.H., 2000. Head Injury in Facial Impact - A Finite Element Analysis of Helmet Chin Bar Performance. Journal of Biomechanical Engineering 21, 640-646.

Chang, L.T., Chang, C.H., Chang, G.L., 2001. Fit effect of motorcycle helmet - a finite element modelling. JSME International Journal 44, 185-192.

Chang, L.T., Chang, G.L., Huang, J.Z., Huang, S.C., Liu D.S., Chang, C.H., 2003. Finite element analysis of the effect of motorcycle helmet materials against impact velocity. Journal of the Chinese Institute of Engineers 26, 835-843.

Chapon, A., Dedoyan, A.J., Verriest, J.P., 1985. Clinical study of head injuries in patients with traumatic unconsciousness. Proceedings of IRCOBI Conference, pp.33-54.

Cheng, S., Bilston, L.E., 2007 Unconfined compression of white matter. J. Biomech. 40, 117-124.

Chinn, B., Hynd, D., 2009. Technical response to the unpublished paper: critical evaluation of the SHARP motorcycle helmet rating. TRL Published Project Report.

Cignoni, ., Callieri, M, Corsini, M, Dellepiane, M, Ganovelli, F, Ranzuglia, G., 2008. MeshLab: an open-source mesh processing tool. Eurographics Italian chapter conference 73:45-46.

Chinn, B., Hynd, D., 2009. Technical response to the Unpublished "Critical Evaluation of the SHARP Motorcycle Helmet Response" by Mills, N.J.. Published Project Report PPR452, TRL.

Claessens, M., Sauren, F., Wismans, J., 1997. Modeling of the human head under impact conditions: a parametric study. SAE Transactions Paper No. 973338, pp.3829-3848.

Cloots, R.J.H., Gervaise, H.M.T., van Dommelen, J.A.W., Geers, M.G.D., 2008. Biomechanics of traumatic brain injury: influences of the morphologic heterogeneities of the cerebral cortex. Annals of Biomedical Engineering 36(7), 1203-1215.

Cloots, R.J.H., van Dommelen, J.A.W., Kleiven, S., Geers, M.G.D., 2010. Traumatic Brain Injury at Multiple Length Scales: Relating Diffuse Axonal Injury to Discrete Axonal Impairment. Proceedings of IRCOBI Conference, Hanover, Germany, pp.119-130.

Coelho, R.M., Alves de Sousa, R.J., Fernandes, F.A.O., Teixeira-Dias, F., 2013. New composite liners for energy absorption purposes. Materials and Design 43, 384-392.

Collins, M.W., Iverson, G.L., Lovell, M.R., McKeag, D.B., Norwig, J., Maroon, J., 2003. On-field predictors of neuropsychological and symptom deficit following sports-related concussion. Clinical Journal of Sport Medicine 13(4), 222-229.

Commission to the European Parliament, 2014. Notice to members: Petition 0710/2008 by Peter Downes (Irish) on the safety standard for horse riding helmets; Petition 0326/2013 by Ulf Olsson (Swedish), on safety of equestrian helmet. European Parliament.

Committee on medical aspects of automotive safety, 1971. Rating the severity of tissue damage, the abbreviated scale. JAMA 215, 277-280.

Conde, E., Cadahia, E., Garcia-Vallejo, M.C., Gonzalez-Adrados, J.R., 1998. Chemical characterization of reproduction cork from Spanish Quercus suber. J Wood Chem Technol 18, 447-469.

Cooper, P.R., 1982. Post-traumatic intracranial mass lesions. Head injury, Williams and Wilkins, Baltimore/London, pp.185-232.

COST327, 2001. Motorcycle safety helmets. Final report of the action, European Communities, Belgium.

Costa, A., Pereira, A., Oliveira, A., 2003. Variability of radial growth in cork oak adult trees under cork production. Forest Ecology and Management 175, 239-246.

Costa, A., Madeira, M., Oliveira, A., 2008. The relationship between cork oak growth patterns and soil, slope and drainage in a cork oak woodland in Southern Portugal. Forest Ecology and Management 255, 1525-1535.

Cui, L., Forero Rueda, M.A., Gilchrist, M.D., 2009. Optimisation of energy absorbing liner for equestrian helmets. Part II: Functionally graded foam liner. Materials & Design 30(9), 3414-3419.

Dart, S.L., Eugene, G., 1946. Elastic properties of cork. I. stress relaxation of compressed cork. Journal of Applied Physics 17(5), 314-318.

Darvish, K.K., Crandall, J.R., 2002. Influence of brain material properties and boundary conditions on brain response during dynamic loading. Proceedings of IRCOBI Conference, Munich, Germany.

Davidsson, J., Angeria, M., Risling, M.G., 2009. Injury threshold for sagittal plane rotational induced diffuse axonal injuries. Proceedings of IRCOBI Conference, York, UK, pp.43-56.

Deck, C., Baumgartner, B., Willinger, R., 2003a. Helmet Optimisation on head-helmet modelling. Structural Materials 13, 319-328.

Deck, C., Willinger, R., Baumgartner, D., Meyer, F., 2003b. Helmet optimisation against biomechanical criteria. Proceedings of IRCOBI Conference, Lisbon, Portugal, pp.351-352.

Deck, C., Nicolle, S., Willinger, R., 2004. Human head FE modelling : improvement of skull geometry and brain constitutive laws. Proceedings of IRCOBI Conference, Graz, Austria, pp.79-92.

Deck, C., Willinger, R., 2006. Multi-directional optimisation against biomechanical criteria of a head-helmet coupling. International Journal of Crashworthiness 11(6), 561-572.

Deck, C., Willinger, R., 2008. Improved Head injury criteria based on head FE model. International Journal of Crashworthiness 13(6), 667-679.

Deck, C., Willinger, R., 2009. Head injury prediction tool for predictive systems optimization. Proceedings of 7^{th} European LS-DYNA Conference.

Delaney, J.S., Lacroix, V.J., Leclerc, S., Johnston, K.M., 2000. Concussions during the 1997 canadian football league season. Clinical Journal of Sport Medicine 10(1), 9-14.

DeMarco, A.L., Chimich, D.D., Gardiner, J.C., Nightingale, R.W., Siegmund, G.P., 2010. The impact response of motorcycle helmets at different impact severities. Accident Analysis and Prevention 42, 1778-1784.

DeMarco, A.L., Chimich, D.D., Gardiner, J.C., Siegmund, G.P., 2016. The impact response of traditional and BMX-style bicycle helmets at different impact severities. Accident Analysis and Prevention 92, 175-183.

Department of Transportation (DOT), 2000. National Highway Traffic Safety Administration: CFR 49 FMVSS 571.201. Occupant Protection in Interior Impact.

Depreitere, B., Van Lierde, C., Vander Sloten, J., Van Audekercke, R., Van der Perre, G., Plets, C., Goffin, J, 2006. Mechanics of acute subdural hematomas resulting from bridging vein rupture. Journal of Neurosurgery 104(6), 950-956.

Di Landro, L., Sala, G., Olivieri, D., 2002. Deformation mechanisms and energy absorption of polystyrene foams for protective helmets. Polymer Testing 21, 217-228.

DiMasi, F., Marcus, J., Eppinger, R., 1991b. Three dimensional anatomic brain model for relating cortical strains to automobile crash loading. Proceedings of the 12^{th} International Technical Conference on Experimental Safety Vehicles, NHTSA, Washington, 2, 617-627.

DiMasi, F., Eppinger, R.H., Bandak, F.A., 1995. Computational analysis of head impact response under car crash loadings. Proceedings of 39^{th} Stapp Car Crash Conference, Society of Automotive Engineers, SAE Paper No. 952718, Society of Automotive Engineers, Warrendale, PA, pp.425-438.

Dirisala, V., Karami, G., Ziejewski, M., 2011. Effects of neck damping properties on brain response under impact loading. International Journal for Numerical Methods in Biomedical Engineering 28(4), 472-494.

Dirnhofer, R., Walz, F., Sigrist, T., 1979. Zur Mechanischen Belastbarkeit des Tentorium Cerebelli. Zeitschrift fur Rechtsmedizin 82, 305-311.

Dixon, C.E., Clifton, G.L., Lighthall, J.W., Yaghmai, A.A., Hayes, R.L., 1991. A controlled cortical impact model of traumatic brain injury in the rat. Journal of Neuroscience Methods 39, 253-262.

Dokko, Y., Anderson, R.W.G., Manavis, J., Blumbergs, P.C., McLean, A.J., Zhang, L., Yang, K.H., King, A.I., 2003. Validation of the human head FE model against pedestrian accidents and its tentative application to the examination of the existing tolerance curve. Proceedings of 18^{th} International Technical Conference on the Enhanced Safety of Vehicles, ESV, Nagoya, Japan.

Doorly, M.C., Gilchrist, M.D., 2006. The use of accident reconstruction for the analysis of traumatic brain injury due to head impacts arising from falls. Computer Methods in Biomechanics and Biomedical Engineering 9(6), 371-377.

Douglass, J.M., Nahum, A.M., Roberts, S.B., 1968. Applications of Experimental Head Injury Research. Proceedings of Stapp Car Crash Conference, pp.317-37.

Duma, S.M., Manoogian, S.J., Bussone, W.R., Brolinson, P.G., Goforth, M.W., Donnenwerth, J.J., Greenwald, R.M., Chu, J.J., Crisco, J.J., 2005. Analysis of real-time head accelerations in collegiate football players. Clinical Journal of Sports Medicine 15, 3-8.

ECE Regulation 22.05, 2002. Uniform provision concerning the approval of protective helmets and their visors for driver and passengers of motor cycles and mopeds. United Nations. www.unece.org

Eiband, A.M., 1959. Human Tolerance to Rapidly Applied Accelerations: A Summary of the Literature. NASA Memo.

El Sayed, T., Mota, A., Fraternali, F., Ortiz, M., 2008. Biomechanics of traumatic brain injury. Computer Methods in Applied Mechanics and Engineering 197, 4692-4701.

Eppinger, R., Sun, E., Kuppa, S., Saul, R., 2000. Supplement: Development of improved injury criteria for the assessment of advanced automotive restraint systems - II. National Highway Traffic Safety Administration.
http://ec.europa.eu/

Ewing, C., Thomas, D., Lustick, L., Becker, E., Becker, G., Willems, G., Muzzy, W., 1975. The Effect of the Initial Position of the Head and Neck to Gx. Impact Acceleration. Proceedings of the 19^{th} Stapp Car Crash Conference, SAE, Warrendale, Pennsylvania, USA.

Fallenstein, G., Hulce, V., Melvin, J., 1969. Dynamic Mechanical Properties of Human Brain Tissue. Journal of Biomechanics 2(3),217-226.

Feist, F., Gugler, J., Arregui-Dalmases, C., del Pozo de Dios, E., Lopez-Valdes, F., Deck, D., Willinger, R., 2009. Pedestrian collisions with flat-fronted vehicles: injury patterns and importance of rotational accelerators as a predictor for traumatic brain injury (TBI). Proceedings of 21^{st} international conference on the enhanced safety of vehicles (ESV), Washington DC, pp.1-19.

Fenner Jr., H., Thomas, D.J., Gennarelli, T., Pintar, F.A., Becker, E.B., Newman, J.A., Yoganandan, N., 2005. HIC Workshop: Final report of workshop on criteria for head injury and helmet standards. Department of Neurosurgery, Medical College of Wisconsin, Milwaukee, WI.

Fernandes, F.A.O., Alves de Sousa, R.J., 2013a. Motorcycle helmets - a state-of-the-art review. Accident Analysis and Prevention 56, 1-21.

Fernandes, F.A.O., Alves de Sousa, R.J., 2013b. Finite element analysis of helmeted oblique impacts and head injury evaluation with a commercial road helmet. Structural Engineering Mechanics 48(5), 661-679.

Fernandes, F.A.O., Alves de Sousa, R.J., Willinger, W., Deck, C., 2013. Finite Element Analysis of Helmeted Impacts and Head Injury Evaluation with a Commercial Road Helmet. In: Proceedings of IRCOBI Conference, Gothenburg, Sweden, pp.431-442, September.

Fernandes, F.A.O., Pascoal, R.J.S., Alves de Sousa, R.J., 2014. Modelling impact response of agglomerated cork. Materials and Design 58, 499-507.

Fernandes, F.A.O., Alves de Sousa, R.J., 2015. Head injury predictors in sports trauma - A state-of-the-art review. Journal of Engineering in Medicine 229(8), 592-608.

Fernandes, F.A.O., Jardin, R.T., Pereira, A.B., Alves de Sousa, R.J., 2015. Comparing the mechanical performance of synthetic and natural cellular materials. Materials and Design 82, 335-341.

Fernandes, F.A.O., Tchepel, D., Alves de Sousa, R.J., Ptak, M., 2017. Development and validation of a new finite element human head model - YEt Another Head Model (YEAHM). Engineering Computations (accepted for publication).

Fernandes, E.M., Correlo, V.M., Mano, J.F., Reis, R.L., 2015b. Cork-polymer biocomposites: Mechanical, structural and thermal properties. Materials and Design 82, 282-289.

Fijalkowski, R.J., Ellingson, B.M., Stemper, B.D., 2006a. Interface Parameters of Impact Induced Mild Traumatic Brain Injury. Biomedical Sciences Instrumentation 42, 108-113.

Fijalkowski, R.J., Stemper, B.D., Ellingson, B.M., Yoganandan, N., Pintar, F.A., Gennarelli, T.A., 2006b. Inducing mild traumatic brain injury in the rodent through coronal plane angular acceleration. Proceedings of IRCOBI Conference, Madrid, Spain, pp.115-125.

Fijalkowski, R.J., Stemper, B.D., Pintar, F.A., Yoganandan, N., Gennarelli, T.A., 2007. Influence of angular acceleration duration on functional outcomes following mild diffuse brain injury. Proceedings of IRCOBI Conference, Maastricht, The Netherlands, pp.161-171.

Forero Rueda, M.A., Cui, L., Gilchrist, M.D., 2009. Optimisation of energy absorbing liner for equestrian helmets. Part I: Layered foam liner. Materials & Design 30(9), 3405-3413.

Forero Rueda, M.A., Cui, L., Gilchrist, M.D., 2011. Finite element modelling of equestrian helmet impacts exposes the need to address rotational kinematics in future helmet designs. Computer Methods in Biomechanics and Biomedical Engineering 14(12), 1021-1031.

Fortes, M.A., Nogueira, M.T., 1989. The Poisson effect in cork. Material Science and Engineering A 122, 227-232.

Fortes, M.A., Rosa, M.E., 1992. Growth stresses and strains in cork. Wood Science and Technology 26(4), 241-258.

Fortes, M.A., Rosa, M.E., Pereira, H., 2004. A cortiça. IST Press, Lisboa.

Franceschini, G., Bigoni, D., Regitnig, P., Holzapfel, G.A., 2006. Brain tissue deforms similarly to filled elastomers and follows consolidation theory. Journal of the Mechanics and Physics of Solids 54(12), 2592-2620.

Franklyn, M., Fildes, B., Dwarampudi, R., Zhang, L., Yang, K., Sparke, L., Eppinger, R., 2003. Analysis of computer models for head injury investigation. Proceedings of the 18^{th} International Technical Conference on Enhanced Safety Vehicles.

Franklyn, M., Fildes, B., Zhang, L., Yang, K.H., Sparke, L., 2005. Analysis of finite element models for head injury investigation: Reconstruction of four real-world impacts. Stapp Car Crash Journal 49, 1-32.

Fruin, A.H., Juhl, G.L., Taylon, C., 1984. Interhemispheric subdural hematoma. Journal of Neurosurgery 60, 1300-1302.

Gadd, C.W., 1966. Use of a weighted-impulse criterion for estimating injury hazard. Proceedings of the 10^{th} Stapp Car Crash Conference, New York, pp.164-174.

Gadd, C.W., 1971. Tolerable Severity Index in whole-head nonmechanical impact. Proceedings of the 15^{th} Stapp Car Crash Conference, pp.809Ű-816.

Galbraith, J.A., Thibault, L.E., Matteson, D.R., 1993. Mechanical and electrical responses of the squid giant axon to simple elongation. Journal of Biomechanical Engineering 115, 13-22.

Galindo-Rosales, F.J., Martinez-Aranda, S., Campo-Deano, L., 2015. CorkSTFμfluidics - A novel concept for the development of eco-friendly light-weight energy absorbing composites. Materials and Design 82, 326-334.

Gameiro, C.P., Cirne, J., Gary, G., Miranda, V., Pinho da Cruz, J., Teixeira-Dias, F., 2005. Numerical and experimental study of the dynamic behaviour of cork. In: F. Teixeira-Dias, B. Dodd, E. Lach, P. Schulz, editors, Proceedings of the 3rd Light-Weight Armour Group Workshop: Design and Use of Light-Weight Materials, pp.65-84.

Gameiro, C.P., Cirne, J., Gary, G., 2007a. Experimental study of the quasi-static and dynamic behaviour of cork under compressive loading. Journal of Materials Science 42, 4316-4324.

Gameiro, C.P., Cirne, J., 2007b. Dynamic axial crushing of short to long circular aluminium tubes with agglomerate cork filler. International Journal of Mechanical Sciences 49, 1029-1037.

Garcia, A., Anjos, O., Iglesias, C., Pereira, H., Martinez, J., Taboada, J., 2015. Prediction of mechanical strength of cork under compression using machine learning techniques. Materials and Design 82, 304-311.

Gean, A.D., 1994. Imaging of head trauma. Raven Press, New York, pp.76-78.

Gennarelli, T.A., Ommaya A.K., Thibault, L.E., 1971. Comparison of translational and rotational head motions in experimental cerebral concussion. Proceedings of 15^{th} Stapp Car Crash Conference, SAE P-39: 797-803.

Gennarelli, T.A., Thibault, L.E., Ommaya, A.K., 1972. Pathophysiological Responses to Rotational and Translational Accelerations of the Head. Proceedings of 16^{th} Stapp Car Crash Conference, Society of Automotive Engineers, SAE Paper No. 720970, pp.296-308.

Gennarelli, T.A., 1981. Mechanistic approach to head injuries: clinical and experimental studies of the important types of injury. Ed. Ommaya, A.K., in Head and neck injury criteria: a consensus workshop, U.S. Dept. of Transportation, National Highway Traffic Safety Administration, Washington DC, pp.20-25.

Gennarelli, T.A., Adams, J.H., Graham, D.I., 1981. Acceleration induced head injury in the monkey: The model, its mechanical and physiological correlates. Acta Neuropathologica Supplementum 7, 23-25.

Gennarelli, T. A., Spielman, G. M., Langfitt, T. W., Gildenberg, P. L., Harrington, T., Jane, J. A., Marshall, L. F.,Miller, J. D., Pitts, L. H., 1982a. Influence of the type of intracranial lesion on outcome from severe head injury. Journal of Neurosurgery 56, 26-32.

Gennarelli, T.A., Thibault, L.E., 1982. Biomechanics of acute subdural hematoma. Journal of Trauma 22, 680-686.

Gennarelli, T.A., Thibault, L.E., Adams, J.H., Graham, D.I., Thompson, C.J., Marcincin, R.P., 1982b. Diffuse axonal injury and traumatic coma in the primate. Annals of Neurology 12, 564-574.

Gennarelli, T.A, 1983. Head injury in man and experimental animals: Clinical aspects. Acta Neurochirurgica Supplementum 32, 1-13.

Gennarelli, T.A., 1985. The state of the art of head injury biomechanics - A review. Proceedings of 29^{th} Conference of the Association for the Advancement of Automotive Medicine, pp.47-63.

Gennarelli, T.A., 1987. Cerebral concussions and diffuse brain injuries. In: Cooper P.R. (Ed.), Head injury, pp.108-124, Wilkins & Wilkins Baltimore.

Gennarelli, T.A., Thibault, L.E., 1995. Biomechanics of head injury. Neurosurgery. Eds. R. H. Wilkins and S. S. Rengachary, 2nd edition, New York: McGraw-Hill Book Company, pp.1531-1536.

Gennarelli, T.A., Thibault, L.E., Tomei, G., 1987. Directional dependence of axonal brain injury due to centroidal and non-centroidal acceleration. Proceedings of 31^{st} Stapp Car Crash Conference, Society of Automotive Engineers, SAE Paper No. 872197, pp.49-53.

Gennarelli, T.I., Thibault, L.E., 1989. Clinical rationale for a head injury angular acceleration criterion. Head Injury Mechanisms, AAAM, Washington, pp.5-8.

Gennarelli, T.A., Thibault, L.E., Tipperman, R., 1989. Axonal Injury in the Optic Nerve: A model of Diffuse Axonal Injury in the brain. Journal of Neurosurgery 71, 244-253.

Gennarelli, T.A., Meaney, D.F., 1996. Mechanisms of primary head injury. Wilkins, R.H., Rengachary, S.S., (eds) Neurosurgery, vol.2, McGraw-Hill, New York, pp.2611-2611.

Gennarelli, T.A., Pintar, F.A., Yoganandan, N., 2003. Biomechanical Tolerances for Diffuse Brain Injury and a Hypothesis for Genotypic Variability in Response to Trauma. Proceedings of the 47^{th} Annual Association for the Advancement of Automotive Medicine, pp.624-628.

Gennarelli, T.A., Wodzin, E., 2006. AIS 2005: A contemporary injury scale. Injury, International Journal of the Care of the Injured 37, 1083-1091.

Ghajari, M., Deck, C., Galvanetto, U., Iannucci, L., Willinger, R., 2009a. Development of numerical models for the investigation of motorcyclists accidents. 7^{th} European LS-DYNA Conference, Salzburg, Austria.

Ghajari, M., Galvanetto, U., Iannucci, L., 2009b. Influence of the body on kinematic and tissue level head injury predictors in motorcyclists accidents. Proceedings of IRCOBI Conference, York, UK, pp.9-11.

Ghajari, M., Galvanetto, U., Iannucci, L., Willinger, R., 2011. Intracranial Response in Helmet Oblique Impacts. Proceedings of IRCOBI Conference, Warsaw, pp.90-94.

Gibson, L.J., Easterling, K.E., Ashby, M.F., 1981. The structure and mechanics of cork. Proceedings of the Royal Society of London A 377, 99-117.

Gibson, L.J., Ashby, M.F., Schajer, G.S., Robertson, C.I., 1982a. The mechanics of three-dimensional cellular materials. Proceedings of the Royal Society of London A 382, 43-59.

Gibson, L.J., Ashby, M.F., Schajer, G.S., Robertson, C.I., 1982b. The mechanics of two-dimensional cellular materials. Proceedings of the Royal Society of London A 382(1782), 25-42.

Gibson, L.J., Ashby, M.F., 1997. Cellular Solids: Structure and Properties - Second edition. Cambridge University Press, Cambridge.

Gibson, L.J., 2005. Biomechanics of cellular solids. Journal of Biomechanics 38, 377-399.

Gil, L., 1994. Effect of hot pressing densification on the cellular structure of black agglomerated cork board. Holz als Roh- und Werkstoff, 52(2), 131-134.

Gil, L., 1996. Densification of black agglomerate cork boards and study of densified agglomerates. Wood Science and Technology 30(3), 217-223.

Gil, L., 2009. Cork Composites: A Review. Materials 2, 776-789.

Gil, L., 2015. New Cork-Based Materials and Applications. Materials 8, 625-637.

Gilchrist, A., Mills, N.J., 1987. Improvements in the design and the performance of motorcycle helmets. Proceedings of IRCOBI Conference, Birmingham, UK, pp.19-32.

Gilchrist, A., Mills, N.J., Khan, T., 1988. Survey of Head, Helmet and Headform Sizes Related to Motorcycle Helmet Design. Ergonomics 31, 1395-1412.

Gilchrist, A., Mills, N.J., 1993. Deformation analysis for motorcycle helmets. Proceedings of IRCOBI conference, Eindhoven, The Netherlands, pp.269Ű-281.

Gilchrist, A., Mills, N.J., 1994a. Impact Deformation of ABS and GRP Motorcycle Helmet Shells. Plastics Rubber and Composites Processing and Applications 21, 141-150.

Gilchrist, A., Mills, N.J., 1994b. Modelling of the impact response of motorcycle helmets. International Journal of Impact Engineering 15(3), 201-218.

Gilchrist, M.D., O'Donoghue, D., 2000. Simulation of the development of frontal head impact injury. Computational Mechanics 26, 229-235.

Gilchrist, M.D., 2003. Modelling and Accident Reconstruction of Head Impact Injuries. Key Engineering Materials 245-246, 417-432.

Gimbel, G.M., Hoshizaki, T.B., 2008. Compressive properties of helmet materials subjected to dynamic impact loading of various energies. European Journal of Sport Science 8(6), 341-349.

Giordano, C., Cloots, R.J.H., van Dommelen, J.A.W., Kleiven,S., 2014. The influence of anisotropy on brain injury prediction. Journal of Biomechanics 47, 1052-1059.

Glaister, D., 1997. Acceleration injury. Graham, J.C., Dudley, H.A.F., Gann, D.S., Little, R.A., Maynard (Eds.), Scientific Foundation of Trauma, Butterworths/Heinemann, London, pp.314-323.

Glowacki, J.W., 1991. Posttraumatic cerebellar contusions and hematomas. Frowein, R.A., (ed) Cerebral contusions, lacerations and hematomas. Springer, Berlin Heidelberg New York, pp.176-200.

Goel, R., 2011. Study of an advanced helmet liner concept to reduce TBI: Experiments & Simulation using sandwich structures. Master thesis, Department of Aeronautics and Astronautics, Massachusetts Institute of Technology, February 2011.

Goggio, A.I., 1941. The mechanism of contre-coup injury. Journal of Neurology and Psychiatry 4, 11-22.

Goldsmith, W., Plunkett, J., 2004. A Biomechanical Analysis of the Causes of Traumatic Brain Injury in Infants and Children. Journal of Forensic Medicine and Pathology 25(2), 89-100.

Goldstein, D.M., Mazuchowski, E.L., Gdula, W., Thibault, L.E., 1997. In vitro and mathematical models of axonal injury in CNS tissue. Prevention Through Biomechanics, Symposium Proceedings, Wayne State University, pp.207-215.

Görgülü A, Çobanoğlu S, Armağan S, Karabağli H, Tervüz M, 2000. Bilateral epidural hematoma. Neurosurg Rev 23, 30-33.

Got, C., Patel, A., Fayon, A., Tarriere, C., Walfisch, G., 1978. Results of experimental head impacts o cadavers: the various data obtained and their relation to some measured physical parameters. SAE Technical Paper 780887, pp.57-99.

Graham, D.I., Adams, J.H., Nicoll, J.A.R., 1995. The nature, distribution and causes of traumatic brain injury. Brain Pathology 5, 397-406.

Gross, A.G., 1958. A new theory on the dynamics of brain concussion and brain injury. Journal of Neurosurgery 15, 548-556.

Gurdjian, E.S., Webster, J.E., 1945. Linear acceleration causing shear in the brain stem in trauma of the central nervous system. Mental Advances in Disease, pp.24-28.

Gurdjian, E .S., 1950. The mechanism of skull fracture. Radiology, 54, 313-339.

Gurdjian, E.S., Lissner, H.R., Latimer, F.R., Haddad, B.F., Webster, J.E., 1953. Quantitative determination of acceleration and intracranial pressure in experimental head injury. Neurology 3, 417-423.

Gurdjian, E.S., Webster, J.E., Lissner, H.R., 1955. Observations on the mechanism of brain concussion, contusion and laceration. Surgery, Gynecology and Obstetrics 101, 680-690.

Gurdjian, E.S., Lissner, H.R., Evans, F.G., 1961. Intracranial Pressure and Acceleration Accompanying Head Impacts in Human Cadavers. Surgery, Gynecology, and Obstetrics 112, 185-190.

Gurdjian, E.S., Lissner H.R., Patrick, L.M., 1963. Concussion-mechanism and pathology. Proceedings of 7^{th} American Association for Automotive Medicine Annual Conference, Los Angeles, pp.470-482.

Gurdjian, E., Robert, V., Thomas, L., 1966a. Tolerance curves of acceleration and intercranial pressure and protective index in experimental head injury. Journal of Trauma 6(5), 600-604.

Gurdjian, E.S., Lissner, H.R., Hodgson, V.R., et al., 1966b. Mechanisms of head injury. Clin. Neurosurg. 12, 112-128.

Gurdjian, E., 1972. Recent advances in the study of the mechanism of impact injury of the head. Clin Neurosurg 19, 1-42.

Gurdjian, E.S., 1975. Impact head injury, mechanistic, clinical and preventive correlations. Thomas, C.C., Springfield, Ill.

Guskiewicz, K.M., Mihalik, J.P., Shankar, V., Marshall, S.W., Crowell, D.H., Oliaro, S.M., Ciocca, M.F., Hooker, D.N., 2007. Measurement of head impacts in collegiate football players: Relationship between head impact biomechanics and acute clinical outcome after concussion. Neurosurgery 61(6), 1244-1253.

Halldin, P., Gilchrist, A., Mills, N.J., 2001. A new oblique impact test for motorcycle helmets. International Journal of Crashworthiness 6, 53-64.

Hansen, K., Dau, N., Feist, F., Deck, C., Willinger, R., Madey, S.M., Bottlang, M., 2013. Angular Impact Mitigation system for bicycle helmets to reduce head acceleration and risk of traumatic brain injury. Accident Analysis & Prevention 59, 109-117.

Hardy, C., Marcal, P., 1973. Elastic analysis of a skull. Journal of applied mechanics, 40(4), 838-842.

Hardy, W.N., Foster, C.D., Mason, M.J., King, K.H., King, A.I., Tashman, S, 2001. Investigation of head injury mechanisms using neutral density technology and high-speed biplanar X-ray. Stapp Car Crash Journal 45, 337-368.

Hardy, W.N., Mason, M.J., Foster, C.D., Shah, C.S., Kopacz, J.M., Yang, K.H., King, A.I., Bishop, J., Bey, M., Anderst, W., Tashman, S., 2007. A study of the response of the human cadaver head to impact. Stapp Car Crash Journal. 51, 17-80.

Hargreaves, E.L., 2006. Meninges. UCSF, University of California, San Francisco. http://missinglink.ucsf.edu/lm/ids_104_cns_injury/Response%20_to_Injury/Injury_Images/MeningesBlum.jpg 09/12/2011

Hartmann, U., Kruggel, F., 1999. Trasient analysis of the biomechanics of the human head with a high-resolution 3D finite element model. Computer Methods in Biomechanics and Biomedical Engineering 2(1), 49-64.

Helmet Boys. http://www.helmetboys.com/images/motorcycle-helmets/ARAI/RAM3/arai-ram3-helmet-overall-airflow.jpg 15/12/2011

Higgins, L.S., Schmall, R.A., 1967. A Device for the Investigation of Head Injury Effected by Non-Deforming Head Accelerations. Proceedings of 11^{th} Stapp Car Crash Conference, pp.57-72.

Hirakawa, K., Hashizume, K., Fuchinoue, T., Takahashi, H., Nomura, K., 1972. Statistical analysis of chronic subdural hematoma in 309 adult cases. Neurologia Medico-chirurgica 12, 71-83.

Hirsch, A.E., Ommaya, A.K., Mahone, R.M., 1968. Tolerance of Subhuman Primate Brain to Cerebral Concussion. The Department of the Navy, Naval Ship Research and Development Center, Washington DC.

Hitosugi, M., Shigeta, A., Takatsu, A., Yokoyama, T., Tokudome, S., 2004. Analysis of fatal injuries to motorcyclists by helmet type. American Journal of Forensic Medicine and Pathology 25, 125-128.

Ho, J., Kleiven, S., 2007. Dynamic response of the brain with vasculature: A three-dimensional computational study. Journal of Biomechanics 40, 3006-3012.

Ho, J., 2008. Generation of patient specific finite element head models. Doctoral Thesis, Division of Neuronic Engineering, School of Technology and Health, Royal Institute of Technology, Trita-STH Report 2008:7.

Ho, J., Kleiven, S., 2009. Can sulci protect the brain from traumatic injury?. Journal of Biomechanics 42, 2074-2080.

Ho, J., von Holst, H., Kleiven, S., 2009. Automatic generation and validation of patient-specific finite element head models suitable for crashworthiness analysis. International Journal of Crashworthiness 14(6), 555-563.

Hodgson, V R., Brinn, J., Thomas, L.M., Greenberg, S.W., 1970. Fracture Behavior of the Skull Frontal Bone Against Cylindrical Surfaces. Proceedings of 14^{th} Stapp Car Crash Conference, SAE International, Warrendale, PA.

Hodgson, V.R., Thomas, L.M., 1971. Breaking strength of the human skull vs impact surface curvature. Report, Department of Neurosurgery, Wayne State University School of Medicine.

Hodgson, V.R., Thomas, L.M., 1979. Acceleration induced shear strains in a monkey brain hemisection. Proceedings of 23^{rd} Stapp Car Crash Conference, Society of Automotive Engineers, SAE Paper No. 791023.

Hodgson, V.R., Thomas, L.M., Khalil, T.B., 1983. The role of impact location in reversible cerebral concussion. Proceedings of 27^{th} Stapp Car Crash Conference, Society of Automotive Engineers, SAE Paper No. 831618, 225-240.

Holbourn, A.H.S., 1943. Mechanics of head injury. British Medical Bulletin 2, 438-441.

Holbourn, A.H.S., 1945. The mechanics of brain injuries. British Medical Bulletin 3, 147-149.

Honey, C. R., 1998. Brain injury in ice hockey. Clinical Journal of Sport Medicine 8(1), 43-46.

Hooke, R., 1665. Micrographia: Or Some Physiological Descriptions of Minute Bodies Made by Magnifying Glasses, with Observations and Inquiries Thereupon. London: J. Martyn and J. Allestry, publishers to the Royal Society.

Hopes, P.D., Chinn, B.P., 1989. Helmets: a new look at design and possible protection. Proceedings of IRCOBI conference, Stockholm, pp.39-54.

Horgan, T.J., Gilchrist, M.D., 2003a. Investigations into finite element modelling aspects of the human head. Proceedings of IRCOBI Conference, Lisbon, Portugal, pp.347-348.

Horgan, T.J., Gilchrist, M.D., 2003b. The creation of three-dimensional finite element models for simulating head impact biomechanics. International Journal of Crashworthiness 8(4), 353-366.

Horgan, T.J., Gilchrist, M.D., 2004. Influence of FE model variability in predicting brain motion and intracranial pressure changes in head impact simulations. International Journal of Crashworthiness 9(4), 401-418.

Horgan, T.J., 2005. A finite element model of the human head for use in the study of pedestrian accidents. PhD thesis, University College Dublin, Dublin.

Hosey, R.R., Liu, Y.K., 1982. A homeomorphic finite element model of the human head and neck. In: Simon, B.R., Gallagher, R.H., Johnson, P.C., Gross, J.F. (Eds.), Finite elements in biomechanics, chapter 18, pp. 379-401. John Wiley & Sons, France.

Hrapko, M., van Dommelen, J.A.W., Peters, G.W.M., Wismans, J.S.H.M., 2008. The influence of test conditions on characterization of the mechanical properties of brain tissue. Journal of Biomechanical Engineering 130(3), 663-676.

Huang, S.C., 1999. Numerical Simulation of Human Head-Neck Dynamics. Bio-Medical Materials and Engineering 9(1), 66-71.

Huang, H.M., Lee, M.C., Chiu, W.T., Chen, C.T., Lee, S.Y., 1999. Three-dimensional finite element analysis of subdural hematoma. The Journal of Trauma: Injury, Infection, and Critical Care 47(3), 538-544.

Huda, M.F., Mohanty, S., Sharma, V., Tiwari, Y., Choudhary, A., Singh, V.P., 2004. Double extradural hematoma: an analysis of 46 cases. Neurol India 52(4), 450-452.

Hughes, K.M., Falcone, R.E., Price, J., Witkoff, M., 1995. Equestrian-related trauma. The American journal of emergency medicine 13(4), 485-487.

Hume, A., Mills, N.J., Gilchrist, A., 1995. Industrial head injuries and the performance of the helmets. Proceedings of IRCOBI Conference, Brunnen, Switzerland, pp.217-231.

Hurt, H.H., Ouellet, J.V., Thom, D.R., 1981. Motorcycle accident cause factors and identification of countermeasures. Final Report, Technical Report, Vol. 1, Traffic Safety Center, University of Southern California, CA.

Huston, R.L., Sears, J., 1981. Effect of Protective Helmet Mass on Head/Neck Dynamics. Journal of Biomechanical Engineering 103, 18-23.

Iglesias, C., Anjos, O., Martinez, J., Pereira, H., Taboada, J., 2015. Prediction of tension properties of cork from its physical properties using neural networks. European Journal of Wood and Wood Products 73(3), 347-356.

International Standards Organisation, 1983. ISO-DIS-6220: Headforms for Use in the Testing of Protective Helmets. Geneva, Switzerland.

Ipek, H., Mayer, C., Deck, C., Luce, H., de Gueselle, P., Willinger, R., 2009. Coupling of Strasbourg University head model to thums human body FE model: validation and application to automotive safety. Paper number 09-0384, pp.1-13.

Ivarsson, J., Viano, D.C., Lövsund, P., Aldman, B., 2000. Strain relief from the cerebral ventricles during head impact: experimental studies on natural protection of the brain. Journal of Biomechanics 33(2), 181-189.

Ivarsson, J., Viano, D.C., Lövsund, P., 2002. Influence of the lateral ventricles and irregular skull base on brain kinematics due to sagittal plane head rotation. Journal of Biomechanical Engineering 124, 422-431.

Iwamoto, M., Yoshikatsu, K., Watanabe, I., Furusu, K., Miki, K., Hasegawa, J., 2002. Development of a finite element model of the total human model for safety (thums) and application to injury reconstruction. Proceedings of IRCOBI Conference, Munich, Germany.

Iwamoto, M., 2003. Recent Advances in THUMS: development of the detailed head-neck and internal organs, and THUMS family. LS-DYNA & JMAG User Conference, Japan.

Iwamoto, M., Nakahira, Y., Tamura, A., Kimpara, H., Watanabe, I., Miki, K., 2007. Development of advanced human models in thums. 6^{th} European LS-DYNA Users Conference, pp.47-56.

Jamieson, K.G., Yelland, J.D.N., 1972. Surgically treated traumatic subdural hematomas. Journal of Neurosurgery 37(2), 137-149.

Jardin, R.T., Fernandes, F.A.O., Pereira, A.B., Alves de Sousa, R.J., 2015. Static and dynamic mechanical response of different cork agglomerates. Materials and Design 68, 121-126.

Johnson, G.I., 2000. Investigations on impact testing of head injury protection helmets. International Journal of Crashworthiness 5(4), 491-502.

Jowitt, S., Clair, V., Scott., A., 2014. Helmet retention report. Project report PPR689, Transport Research Laboratory, Wokingham.

Juntikka, R., Kleiven, S., Hallströmm, S., 2004. Optimization of single skin surfaces for head injury prevention - a comparison of optima calculated for global versus local injury thresholds. International Journal of Crashworthiness 9(4), 365-379.

KALI sports, 2016. https://kaliprotectives.com/ 10/11/2016

Kang, H., Willinger, R., Diaw, B.M., Chinn, B., 1997. Validation of a 3D anatomic human head model and replication of head impact in motorcycle accident by finite element modelling. SAE Transactions Paper No. 973339, pp.849-858.

Khalil, T.B., Goldsmith, W., Sackman, J.L., 1974. Impact on a model head-helmet system. International Journal of Mechanical Sciences 16, 609-625.

Khalil, T.B., Hubbard, R.P., 1977. Parametric study of head response by finite element modelling. Journal of Biomechanics 10, 119-132.

Khalil, T.B., Viano, D.C., 1982. Critical issues in finite element modelling of head impact. Proceedings of 26^{th} Stapp Car Crash Conference, SAE paper, vol 821150, pp.87-102.

Kim, G.H., Lee, O.S., Yoo, S.S., 1997. Experimental Study on impact absorbing performance of motorcycle Helmets. KSME International Journal 11, 292-299.

Kim, J.E., Kim, Y.H., Li, Z., Eberhardt, A.W., Soni, B.K., 2005. Evaluation of Traumatic Brain Injury using Multi-Body and Finite Element Models. 17^{th} IMACS World Congress, Scientific Computation, Applied Mathematics and Simulation, Paris, France.

Kimpara, H., Nakahira, Y., Iwamoto, M., Miki, K., Ichihara, K., Kawano Taguchi, T., 2006. Investigation of anteroposterior head-neck responses during severe frontal impacts using a brain-spinal cord complex FE model. Proceedings 50^{th} Stapp Car Crash Conference, pp. 509-544.

Kimpara, H., Nakahira, Y., Iwamoto, M., Rowson, S., Duma, S., 2011. Head injury prediction methods based on 6 degree of freedom head acceleration measurements during impact. International Journal of Automotive Engineering 2, 13-19.

Kimpara, H., Iwamoto, M., 2012. Mild traumatic brain injury predictors based on angular accelerations during impacts. Annals of Biomedical Engineering 40(1), 114-126.

King, A., Yang, K., Zhang, L., Hardy, W., Viano, D., 2003. Is Head Injury Caused by linear or angular acceleration?. Proceedings of IRCOBI Conference, Lisbon, pp.1-10.

Kleinberger, M., 1998. Development of improved injury criteria for the assessment of advanced automotive restraint systems. National Highway Traffic Safety Administration.

Kleiven, S., von Holst, H., 2001. Consequences of brain size following impact in prediction of subdural hematoma evaluated with numerical techniques. Proceedings of IRCOBI Conference, Isle of Man, UK, pp.161-172.

Kleiven, S., 2002. Finite Element Modeling of the Human Head. Doctoral Thesis, Technical Report, School of Technology an Health, Royal Institute of Technology, Stockholm, Sweden.

Kleiven, S., Hardy, W.N., 2002. Correlation of an FE Model of the Human Head with Experiments on Localized Motion of the Brain: Consequences for Injury Prediction. Proceedings 45^{th} Stapp Car Crash Journal, Society of Automotive Engineers, SAE Paper No. 02S-76.

Kleiven, S., von Holst, H., 2002. Consequences of head size following trauma to the human head. Journal of Biomechanics 35(2), 153-160.

Kleiven, S., 2003. Influence of Impact Direction to the Human Head in Prediction of Subdural Hematoma. Journal of Neurotrauma 20(4), 365-379.

Kleiven, S., Peloso, P., von Holst, H., 2003. The Epidemiology of Head Injuries in Sweden From 1987 to 2000. Journal of Injury Control and Safety Promotion 10, 173-180.

Kleiven, S., von Holst, H., 2003. Review and evaluation of head injury criteria. Proceedings RTO Specialist Meeting, the NATO, Koblenz, Germany.

Kleiven, S., 2005. Influence of direction and duration of impacts to the human head evaluated using the finite element method. Proceedings of IRCOBI Conference, Prague, Czech Republic, pp.41-57.

Kleiven, S., 2006a. Biomechanics as a forensic science tool - Reconstruction of a traumatic head injury using the finite element method. Scandinavian Journal of Forensic Science 2, 73-78.

Kleiven, S., 2006b. Evaluation of head injury criteria using an FE model validated against experiments on localized brain motion, intra-cerebral acceleration, and intra-cranial pressure. International Journal of Crashworthiness 11(1), 65-79.

Kleiven, S., 2007a. A parametric study of energy absorbing foams for head injury prevention. The 20^{th} International Technical Conference on the Enhanced Safety of Vehicles Conference (ESV), Paper Number 07-0385, Lyon, France, 18-21.

Kleiven, S., 2007b. Head injury biomechanics and criteria. Biomechanics and Neuronics, course literature, KTH.

Kleiven, S., 2007c. Predictors for traumatic brain injuries evaluated through accident reconstructions. Proceedings of the 51^{st} Stapp Car Crash Conference, pp.81-114.

Klug, C., Feist, F., Tomasch, E., 2015. Testing of bicycle helmets for preadolescents. In: IRCOBI Conference, IRC-15-24.

Koerte, I.K., Ertl-Wagner, B., Reiser, M., Zafonte, R., Shenton, M.E., 2012a. White matter integrity in the brains of professional soccer players without a symptomatic concussion. Journal of the American Medical Association 308(18), 1859-1861.

Koerte, I.K., Kaufmann, D., Hartl, E., Bouix, S., Pasternak, O., Kubicki, M., Rauscher, A., Li, D.K.B., Dadachanji, S.B., Taunton, J.A., Forwell, L.A., Johnson, A.M., Echlin, P.S., Shenton, M.E., 2012b. A prospective study of physician-observed concussion during a varsity university hockey season: white matter integrity in ice hockey players. part 3 of 4. Neurosurgical Focus 33(6), E3.

Köstner, H., Stöcker, U.W., 1987. Mathematische Analyse der Sto absorption im Schutzhelmmaterial. VDI-bericht 657, 211-244.

Kostopoulos, V., Markopoulos, Y.P. ,Giannopoulos, G., Vlachos, D.E., 2002. Crashworthiness Study of Composite Motorcycle Safety Helmet. Composites Part B 33, 99-107.

Krabbel, G., Müller, R., 1996. Development of a Finite Element Model of the Head using the Visible Human Data. Abstracts of the Visible Human Project Conference, 71-72, Bethesda.

Kramer, F., 1998. Passive Sicherheit von Kraftfahrzeugen. Vieweg Verlag, Braunschweig, Germany.

Krames StayWell health encyclopedia library, 2011. http://ssov3.staywellsolutionsonline.com/Library/Encyclopedia/85,P00785 13/12/2011

Krave, U., Al-Olama, M., Hansson, H.A., 2011. Rotational Acceleration Closed Head Flexion Trauma Generates More Extensive Diffuse Brain Injury than Extension Trauma. Journal of Neurotrauma 28, 57-70.

Lagorce-Tachon, A., Karbowiak, T., Champion, D., Gougeon, R.D., Bellat, J.P., 2016. How does hydration affect the mechanical properties of wine stoppers?. Journal of Materials Science 51, 4227-4237.

Lakreb, N., Bezzazi, B., Pereira, H., 2015a. Mechanical strength properties of innovative sandwich panels with expanded cork agglomerates. European Journal of Wood and Wood Products 73(4), 46-473.

Lakreb, N., Bezzazi, B., Pereira, H., 2015b. Mechanical behavior of multilayered sandwich panels of wood veneer and a core of cork agglomerates. Materials and Design 65, 627-636.

Langlois, J.A., Rutland-Brown, W., Wald, M.M., 2006. The epidemiology and impact of traumatic brain injury: a brief overview. Journal of Head Trauma Rehabilitation 21(5), 375-378.

Lauret, C., Hrapko, M., van Dommelen, J.A.W., Peters, G.W.M., Wismans, J.S.H.M., 2009. Optical characterization of acceleration-induced strain fields in inhomogeneous brain slices. Medical Engineering & Physics 31, 392-399.

Lee, M.C., Melvin, J.W., Ueno, K., 1987. Finite element analysis of traumatic subdural hematoma. Proceedings of 31^{st} Stapp Car Crash Conference, Society of Automotive Engineers, SAE Paper No. 872201.

Lee, M.C., Haut, R.C., 1989. Insensitivity of tensile failure properties of human bridging veins to strain rate: Implications in biomechanics of subdural hematoma. Journal of Biomechanics 22, 537-542.

Levy, A.S., Hawkes, A.P., Hemminger, L.M., Knight, S., 2002. An analysis of head injuries among skiers and snowboarders. Journal of Trauma 53(4), 695-704.

Levy, M.L., Kasasbeh, A.S., Baird, L.C., Amene, C., Skeen, J., Marshall, L., 2012. Concussions in soccer: a current understanding. World Neurosurgery 78(5), 535-544.

Li, X., von Holst, H., Kleiven, S., 2011. Influence of gravity for optimal head positions in the treatment of head injury patients. Acta Neurochirurgica 153, 2057-2064.

Lighthall, J.W., Dixon, C.E., Anderson, T.E., 1989. Experimental models of brain injury. Journal of Neurotrauma 6, 83-97.

Lin, M., Kraus, J., 2008. Methodological issues in motorcycle injury epidemiology. Accident Analysis and Prevention 40(5), 1653-1660.

Lin, D.C., Shreiber, D.I., Dimitriadis, E.K., Horkay, F., 2008. Spherical indentation of soft matter beyond the Hertzian regime: numerical and experimental validation of hyperelastic models. Biomech. Model. Mechanobiol. 8, 345-358.

Lindenberg, R., Freytag, E., 1960. The Mechanism of Cerebral Contusions. A.M.A. Archives of Pathology 69, 440-469.

Lissner, H.R., Lebow, M., Evans, F.G., 1960. Experimental Studies on the Relation Between Acceleration and Intracranial Pressure Changes in Man. Surgery, Gynecology, and Obstetrics 3, 329-338.

Lister, D.G., Carl, III J., Morgan, III J.H., Denning, D.A., Valentovic, M., Trent, B., Beaver, B.L., 1998. Pediatric all-terrain vehicle trauma: A 5-year statewide experience. Journal of Pediatric Surgery 33(7), 1081-1083.

Liu, D.S., Fan, C.M., Lee, M.C., Yen, C.Y., 1997. A dynamic finite element simulation of the impact of motorcycle helmets. Crashworthiness, Occupant Protection and Biomechanics in Transportation Systems 38, 199-207.

Liu, D.S., Fan, C.M., 1998. Applied pressure tolerance to evaluate motorcycle helmet design. Proceedings of International Crashworthiness Conference, Dearborn, Michigan, USA.

Liu, D.S., Fan, C.M., Lee, M.C., Yen, C.Y., 1998. Development and Application of a 3D Finite Element Simulation Model of Impact of Motorcycle Helmet. International Crashworthiness Conference, Dearborn, Michigan, USA.

Liu, D.S., Chang, C.Y., Fan, C.M., Hsu, S.L., 2003. Influence of environmental factors on energy absorption degradation of polystyrene foam in protective helmets. Engineering Failure Analysis 10, 581-591.

Löwenhielm, P., 1974a. Dynamic properties of the parasagittal bridging veins. Zeitschrift fur Rechtsmedizin 74, 55-62.

Löwenhielm, P., 1974b. Strain tolerance of the Vv. Cerebri Sup. (bridging veins) calculated from head-on collision tests with cadavers. Zeitschrift fur Rechtsmedizin 75(2), 131-144.

Löwenhielm, P., 1975. Mathematical simulation of gliding contusions. Journal of Biomechanics 8, 351-356.

Löwenhielm, P., 1978. Tolerance levels for bridging vein disruption calculated with a mathematical model. Journal of Bioscience and Bioengineering 2, 501-507.

Macnab, A.J., Cadman, R., 1996. Demographics of alpine skiing and snowboarding injury: lessons for prevention programs. Injury Prevention 2(4), 286-289.

MAIDS, 2004. In depth investigations of accidents involving powered two wheelers. Final Report 1.2, Brussels. http://ec.europa.eu/

Maimi, P., Camanho, P.P., Mayugo, J.A., Turon, A., 2011. Matrix cracking and delamination in laminated composites. Part I: Ply constitutive law, first ply failure and onset of delamination. Mechanics of Materials 43(4),169-185.

Mao, H., Zhang, L., Jiang, B., et al., 2013. Development of a Finite Element Human Head Model Partially Validated With Thirty Five Experimental Cases. Journal of Biomechanical Engineering 135, 111002-15.

Mano, J.F., 2002. The viscoelastic properties of cork. Journal of Materials Science 37, 257-263.

Mano, J.F., 2007. Creep-recovery behaviour of cork. Materials Letters 61(11-12), 2473-2477.

Margulies S.S., Thibault, L.E., 1989. An analytical model of traumatic diffuse brain injury. Journal of Biomechanical Engineering 111(3), 241-249.

Margulies, S.S., Thibault, L.E., Gennarelli, T.A., 1990. Physical model simulations of brain injury in the primate. Journal of Biomechanics 23(8), 823-836.

Margulies, S.S., Thibault, L.E., 1992. A proposed tolerance criterion for diffuse axonal injury in man. Journal of Biomechanics 25(8), 917-923.

Marjoux, D., Baumgartner, D., Deck, C., Willinger, R., 2008. Head injury prediction capability of the HIC, HIP, SIMon and ULP criteria. Accident Analysis and Prevention 40(3), 1135-1148.

Markopoulos, Y.P., Vlachos, D.E., Kostopoulos, V., 1999. Impact response of a polycarbonate motorcycle safety helmet. Third National Congress on Computational Mechanics, Volos, Greece, pp.609-616.

Masso-Moreu, Y., Mills, N.J., 2003. Impact compression of polystyrene foam pyramids. International Journal of Impact Engineering 28, 653-676.

Maxeiner, H., 1997. Detection of ruptured cerebral bridging veins at autopsy. Forensic Science International 89(1-2), pp.103-110.

Maxwell, W.L., Watt, C., Graham, D.I., Gennarelli, T.A., 1993. Ultrastructural evidence of axonal shearing as a result of lateral acceleration of the head in non-human primates. Acta Neuropathologica (Berlin), 86(2), 136-144.

McAllister, T.W., Ford, J.C., Ji, S., Beckwith, J.G., Flashman, L.A., Paulsen, K., Greenwald, R.M., 2012. Maximum principal strain and strain rate associated with concussion diagnosis correlates with changes in corpus callosum white matter indices. Annals of Biomedical Engineering 40(1), 127-140.

McElhaney, J.H., Fogle, J.H., Melvin, J.W., Haynes, R.R., Roberts, V.L., Alem, N.B., 1970. Mechanical properties of cranial bone. Journal of Biomechanics 3, 495-511.

McElhaney, J.H., Roberts, V.L., Hilyard, J.F., 1976. Handbook of Human Tolerance. Japan Automobile Research Institute, Inc., pp.143.

McIntosh, A., Dowdell, B., Svensson, N., 1998. Pedal cycle helmet effectiveness: a field study of pedal cycle accidents. Accident Analysis and Prevention 30(2), 161-168.

McIntosh, A.S, Patton, D.A, Frechede, B., Pierre, P., Ferry, E., Barthels, T., 2014. The biomechanics of concussion in unhelmeted football players in australia: a case-control study. British Medical Journal Open 4(5), 1-9.

McLean, A.J., 1995. Brain injury without head impact?, Journal of Neurotrauma 12, 621-625.

Meaney, D.F., Thibault, L.E., 1990. Physical model studies of cortical brain deformation in response to high strain rate inertial loading, International Conference on the Biomechanics of Impacts. IRCOBI, Lyon, France.

Meaney, D.F., Smith, D., Ross, D.T., 1993. Diffuse Axonal Injury in the Miniature Pig: Biomechanical Development and Injury Threshold. Crashworthiness and Occupant Protection in Transportation Systems 25, 169-175.

Meaney, D.F., Smith, D.H., Shreiber, D.I., Bain, A.C., Miller, R.T., Ross, D.T., Gennarelli, T.A., 1995. Biomechanical analysis of experimental diffuse axonal injury. Journal of Neurotrauma 12(4), 689-694.

Mellion, M.B., 1991. Common cycling injuries. Sports Medicine 11(1), 52-70.

Mellor, A., Dixon, P., 1997. Improved motorcycle helmet design: the relationship between shell design and injury potential. Vehicle Engineering Resource Centre, TRL, Project Report-PR/VE/263/97.

Mellor, A., StClair, V., 2005. Advanced motorcycle helmets. Proceedings of the 19^{th} International Technical Conference of the Enhanced Safety of Vehicles, Washington, DC, pp.1-13.

Melvin, J.W., McElhaney, J.H., Roberts, V.L., 1970. Development of a Mechanical Model of the Human Head - Determination of Tissue Properties and Synthetic Substitute Materials. Proceedings of 14^{th} Stapp Car Crash Conf, Society of Automotive Engineers, SAE Paper No. 700903.

Melvin, J., Lighthall, J., Ueno, K., 1993. Brain Injury Biomechanics. Accidental Injury, Nahum, A.M. and Melvin, J.W. (eds), Springer-Verlag, New York, pp.269-290.

Melvin, J.W., 1995. Injury assessment reference values for the CRABI 6-Month Infant Dummy in a Rear-Facing Infant Restraint with Air Bag Deployment. SAE International Congress and Exposition, Society of Automotive Engineers, SAE Paper No. 950872.

Melvin, J., Lighthall, J., 2002. Brain injury biomechanics. In: A.M. Nahum and J.W. Melvin (Eds.), Accidental Injury - Biomechanics and Prevention, pp.277-302, Springer Verlag, New York.

Mendis, K., 1992. Finite element modelling of the brain to establish diffuse axonal injury criteria. PhD Dissertation, Ohio State University.

Mertz, H., Prasad, P., Irwin, A., 1997. Injury risk curves for children and adults in frontal and rear collisions. SAE paper 973318, Lake Buena Vista, pp.13-30.

Meshmixer manual. Autodesk; 2012.

Meythaler, J.M., Peduzz ,J.D., Eleftheriou, E., 2001. Current concepts: diffuse axonal injury-associated traumatic brain injury. Archives of Physical Medicine and Rehabilitation 82(10), 1461-1471.

Miller, K., 2011. Biomechanics of the brain. Springer-Verlag New York.

Miller, K., Chinzei, K., 1977. Constitutive modelling of brain tissue: experiment and theory. J. Biomech. 30, 1115-1121.

Miller, K., Chinzei, K., 2002. Mechanical properties of brain tissue in tension. J. Biomech. 35, 483-490.

Miller, K., Chinzei, K., Orssengo, G., et al., 2000. Mechanical properties of brain tissue in-vivo: experiment and computer simulation. J. Biomech. 33, 1369-1376.

Miller, K., Wittek, A., Joldes, G., 2011. Biomechanical modeling of the brain for computer-assisted neurosurgery. In: K. Miller (Ed.), Biomechanics of the brain, pp.111-136, Springer-Verlag New York.

Miller, R.T., Margulies, S.S., Leoni, M., Nonaka, M., Chen, X.H., Smith, D.H., Meaney, D.F., 1998. Finite element modeling approaches for predicting injury in an experimental model of severe diffuse axonal injury. Proceedings of 42^{nd} Stapp Car Crash Conference, SAE Paper 983154, pp. 155-166.

Mills, N.J., Gilchrist, A., 1988. Mathematical modelling of the effectiveness of helmets in head protection. Proceedings of IRCOBI conference, Bergisch Gladbach, W. Germany, pp.215-226.

Mills, N.J., Gilchrist, A., 1991. The Effectiveness of Foams in Bicycle and Motorcycle Helmets. Accident Analysis and Prevention 23(2-3), 153-163.

Mills, N.J., Gilchrist, A., 1992. Motorcycle helmet shell optimisation. Proceedings Association for Advancement of Automotive Medicine Conference, Portland, Oregon, pp.149-162.

Mills, N.J., 1995. Role of components of motorcycle helmets. Report-B15 2TT, School of Metallurgy and Materials, University of Birmingham, UK.

Mills, N.J., 1996. Accident investigation of motorcycle helmets. Impact 5, 46-51.

Mills, N.J., 2007. Polymer Foams Handbook- Engineering and biomechanics applications and design guide. Butterworth-Heinemann.

Mills, N.J., Wilkes, S., Derler, S., Flisch, A., 2009a. FEA of oblique impact tests on a motorcycle helmet. International Journal of Impact Engineering 36, 913-925.

Mills, N.J., Stämpfli, R., Marone, F., Brühwiler, P.A., 2009b. Finite element micromechanics model of impact compression of closed-cell polymer foams. International Journal of Solids and Structures 46(3-4), 677-697.

MIPS helmet. http://www.mipsprotection.com/ 26/02/2016

Monea, A.G., Van der Perre, G., Baeck, K., Delye, H., Verschueren, P., Forausebergher, E., Van Lierdem C., Verpoestm I., Slotenm J.V., Goffin, J., Depreitere, B., 2014. The relation between mechanical impact parameters and most frequent bicycle related head injuries. Journal of the Mechanical Behavior of Biomedical Materials 33, 3-15.

Monson, K.L., Goldsmith W., Barbaro N.M., Manley G.T., 2003. Axial mechanical properties of fresh human cerebral blood vessels. Journal of Biomechanical Engineering 125(2), 288-294.

Mordaka, J., Kleiven, S., van Schijndel de Nooij, M., de Lange, R., Casanova, L.J.G., Carter, E.L., von Holst, H., 2007. The importance of rotational kinematics in pedestrian head to windshield impacts. Proceedings of IRCOBI Conference, Maastricht, The Netherlands, pp.83-94.

Moreira, R.A.S., Melo, F.J.Q.,Dias Rodrigues, J.F., 2010. Static and dynamic characterization of composition cork for sandwich beam cores. Journal of Materials Science 45, 3350-3366.

Morgan, D.E., Cone-head technology, 2007. http://www.coneheadhelmets.com.au/ 17/12/2016.

Mori, T., Katayama Y., Kawamata, T., 2006. Acute hemispheric swelling associated with thin subdural hematomas: Pathophysiology of repetitive head injury in sports. Acta Neurochirurgica Supplementum 96, 40-43.

Morrison III, B., Cater, H.L., Wang, C.C.B., Thomas, F.C., Hung, C.T., Ateshian, G.A., Sundström, L.E., 2003. A tissue level tolerance criterion for living brain developed in an in vitro model of traumatic mechanical loading. Proceedings of 47^{th} Stapp Car Crash Conference, SAE Paper No. 2003-22-0006.

Morrison, B.I., Cater, H.L., Benham, C.D., Sundstrom, L.E., 2006. An in vitro model of traumatic brain injury utilizing two-dimensional stretch of organotypic hippocampal slice cultures. J. Neurosci. Methods. 150, 192-201.

Motherway, J., Doorly, M.C., Curtis, M., Gilchrist, M.D., 2009. Head impact biomechanics simulations: A forensic tool for reconstructing head injury?. Legal Medicine 11, S220-S222.

Motherway, J.A., Verschueren, P., van der Perre, G., van der Sloten, J., Gilchrist, M.D., 2010. The mechanical properties cranial bone. Proceedings of IRCOBI Conference, Hanover, Germany, pp.131-134.

Mustafa, H., Pang, T.Y., Perret-Ellena, T., Subic, A., 2015. Finite element bicycle helmet models development. Procedia Technology 20, 91-97.

Nahum, A., Gatts, J., Gadd, C., Danforth, J., 1968. Impact tolerance of the skull and face. In: Proceedings of 12^{nd} Stapp Car Crash Conference, SAE 680785, Detroit.

Nahum, A.M., Smith, R., 1976. An experimental model for closed head impact injury. SAE Technical Paper 760825, pp. 2638-2651.

Nahum, A.M., Smith, R., Ward, C.C., 1977. Intracranial pressure dynamics during head impact. Proceeding of 21^{st} Stapp Car Crash Conference, pp. 339-366

Nahum, A.M., Melvin, J.W., 1993. Accidental Injury. Biomechanics and Prevention, pp.292-300.

Nakadate, H., Fukumura, Y., Kaneko, Y., Kakuta, A., Furukawa, H., Aomura, S., 2014. In vitro uniaxial stretch model for evaluating the effect of strain along axon on damage to neurons. Journal of Biomechanical Science and Engineering 9(3), 14-36.

Neale, M., McGrath, M., Baumgartner, D., Willinger, R., 2004. Comparative study between finite element human head and dummy head model responses under impact. Proceedings of IRCOBI Conference, Graz, Austria, pp.69-78.

Newman, J., 1975. On the Use of the Head Injury Criterion (HIC) in Protective Headgear Evaluation. Proceedings of 9^{th} Stapp Car Crash Conference, San Diego, California, pp.17-19.

Newman, J.A., 1980. Head injury criteria in automotive crash testing. Society Automotive Engineers, SAE 801317.

Newman, J.A., 1986. A generalized model for brain injury threshold (GAMBIT). Proceedings of IRCOBI Conference, Zurich, Switzerland, pp.121-131.

Newman, J., Barr, C., Beusenberg, M., Fournier, E., Shewchenko, N., Welbourne, E., Withnall, C., 2000a. A New Biomechanical Assessment of Mild Traumatic Brain Injury Part 2 - Results and Conclusions. Proceedings of IRCOBI Conference, Montpellier, France.

Newman, J.A., Shewchenko, N., Welbourne, E., 2000b. A New Biomechanical Head Injury Assessment Function: The Maximum Power Index. Stapp Car Crash Journal 44, 215-247.

Newman, J., 2005. The biomechanics of head trauma and the development of the modern helmet. How far have we really come?. Proceedings of the IRCOBI Conference, Prague.

NHTSA, 1972. Occupant crash protection - Head Injury Criterion. Report No. FMVSS 208, Docket Number 69-7, Notice 17, US Departement of Transportation.

NHTSA, 2008. Traffic Safety Facts, Data: Motorcycles. DOT HS 811 159, National Highway Traffic Safety Administration, Washington DC. http://www-nrd.nhtsa.dot.gov/Pubs/811159.pdf

NHTSA, 2011. Determining Estimates of Lives and Costs Saved by Motorcycle Helmets. DOT HS 811 433, National Highway Traffic Safety Administration, Washington DC. http://www-nrd.nhtsa.dot.gov/Pubs/811433.pdf 15/03/2012

Nicolle, S., Lounis, M., Willinger, R., 2004. Shear properties of brain tissue over a frequency range relevant for automotive impact situations: New experimental results. Stapp Car Crash Journal 48, 239-258.

Nicolle, S., Lounis, M., Willinger, R., Palierne, J.F., 2005. Shear linear behaviour of brain tissue over a large frequency range. Biorheology 42, 209-223.

Niknejad, A., Moradi, A., 2016. A novel solid cylindrical composite material made of agglomerated cork inserts and silicone rubber resin during the flattening process. International Journal of Mechanical Sciences 115-116, 105-122.

Nishimoto, T., Murakami, S., 1998. Relation between diffuse axonal injury and internal head structure on blunt impact. Journal of Biomechanical Engineering 120(1), 140-147.

Nishimoto, T., Murakami, S., 2000. Direct impact simulation of diffuse axonal injury by axial head model. JSAE Review 21(1), 117-123.

Nóvoa, P.J.R.O., Ribeiro, M.C.S., Ferreira, A.J.M., Marques, A.t:, 2004. Mechanical characterization of lightweight polymer mortar modified with cork granulates. Composites Science and Technology 64, 2197-2205.

Oehmichen, M., Auer, R.N., König, H.G., 2006. Forensic Neuropathology and Associated Neurology. Springer, Part II, pp.177-215.

Ogden, R.W., 1972. Large deformation isotropic elasticity-on the correlation of theory and experiment for incompressible rubber like solids. Proc R Soc Lond A Math Phys Sci. 326, 565-584.

Ogden, R.W., Roxburgh, D.G., 1999. A Pseudo-Elastic Model for the Mullins Effect in Filled Rubber. Proceedings of the Royal Society of London A 455, 2861-2877.

Oliveira, V., Rosa, M.E., Pereira, H., 2014. Variability of the compression properties of cork. Wood Science and Technology 48, 937-948.

Ommaya, A.K., Hirsch, A.E., Martinez, J.L., 1966. The role of whiplash in cerebral concussion. Proceedings of 10^{th} Stapp Car Crash Conference, SAE Paper No. 660804.

Ommaya, A.K., Hirsch, A.E., Harris, E., Yarnell, P., 1967. Scaling of experimental data in cerebral concussion in sub-human primates to concussive threshold for man. Proceedings of the 11^{th} Stapp Car Crash Conference, Society of Automotive Engineers, pp.47-52, New York,.

Ommaya, A.K., Hirsch, A.E., 1971. Tolerances for Cerebral Concussion from Head Impact and Whiplash in Primates. Journal of Biomechanics 4, 13-31.

Ommaya, A.K., Grubb, R.L., Naumann, R.A., 1971. Coup and contrecoup injury: observations on the mechanics of visible brain injuries in the rhesus monkey. J. Neurosurg. 35, 503-516.

Ommaya, A.K., Paul Corrao, F.R.C.S., Letcher F.S., 1973. Head injury in the chimpanzee - Part 1: Biodynamics of traumatic unconsciousness. Journal of Neurosurgery 39(2), 152-166.

Ommaya, A.K., Gennarelli T.A., 1974. Cerebral concussion and traumatic unconsciousness, Correlation of experimental and clinical observations of blunt head injuries. Brain 97, 633-654.

Ommaya, A.K., 1984a. Head injury biomechanics. In: George G. Snively Memorial Lecture, Association for the Advancement of Automotive Medicine, Denver.

Ommaya, A.K., 1984b. Biomechanics of head injury. Biomechanics of Trauma, Eds. Nahum, Melvis, Appleton-Century-Crofts, Norwalk.

Ommaya, A.K., 1988. Mechanisms and preventive Management of head injuries, a paradigm for injury control. Proceedings of 32^{nd} AAAM Conference.

Ommaya, A., Goldsmith, W., Thibault, L., 2002. Biomechanics and neuropathology of adult and paediatric head injury. British Journal of Neurosurgery 16(3), 220-242.

Ono, K., Kikuchi, A., Nakamura, M., Kobayashi, H., Nakamura, N., 1980. Human Head Tolerance to Sagittal Impact: Reliable Estimation deduced from Experimental Head Injury using Subhuman Primates and Human Cadaver Skulls. Proceedings of 24^{th} Stapp Car Crash Conference, SAE Paper No. 801302.

Otte, D., 1991. Technical demands on safety in the design of crash helmets. Proceedings of 35^{th} Stapp Car Crash Conference, SAE paper 912911, pp.335-148, Warrendale, PA.

Otte, D., Chinn, B., Doyle, D., Strurrock, K., Schuller, E., 1997. Accident description and analysis of motorcycle safety helmets. Cost 327 Interim Reports, Accident Research Unit, Medical University Hanover, Germany.

Otte, D., Chinn, B., Doyl,e D., Mäkitupa, S., Sturrock, K., Schuller E., 1999. Contribution to Final Report of COST 327 Project. University of Hannover.

Ouellet, S., Cronin, D., Worswick, M., 2006. Compressive response of polymeric foams under quasi-static, medium and high strain rate conditions. Polymer Testing 25(6), 731-743.

Osirix user manual. Pixmeo; 2003.

Ozturk, U.E., Anlas, G., 2011. Finite element analysis of expanded polystyrene foam under multiple compressive loading and unloading. Materials and Design 32(2),773-780.

Parizel, P.M., Ozsarlak, O., Van Goethem, J.W., 1998. Imaging findings in diffuse axonal injury after closed head trauma. European Radiology 8, 965-969.

Patton, D.A., McIntosh, A.S., Kleiven, S., 2013. The biomechanical determinants of concussion: Finite element simulations to investigate brain tissue deformations during sporting impacts to the unprotected head. Journal of Applied Biomechanics 29, 721-730.

Paulino, M., Teixeira-Dias, F., 2011. An energy absorption performance index for cellular materials - development of a side-impact cork padding. International Journal of Crashworthiness 16(2), 135-153.

Paulino, M., Teixeira-Dias, F., 2012. On the Use of Polyurethane Foam Paddings to Improve Passive Safety in Crashworthiness Applications. In: F., Zafar, E., Sharmin, Polyurethane, InTech, pp.337-354.

Pellman, E.J., Viano, D.C., Tucker, A.M., Casson, I.R., Waeckerle, J.F., 2003. Concussion in professional football: Reconstruction of game impacts and injuries. Neurosurgery 53(4), 799-814.

Pellman, E.J., Viano, D.C., Withnall, C., Shewchenko, N., Bir, C.A., Halstead, P.D., 2006. Concussion in professional football: helmet testing to assess impact performance-part 11. Neurosurgery 58, 78-96.

Peng, Y., Deck, C., Yang, J., Otte, D., Willinger, R., 2012. A study of kinematics of adult pedestrian and head impact conditions in case of passenger car collisions based on real world accident data. Proceedings of IRCOBI Conference 2012, IRC-12-82, Dublin, pp.766-778.

Pereira H, Rosa ME, Fortes MA, 1987. The cellular structure of cork from Quercus suber L. IAWA Bulletin 8(3), 213-218.

Pereira, H., 1988. Chemical composition and variability of cork form Quercus suber L. Wood Science and Technology 22(3), 211-218.

Pereira, H., Graça, J., Baptista, C., 1992. The effect of growth-rate on the structure and compressive properties of cork. IAWA Bulletin 13(4), 389-396.

Pereira, H., 2007. Cork: biology, production and uses. Elsevier, Amsterdam.

Pereira, H., 2013. Variability of the chemical composition of cork. Bioresources 8, 2246-2256.

Pervin, F., Chen, W.W., 2009. Dynamic mechanical response of bovine gray matter and white matter brain tissues under compression. J. Biomech. 42, 731-735.

Phillips, K.D., 2004. Protective headgear and protective armour and a method of modifying protective headgear and protective armour. European Patent, EP1404189.

Phillips Head Protection System. http://www.phillipshelmets.com/HOME.htm 26/02/2012

Pike, J.A., 1990. Automotive Safety: Anatomy, Injury, Testing and Regulation. Society of Automotive Engineers Inc.

Pincemaille, Y., Trosseille, X., Mack, P., Tarriere, C., 1989. Some new data related to human tolerance obtained from volunteer boxers. SAE Technical Paper 892435.

Pinnoji, P.K., Mahajan, P., 2006. Impact analysis of helmets for improved ventilation with deformable head model. Proceedings of IRCOBI conference, pp.159-170, Madrid.

Pinnoji, P.K., Bourdet, N., Mahajan, P., Willinger, R., 2008a. New motorcycle helmets with metal foam shell. Proceedings of IRCOBI Conference, Bern, Switzerland, pp.449-452.

Pinnoji, P.K., Haider, Z., Mahajan, P., 2008b. Design of motorcycle helmets: computational fluid and impact dynamics studies. International Journal of Crashworthiness 13(3), 265-278.

Pinnoji, P.K., Mahajan, P., 2008. Two Wheeler Helmets with Ventilation and Metal Foam. Defence Science Journal 58, 304-311.

Pinnoji, P.K., Mahajan, P., 2010. Analysis of impact-induced damage and delamination in the composite shell of a helmet. Materials and Design 31, 3716-3723.

Pinnoji, P.K., Mahajan, P., Bourdet, N., Deck, C., Willinger, R., 2010. Impact dynamics of metal foam shells for motorcycle helmets: Experiments & numerical modelling. International Journal of Impact Engineering 37, 274-284.

Pinto, P., Sousa, A.R., Silvestre, A., Neto, C.P., Gandini, A., Eckerman, C., 2009. Quercus suber and Betula pendula outer barks as renewable sources of oleochemicals: a comparative study. Ind Crops Prod 29, 126-132.

POC sports, 2016. http://www.pocsports.com/ 17/08/2016

Post, A., Hoshizaki, B., Gilchrist, M.D., 2012a. Finite element analysis of the effect of loading curve shape on brain injury predictors. Journal of Biomechanics 45, 679-683.

Post, A., Oeur, A., Hoshizaki, B., Gilchrist, M.D., 2012b. The influence of centric and non-centric impacts to American football helmets on the correlation between commonly used metrics in brain injury research. Proceedings of IRCOBI Conference 2012, IRC-12-52, Dublin, pp.419-429.

Post, A., Karton, C., Hoshizaki, B., Gilchrist, M.D., 2014. Analysis of the protective capacity of ice hockey helmets in a concussion injury reconstruction. Proceedings of IRCOBI Conference 2014, IRC-14-17, pp.72-80.

Povlishock, J.T., 1993. Pathobiology of traumatically induced axonal injury in animals and man. Annals of Emergency Medicine 22, 980-986.

Prange, M.T., Margulies, S.S., 2002. Regional, directional, and age-dependent properties of the brain undergoing large deformation. Journal of Biomechanical Engineering 124(2), 244-252.

Prasad, P., 1985. Review of biomechanical impact response and injury in the automotive environment. Head, report no. DOT HS 807 042, Chapter 1, U.S. Department of transport - NHTSA, Washington D.C., USA.

Pratellesi, A., Turrin, S., Haag, T., Scippa, A., Baldanzini N., 2011. On the effect of testing uncertainties in the homologation tests of motorcycle helmets according to ECE 22.05. International Journal of Crashworthiness 16(5), 523-536.

Ptak, M., Kaczynski, P., Fernandes, F.A.O., Alves de Sousa, R.J., 2016. Computer simulations for head injuries verification after impact. In: Proceedings of the 13^{th} International Scientific Conference of Computer Aided Engineering, Springer, Polanica-Zdrój, Poland.

Pudenz, R., Shelden, C., 1946. The lucite calvarium - a method for direct observation of the brain. Journal of Neurosurgery 3, 487-505.

Pullar, R.C., Marques, P., Amaral, J., Labrincha, J.A., 2015. Magnetic wood-based biomorphic Sr3Co2Fe24O41 Z-type hexaferrite ecoceramics made from cork templates. Materials and Design 82, 297-303.

Rashid, B., Destrade, M., Gilchrist, M.D., 2012. Mechanical characterization of brain tissue in compression at dynamic strain rates. Journal of the Mechanical Behavior of Biomedical Materials 10, 23-38.

Rashid, B., Destrade, M., Gilchrist, M.D., 2012. Hyperelastic and viscoelastic properties of brain tissue in tension. In: Proceedings of the ASME 2012 International Mechanical Engineering Congress & Exposition, IMECE2012, pp.9-15, Houston, Texas, USA.

Rashid, B., Destrade, M., Gilchrist, M.D., 2012. Temperature effects on brain tissue in compression. Journal of the Mechanical Behavior of Biomedical Materials 14, 113-118.

Raul, J.S., Baumgartner, D., Willinger, R., Ludes, B., 2006. Finite element modelling of human head injuries caused by a fall. International Journal of Legal Medicine 120, 212-218.

Raul, J.S., Deck, C., Willinger, R., Ludes, B., 2008. Finite-element models of the human head and their applications in forensic practice. International Journal of Legal Medicine 122, 359-366.

Reis, L., Silva, A., 2009. Mechanical Behavior of Sandwich Structures using Natural Cork Agglomerates as Core Materials. Journal of Sandwich Structures and Materials 11, 487-500.

Rice, T.M., Troszak, L., Ouellet, J.V., Erhardt, T., Smith, G.S., Tsai, B.W., 2016. Motorcycle helmet use and the risk of head, neck, and fatal injury: Revisiting the Hurt Study. Accident Analysis and Prevention 91, 200-207.

Richter, M., Otte, D., Lehmann, U., Chinn, B., Schuller, E., Doyle, D., Sturrock, K., Krettek, C., 2001. Head Injury Mechanisms in Helmet-Protected Motorcyclists: Prospective Multicenter Study. Journal of Trauma 51, 949-958.

Robbins, D.H., Wood, J.L., 1969. Determination of mechanical properties of the bones of the skull. Experimental Mechanics 9(5), 236-240.

Rosa, M.E., Fortes, M.A., 1988a. Rate effects on the compression and recovery of dimensions of cork. Journal of Materials Science 23(3), 879-885.

Rosa, M.E., Fortes, M.A., 1988b. Stress relaxation and creep of cork. Journal of Materials Science 23(1), 35-42.

Rosa, M.E., Fortes, M.A., 1991. Deformation and fracture of cork in tension. Journal of Materials Science 26(2), 341-348.

Rosa, M.E., Osorio, J., Gree, V., 2004. Torsion of cork under compression. Materials Science Forum 455-456, 235-238.

Roth, H., Lombard, C., 1953. Crash helmet. US patent, US2625683. http://ip.com/pdf/patent/US2625683.pdf 15/12/2011

Rowson, S., Duma, S., 2011. Development of the star evaluation system for football helmets: Integrating player head impact exposure and risk of concussion. Annals of Biomedical Engineering 39(8), 2130-2140.

Rowson, S., Duma, S.M., Beckwith, J.G., Chu, J.J., Greenwald, R.M., Crisco, J.J., Brolinson, P.G., Duhaime, A.C., McAllister, T.W., Maerlender, A.C., 2012. Rotational head kinematics in football impacts: An injury risk function for concussion. Annals of Biomedical Engineering 40(1), 1-13.

Ruan, J.S., Khalil, T., King, A.I., 1991. Human head dynamic response to side impact by finite element modeling. Journal of Biomechanical Engineering 113(3), 276-283.

Ruan, J.S., Khalil, T.B., King, A.I., 1993. Finite Element modeling of direct head impact. Proceedings of 37^{th} Stapp Car Conference, SAE Paper No.933114.

Ruan, J.S., Prasad, P., 1995. Coupling of a finite element human head model with lumped parameter hybrid III dummy model: preliminary results. Journal of Neurotrauma 12(4), 725-734.

Ruan, J., Prasad, P., 2001. The effects of skull thickness variations on human head dynamic impact responses. Stapp Car Crash J. 45, 395-414.

Sahoo, D., Deck, C., Yoganandan, N., Willinger, R., 2013. Anisotropic composite human skull model and skull fracture validation against temporo-parietal skull fracture. Journal of the Mechanical Behavior of Biomedical Materials 28, 340-353.

Sahoo, D, Deck, C, Willinger, R, 2014a. Development and validation of an advanced anisotropic visco-hyperelastic human brain FE model. Journal of the Mechanical Behavior of Biomedical Materials 33, 24-42.

Sahoo, D., Deck, C., Willinger, R., 2014b. Composite FE human skull model validation and development of skull fracture criteria. Proceedings of IRCOBI Conference, Berlin, pp.106-118.

Sahoo, D., Deck, C., Willinger, R., 2016. Brain injury tolerance limit based on computation of axonal strain. Accident Analysis and Prevention 92, 53-70.

Sahoo, D., Deck, C., Yoganandan, N., Willinger, R., 2016b. Development of skull fracture criterion based on real-world head trauma simulations using finite element head model. Journal of the Mechanical Behavior of Biomedical Materials 57, 24-41.

Sahuquillo-Barris, J., Lamarca-Ciuro, J., Vilalta-Castan, J., Rubio-Garcia, E., Rodriguez-Pazos, M., 1988. Acute subdural hematoma and diffuse axonal injury after severe head trauma. Journal of Neurosurgery 68(6), 894-900.

Sanchez-Saez, S., García-Castillo, S.K., Barbero, E., Cirne, J., 2015a. Dynamic crushing behaviour of agglomerated cork. Materials and Design 65, 743-748.

Sanchez-Saez, S., Barbero, E., Garcia-Castillo, S.K., Ivañez, I., Cirne, J., 2015b. Experimental response of agglomerated cork under multi-impact loads. Materials Letters 160, 327-330.

Schmitt, K., Niederer, P., Muser, M., Walz, F., 2007. Trauma Biomechanics - Accidental injury in traffic and sports. Springer Berlin Heidelberg, Second edition, chapter 3.

Schneider, D., Nahum A., 1972. Impact studies of facial bones and skull. In: Proceeding of 16^{th} Stapp Car Crash Conference, SAE 720965, pp.186-203, Detroit.

Schulz, M.R., Marshall, S.W., Mueller, F.O., Yang, J., Weaver, N.L., Kalsbeek, W.D., Bowling, J.M., 2004. Incidence and risk factors for concussion in high school athletes, North Carolina, 1996-1999. American Journal of Epidemiology 160(10), 937-944.

Schwartz, D., Guleyupoglu, B., Koya, B., Stitzel, J.D., Gayzik, F.S., 2015. Development of a computationally efficient full human body finite element model. Traffic Injury Prevention 16(sup1), S49-S56.

Scott, R.S., 1997. A dynamic FE simulation of the impact of motorcycle helmets. Crashworthiness, occupant protection and biomechanics in transportation systems, AMD vol. 225, New York: ASME.

Sellier, K., Unterharnscheidt, F., 1963. Mechanik und Pathomorphologie der Hirnschäden nach stumpfer Gewalteinwirkung auf den Schädel. Hefte zur Unfallheilkunde, Heft 76. Springer, Berlin Heidelberg New York.

Shatsky, S.A., Alter, W.A., Evans, D.E., 1974. Traumatic Distortions of the Primate Head and Chest: Correlation of Biomechanical, Radiological and Pathological Data. Proceedings of 18^{th} Stapp Car Crash Conference, pp.351-81.

Shaw, T.L., 2014. Biomechanic analysis of injury mitigation performance for novel helmet design. Master thesis, Faculty of San Diego State University. https://www.6dhelmets.com/innovation/

Shreiber, D.I., Bain, A.C., Meaney D.F., 1997. In vivo thresholds for mechanical injury to the blood-brain barrier, SAE Paper No. 973335. Proceedings of 41^{th} Stapp Car Crash Conference, Society of Automotive Engineers, pp.177-190.

Shuaeib, F.M., Hamouda, A.M.S., Radin Umar, R.S., Hamdan, M.M., Hasmi, M.S.J., 2002a. Motorcycle helmet part I. Biomechanics and computational issues. Journal of Materials Processing Technology 123, 406-421.

Shuaeib, F.M., Hamouda, A.M.S, Hamdan, M.M., Radin Umar, R.S., Hashmi, M.S.J., 2002b. Motorcycle helmet: Part II, Materials and design issues. Journal of Materials Processing Technology 123, 422-431.

Shuaeib, F.M., Hamouda, A.M.S., Radin Umar, R.S., Hamdan, M.M., Hashmi, M.S.J., 2002c. Motorcycle helmet, Part III, Manufacturing issues. Journal of Materials Processing Technology 123, 432-439.

Shuaeib, F.M., Hamouda, A.M.S., Wong, S.V., Radin Umar, R.S., Megat Ahmed, M.M.H., 2007. A new motorcycle helmet liner material: the finite element simulation and design of experiment optimization. Materials and Design 28, 182-195.

Shugar, T.A., Katona, M.C., 1975. Development of finite element head injury model. Journal of Structural Engineering 101, 223-239.

Shugar, T.A., 1977. A finite element head injury model. Report DOT HS 289-3-550-TA.

Siegel, J.H., Loo, G., Dischinger, P.C., Burgess, A.R., Wang, S.C., Schneider, L.W., 2001. Factors influencing the patterns of injuries and outcomes in car versus car crashes compared to sport utility, van, or pick-up truck versus car crashes: Crash injury research engineering network study. Journal of Trauma and Acute Care Surgery 51(5), 975-990.

Silva, A., 2016. Utilização da cortiça em design de produto - Novas soluções para capacetes desportivos. Master thesis, Department of Communications and Arts, University of Aveiro.

Silva, S.P., Sabino, M.A., Fernandes, E.M., Correlo, V.M., Boesel, L.F., Reis, R.L., 2005. Cork: properties, capabilities and applications. International Materials Reviews 50(6), 345-365.

Singh, A., Lu, Y., Chen, C., KallaKuri, S., Cavanaugh, J.M., 2006. A new model of Traumatic Injury to determine the effect of strain and displacement rates. Stapp Car Crash J. 50, 601-23.

Smith, D.H., Wolf, J.A., Lusardi, T.A., Lee, V.M.Y., Meaney, D.F., 1999. High tolerance and delayed elastic response of cultured axons to dynamic stretch injury. Journal of Neuroscience 19(11), 4263-4269.

Smith, D.H., Meaney, D.F., 2000. Axonal damage in traumatic brain injury. Neuroscientist 6(6), 483-495.

Smith, D.H., Nonaka, M., Miller, R.T., 2000. Immediate Coma Following Inertial Brain Injury Dependent on Axonal Damage in the Brainstem. Journal of Neurosurgery 93, 315-322.

Smith, D.H., Meaney, D.F., Shull, W.H., 2003. Diffuse axonal injury in head trauma. Journal of Head Trauma Rehabilitation 18, 307-316.

Smith, T., Pomerening, D., 2014. Theoretical Calculation of Helmet Thickness Necessary to achieve 100g for a 6.2 m/s impact. Technical report, Dynamic Research Inc, Torrance, CA.

Snell M2015, 2015. Standard for Protective Headgear - For Use with Motorcycles and Other Motorized Vehicles. Snell Memorial Foundation, North Highlands, CA. http://www.smf.org 17/12/2016

Snell SA2015, 2015. Standard for Protective Headgear - For Use in Competitive Automotive Sports. Snell Memorial Foundation, North Highlands, CA. http://www.smf.org 17/12/2016

Snively, G.G., 1957. Skull Busting for Safety. Sports Car Illustrated.

Sousa-Martins, J., Kakogiannis, D., Coghe, F., Reymen, B., Teixeira-Dias, F., 2013. Response of cork compounds subjected to impulsive blast loads. Engineering Structures 46, 140-146.

Stalnaker, R.L., 1969. Mechanical properties of the head. PhD Dissertation Thesis, West Virginia University, Morgantown, WV, USA.

Stalnaker, R.L., McElhaney, J.H., Roberts, V.L., 1971. MSC tolerance curve for human heads to impact. ASME paper 71-WA/BHF-10, New York, pp.1-9.

Stalnaker, R.L., Robers, V.L., McElhaney, J.H., 1973. Side Impact Tolerance to Blunt Trauma. Proceedings of 17^{th} Stapp Car Crash Conference, pp.377-408.

Strich, S.J., 1956. Diffuse degeneration of the cerebral white matter in severe dementia following head injury. Journal of Neurology, Neurosurgery & Psychiatry 19, 163-185.

Strich, S.J., 1961. Shearing of Nerve Fibres as a Cause of Brain Damage due to Head Injury. Lancet 2, 443.

Suh, C.M., Kim, S.H., Oh, S.Y., 2005. Analysis of traumatic brain injury using a finite element model. Journal of Mechanical Science and Technology 19(7), 1424-1431.

Supprian, T., Bendszus, M., Hofmann, E., Becker, T., Retz, W., Rosler, M., 2000. The role of diffuse axonal injury in medical assessment of brain injured patients. Fortschritre der Neurologie Psychiatrie 68(3), 121-128.

Svec, P., Rosik, L., 1990. Styrene based plastics and their modification. Ellis Horwood, London.

Taher Halimi, M., Ben Hassen, M., Sakli, F., 2012. Design of a novel comfort liner for a motorcycle helmet. International Journal of Sustainable Engineering 5(2), 128-134.

Takhounts, G.E., Eppinger, R.H., Campbell, J.Q., Tannous, E.R., Power, E.D., Shook, L.S., 2003. On the development of the SIMon finite element head model human. Stapp Car Crash Journal, 47, 107-133.

Takhounts, E.G., Ridella, S.A., Hasija, V., Tannous, R.E., Campbell, J.Q., Malone, D., Danelson, K., Stitzel, J., Rowson, S., Duma, S., 2008. Investigation of Traumatic Brain Injuries Using the Next Generation of Simulated Injury Monitor (SIMon) Finite Element Head Model. Stapp Car Crash Journal 52, 1-31.

Tamura, A., Hayashi, S., Watanabe, I., et al., 2007. Mechanical characterization of brain tissue in high-rate compression. Journal of Biomechanical Science and Engineering 2, 115-126.

Tan, H., Qu, S., 2010. Impact of cellular materials. In: H. Altenbach, A. Öchsner, eds, Cellular and Porous Materials in Structures and Processes, Springer Vienna, pp. 309-334.

Tarriere, C., 1985. Depressurized cadaver head impacts - some findings. Biomechanics Symposium on Head Injury Prevention Past and Present Research, Wayne State University, pp.93-144.

Tarriere, C., 1987. Relationship between experimental measuring techniques and real world accidents. Head Injury Symposium, New Orleans, AAAM report.

Tchepel, D., Fernandes, F.A.O., Anjos, O., Alves de Sousa, R.J., 2016a. Mechanical Properties of Natural Cellular Materials. In: Reference Module in Materials Science and Materials Engineering, Elsevier. ISBN 9780128035818, http://dx.doi.org/10.1016/B978-0-12-803581-8.04056-X.

Tchepel, D., Fernandes, F.A.O., Alves de Sousa, R.J., 2016b. Forensic Biomechanics: New perspectives and challenges. In: What are forensic sciences? Concepts, scope and future perspectives, Ed. Pactor, pp 35-42, ISBN 978-989-693-058-5.

Tegner, Y., Lorentzon, R., 1996. Concussion among swedish elite ice hockey players. British Journal of Sports Medicine 30(3), 251-255.

Teixeira, J., Fernandes, A.C., Saramago, B.R., Emilia, M., Bordado, J.C., 1996. Influence of the wetting properties of polymeric adhesives on the mechanical behaviour of cork agglomerates. Journal of Adhesion Science and Technology 10(17), 1111-1127.

Teng, T., Liang, C., Nguyen, C., 2013. Development and validation of finite element model of helmet impact test. Journal of Materials Design and Applications 227, 82-88.

Thibault, L.E., Gennarelli, T.A., 1985. Biomechanics of diffuse brain injuries. Proceedings of 29^{th} Stapp Car Crash Conference, SAE Paper No. 856022.

Thibault, L.E., Gennarelli, T.A., Margulies, S.S., Marcus, J., Eppinger R., 1990. The strain dependant pathophysiological consequences of inertial loading on central nervous system tissue. Proceedings of IRCOBI Conference, pp.191-202.

Thibault, L.E., 1993. Brain injury from the macro to the micro level and back again: What have we learned to date?. Proceedings of IRCOBI Conference, Eindhoven, The Netherlands, pp.3-25.

Thibault, K.L., Margulies, S.S., 1998. Age-dependent material properties of the porcine cerebrum: effect on pediatric inertial head injury criteria. J. Biomech. 31, 1119-1126.

Thom, D.R., Hurt, H.H., Smith, T.A., 1998. Motorcycle helmet headform and test apparatus comparison. Head protection research laboratory, United States, Paper Number 98-S10-P-29.

Thom, D.R., 2006. Comparison Tests of Motorcycle Helmets Qualified to International Standards. Proceedings of the 2006 International Motorcycle Safety Conference, Motorcycle Safety Foundation.

Thomas, D .R., Hodgson, V .R., 1973. Skull fracture and management of open head injury. Neurological surgery (Edited by Youmans, J .R.), Philadelphia, Saunders, pp.969-977.

Thomson, R., Lövsund, P., Norin, H., Jakobsson, L., Boström, O., Håland, Y., 2001. Brain injuries in real world accidents - a multidisciplinary investigation. Proceedings of IRCOBI Conference, Isle of Man, UK, pp.173-188.

Tinard, V., Deck, C., Bourdet, N., Willinger, R., 2011. Motorcyclist helmet composite outer shell characterisation and modelling. Materials and Design 32, 3112-3119.

Tinard, V., Deck, C., Willinger, R., 2012a. Modelling and validation of motorcyclist helmet with composite shell. International Journal of Crashworthiness 17(2), 209-215.

Tinard V., Deck C., Willinger R.,2012b. New methodology for improvement of helmet performance during impacts with regards to biomechanical criteria. Materials and Design 37, 79-88.

Trammell, T.R., Olivary, S.E., 1991. Crash and injury statistics from indy-car racing 1985-1989. In: Proceedings of the 34th Annual Conference for the Advancement of Automotive Medicine, Chicago, United States of America, pp.329-335.

Trosseille, X., Tarriére, C., Lavaste, F., Guillon, F., 1992. Development of a FEM of the human head according to specific test protocol. Proceedings of the 36^{th} Stapp Car Crash Conference, pp.235-253.

Tse, K., Lim, S., Tan, V., Lee, H., 2014. A review of head injury and finite element head models. American journal of engineering, technology and society 1(5), 28-52.

Turner, A., Havey, J., 1953. Helmet. US patent, US2634415. http://ip.com/pdf/patent/US2634415.pdf 15/12/2011

Turquier, F., Kang, H., Trosseille, X., Willinger, R., Lavaste, F., Tarriere, C., Domont, A., 1996. Validation study of a 3D finite element head model against experimental data. SAE Transactions Paper No. 962431, pp.1912-1923.

Ueno, K., Melvin, J.W., 1995. Finite element model study of head impact based on hybrid III head acceleration: The effects of rotational and translational acceleration. Journal of Biomechanical Engineering 117(3), 319-328.

Unterharnscheidt, F., Higgins, L.S., 1969. Traumatic lesions of brain and spinal cord due to non-deforming angular acceleration of the head. Texas Reports on Biology and Medicine 27(1), 127-166.

Unterharnscheidt, F.J., 1971. Translational versus rotational acceleration: animal experiments with measured input. Proceedings of 15^{th} Stapp Car Crash Conference, SAE Paper No. 710880.

U.S. Department of Transportation, Federal Motor Carrier Safety Administration, Standard No. 218, Motorcycle helmets, Regulations current to 29/02/2012. http://www.fmcsa.dot.gov/rules-regulations/administration/fmcsr/fmcsrruletext.aspx?reg=571.218 26/03/2012

Vaiktus, S., Lauykaitis, A., Gnipas, I., Kersulis, V., Vejelis, S., 2006. Experimental Analysis of Structure and Deformation Mechanisms of Expanded Polystyrene (EPS) Slabs. Materials Science 12(4), 323-327.

Vallee, H., Hartemann, F., Thomas, C., Tarriere, C., Patel, A., Got, C., 1984. The fracturing of helmet shells. Proceedings of IRCOBI Conference, Delft, pp.99-109.

van den Bosch, H.L.A., 1998. Modelling and specifications for an improved helmet design. Master thesis, Technische Universiteit Eindhoven.

van den Bosch, H.L.A., 2006. Crash Helmet Testing and Design Specifications. PhD thesis, Technische Universiteit Eindhoven.

van Dommelen, J., 2011. Constitutive modelling of brain tissue for prediction of traumatic brain injury. Neural tissue biomechanics 3, 41-67.

van Schalkwijk, R., Helmet shock simulation with MARC using a hypo-elastic foam model. MTR-9304, MARC Analysis Research Corporation, The Netherlands, 1993.

Varley, G.W., Spencer-Jones, R., Thomas, P., Andrews, D., Green, A.D., Stevens, D.B., 1993. Injury patterns in motorcycle road racers: experience on the isle of man 1989-1991. Injury 24(7), 443-446.

Vaz, M.F., Fortes, M.A., 1998. Friction properties of cork. Journal of Materials Science 33, 2087-2093.

Velardi, F., Fraternali, F., Angelillo, M., 2006. Anisotropic constitutive equations and experimental tensile behavior of brain tissue. Biomech. Model. Mechanobiol. 5, 53-61.

Versace, J., 1971. A review of the severity index. Proceedings of 15^{th} Stapp Car Crash Conference, SAE paper 710881, pp. 771-796.

Vezin, P., Verriest, J.P., 2004. Evaluation of the simulated response of the human brain subjected to different accelerations during a frontal impact. Proceedings of IRCOBI Conference, Graz, Austria, pp.319-320.

Viano, D., 1988. Biomechanics of head injury - toward a theory linking head dynamic motion, brain tissue deformation and neural trauma. SAE Technical Paper 881708.

Viano, D., King, A.I., 1997. Injury Mechanisms and biofidelity of dummies. Crashworthiness of Transportation Systems: Structural Impact and Occupant Protection, Kluwer Academic Publishers, Dordrecht.

Viano, D., Aldman, B., Pape, K., van Hoof, J., von Holst, H., 1997. Brain kinematics in physical model tests with translational and rotational acceleration. International Journal of Crashworthiness 2(2), 191-206.

Viano, D.C., Lövsund, P., 1999. Biomechanics of brain and spinal-cord injury: analysis of neuropathologic and neurophysiologic experiments. Journal of Crash Prevention and Injury Control 1, 35-43.

Viano, D.C., Casson, I.R., Pellman, E.J., Zhang, L., Yang, K.H., King, A.I., 2005. Concussion in professional football: Brain responses by finite element analysis - Part 9. Neurosurgery 57, 891-916.

Vilela, C., Sousa, A.F., Freire, C.S.R., Silvestre, A.J.D., Neto, C.P., 2013. Novel sustainable composites prepared from cork residues and biopolymers. Biomass and Bioenergy 55, 148-155.

Voigt, G.E., Löwenhielm, C.G.P., Ljung, C.B.A., 1977. Rotational cerebral injuries near the superior margin of the brain. Acta Neuropathologica 39, 201-209.

Voo, L., Pintar, F.A., Yoganandan, N., Sances, A., Ewing, C.L., Thomas, D.J., Synder, R.G., 1994. Biomechanical analysis of tractor-induced head injury. SAE Transaction Paper no. 941725, Warrendale, pp.178-183.

Ward, C.C., Thompson, R.B., 1975. The development of a detailed finite element brain model. Proceedings of 19^{th} Stapp Car Crash Conference, SAE Paper, vol 751163, New York, pp.641-674.

Ward, C., Chan, M., 1980. Rotation generated shear strains in the brain. Proceedings of 8^{th} annual International Workshop on Human Subjects for Biomechanical Research, Troy, MI, USA.

Ward, C.C., Chan, M., Nahum, A.M., 1980. Intracranial Pressure: a Brain Injury Criterion. Proceedings of 24^{th} Stapp Car Crash Conference, SAE 801304.

Web Bike World. http://www.webbikeworld.com/r2/zeus-helmet/zeus-zs-3000/ 16/05/2012

Whitaker, J., 1980. A survey of motorcycle accidents. TRRL Laboratory Report LR 913, Crowthorne.

WHO, 2009. Global status report on road safety: time for action. The World Health Organization, Geneva. http://www.who.int/

Willinger, R., Kang, H.S., Diaw, B.M., 1999a. Développement et validation d'un modèle mécanique de la tête humaine (Development and validation of a human head mechanical model). Comptes Rendus de l'Académie des Sciences - Series IIB - Mechanics-Physics-Astronomy 327(1), 125-131.

Willinger, R., Kang, H.S., Diaw, B.M., 1999b. Three-dimensional human head finite-element model validation against two experimental impacts. Annals of Biomedical Engineering 27(3), 403-410.

Willinger, R., Baumgartner, D., Chinn, B., Neale, M., 2000a. Head tolerance limits derived from numerical replication of real world accidents. Proceedings of IRCOBI Conference, Isle of Man, UK, pp.209-222.

Willinger, R., Baumgartner, D., Guimberteau, T., 2000b. Dynamic characterization of motorcycle helmets: modelling and coupling with the human head. Journal of Sound and Vibration 235, 611-625.

Willinger, R., Diaw, B.M., Kang, H.S., 2000c. Finite element modeling of skull fractures caused by direct impact. International Journal of Crashworthiness 5(3), 249-258.

Willinger, R., Baumgartner, D., Chinn, B., Schuller, E., 2001. New dummy head prototype: development, validation and injury criteria. International Journal of Crashworthiness 6, 281-293.

Willinger, R., Diaw, B.M., Baumgartner, D., Chinn, B., 2002. Full face protective helmet modelling and coupling with a Human head model. International Journal of Crashworthiness 7(2), 167-178.

Willinger, R., Baumgartner, D., 2003a. Human head tolerance limits to specific injury mechanisms. International journal of Crashworthiness 8(6), 605-617.

Willinger, R., Baumgartner, D., 2003b. Numerical and physical modelling of the human head under impact: towards new injury criteria. International Journal of Vehicle Design 32(1-2), 94-115.

Wilson, K.H., Carr, D.J., 1993. Head protection the application of mathematical modeling. Proceedings of IRCOBI Conference, Eindhoven Technical University, Eindhoven, The Netherlands.

Wismans, J., 1994. Injury biomechanics. Second printing edn, no. 4552, Eindhoven University of Technology, The Netherlands.

Wright, R.M., Ramesh, K.T., 2012. An axonal strain injury criterion for traumatic brain injury. Biomechanics and Modeling in Mechanobiology 11, 245-260.

Yamakawa, H., Murase, S., Sakai, H., Iwama, T., Katada, M., Niikawa, S., Sumi, Y., Nishimura, Y., Sakai, N., 2001. Spinal injuries in snowboarders: Risk of jumping as an integral part of snowboarding. Journal of Trauma and Acute Care Surgery 50(6), 1101-1105.

Yan, W., Pangestu, O.D., 2011. A modified human head model for the study of impact head injury. Computer Methods in Biomechanics and Biomedical Engineering 14(12), 1049-1057.

Yang, J., 2011. Investigation of brain trauma biomechanics in Vehicle Traffic Accidents Using Human Body Computational Models. In: A. Wittek et al. (eds.), Computational Biomechanics for Medicine: Soft Tissues and the Musculoskeletal System, Springer Science+Business Media, LLC.

Yang, K., 2011. Head Injury Biomechanics. ICB 118 - Injury Biomechanics Short Course, Warsaw, Poland.

Yang, K.H., King, A.I., 2011. Modeling of the brain for injury simulation and prevention. In: K. Miller (Ed.), Biomechanics of the brain, pp.91-110, Springer-Verlag New York.

Yao, J., Yang, J., Otte, J., 2006. Investigation of brain injuries by reconstructions of real world adult pedestrian accidents. Proceedings of IRCOBI Conference, Madrid, Spain, pp.241-252.

Yao, J.F., Yang, J.K., Otte, D., 2008. Investigation of head injuries by reconstructions of real-world vehicle-versus-adult-pedestrian accidents. Safety Science 46(7), 1103-1114.

Yettram, A.L., Godfrey, N.P., Chinn, B.P., 1994. Materials for motorcycle crash helmets - a finite element parametric study. Plastics and Rubber Processing and Applications 22, 215-221.

Yoganandan, N., Sances, A., Pintar, F.A., Walsh, P.R., Ewing, C.L., Thomas, D.J., Snyder, R.G., Reinartz, J., Droese, K., 1994. Biomechanical tolerance of the cranium. SAE Transactions Paper No. 94172, Warrendale, pp.184-188.

Yoganandan N., Pintar F.A., Sances A., Walsh ER., Ewing C.L., Thomas D.J., Snyder R.G., 1995. Biomechanics of Skull Fracture. Journal of Neurotrauma 12(4), 659-668.

Yoganandan, N., Pintar, F.A., Zhang, J., Gennarelli, T.A., Beuse, N., 2005. Biomechanical aspects of blunt and penetrating head injuries. Dublin: IUTAM Symposium Biomechanics of Impacts, pp.173-184.

Yoganandan, N., Li, J., Zhang, J., Pintar, F.A., Gennarelli, T.A., 2008. Influence of angular acceleration-deceleration pulse shapes on regional brain strains. Journal of Biomechanics 41, 2253-2262.

Yu, W.Y., Chen, C.Y., Chiu, W.T., Lin, M.R., 2011. Effectiveness of different types of motorcycle helmets and effects of their improper use on head injuries. International Journal of Epidemiology 40, 794-803.

Zellmer, H., 1993. Investigation of the Performance of Motorcycle Helmets Under Impact Condition. SAE Technical Paper 933113.

Zhang, L., Yang, K., Dwarampudi, R., Omori, K., Li, T., Chang, K., Hardy, W.N., Khalil, T.B., King, A.I., 2001a. Recent advances in brain injury research: a new human head model development and validation. Stapp car crash journal 45, 369-394.

Zhang, L., Yang, K.H., King, A.I., 2001b. Comparison of brain responses between frontal and lateral impacts by finite element modelling. Journal of Neurotrauma 18(1), 21-30.

Zhang, L., Bae, J., Hardy, W.N., et al., 2002. Computational study of the contribution of the vasculature on the dynamic response of the brain. Stapp Car Crash J. 46, 145-164.

Zhang, L., Ramesh, D., Yang, K.H., King, A.I., 2003a. Effectiveness of the football helmet assessed by finite element modeling and impact testing. Proceedings of IRCOBI Conference, Lisbon, Portugal, pp.27-38.

Zhang, L., Yang, K.H., King, A.I., Viano, D.C., 2003b. A new biomechanical predictor for mild traumatic brain injury - a preliminary finding. ASME Bioengineering Conference Proceedings, Florida, USA, pp.25-29.

Zhang, L., Yang, K., King, A., 2004. A proposed injury threshold for mild traumatic brain injury. Journal of Biomechanical Engineering 126(2), 226-236.

Zhang, J., Yoganandan, N., Pintar, F.A., Guan, Y., Gennarelli, T.A., 2007. Biomechanical differences between contact and non-contact head impacts in vehicle crash tests. Department of Neurosurgery, Medical College of Wisconsin, United States, Paper Number 07-0352.

Zhang, L., Yang, K., Gennarelli, T.A., 2008. Mathematical modeling of cerebral concussion: correlations of regional brain strain with clinical symptoms. Proceedings of IRCOBI Conference, Bern, Switzerland, pp.123-132.

Zhang, J., Yoganandan, N., Pintar, F.A., Guan, Y., Shender, B., Paskoff, G., Laud, P., 2011. Effects of tissue preservation temperature on high strain-rate material properties of brain. J. Biomech. 44, 391-396.

Zheng, Z., Yu, J., Wang, C., Liao, S., Liu, Y., 2013. Dynamic crushing of cellular materials: A unified framework of plastic shock wave models. International Journal of Impact Engineering 53, 29-43.

Zhou, C., Khalil, T.B., King, A.I., 1995. A new model comparing impact responses of the homogeneous and inhomogeneous human brain. Proceedings of 39^{th} Stapp Car Crash Conference, Society of Automotive Engineers, pp.121-137.

Zhou, C., Kahlil, T.B., Dragovic, L.J., 1996a. Head injury assessment of a real world crash by finite element modelling. Proceedings of the Advisory Group for Aerospace Research and Development, AGARD-Conference Proceedings, New Mexico, pp.81-87.

Zhou, C., Khalil, T.B., King, A.I., 1996b. Visoelastic response of the human brain to sagittal and lateral rotational acceleration by finite element analysis. Proceedings of IRCOBI Conference, Dublin, Ireland.

Zhu, H.X., Mills, N.J., 1999. Modelling the creep of open-cell polymer foams. Journal of the Mechanics and Physics of Solids 47(7), 1437-1457.

Ziejewski, M., Karami, G., Orrison, W.W., Hanson, E.H., 2009. Dynamic Response of Head Under Vehicle Crash Loading. Paper 09-0432, Proceedings of the 21^{st} International Conference on the Enhanced Safety of Vehicles (ESV), NHTSA, Washington DC.